Universidad Autónoma de Madrid | Escuela de Doctorado

FACULTAD DE CIENCIAS
UNIVERSIDAD AUTÓNOMA DE MADRID

Facultad de Ciencias

Departamento de Química Orgánica

Organic Anolytes Design and Membrane Modification Through Efficient Redox Flow Batteries

Juan Asenjo Pascual

Supervisors: Dra. Pilar Ocón Esteban

Dr. Pablo Mauleon Pérez

Madrid, 2023

HIGREEW

Esta Tesis Doctoral se ha realizado en el Departamento de Química Física Aplicada y en el Departamento de Química Orgánica, bajo la supervisión de los profesores Pilar Ocón Esteban y Pablo Mauleon Pérez.

El presente trabajo ha sido financiado por la Comunidad Europea mediante el Proyecto de investigación HIGREEW, *Affordable High-performance Green Redox Flow Batteries. Grant agreement 875613. H2020: LC-BAT-4-2019.* Además, durante la tesis doctoral se ha realizado una estancia en el grupo del Prof. Pekka Peljo en la Universidad de Turku (Finlandia) financiada por el programa *Erasmus+*.

AGRADECIMIENTOS

Parece mentira que hayan pasado ya cuatro años y este a punto de entregar mi tesis doctoral. Durante este periodo han pasado muchísimas cosas, algunas maravillosas, otras no tan buenas, pero ha sido una magnifica experiencia. En primer lugar, quiero agradecer al Juan del pasado, aquel que tomo una decisión que no era fácil, él decidió cambiar de tesis, volver a empezar el camino porque no estaba motivado en la tesis que empezó. Todo esto supuso un cambio enorme puesto que aquella persona por aquel entonces no tenía ni idea de donde se metía. Por ende, los siguientes en a la lista de agradecimiento son mis supervisores Pilar y Pablo, en primer lugar, porque durante aquel inicio les puse en una situación comprometida y siempre me apoyaron en todo momento. Muchísimas gracias a Pilar por toda la electroquímica y otras muchas cosas que me has ensenado, además de nuestras maravillosas discusiones para ver quien tenía la cabeza más dura. También, agradecer a Pablo que, aunque ha pasado malos momentos también me ha ayudado cuando ha podido. Mención especial merece Juan Ramon que, aunque yo no "era nada suyo" siempre ha estado ahí para ayudarme en todo lo que ha podido en todo momento y gracias a él he aprendido todo lo que sé sobre cálculos computacionales y muchas otras cosas más. Quiero agradecer a mis compañeros de laboratorio por todos esos buenos y malos momentos vividos, por esos ratos de risas en el laboratorio, por las pocas actividades a las que he conseguido llevarlos. A Iván, mi compañero más cercano puesto que ha sufrido tanto como yo los derroteros del HIGREEW, ha habido días que lo hubiese matado y otros en los que hemos disfrutado como enanos en nuestros viajes, aunque sea un "catalufi mohíno" hay que quererlo y le deseo suerte en su nueva etapa. A Laura un millón de gracias por las infinitas veces que me ha ayudado en el laboratorio con cualquier cosa, cuidando de todos nosotros como si fuse nuestra madre. A Carlos y Dani que, aunque nos abandonaron pronto para empezar otro camino siempre han sido un placer estar con ellos y aprender de ellos. Alberto y Carlos que llegaban con su toque de empresa para revolucionar durante unos días el gallinero. Siempre el ambiente en el laboratorio (o casi siempre) ha sido una atmosfera increíble de trabajo y Amistad y eso es lo que son estas personas, amigos.

Con el cambio de doctorado llego un cambio de vida y así aparecí en Mauricio Legendre n4 para revolucionar el piso y pasar unas cuantas fatigas. Aquí hay que destacar al Marco, el Orellana, el Leño. Incontables momentos buenos que hemos pasado juntos en un millón de sitios como nuestro barrio favorito Delicias, la Media Noche, la Bahía Negra, Ponzano, Córdoba, Soria, Finlandia e incluso escalando que aunque nunca ha sido lo suyo siempre lo ha intentado de buena gana. Siempre dispuesto a ir donde quiera que le caliente la cabeza para ir. Con el conocí a los míticos vallisoletanos Diego, Viru, Gonzalo y algún que otro fichaje que siempre me han acogido como uno más de la cuadrilla. En el piso, también estaba "el Viejo" que alguna que otra anécdota nos ha dejado siempre intentando enseñarnos algo. Otros compañeros muy especiales de piso que he tenido han sido dos de mis mejores amigos: "El Migueladas" siempre ha venido a pasar buenos momentos de desconexión y de ocio en Madrid, a liar alguna fiesta en el piso, a ver el futbol o cualquier cosa que se nos pasase por la cabeza, gracias amigo! Como me iba a olvidar del pequeño Timmy, esa persona con la que he pasado tantas y tantas cosas,

durante la carrera, el máster, el doctorado y el resto de la vida indudablemente. Hemos viajado por todos lados Bélgica, Irlanda, México, Italia, Finlandia, Suecia, Estonia y algún sitio más que visitaremos. En todos ellos hemos discutido como cabezones y lo hemos pasado como hermanos (rozando la Muerte en algunos casos) y de la misma manera ha aportado a este doctorado haciendo visitas siempre que he necesitado despejar la cabeza. Aparecía hacíamos dos mil cosas en 48 horas y ya me cansaba de él hasta dentro de varios meses de descanso. NO cambies Timmy. Otra persona que frecuentaba el piso (aunque viviese en Madrid) es mi buen amigo Parla siempre está ahí para cualquier plan de fin de semana para pasarlo en grande, juntarse con mis amigos o acercarme a los suyos, siempre me ha cuidado bien y se lo agradezco.

Con este cambio de vida empecé a escalar más asiduamente con mi gran maestro Jairo que siempre ha intentado hacer de mi un gran escalador, aunque hasta la fecha no lo ha conseguido, incansable amigo. Aquí es donde aparece un grupo de escaladores aficionados Isa, Oscar, Isa (la mala, porque nunca viene), Juanki y todas esas personas que he intentado incluir en la secta. Aquí fue donde conocí una persona que ahora ya es mi vida, Paula. Como si el destino me gastase una broma, presentada por "una covaleda" llego a mi vida y la revolucionó. Empezamos mal, ella no creía que fuese a venir a verme a Finlandia, pero antes de que nos diésemos cuenta estábamos unidos para siempre. Siempre ha hecho que todo sea fácil y maravilloso, siempre ha cuidado de mí y hemos pasado increíbles momentos desde entonces. Tuvo que venir a Laponia a buscarme como un esquimal, perdimos los móviles, mojamos las zapatillas y robamos un langostino en el País Vasco, pero siempre esta hay para ayudarme, quererme y sacarme una sonrisa. ¡Te quiero!

Ahora es el momento de mi familia, a mis padres que siempre me han apoyado en todas las decisiones que he tomado (diciendo que vaya trabajo más tonto tenía o que si me iban a subir el sueldo por sacar alguna publicación) pero siempre han estado y estarán ahí. PD: ¡Que hubiese sido de mi sin la comida de mi madre y sus maravillosas recetas que ahora reproduzco como buen químico! Mil gracias a mi hermana porque indudablemente no sería quien soy sin ella. Ella me ha ensenado a luchar por todo, a tener valores y a pensar más allá. No puedo ni pensar la cantidad de veces que me ha salvado cuando he tenido cualquier tipo de problema y siempre, siempre se ha preocupado por mi (a veces demasiado) pero agradezco muchísimo que sea mi hermana y que no me falte nunca. A mi hermano (y la Raquel) también le agradezco el millón de cosas que me han ensenado, cosas que no aparecen en los libros pero que indudablemente me han hecho llegar a donde estoy ahora, siempre dispuestos para preparar alguna zalagarda que otra. Es el momento de agradecer a los bichos de la casa Alba y Samuel esas pequeñas tempestades que llegaron para alegrarme la vida y que no podría vivir sin ellos, os quiero pequeños!

Me he acordado de los hobbies nuevos, pero también quiero destacar gente de los viejos, esos compañeros de waterpolo con lo que he disfrutado muchísimo y he sufrido muchísimo, especialmente algunos que quedan en mi vida como Monty (y Vero), y Arturo que, aunque no nos vemos todo lo que nos gustaría sé que siempre están ahí.

A mi gente de Duruelo, a mis amigos del librillo incontables momentos que hemos pasado estos 4 años contando con bodas y bautizos. Especial mención a mis quintos de siempre Toma, Pelu, Cuba y Marino que son como una familia. A los bandidos de la banda y a la banda de Sanse que con nuestros ratos musicales y los post ensayos siempre han conseguido alegrarme los fines de semana. A mi buen maestro Rodrigo Nieto que siempre ha sido un ejemplo de todo clarinete, futbol, pasión por el pueblo y persona.

Quiero agradecer a mis antiguos compañeros de laboratorio FRONCAT que como yo han sufrido una tesis bastante dura y que aunque abandoné el laboratorio pronto siempre me han tenido en cuenta e invitado a sus jaleos. Entre ellos destaco a Thomas, Andrea y Tushar (jajajaja) con los que desarrollé parte de los trabajos que hice allí. A mis compañeros más cercanos del departamento, Javi, Shin (increíbles profesionales de la química que no hemos pasado mucho tiempo juntos en el laboratorio pero si fuera de él), Inés, Cristian el Grandullón, Jorge (por ensenarme todo lo que se en una servilleta de papel según él), Miki, (soriano como yo y que llevo en el corazón), Oscarinho, Ogcar, Sonia con su buen humor y sus palmeritas, siempre me habéis ayudado ya sea con ideas consejos o dejándome reactivos sois una gente maravillosa.

Por último, me gustaría agradecer a los colaboradores que he tenido en otras instituciones:

- En el CICenergigune gracias al padrazo Edu que me permitió visitarlo unas semanas y trabajar con él, siempre me ha dado buenos consejos y ayudado en todo lo que ha podido con el HIGREEW y todo lo demás.
- For my good colleague from Prague, Petr Mazur, he is one of the most talented chemists that I have never ever known and a great guy. I have learnt a lot from him about RFB and enjoy each one of our discussions.
- From Finland, there I spent almost four amazing months where I met amazing people in the lab: Jenna, Mahsa, Ali, Mahdi, Cedrik, Lena. I thank to prof. Pekka Peljo for allowing me to be there and for all the work done together. En Finlandia también conocí a un compañero de trabajo y de vida, mi grandísimo amigo el boludo Gabriel. Siempre me acogió con los brazos abiertos y me llevo a todo tipo de lugares, saunas, futbol, viajes etc. Jenna (and Urjo) is the most adorable person in the world opening her house and always with a smile on her face. Por último, el güero Eduardo, un mexicano con el que aprendí mucho de sus pinches adsorciones y con el que pasé buenos ratos dentro y fuera del lab. Además de la gente del lab, conocí (gracias como no a Gabriel) el grupo de españoles más maravilloso del mundo y que hizo mucho más amena la estancia en Finlandia. Siempre contaban conmigo para cualquier tipo de excursión o actividad son una gente maravillosa y los llevo en mi corazón: Gracias Fabi, Yoli (la filósofa), Bhanu, Bea, Fran, Miguel y Noelia entre otros.

Table of Contents

NOTE: Each section presents their own references.

1 Abstract / Resumen

1. Abstract

Human development has brought about advancements in technology, healthcare, and human rights, contributing to an improved quality of life. However, this progress has also led to certain challenges, such as the ever-increasing demand for resources. To address the energy demand, the utilization of renewable energy sources has emerged as a clear solution, offering eco-friendly and virtually unlimited energy options. Solar and wind energy are among the most developed renewable energy sources. However, the intermittent nature of wind and solar power poses a significant challenge.

Energy storage has become crucial to store surplus energy generated by renewable sources for later use. Electrochemical Energy Storage (EES), particularly Redox Flow Batteries, have emerged as a versatile solution for energy storage, ranging from domestic applications to large-scale storage. Redox Flow Batteries offer fast response times, long lifetimes, reduced environmental impact, low cost, and high round-trip efficiency. The scientific community has dedicated significant attention to the development of this technology, resulting in a growing number of research papers, patents, projects, and companies.

Vanadium Redox Flow Batteries (VRFB) currently represent the state-of-the-art technology, with many companies and large-scale batteries utilizing this system. However, challenges persist, including the limited availability and high cost of vanadium electrolyte, the precipitation of V_2O_5 at high temperatures (> 40 °C), low solubility at low temperatures, and the volatile price of vanadium. Recognizing the European Union's reliance on China, Australia, and Africa for 85% of the vanadium supply required for VRFB, the European Commission has been funding research projects to develop new organic earth-abundant electrolytes as potential substitutes for vanadium electrolyte in Redox Flow Batteries.

This thesis has received funding from the HIGREEW project, which aims to develop and validate a redox flow battery utilizing a new water-soluble, low-cost organic electrolyte. The project also focuses on optimizing low-resistance membranes and fast electrode kinetics to achieve high energy density and long-term durability. The thesis is structured around three key components: the investigation of organic electrolytes (**Chapter 1**), the development of ion exchange membranes (**Chapter 2**), and the testing of single-cell RFB systems (**Chapter 3**).

- **Organic electrolyte:** In this chapter, we focused on the synthesis and electrochemical characterization of 2,2'-bipyridinium anolytes as the initial candidates for the project, in collaboration with CIC EnergiGUNE. DFT calculations were employed to investigate the impact of structural parameters and the incorporation of various substituents on their electrochemical properties, including redox potential and kinetic constants. We developed a predictive model based on Natural Bond Orbitals (NBO) delocalization and Atomic Dipole Corrected Hirshfeld

(ADCH) charge distribution of the radical-reduced species to understand and predict the stability and performance of the 2,2'-bipyridinium anolytes in the battery. Our findings identified compound **4** as the most stable and promising anolyte for further testing.

Additionally, during my international research stay in Turku, Finland, we successfully synthesized and electrochemically characterized a novel triazine anolyte for multiple electron storage. This new triazine anolyte exhibited three reversible redox processes for 4 electrons at -0.47 V, -0.62 V, and -0.82 V *vs* Ag|AgCl (3 M KCl), demonstrating fast kinetics, high solubility (>0.9 M), and diffusion coefficients. These properties make the new derivative a compelling candidate for multiple electron storage in RFB. Moreover, we observed a strong correlation between the solubility of the new triazine and the salt concentration, suggesting a significant interaction between the solubilizing group ($-SO_3^-$) and the pyridinium moieties. The details of this work on the organic electrolyte can be found in **Chapter 1**.

- **Ion Exchange Membrane:** The primary objective of our research group within the HIGREEW consortium was to select, characterize, and modify commercially available ion exchange membranes (IEM) that meet the requirements of HIGREEW in terms of permeability, cost, and performance. To achieve this, we conducted electrochemical characterization of various commercial membranes, evaluating important parameters such as swelling ratio, water uptake, ion exchange capacity, ionic conductivity, and permeability. Based on this initial screening, we identified the most promising membranes: two cationic membranes (FS-950 and E-630(K)) and two anionic membranes (FAA-3-50 and FAA-3-30PE).

  Subsequently, these selected membranes were subjected to modification through a cost-effective and scalable *in situ* polymerization method using pyrrole and aniline. The modification of membranes with polypyrrole resulted in a significant reduction in permeability while maintaining a reasonable level of resistance. The modified membranes were thoroughly analyzed and characterized to understand the impact of the modification on transport phenomena. A detailed account of the selection, characterization, and modification processes can be found in **Chapter 2**.

- **Single-cell results:** First, a comprehensive study was conducted to establish a strong theoretical foundation for redox flow batteries and align it with the experimental techniques used for battery characterization. This provided a solid background for the subsequent research. The anolytes developed in Chapter 1 underwent thorough evaluation, yielding the following corroborations:

  i) The predicting model and experimental results regarding the stability of bipyridinium anolytes were found to align. Compound **4** exhibited the highest stability, with a capacity decay of 0.16% per day compared to the unsubstituted 2,2'-bipyridinium (Compound **2**) which showed a capacity decay of 0.75% per day.

Furthermore, a detailed characterization of the plausible degradation pathway for the bipyridinium anolyte was achieved.

ii) In this same chapter, the **$(SPr)_3$4TpyTz** anolyte demonstrated the ability to store multiple electrons without significant capacity decay. The concentration of the supporting electrolyte was found to have a significant effect on the solubility of the reduced state. A battery using 100 mM of the triazine anolyte against 100 mM $K_4[Fe(CN)_6]$ showed no capacity decay and achieved an energy efficiency of approximately 75% under appropriate conditions. Increasing the concentration to 200 mM of **$(SPr)_3$4TpyTz** against 300 mM $K_4[Fe(CN)_6]$ resulted in a small capacity decay of 0.44% per day and no crossover within a 14-day period. Furthermore, the system was investigated using the third and fourth electrons, revealing a significant capacity decay and an increase in electrolyte pH, suggesting a degradation mechanism involving the protonation of the reduced triazine.

1. Resumen

El desarrollo humano ha traído avances en tecnología, salud, y derechos humanos contribuyendo a aumentar la calidad de vida. Sin embargo, este progreso también ha traído ciertos desafíos como la creciente demanda de recursos. Para paliar este reto, la utilización de fuentes de energía renovables ha aparecido como una clara solución ofreciendo una versión medio ambientalmente favorable y virtualmente ilimitada. Las energías solar y fotovoltaica son las mas desarrolladas entre todas las energías renovables a pesar de la naturaleza intermitente del sol y el viento.

El almacenamiento de energía se ha convertido en un elemento crucial para almacenar los excesos energéticos generada por fuentes renovables, para su uso posterior. El almacenamiento electroquímico de energía (EES), en particular, las baterías de flujo redox, se ha revelado como una versátil solución para el almacenamiento de energía, desde uso doméstico hasta el almacenamiento a gran escala. Las baterías de flujo redox ofrecen tiempo de respuesta rápida, larga durabilidad, menor impacto ambiental, bajo coste y alta eficiencia global. La comunidad científica ha centrado parte de su atención en el desarrollo de esta tecnología, lo que ha dado lugar a un número creciente de artículos científicos, patentes, proyectos de investigación y compañías.

La batería de flujo redox de todo Vanadio representa actualmente el estado del arte de esta tecnología y varias compañías y baterías a gran escala utilizan este sistema. Sin embargo, persisten ciertos retos, como la limitada disponibilidad y el elevado coste del electrolito de vanadio, la precipitación del V_2O_5 a temperaturas (> 40 °C), la baja solubilidad a bajas temperaturas y la volatilidad de su precio. La unión europea ha reconocido su mala posición en este tema puesto que China, Australia y África concentran el 85% del vanadio disponible en la tierra. Por esta razón, la Comisión Europea ha estado financiando diferentes proyectos de investigación con el objetivo de desarrollar nuevos electrolitos basados en material abundantes en la tierra para baterías de flujo redox como posible sustituto al electrolito de vanadio.

Esta tesis ha recibido financiación del proyecto HIGREEW, el cual pretende desarrollar y validar una batería de flujo redox usando un nuevo el electrolito orgánico, soluble en agua y barato. El proyecto también se centra en la optimización de membranas con baja resistencia y electrodos con rápidas cinéticas para alcanzar altas densidades energéticas y larga durabilidad. Esta tesis se ha estructurado en torno a tres componentes claves: la investigación de electrolitos orgánicos (**Capítulo 1**), el desarrollo de membranas iónicas de intercambio (**Capítulo 2**), y el testeo de sistemas monocelda de baterías de flujo redox (**Capítulo 3**).

- **Electrolito orgánico:** En este capítulo nos hemos centrado en la síntesis y la caracterización electroquímica de anolitos de 2,2'-bipiridinio como candidatos iniciales para el proyecto, en colaboración con el CIC EnergiGUNE. Se han empleado cálculos computacionales DFT para investigar el impacto de los parámetros estructurales y la incorporación de varios sustituyentes en sus propiedades electroquímicas incluyendo los potenciales redox y las constantes

cinéticas. Se ha desarrollado un modelo predictivo basado en la deslocalización NBO (del inglés, "*Natural Bond Orbitals*") y en la distribución de cargas ADCH (del inglés, "*Atomic Dipole Corrected Hirshfeld*") de las especies reducidas radicalarias para entender y predecir la estabilidad y el rendimiento de los anolitos de 2,2'-bipiridio en la batería. Este modelo identifico el compuesto **4** como el más estable y prometedor anolito para un posterior testeo.

Adicionalmente, durante mi estancia de investigación internacional en Turku, Finlandia, se desarrolló exitosamente la síntesis y caracterización electroquímica de un novedoso anolito basado en la molécula de triazina para el almacenamiento de varios electrones. Este nuevo anolito de triazina presenta tres procesos redox reversibles de 4 electrones a -0.47 V, -0.62 V, and -0.82 V *vs* Ag|AgCl (3 M KCl), demostrando rápidas cinéticas, alta solubilidad (>0.9 M) y coeficientes de difusión. Estas propiedades hacen de este nuevo derivado un competente candidato para el almacenamiento multielectronico en baterías de flujo redox. Además, se observó una fuerte relación entre la solubilidad de la nueva triazina y la concentración de sal sugiriendo una significante interacción entre los grupos solubilizantes ($-SO_3^-$) y los fragmentos piridinicos. Los detalles de este trabajo sobre electrolitos orgánicos pueden encontrarse en el **Capítulo 1**.

- **Membranas de intercambio iónico:** El principal objetivo de nuestro grupo de investigación en el consorcio HIGREEW fue seleccionar, caracterizar y modificar membranas de intercambio iónico comercialmente disponibles que cumplieran los requisitos del HIGREEW en términos de permeabilidad, coste y rendimiento. Para alcanzar este objetivo, se llevó a cabo la caracterización electroquímica de varias membranas evaluando importantes parámetros como el *swelling ratio,* adsorción de agua, capacidad de intercambio iónico, conductividad iónica y la permeabilidad. Basado en este cribado inicial se identificaron las membranas más prometedoras: dos membranas catiónicas (FS-950 y E-630(K)) y dos aniónicas (FAA-3-50 y FAA-3-30PE).

  Después, esas membranas fueron modificadas mediante un método económicamente viable y escalable, la polimerización *in situ* de pirrol y anilina. La modificación de membranas con polipirrol resulto en una significante reducción de la permeabilidad mientras se mantenía una razonable resistencia. Las membranas modificadas fueron intensamente analizadas y caracterizadas para entender el impacto de esta modificación en el fenómeno de transporte. Un detallado informe de la selección, caracterización, y procesos de modificación se halla en el **Capítulo 2**.
- **Resultados de monocelda:** En primer lugar, se realizó un estudio exhaustivo para establecer una base teórica sólida para el estudio de baterías de flujo redox y su relación con las técnicas experimentales utilizadas en la caracterización de baterías. Esto proporciono una buena base para la investigación posterior. Los anolitos desarrollados en el capítulo 1 se sometieron a evaluación resultando en las siguientes demostraciones:

i) El modelo predictivo y los resultados experimentales con respecto a la estabilidad de los anolitos de 2,2'-bipiridinio confluyeron en los mismos resultados. El compuesto **4** exhibió la estabilidad más alta con un Perdida de capacidad de 0.16% por día comparado con el derivado de 2,2'-bipiridinio sin sustituir (Compuesto **2**), el cual mostro una pérdida de capacidad de 0.75% por día. Además, una detallada caracterización del posible mecanismo de degradación para los anolitos de bipiridinio fue propuesto.

ii) En este mismo capitulo, el anolito **(SPr)$_3$4TpyTz** demostró su habilidad para el almacenamiento de múltiples electrones sin mostrar una significante Perdida de capacidad. La concentración del electrolito soporte demostró tener un efecto significativo en la solubilidad de la especie reducida. Una batería que utilizaba 100 mM del anolito de triazina contra 100 mM de $K_4[Fe(CN)_6]$ no mostró ninguna pérdida de capacidad y además alcanzaba una eficiencia energética del 75% en las condiciones adecuadas. Aumentando la concentración del anolito a 200 mM de **(SPr)$_3$4TpyTz** contra 300 mM $K_4[Fe(CN)_6]$ resultó en una pequeña pérdida de capacidad de 0.44% por día sin mostrar *crossover* en un periodo de 14 días. Además, el uso del tercer y cuarto electrón de esta triazina fue investigado, revelando una significante pérdida de capacidad y un aumento del pH del electrolito, sugiriendo un posible mecanismo de degradación basado en una protonación de la triazina reducida.

2. Introduction

2. Introduction

The rise in temperatures and CO_2 concentration in the atmosphere, as well as the melting of polar ice caps, among other phenomena, are clear signs of climate change.[1] This climate change is primarily caused by the consumption of fossil fuels, which result in greenhouse gas emissions. Therefore, it is crucial to drastically reduce the consumption of fossil fuels. Various strategies have been proposed to address this issue, such as the electrification of transportation and the integration of renewable energies into the electrical grid.[1-3]

Renewable energy sources are expected to become the primary energy source by 2050, with solar and wind energies projected to account for 70% of global production.[4] Despite their natural, self-replenishing nature and low or zero carbon footprint, the implementation of these energy sources has been hindered by their intrinsic intermittency.[5] Therefore, achieving significant advancements in areas like road electrification and the integration of renewable energies into the electrical grid requires efficient Energy Storage Systems (ESS).[6,7]

Consequently, over the past few years, the development of various ESS technologies, including fuel cells,[8] flywheels,[9] compressed air systems,[10] supercapacitors,[11] and different types of batteries, has gained significant attention and become a widely studied field.[12-16]

However, most ESSs suffer from notable drawbacks. For instance, capacitors and supercapacitors store energy through charge separation, providing a quick response but delivering low energy density.[17] Compressed air systems can store large quantities of energy but have a considerable environmental impact due to land use and the construction of reservoirs.[10] Flywheels, which store kinetic energy using a rotating disk connected to a generator, can achieve high power and energy density but exhibit very low efficiencies over long periods.[18]

Among the various battery technologies developed, Lithium-ion batteries (LIB) have found widespread use in portable electronic devices such as mobile phones, laptops, and electric vehicles, as well as in grid-scale energy storage. LIB offer high energy density, efficiency, specific capacity, voltage, and excellent cycling performance. They also have features like lack of memory, little self-discharge, and wide temperature operation.[19] However, LIB face challenges related to safety, such as the risk of fires and explosions,[20] as well as issues concerning the formation of the solid-electrolyte interphase and volume expansion, which can compromise battery performance.[21]

Sodium-ion batteries (SIB) have been proposed as potential competitors to LIB due to their lower cost and higher availability. However, the higher weight of SIB hinders their substitution for LIB in portable electronic devices. Moreover, SIB exhibit poorer electrochemical cycling performance and lower voltages compared to LIB, making them less suitable for large-scale energy storage.[16]

As a result, attention has recently turned to Redox Flow Batteries (RFB) due to their higher efficiencies, extended operational times, low cost per unit energy and cycle, ability to decouple power and capacity, and suitability for large-scale energy storage. These characteristics make RFB well-suited to stabilize the inherent intermittency of renewable energies and ensure a steady input of energy to the grid.[22,23] The working principles of RFB will be discussed in the following section.

2.1. Redox Flow Batteries

A Redox Flow Battery (RFB) is an electrochemical energy storage device that directly and reversibly converts chemical energy, stored in two or more chemical components, into electrical energy. RFB have emerged as highly promising options for large-scale energy storage systems ranging from kilowatt-hours (kWh) to megawatt-hours (MWh) due to their unique ability to decouple capacity (volume of external tanks) and power (size of the electrochemical cell or stack).[24]

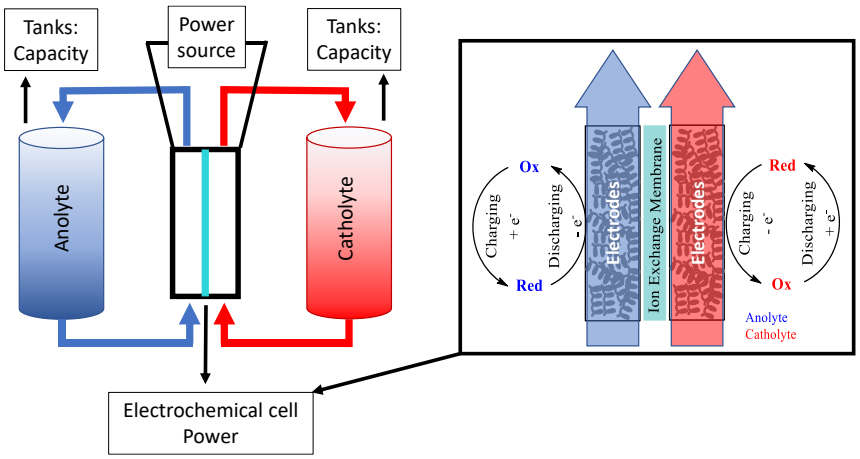

Figure 1: Schematic representation of a redox flow battery and the electrochemical cell. The blue side and red side correspond to the anolyte and catholyte, respectively.

In an RFB (Figure 1), two active redox materials or electrolytes, dissolved in aqueous or organic solvents, are housed in external tanks and continuously pumped through an electrochemical cell. The electrochemical reactions of the redox species occur on the surface of inert porous electrodes, typically made of carbonaceous-based materials. These electrodes are usually separated by ion-exchange membranes (IEM), which prevent electronic connection between the electrodes and the mixing of electrolytes, while allowing ion passage to maintain electrolyte electroneutrality. The electrolytes contain one or more redox active materials (RAM) used for energy storage. Additionally, electrolyte solutions often contain other components such as dissolved salts or acidic/alkaline additives as supporting electrolytes, which enhance ionic conductivity and establish a specific pH in the solution. Efficient ion transport through the IEM is crucial for completing

the electrical circuit of the entire battery and plays a vital role in achieving optimal battery performance.[25]

Overall, RFB are complex systems comprising different components and interactions that significantly influence the characteristics and performance of the battery.

2.2. RFB parameters

Understanding the different RFB characteristics and experimental protocols is mandatory for further progress in the development of this technology. To this end, several parameters have been designed which show the quality of the battery performance. These are summarized below.[26,27,28]

1. The *Coulombic Efficiency* (CE) describes the relationship between the total charge extracted from the battery during the discharging process and the charge supplied during the charge process (Equation 1). All batteries have CE losses due to parasitic electrochemical and chemical reactions (hydrogen evolution, self-discharge reaction with oxygen), active species crossover, and degradation of the active materials, among others.

$$Coulombic\ Efficiency\ (CE) = \frac{Q_{discharge}}{Q_{charge}} = \frac{\int_0^t I_{discharge} dt}{\int_0^t I_{charge} dt} \quad (1)$$

2. *Voltage Efficiency* (VE) is another important parameter to evaluate the battery efficiency. VE represents the ratio between the average discharge voltage and the average charge voltage, and it is related to the operation current density, ionic conductivity of the membrane and electrolytes, electronic conductivity and catalytic activity of electrode materials, flow rate of electrolyte, and mass transport of active species to the electrode surface (Equation 2).

$$Voltage\ Efficiency\ (VE) = \frac{\bar{V}_{discharge}}{\bar{V}_{charge}} = \frac{\int_0^t V_{discharge} dt}{\int_0^t V_{charge} dt} \quad (2)$$

The difference between these key values is caused by a variety of overpotentials which have been widely studied by polarization curves (Figure 2a). The main contributions to the losses in a Redox Flow Battery originate from i) activation loss, ii) ohmic loss (*iR*), and iii) mass transport loss. Activation loss is associated to the activation/polarization of the electrodes: the main contribution appears at low current densities, and it is related to the kinetics of the charge transfer reaction (the energy needed to overcome the activation energy associated with the redox process in the electrode-electrolyte interfaces). Ohmic loss causes a voltage drop and is associated to resistance of the flow of electrons through the electrically conductive components, as well as to the flow of ions through the membrane, and can be expressed by Ohm´s law. Thus, in this region, the cell voltage linearly decreases with current densities. Finally, the last contribution is related with the lack of active material in the electrode surface proximity due to conversion at high

current density, significantly decreasing cell voltage. The individual contribution of the overall cell resistance can be differentiated by Electrochemical Impedance Spectroscopy (EIS, Figure 2b). The intercept in the real axis at high frequencies from the Nyquist plot corresponds to the ohmic resistance of the cell (R_Ω). This parameter includes the contribution of ohmic resistances of the ion exchange membrane, the carbon felt electrode and the contact resistance between the bipolar plates and the felt electrodes. In the middle frequency range, the charge transfer resistance is observed (its value is proportional to width of the semicircle), while at low frequency range diffusion and mass transport are dominant. Furthermore, variation in the EIS during the battery cycling could suggest changes in polarization resistance associated to electrode modification, degradation of materials, and optimizing parameters.[29] From the discharging polarization curve (Figure 2a), the power density (mW/cm^2) of the system can be calculated by multiplying the current density (j) with the cell potential (U). This parameter gives us a quick idea about optimal range of current densities with respect to its performance. Typically, these curves are measured under various conditions such as SOC (State Of Charge), temperature, or flow rate to see the effect of these parameters on the battery performance. Also, it can be significantly affected by the flow dynamic of the system.[23,30]

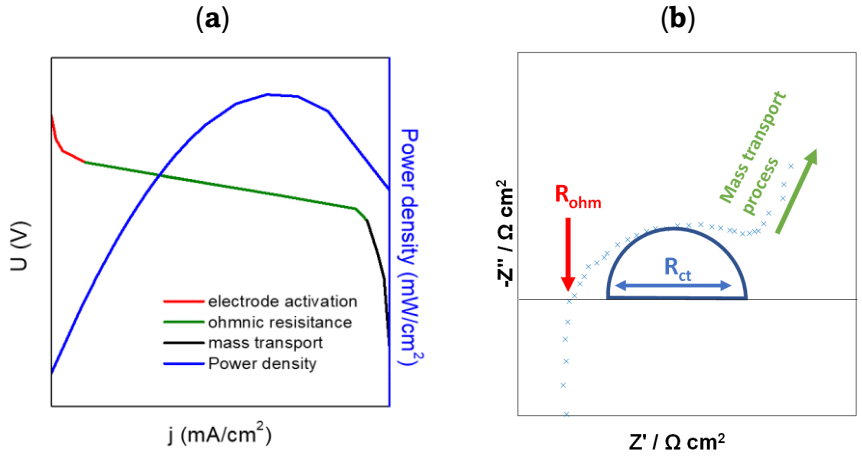

Figure 2: (a) Schematic representation of the discharging polarization curve showing the main losses regarding each resistance in the system and the power density achieved (b) Schematic representation of the different resistance identified in EIS of the whole system.

3. Finally, both parameters (Voltage efficiency and Coulombic Efficiency) merge as a final parameter called *Energy Efficiency* (EE). EE is the relationship between the energy stored during the charging and the energy released during discharging processes (Equation 3). Typical EE values of RFB are in the 50-90% range, depending on the applied current density, operating conditions, and internal component quality.

$$Energy\ Efficiency\ (EE) = CE \cdot VE = \frac{\int_0^t I_{discharge} \cdot \bar{V}_{discharge} \cdot dt}{\int_0^t I_{charge} \cdot \bar{V}_{charge} \cdot dt} \quad (3)$$

4. The RFB can work at different operation modes. One of the most used methods to charge/discharge the battery is carried out galvanostatically, i.e., at constant current, until the battery reaches the given charging or discharging voltage limits (cut-offs). The use of higher currents to charge/discharge the battery leads to use smaller use of theoretical capacity of the active material (i.e., lower capacity utilization, Equation 4), because higher currents involve higher overpotential in the system (and thus the charging voltage limit is reached at lower SOC, and similarly for discharging). *Capacity Utilization* is the relationship between the practical capacity storage in the system *vs*. the theoretical capacity that could be stored at a given testing condition and it is calculated by Equation 4:

$$Capacity\ Utilization\ (CU) = \frac{Q_{discharge}}{Q_{theoretical}} \quad (4)$$

Where $Q_{theoretical}$ is the number of moles of electrons that the redox active material in the limiting side can store (Faraday's law).

5. For most RFB technologies, Potential - Current density (U-*j*) dependence is linear in a relatively broad range of current densities, and thus, the so-called *Area Specific Resistance* (ASR) parameter can be used to describe the battery performance under given conditions (SOC, electrolyte flow rate, temperature, etc.) (Equation 5). It provides information about the total resistance of the cell, and its units are Ohm·cm^2. ASR represents the resistance of the different contacts, current collectors, bipolar plates, carbon felts, electrolyte, and membrane contributions. It can be determined following Ohm's Law and can be calculated from the linear part of the Load Curves (LC).

$$Area\ Specific\ Resistance\ (ASR) = \frac{V_2 - V_1}{I_2 - I_1} \cdot A \quad (5)$$

Redox Flow Batteries (RFB) are not ideal devices, so a significant amount of work must be done to implement them in the electrical grid. All batteries present certain inefficiencies that make them unsuitable for worldwide implementation. Each component incorporated in the RFB contributes to these inefficiencies in different ways. The most common parameters that cause efficiency losses are outlined below.

In the case of the electrolyte, various side reactions lead to capacity fade, compromising the battery's lifetime. Aziz *et al.*[31] have reported that redox active materials generally degrade faster at higher state of charge (SOC). This is consistent because charged species are more reactive, so a higher SOC means a higher amount of these sensitive species. It is worth mentioning the electrochemical degradation that a RFB could undergo at any SOC during charging, due to the generation of H_2 and O_2, among other phenomena. Different mechanisms for these side reactions have been studied over the last ten years, including precipitation of inorganic electrolytes, π-π stacking, de-alkalization of viologen derivatives, self-oxidation, ring opening of TEMPO derivatives, Michael addition, and dimerization of quinones.[32]

Loss of stability in the redox active material leads to a decrease in battery capacity, known as *Capacity Decay* or *Capacity Fade*. The capacity loss per cycle is typically evaluated through charge-discharge cycling and can be expressed in absolute values (mAh/cycle or per day) or as a percentage of theoretical capacity (Equations 6 and 7, respectively). It is true that time-related capacity decay provides more information because the duration of the cycle depends on the battery capacity. (tank volume) Therefore, the longer the cycles, the more significant the negative effects of crossover and degradation will be. When high Capacity Utilization (CU) values are achieved, higher concentrations of charged species are present, increasing the probability of experiencing significant decomposition or secondary reactions. Here is the formula to calculate Capacity Decay:

$$Capacity\ decay\ (CD) = \frac{(-dQ_{discharge})}{cycles}\left(\frac{mAh}{cycle}\right); \quad (6)$$

$$Capacity\ decay\ (CD') = \frac{(-dQ_{discharge})}{(Q_{theoretical} \cdot cycles)} \cdot 100\ \left(\frac{\%}{cycle}\right); \quad (7)$$

Another parameter related to capacity decay is capacity retention, which represents the remaining capacity after a given number of cycles and/or a certain period of time. It is commonly expressed as a percentage of the initial capacity.

In addition to the degradation of active species, the cross-mixing of active species between the two tanks across the ion-exchange membrane can significantly contribute to capacity fade. This phenomenon, known as *crossover*, not only leads to self-discharge but also contributes to capacity decay. In the case of asymmetric (non-mixed) electrolytes, cross-contamination can cause changes in crucial parameters such as conductivity, viscosity, and redox potential of the electrolytes. Moreover, the interaction between charged species and ion-exchange groups with opposite charges on the membrane can promote adsorption or fouling, thereby increasing membrane resistivity.

The last significant contributor to capacity fade is parasitic electrode reactions, such as hydrogen and oxygen evolution reactions at the negative and positive electrodes, respectively. These reactions can occur whenever the electrode potential extends beyond the water stability potential window (1.23 V). Their occurrence is more prominent at higher SOC and high charging currents.[33]

2.3. Internal cell-components

Once the fundamental principles of RFB have been described, let's now delve into the various components and how they can affect battery performance.

2.3.1. Ion-Exchange Membranes (IEM).

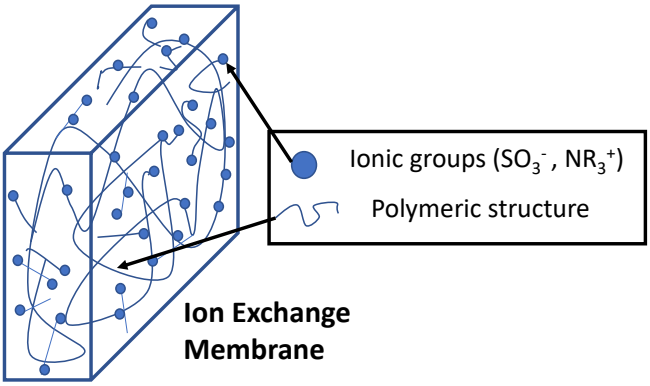

Figure 3: Schematic representation of an ion exchange membrane.

The ion-exchange membrane is one of the key components of RFB. As mentioned earlier, it separates the anolyte and catholyte while allowing the passage of ions (anions and/or cations) to balance the charges during the redox processes. Generally, homogeneous membranes consist of polymeric structures with different grafted ionic groups that facilitate ionic movement and provide selectivity to transfer ions with positive or negative charge (Figure 3).[34] The membranes can be divided into two main groups based on the nature of the fixed ionic groups: Cation Exchange Membrane (CEM) and Anion Exchange Membrane (AEM). CEM have negatively charged groups that allow the exchange of cations (typically sulfonate, carboxylate, or phosphate groups). On the other hand, AEM have positively charged ionic groups (typically ammonium, sulfonium, or phosphonium groups) that allow the passage of anions.

The most well-known and widely used ion-exchange membrane (IEM) was developed by DuPont in the 1960s. This membrane is a copolymer of Perfluorosulfonicacid (PFSA) and Polytetrafluoroethylene (PTFE). Nafion® has been extensively employed as a separator in fuel cells and now in RFB due to its high chemical and mechanical stability in harsh conditions. Additionally, it exhibits high ionic conductivity, especially in highly acidic solutions. However, despite the excellent characteristics of Nafion® membranes, one of the main disadvantages is the high crossover and/or migration of active species through the membrane, as well as the high cost, representing up to 30% of the total system cost.[35] The issue of crossover has been mentioned before, and therefore, considerable efforts are being made to develop and modify IEM.[36-39] IEM can also be classified into fluorinated, partially fluorinated, and non-fluorinated membranes based on the chemical nature of the ionomers. For instance, Nafion membrane is an example of a fluorinated membrane, which contributes to its elevated cost. Fluorinated membranes are more stable under harsh conditions, but the starting materials are more expensive. To reduce the cost of IEM, new non-fluorinated and partially fluorinated membranes have been developed. Porous non-ionic separators have

also been used when the redox active materials are too large to pass through the pores, allowing only ions to pass.[40]

The main characteristic parameters of ion-exchange membranes include Ion Exchange Capacity, Water-Uptake, Swelling Ratio, Ionic Conductivity, Permeability, and Permselectivity, among others (see experimental and theoretical procedures). Ion Exchange Capacity (IEC) represents the concentration of ion-exchange groups (typically related to the mass of the dry membrane) that allow ions to pass through. Various methods have been reported to measure the IEC, such as ion-exchange with acid-base titration or pH measurement.[41] An ideal membrane should exhibit high IEC values, but this value cannot be too high as it may render the membranes mechanically unstable or less selective, compromising battery performance.[42] It should be noted that the membranes must have good chemical and mechanical stability under battery operating conditions. The ionic conductivity of the membrane is one of the most crucial parameters since increasing it improves cell performance in terms of voltage efficiency by reducing the ohmic resistance. At the same time, the membrane must be electronically insulating, otherwise, the battery will short-circuit. The ionic conductivity can be measured by different methods, either in the in-plane or through-plane direction. The ohmic resistance can be determined as the intercept of the Nyquist diagram with the real axis in the high-frequency zone of the electrochemical impedance spectroscopy (EIS), which is the most commonly used technique. Additionally, by measuring polarization curves (also referred to as load curves) of the battery cell at different SOC, the area-specific resistance of the cell can be determined, which typically includes the significant contribution of membrane ohmic resistance.

The membrane should exhibit suitable physical properties in terms of reasonable water uptake and swelling ratio (typically found to be <35%). Highly hydrophilic membranes would likely dissolve in the operating media, compromising their mechanical characteristics, especially those with a low degree of grafting.[43] and could potentially lead to battery failure. Therefore, different pretreatments or conditioning methods have been implemented to improve the performance of the ion-exchange membrane. This conditioning step plays a vital role in affecting the battery's resistance, self-discharge time, coulombic efficiency, and permeability.[44,45]

IEM play a vital role in battery performance as the major resistance in the entire system comes from the membrane. Therefore, important parameters such as coulombic efficiency (related to the crossover of redox active materials), voltage and energy efficiency (linked to the resistance of the battery), and energy density depend on the performance of the membrane.

2.3.2. Porous inert electrodes

In the case of electrodes, the main difference with conventional batteries (e.g., Li-ion and Na-ion batteries[46]) is that the energy is not stored in the electrodes but in

the electrolyte solutions. The electrodes simply provide the surface sites where the charge transfer of the electrode reactions takes place. In contrast, in batteries where the electrode participates in the electrochemical reaction, the electrode undergoes transformation, including phase and/or structural changes.

Electrodes in RFB are primarily made from carbonaceous materials. These electrodes have a high porosity, with almost the entire electrode being air. Therefore, the electrode must be compressed in the RFB to ensure contact with the bipolar plate. Electrodes must be chemically stable as they are constantly in contact with electrolytes (strong acids, bases, oxidizing, and reducing agents), and electrochemically stable within the potential window of the battery. However, the most important characteristic is excellent electrical conductivity, allowing fast redox reactions.[47]

Graphite, which consists of stacked 2D sheets of six-membered aromatic rings of sp^2 hybridized atoms, is the most thermodynamically stable allotrope of carbon. This allotrope is typically of high interest for electrochemical energy conversion, especially if it contains defect-rich variants or amorphous carbon (to increase electrical conductivity). Other allotropes such as graphene[48] and Carbon nanotubes (CNT)[49] have attracted researchers' attention, opening new possibilities for the application of carbonaceous electrodes in energy storage. These carbon materials are prepared by pyrolysis of carbon, leading to more graphitic materials at higher temperatures. Apart from pyrolysis, catalytic growth of CNT and graphene by chemical vapor deposition (CVD) allows the introduction of heteroatoms. Different carbon materials have been developed in recent years, such as carbon felt, graphite felt, carbon paper[50], and carbon cloth[51], each with different characteristics. For example, carbon and graphite felt exhibit high surface area, electrical conductivity, and chemical stability. Other non-carbon materials, such as IrO_2-coated dimensionally stable anode (DSA) electrodes, have been studied in VRFB by Rychcik and Skyllas-Kazacos. Although DSA showed good electrochemical activity, the reduction of oxide coating at the negative potentials of the V^{2+}/V^{3+} reactions made it unsuitable for use on the negative side[52].

In the past decades, various surface treatments have been developed to enhance the electrochemical activity of electrodes, including structural modification, thermal treatment[53], acid treatment[54], and metal doping[55]. Some studies have modified the structure of these electrodes to increase surface hydrophilicity, enhance charge transfer kinetics, and improve the diffusion of redox-active materials.[56-59] Activation procedures, typically thermal methods, have been reported and employed to clean and activate the electrode surface.[60,61] It should be noted that almost all the research on electrodes for RFB has focused on vanadium chemistry. Future work may focus on developing efficient electrodes for organic redox-active materials.

2.3.3. Redox active materials

Redox active materials are chemical compounds capable of transforming chemical energy into electrical energy. When this process is reversible, these materials can return to their initial state by applying electrical energy. The mixture of the redox active material, supporting electrolyte (if needed), and solvent is called the electrolyte. If the electrolyte operates on the positive side, it is referred to as the catholyte or posolyte. Conversely, if the electrolyte operates on the negative side of the battery, it is called the anolyte or negolyte.

Redox active materials can be dissolved in water or other organic solvents. The choice of solvent has a significant impact on the battery's performance, with each strategy offering distinct advantages and disadvantages.

- *Aqueous vs Non-Aqueous Redox Flow Batteries*

During the last years, various systems have been developed utilizing different redox active materials, ion exchange membranes, and electrodes in different media. Specifically, redox flow batteries (RFB) can be categorized based on the use of either water (aqueous) or organic solvents (non-aqueous) (Figure 4). Each strategy offers distinct advantages and disadvantages, as outlined below:

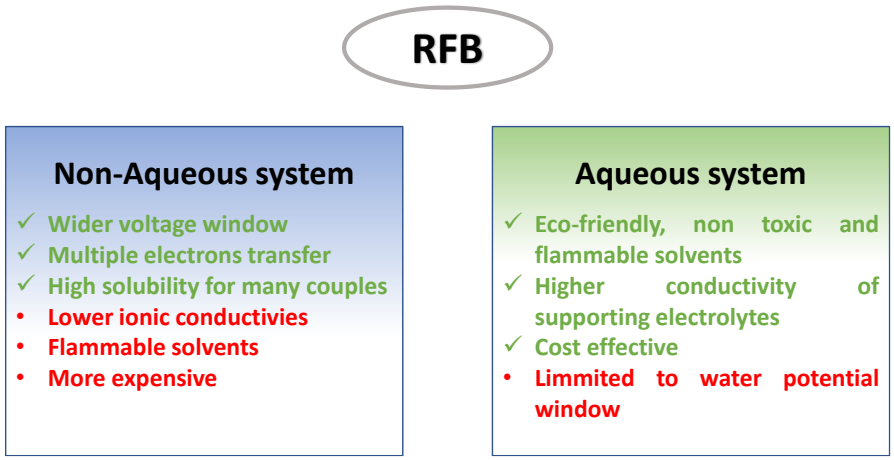

Figure 4: Different systems for Redox Flow Batteries and their main advantages and disadvantages.

Non-Aqueous Redox Flow Batteries utilize organic solvents to expand the operating voltage window beyond the limitations of water (typically <1.5 V, where hydrogen and oxygen are produced) and extend the temperature ranges, including sub-zero temperatures. This approach enables multiple electron transfers and increased solubilities for specific chemistries.[62-64] However, NARFB face certain challenges that make them less feasible than aqueous batteries. These challenges include the use of flammable and volatile solvents, expensive supporting

electrolytes with low ionic conductivity, and limited ion mobility through the ion exchange membrane (IEM).[65,66]

On the other hand, **Aqueous Redox Flow Batteries** employ water and commonly available salts, acids, or bases (e.g., NaCl, LiCl, KOH, HCl) for the preparation of the electrolyte. This makes the ARFB strategy safer and more cost-effective.[67-69] Additionally, ARFB offer higher ion mobility, resulting in higher ionic conductivities, lower resistance, and improved energy efficiency. Water also provides moderate viscosities and a wide temperature range, further enhancing the performance of ARFB.

Given that this thesis is conducted within a European research project (HIGREEW) focused on developing an efficient aqueous redox flow battery, the subsequent sections will concentrate on aqueous systems.[70,71] Among the various aqueous systems, the Vanadium Redox Flow Battery (VRFB) is considered the state-of-the-art technology and has already reached the market. Therefore, its chemistry will be briefly described below. It is worth mentioning that Zinc/Bromine Redox Flow Batteries (Zn/Br RFB) are also mature systems too.[72,73]

2.3.4. Other components

- Bipolar plates: These plates serve as electrical connections between cells and collect the generated electric current. They are typically made using a polymer filler, graphite particles, resins, or conductive additives such as PVA, PVDF, and HDPE. Bipolar plates should possess qualities such as robustness, chemical stability, ease of sealing, low weight, and low cost. However, they are susceptible to corrosion or oxidation, which can increase the resistance of the system and decrease battery efficiency. In the case of hybrid redox flow batteries, bipolar plates are used as electrodes and are made of the corresponding metal or metal oxide.

- Current collectors: These are typically made of metals such as copper and serve as electrical connections to the bipolar plates.

- Flow frame: The flow frame forms the flow channel between the bipolar plates and the membranes and usually contains a porous electrode. It must be chemically resistant as it is constantly in contact with the electrolytes.

- Electrolyte storage and flow: Tanks and tubing (or piping) are used for electrolyte storage and flow. Common materials for these components are PVC or fluorinated materials, chosen for their high chemical stability. Pumps, with centrifugal pumps being the most common choice for RFB, are used to facilitate the flow. These pumps must be chemical resistant and nonconductive.

- Electrical components: The Power Management System consists of an AC-DC inverter that converts the DC output of the electrochemical cell to AC power used in the grid. The Battery Management System incorporates control

algorithms that analyze and regulate parameters such as state of charge, current, voltage, temperature, pressure, and other relevant factors.

2.4. Types of Redox Flow Batteries

Redox Flow Batteries (RFB) can be classified into different categories based on their mode of operation, components, and composition of active materials. While batteries like the Vanadium Redox Flow Battery (VRFB) and Zinc-Bromine ($Zn-Br_2$) RFB have achieved commercialization after years of development, ongoing research aims to overcome their limitations. Here is a brief classification of the various types of RFB found in the literature:

- Phase changes at the electrodes:
  - Classical or true: no phase changes occur during the redox process, redox species remain in the liquid state. Examples: VRFB.
  - Hybrid: a phase change takes place at one of the electrodes. Examples: $Zn-Br_2$ RFB.
- Elemental composition of the redox active materials:
  - Inorganic: Lacking the carbon element. Example: VRFB.
  - Organic or organometallic: Containing earth abundant elements. Example: Anthraquinone-based RFB.
- Form of the redox active material:
  - Ions: Redox ions coordinated with water or hydroxyl. Example: VRFB
  - Complexes: Specially used in non-aqueous systems. Example: $Ru(bpy)_3$
  - Molecules: all organic redox active materials. Examples: quinones, triazine, viologens…
  - Polymers: polymers functionalized with redox active groups. Example: poly viologen or poly tempol
- Composition of the electrolyte:
  - Aqueous: will be discussed in section 2.3.3 and 2.6.
  - Non-aqueous: will be discussed in section 2.3.3.
- Form of electrolyte:
  - Solution. Redox active materials are dissolved.
  - Suspension/Dispersion. RAM present in immiscible phase. Bromine RFB.
  - Slurry. Specially used in all-iron RFB. Required high pump power.
- Ion permeable separator:
  - Ion Exchange membrane. In most of the RFB, both half cells are divided using anion or cation exchange membranes (AEM and CEM, respectively)
  - Microporous separator. Specially used in hybrid RFB or RFB which use polymers as RAM.
  - No separator. Membrane-less RFB using two immiscible aqueous electrolytes or using laminar flow.
- Type of tank storage
  - Conventional: the energy is stored in the liquid electrolyte.

- With solid boosters: Solid redox active materials store the energy in the tank. Example: copper hexacyanoferrate and Prussian blue solid booster RFB.

Since this thesis focuses exclusively on Aqueous Redox Flow Batteries (ARFB), the remaining introduction will be centered on this specific type of battery. However, the quick classification provided demonstrates the wide range of systems currently under development. Each system has its own set of advantages and disadvantages, all contributing towards the shared goal of developing an efficient energy storage system.

The variety of systems in development highlights the ongoing efforts to improve energy storage technologies. Researchers aim to overcome limitations and optimize various aspects such as energy density, cost-effectiveness, scalability, and environmental impact. By exploring different redox chemistries, materials, and system designs, they strive to enhance the overall performance and feasibility of energy storage systems.

The ultimate objective is to develop energy storage solutions that can effectively integrate with renewable energy sources, stabilize electrical grids, support off-grid applications, and contribute to the transition towards a more sustainable and clean energy future.

2.5. State-of-the-art: Vanadium Redox Flow Batteries

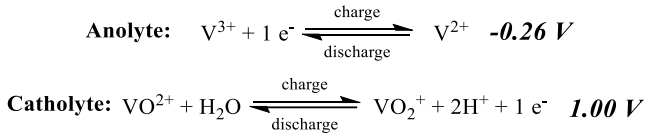

Figure 5: Redox reaction of all-Vanadium Redox Flow Batteries

Historically, the first group of RFB tested used aqueous metallic inorganic ions. Most metallic ions have at least two oxidation states with good stability and solubility, along with a broad range of redox potentials. Therefore, it is easy to understand why this group was the first to be tested. The first successful RFB was developed by NASA in the early '70s using iron-chromium chemistry.[74] Ten years later, Maria Skyllas-Kazakos developed an all-vanadium system where four stable oxidation states were used as two redox couples in the RFB (Figure 5).[70,71] This system has become the first commercially available option and represents the state-of-the-art for Redox Flow Batteries, with the chemistry involved depicted in Figure 5.

Firstly, the commercial electrolyte $V^{3.5+}$ (equimolar mixture of V(III) and V (IV)) in 1 M H_2SO_4 must be pre-charged via chronopotentiometry, resulting in V^{3+} in the anolyte and VO^{2+} in the catholyte. During the charging process, the reduction of V^{3+} to V^{2+} occurs in the negative side, while in the positive side, the oxidation of VO^{2+} to VO_2^+ takes place simultaneously. This flow of electrons from the catholyte

to the anolyte increases the potential of the battery. To maintain the electroneutrality of the system, protons from the anolyte cross through the IEM (ion exchange membrane) to the catholyte. In the discharging process, the opposite reactions and movements occur, releasing the energy stored during the charging process (decreasing the potential). This is a simplified way to understand the redox reactions involved in VRFB. In reality, the reaction mechanism on the electrode surface with oxygen functional groups (-OH and -COOH) for the positive and negative half cells during the charging process is described as follows:[47]

i) The vanadium reactant ions (VO^{2+} and V^{3+} for the positive and negative side, respectively) diffuse from the bulk electrolyte and get absorbed into the oxygen functional groups on the electrode surface.
ii) Ion exchange occurs between the protons and the absorbed vanadium ions. In this step, the ion exchange between vanadium ions can also take place at other functional groups that act as active sites and catalysts, such as nitrogen functional groups,[75] carbon functional groups on carbon nanofibers,[76] and metal or metal oxide catalysts.[77-81]
iii) On the positive electrode, one oxygen atom from H_2O transfers to the VO^{2+}, forming VO_2H^+ with electron transfer from the OH functional groups to the electrode.[82] The electrons from the positive electrode travel to the negative electrode, combining with V^{3+} on the electrode surface along the C-O-V bond to form V^{2+} on the surface. On the positive side, oxygen reactions and electron transfers take place, while on the negative side, only electron transfer occurs. Therefore, the development of a positive electrode for VRFB involves introducing oxygen functional groups on the electrode surface to facilitate the oxygen transfer step.
iv) Ion exchange occurs between the vanadium species attached to the electrode surface and the protons in the electrolyte. The discharging process involves the opposite reactions and mechanisms.

Based on the latest results of VRFB, with a vanadium concentration of 1.6 M, a voltage of 1.26 V can be expected, leading to a volumetric capacity of approximately 42 A/h·L. To prevent battery damage, VRFB typically operate between 15% and 85% state of charge (SOC), avoiding deep charge and discharge. Therefore, a volumetric power of 38-42 Wh/L can be expected. If the cost of 1 L of vanadium electrolyte is around $ 6 to $ 10, the estimated cost would be $ 200-300/kWh.

In this battery, both electrolytes contain related vanadium species, which mitigates the chemical contamination challenge associated with electrolyte crossover. However, after long-term VRFB operation, some imbalance between the two electrolytes can be identified. This imbalance can occur due to different reasons (such as cross-contamination or side reactions), and its effects can deteriorate battery performance, leading to capacity loss. The major advantage of this battery is that the capacity can be recovered by rebalancing the battery. Different methods have been developed depending on the causes of the imbalance.[83] Despite the

advantages of this battery and others, such as the Fe/Cr[84-86] and Zn/bromine RFB,[87-89] the use of critical and high-priced metal salts, hazardous and corrosive electrolytes (sulfuric acid solutions), and expensive ion exchange membranes like Nafion® exclude these systems as "green" energy storage solutions. These issues can be addressed by using organic molecules as redox-active materials for aqueous systems.

2.6. Aqueous Organic Redox Flow Batteries

The use of organic redox-active materials eliminates the need for metals as redox-active materials. Metals not only make the system less cost-effective (due to their high price resulting from their low abundance in the Earth's crust), but they also pose environmental risks. An alternative approach is the utilization of organic electrolytes, which can be produced on a large scale at a low cost. Furthermore, these organic electrolytes offer a high degree of tunability in terms of their properties.[32,54,90,91,92] In theory, the solubility, redox potential, and stability of the active materials can be easily adjusted, thereby enabling the production of batteries with higher energy density, increased cell voltage, and improved long-term performance. In terms of designing the active materials, the field of chemistry provides numerous combinations that can be synthesized following the principles of organic chemistry. Consequently, different families and strategies have been extensively studied and optimized over the years.

2.6.1. Organic compounds as Redox Active Materials

Different organic families have been developed as redox-active materials for RFB in an effort to meet the demanding requirements for their implementation. The electrolytes in RFB must possess the following characteristics:

i) Wide potential window: The potential difference between the two standard potentials of the redox couples involved should be maximized to achieve a high cell potential and high energy density. However, this is limited by the stability of water.

ii) High solubility: A higher concentration of redox-active species leads to a higher capacity and energy density. Solubility determines the theoretical volumetric charge capacity of the electrolyte, indicating the amount of charge that can be stored in a certain volume of electrolyte.

iii) High ionic conductivity: Great mobility of active species and ions facilitates their transport to the electrode, enabling redox processes, and through the membrane to maintain electroneutrality in the system. The low ionic conductivity of non-aqueous systems is the main cause of their ohmic losses.[93]

iv) Fast kinetics: Fast electronic exchange associated with the charge/discharge of the battery occurs at the surface of the electrodes. Elevated reaction rates minimize side reactions, gas evolution (oxygen or hydrogen),[94] and cell

resistance,[54] leading to higher efficiencies and stabilities of redox-active materials (RAM). Improved charge transfer kinetics also help avoid electrode degradation. In this regard, many research groups have focused their attention on optimizing electrodes for RFB.[57,95]

v) Low viscosity: A higher viscosity of the electrolyte results in greater energy waste from the pumping system, making the battery less effective in terms of lower round-trip efficiency. It should be noted that while the battery is charging/discharging, the composition of the electrolytes varies, affecting all its properties.[96] Furthermore, mass transfers are directly related to viscosity, so an increase in viscosity leads to a decay in conductivity.[97]

vi) High chemical stability: Redox Flow Batteries are considered one of the most promising long-term energy storage systems. Therefore, ensuring the stability of the electrolyte, as well as the entire system, is crucial. In the case of organic molecules, reactive species can be generated during the charging/discharging process, which may result in irreversible capacity loss due to the formation of dimers[98] or free radical reactions[99]. Additionally, side reactions during battery operation can lead to the generation of non-redox-active or less soluble/active species. Aziz *et al.*[100] proposed a useful method to assess the stability of the electrolyte at different SOC, which corresponds to varying concentrations of the oxidized and reduced forms. Ideally, a *post-mortem* analysis of the electrolyte should be performed after battery testing to elucidate the degradation mechanism and identify the structure of the by-products.

vii) Thermal stability: The electrolyte may experience precipitation at different temperatures. For instance, vanadium electrolyte tends to dimerize and precipitate at temperatures above 40 °C.[96]

viii) Low cost: Since the primary objective of RFB is to integrate renewable energies into the grid, it is essential for the system to be cost-effective.

ix) Safety and environmental friendliness: Given that Redox Flow Batteries are designed to store megawatt-hours of energy, the preparation and disposal of electrolytes must be safe and environmentally friendly. To address this concern, reducing the use of metals in favor of organic molecules and minimizing the reliance on organic solvents have become trends in RFB development.[101]

2.6.2. Different families of Redox Active Materials

Considering the aforementioned aspects, it is evident that we encounter significant challenges when designing a new class of redox active materials. However, researchers have made considerable progress in developing different groups of molecules that incorporate many of these features, making them promising candidates for RFB. Each family of compounds offers specific advantages and disadvantages that need to be optimized to guide the future of RFB towards the utilization of organic molecules as Redox Active Materials (Figure 6). In the

following paragraphs, we will provide a brief overview of these compound families and their respective characteristics. The first three families of compounds (viologens/diquats, quinones, and alloxazines/phenazines) are typically used as anolytes.

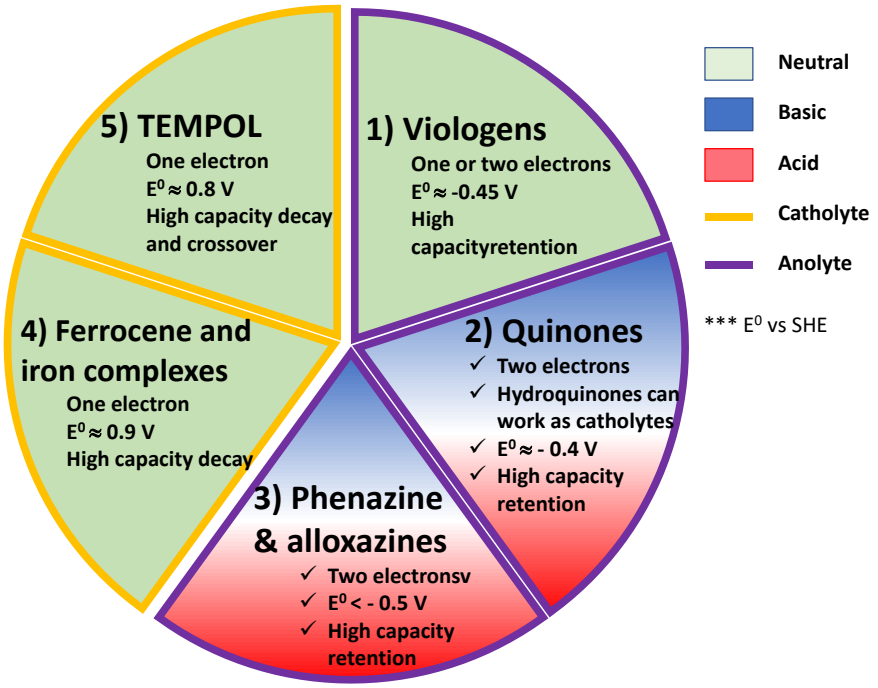

Figure 6: Classification of the different organic families for organic redox active materials in aqueous system.

2.6.2.1 Viologens and diquats

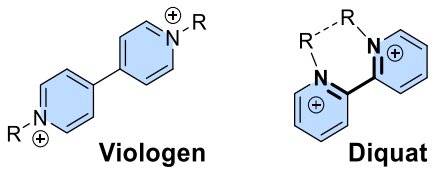

Figure 7: Viologen and Diquat core.

Nitrogen-containing aromatic compounds are considered redox active species, particularly those that contain two or more nitrogen atoms, enabling them to undergo two consecutive one-electron reductions (Figure 7). One well-known and widely utilized structure in this context is 4,4-bipyridine derivatives, also known as viologens. These derivatives exhibit good stability and undergo a first reversible reduction at -0.45 V, leading to a cation radical intermediate. Further reduction results in the formation of a neutral species that is insoluble in water at potentials

above -0.65 V. Additionally, viologens demonstrate excellent solubility, and their cost-effective synthesis route is a significant advantage.[102]

One of the most extensively studied viologens is 4,4-dimethyl bipyridinium (Methyl Viologen), which has been widely employed as an anolyte in Aqueous Organic Redox Flow Batteries (AORFB).[102-105] Despite its favorable properties, Methyl Viologen does have two main drawbacks: a tendency for dimerization[106] and dealkylation in the presence of oxygen.[107] These side reactions result in the formation of insoluble by-products, leading to a loss in capacity. To address these limitations, numerous examples utilizing the same 4,4'-bipyridine core (viologens) have been developed with the aim of utilizing both electrons[86,108,109], increasing solubility and enhancing stability.[105,110,111,94,113,114]

To the best of our knowledge, the three most promising candidates reported to date, with respect to capacity decay, are dextrosil-viologen[110], carboxylate-viologen[113], and asymmetric sulfonate viologen[114] (Figure 8). These compounds exhibit either no capacity decay in the case of the first two examples or a decay rate of only -0.045% per day over 30-50 days in the case of the asymmetric sulfonate viologen.

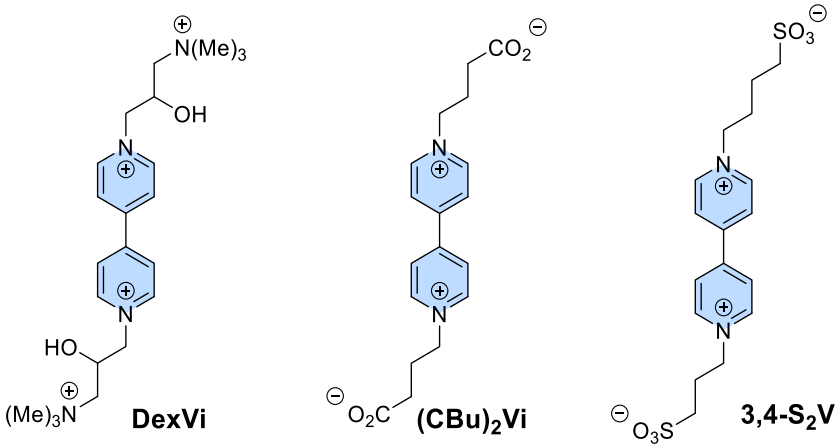

Figure 8: Three best candidates of the viologen family.

In addition to viologens, another group of compounds that has been studied for their redox activity in RFB is the diquat or 2,2-bipyridinium derivatives. However, the diquat family has not achieved the same level of success as viologens, and only a few studies have utilized them as anolytes in Aqueous Organic Redox Flow Batteries (AORFB). These studies have shown lower redox potentials, but higher capacity decays compared to viologens.[115-117]

The electrochemical performance of diquat derivatives is inherently linked to the dihedral angle (N-C-C-N), which will be discussed in the results section of this thesis. Understanding and studying this dihedral angle and its impact on the

electrochemical properties of diquat derivatives is crucial for optimizing their performance in RFB.

2.6.2.2. Quinones and hydroquinones

Quinones are aromatic compounds in which an even number of carbon atoms are substituted by a carboxyl group, resulting in a conjugated cyclic dione molecule. Through electrochemical reduction, the carboxyl group undergoes enolization, leading to the stabilization of the anionic species through the delocalization of accepted electrons over the conjugated structure. The selection of quinones as redox-active materials in electrochemistry is driven by their natural occurrence in processes such as respiration and ATP production.[118,119] Quinones are the oxidized form of aromatic compounds, and their corresponding reduced forms, featuring two hydroxyl groups as substituents, are known as hydroquinones.

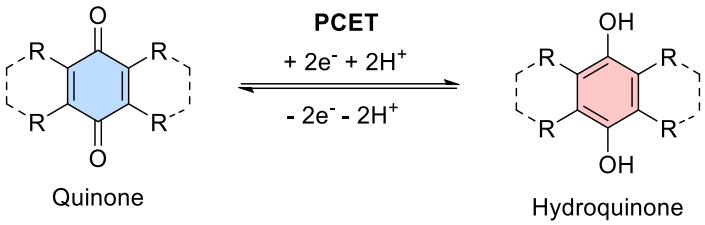

Figure 9: Quinone – hydroquinone transformation *via* redox reaction.

Both quinones (as anolytes) and hydroquinones (as catholytes) are well-known redox species, and their fast and reversible two-electron redox reactions have been extensively studied (Figure 9). In aqueous acidic solutions, where the proton concentration exceeds the concentration of quinone, a single-step fast proton-coupled electron transfer (PCET) process occurs, leading to the formation of dihydroquinone. However, in situations where the concentration of quinone surpasses that of protons (e.g., neutral pH), a stepwise two-step one-electron transfer takes place, resulting in the formation of monoprotonated anion hydroquinone. In alkaline solutions, oxyanions are preferentially formed through a single-step two-electron transfer process. In this case, PCET does not occur, and the oxyanions are strongly stabilized by the surrounding water molecules through hydrogen bonding (Figure 10).[120,121]

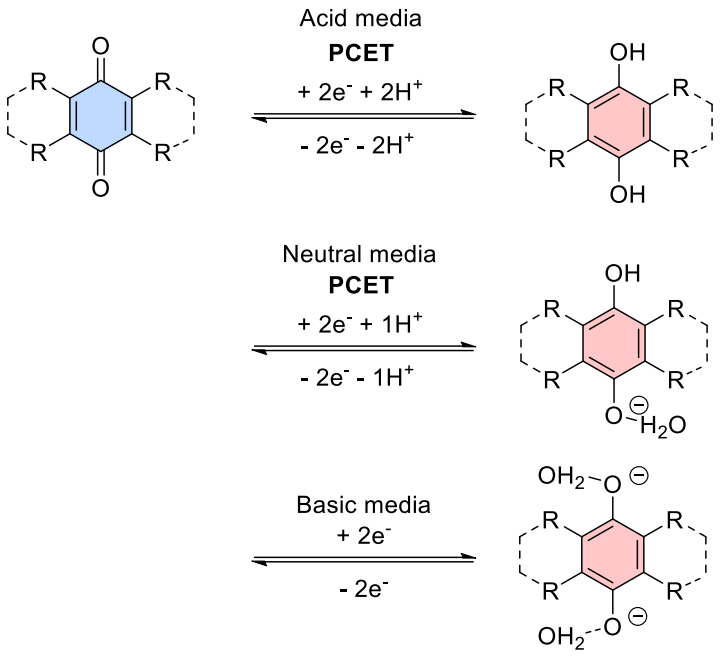

Figure 10: Three mechanisms of quinone reduction based on the pH of the electrolyte.

From this family, various anolytes and catholytes have been developed. Starting with the simplest chemistry of hydroquinones, different positive electrolytes have been utilized in RFB. By introducing solubilizing groups such as sulfonic acid and morpholine, the solubility of hydroquinones has been enhanced, and their redox potential has shifted towards more positive values.[122-124] The main identified degradation pathway is hydroxylation through Michael addition. [125,126] To mitigate this undesired reaction, methyl groups have been attached to the hydroquinone core.[124,126]

However, despite these improvements, the hydroquinones used in these systems were relatively small, and the main reason for capacity decay in the batteries was the crossover of active species through the membrane. This crossover phenomenon needs to be addressed to achieve improved performance and durability in RFB.

Quinones have emerged as promising anolytes in RFB, with different materials such as quinones, naphthoquinones, and anthraquinones being studied.[121] The solubility of quinones has been improved by attaching hydroxyl groups and operating in basic media. These substituents not only enhance solubility but also play a significant role in shifting the redox potential to more negative values, as they act as electron-donating groups (EDGs).[127] However, the small molecular size of quinones leads to high crossover through the membranes, resulting in significant capacity decay. To address this issue, larger molecules such as naphthoquinones and anthraquinones have been designed.

Naphthoquinones exhibit lower solubility in water, which can be enhanced by attaching polar groups such as hydroxyl and carboxyl groups. However, they are prone to hydroxylation via Michael addition.[121,128] The best candidate is HCNQ, which exhibits a capacity decay of 6.4% per day at high concentrations (1 M) in single-cell. However, even the best candidate shows significant capacity decay to be suitable for commercial purposes.[128]

Among the quinone family, the most promising branch is the anthraquinones, which possess extended π-conjugation and high stability. The fully delocalized electrons throughout the three rings reduce the possibility of Michael addition, and the larger size of the molecule inhibits crossover through the ion exchange membrane. Additionally, various functional groups can be attached to anthraquinones to increase their solubility. Aziz *et al.* [129] compared the performance of anthraquinones with one or two sulfonic acid groups attached to the core. While the sulfonic groups increase solubility and redox potential, they make these compounds less suitable as negolytes due to the reaction between bromine (present in the anolyte due to crossover) and the sulfonic acid groups, leading to capacity decay. Leo Liu *et al.* [111] improved the stability and solubility of anthraquinone disulfonic acid (AQDS) by cation exchange using ammonium as a counterion. AQDS$(NH_4)_2$, coupled with iodine/iodide, exhibited no capacity decay over 14 days in an RFB.

By introducing electron-donating groups such as hydroxyl groups, the redox potential of anthraquinones can be modulated to more negative values. These candidates have been tested against bromine and have shown similar results in RFB. The addition of hydroxyl groups shifts the redox potential by 100 mV to more negative values, enhancing the cell potential. The problem of redox potential modulation can be overcome by adding an extra carbon between the sulfonic acid and the anthraquinone (DHAQDMS).[130] However, the cycling performance of this molecule was compromised due to the loss of conjugation between the aromatic ring and the sulfonic acid. Aziz *et al.*[131] addressed these issues by studying hydroxylated anthraquinone in alkaline media, where the redox potential shifted to more negative values and solubility was enhanced by the deprotonated hydroxyl group. Thus, alkaline anthraquinone-based RFB have paved the way for the development of the next generation of anthraquinones.

To the best of our knowledge, the most promising anthraquinones have been designed by Aziz by introducing carboxylate or phosphate groups spaced by carbon or oxygen atoms from the anthraquinone core, demonstrating promising results in terms of capacity retention.[132-135] The three most stable compounds reported by Aziz, along with AQDS$(NH_4)_2$ reported by Liu, represent this new generation of anthraquinones. The main reasons for capacity decay in these new Redox Active Materials are chain loss and/or anthrone and its dimer formation (Figure 11).[136,137]

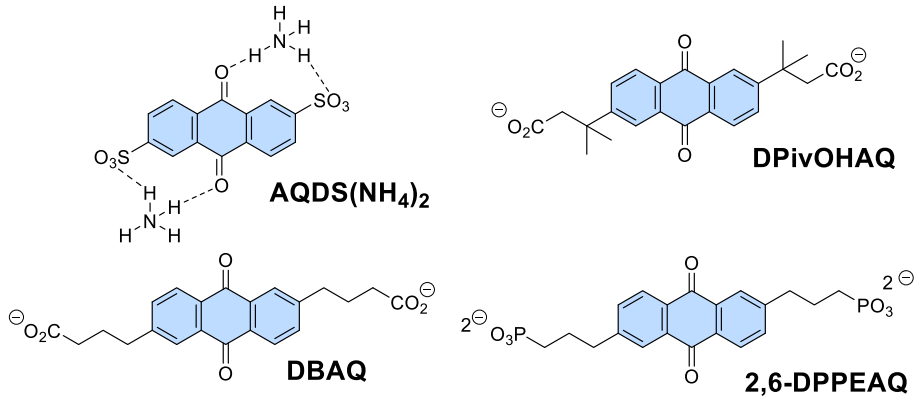

Figure 11: Best four candidates reported for the quinone family.

Indeed, one of the significant advantages of quinones is their ambivalence to be used as both anolyte (quinone) and catholyte (hydroquinone). Aziz *et al.* [138] have made notable advancements in this area by developing a symmetric all-quinone aqueous battery that can function as both catholyte and anolyte simultaneously, known as a combi-molecule (Figure 12). The concept of combi-molecules holds great potential for the future of RFB because the capacity decay resulting from crossover can be mitigated by rebalancing the electrolyte, similar to the approach used in Vanadium Redox Flow Batteries (VRFB) described earlier. This innovative approach offers the possibility of improving the overall performance and stability of RFB.

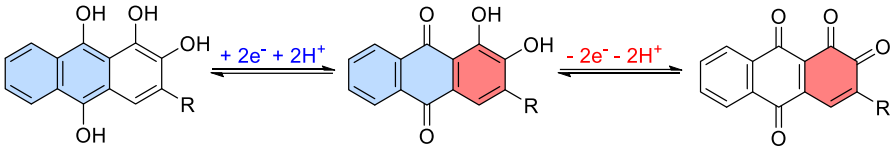

Figure 12: Combi-molecule reported by Aziz *et al* matching the quinone and hydroquinone chemistry.

2.6.2.3. Alloxazines and phenazines

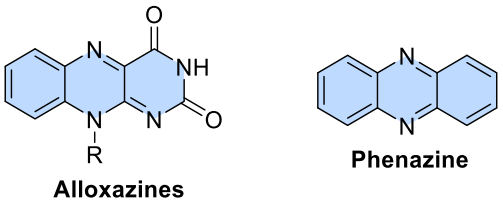

Figure 13: Alloxazine and phenazine cores.

For many years, viologen, quinone, and TEMPO families have been the predominant organic redox active materials. However, in recent times, new nitrogen-containing aromatic compounds have been investigated electrochemically and tested in RFB (Figure 13).[139,140] Taking inspiration from nature, alloxazines have emerged in the battery field, mimicking the redox reactions of flavin cofactors.[141] Alloxazines are the redox-active backbone of flavins and consist of fused benzene and pyrazine rings. This family exhibits high solubility in water (4.5 M) and undergoes a pH-dependent, two-electron redox reaction at low redox potentials (specific potentials to be added). Additionally, alloxazines have a low molecular weight, resulting in higher battery capacity. Their synthesis is relatively simple, involving a high atom-economical coupling between *o*-phenylenediamine derivatives and alloxan in acetic acid and boric acid at room temperature.[142-144]

Although alloxazines have been previously studied as anode materials for non-aqueous lithium and sodium-ion batteries, their limited solubility has hindered their use in RFB. To enhance aqueous solubility, Aziz and Gordon *et al.*[140] introduced a carboxylate group into the alloxazine core, resulting in ACA (alloxazine carboxylate) as an anolyte. Despite limited kinetics, ACA demonstrates sufficient solubility, low redox potential, and stability to be employed as an anolyte in RFB. In the same vein, Meng *et al.*[145] utilized a sodium salt of flavin mononucleotide as an anolyte in RFB. While these examples have opened doors for exploring new derivatives of alloxazines, the challenges of low capacity retention impede further development in this family. The main degradation pathways observed include precipitation due to π-stacking interactions[146] and hydrolysis, leading to the formation of inactive redox species.[140,147,148]

Phenazines, which exhibit redox-active behavior,[149] have been studied as potential redox-active materials. However, it was not until 2018 that Schubert *et al.* utilized the phenazine core in the design of a combi-molecule coupled with a TEMPO moiety, enabling it to function as both an anolyte and a catholyte. One challenge encountered in this work was the poor solubility of the combi-molecule in water.[150] Subsequently, researchers have focused on designing phenazine derivatives by introducing different solubilizing groups such as hydroxyl, sulfonate, carboxylate, and amino groups at various positions.[121,133,152,153.]

The degradation mechanisms of phenazine anolytes are not yet fully understood due to limited examples studied. However, tautomerism has been identified as a primary degradation pathway, leading to a loss of redox activity. Among the phenazine derivatives, **1,8-PFP** has emerged as the most promising candidate, demonstrating no capacity decay during galvanostatic and galvanostatic-potentiostatic cycling at different temperatures for over 40 days.[154] Another notable candidate is **1,6-DPAP**, which exhibits a low capacity decay rate of 0.0015% per day due to its high resistance to tautomerization. This highlights the potential of amino acid substituents as stabilizing groups for redox-active materials (Figure 14).[152]

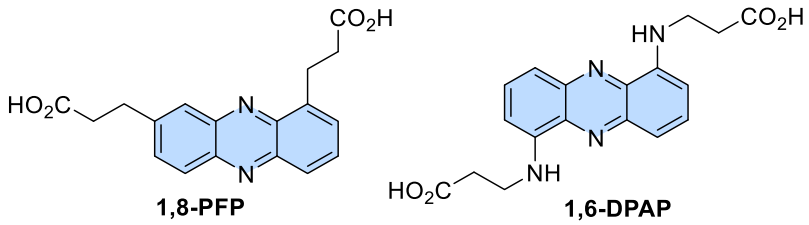

Figure 14: Two best phenazine reported anolytes.

Despite the impressive performance of **1,8-PFP** and **1,6-DPAP**, their synthesis and purification processes are laborious and require the use of expensive catalysts, which could pose challenges for scale-up. Thus, only a few examples have been developed using this chemistry, and the development of new phenazine-based candidates is expected in the coming years.

- *Other studied systems:*

One of the main challenges in the field of aqueous organic Redox Flow Batteries (RFB) is the limited availability of suitable catholytes. Various compounds have been explored as catholytes in RFB, including I^-/I_3^-, Br^-/Br_3^-, metal complexes, ferrocene derivatives, $[Fe(CN)_6]_4^-/[Fe(CN)_6]_3^-$, hydroxyquinones, and TEMPO.[103,125,155,156] On the other hand, inorganic compounds such as $FeCl_2$, Zn halides, and $VOSO_4$ have been utilized in aqueous inorganic RFB. However, these chemistries require further improvement in terms of technology and cost-effectiveness to enable widespread energy storage due to factors such as expensive materials, side reactions, and corrosive electrolytes.

Therefore, considerable efforts have been directed towards the development of new organic and organometallic catholytes specifically tailored for aqueous RFB.[103,125,155,156] The aim is to overcome the limitations of current catholyte options and find alternatives that offer improved performance, cost-effectiveness, and compatibility with aqueous systems. The next two sections describe two families of RAM generally used as catholytes.

2.6.2.4. Ferrocyanide and iron complexes

Iron, being one of the most abundant elements on Earth and possessing a high redox potential (approximately 0.77 V *vs* SHE), is a promising candidate for catholytes in aqueous RFB.[157,158] However, the slow electrochemical reaction, poor stability, and high crossover through the membrane necessitate structural modifications.

In this regard, ferrocyanide was first incorporated into the positive side of an aqueous RFB in 1979. Ferro- and ferricyanide constitute a highly stable and non-toxic redox couple due to the strong coordination of cyanide ions to the iron center. This redox couple has recently been used in alkaline redox flow batteries.[121,122,131,145] The stability of ferro-ferricyanide has also been studied in strongly alkaline media

in RFB, as ligand exchange between hydroxide and cyanide can occur.[159] One limitation of this redox couple is its low solubility in water, with potassium and sodium ferrocyanide having solubilities of 0.76 M and 0.5 M, respectively. A patent was filed for a 1:1 ratio of sodium-potassium ferrocyanide, resulting in a 1.5 M $[Fe(CN)_6]_4^-$ solution in water. However, this mixture may cause precipitation due to variations in cation concentration in RFB.[160] Leo Liu *et al.*[161] reported the use of ammonium ferrocyanide, which increases the solubility up to 1.6 M for ferrocyanide and 1.9 M for ferricyanide in deionized water. Despite the significant increase in solubility, some issues with the formation of insoluble *Prussian blue* from ammonium ferrocyanide have been observed during the European project in which this thesis is ascribed.

Another intriguing iron compound that has been developed as a catholyte in aqueous RFB is ferrocene (Fc). Since ferrocene is insoluble in water, functionalization is required to enhance its solubility. Hu *et al.*[103] achieved solubility by incorporating one or two charged polar substituents, such as quaternary ammonium (FcNCl), while Boika *et al.*[162] utilized sulfonate (FcDS). The FcNCl coupled with methyl viologen battery exhibited longer cycling stability than the FcDS coupled with AQDS, attributed to nucleophilic attacks by acetate and sulfate ions on the iron complex. The influence of chain length has also been investigated by Xu *et al.*[163], who found that the presence of two ammonium groups separated by a hexane chain (BQH-Fc) led to optimum performance. The proposed degradation mechanism in this work involves ligand exchange between water and cyclopentadienyl, resulting in the dimerization and polymerization of the latter.

Other ligands, such as ethylenediaminetetraacetate (EDTA) and 2,2'-bipyridine, can coordinate with iron to form stable complexes.[164-166] 2,2'-bipyridine complexes have been utilized as catholytes in non-aqueous redox flow batteries and as solar dyes.[167] Zhu *et al.*[168] developed an asymmetric iron complex using 2,2'-bipyridine-4,4'-dicarboxylic acid and cyanide as ligands **$Fe(Dcbpy)_2(CN)_2$**. The use of bipyridine ligands in the design of iron complexes for non-aqueous redox flow batteries and solar dyes can increase the potential and volume, thereby reducing crossover through the ion-exchange membrane (IEM). By breaking the symmetry in their design, they demonstrated an increase in solubility and stability of the redox-active materials, with a capacity decay of 0.25% per day.

Similarly, Aziz *et al.*[169] reported different iron complexes with various substituents using bipyridine ligands that can serve as catholytes in aqueous RFB. Among the different compounds, the iron complex formed using 4,4'-bis(hydroxymethyl)-2,2'-bipyridine **$Fe(Bhmbpy)_3$)** as the ligand exhibited the best characteristics in terms of solubility and high redox potential. In a near-neutral aqueous organic RFB, this iron catholyte, coupled with the anolyte BTMAP-Vi, demonstrated excellent stability with a capacity decay rate of 0.07% per day (Figure 15). Despite the progress in developing stable organometallic catholytes, the issue of capacity decay remains a challenge, and the search for suitable catholytes in the RFB field continues.

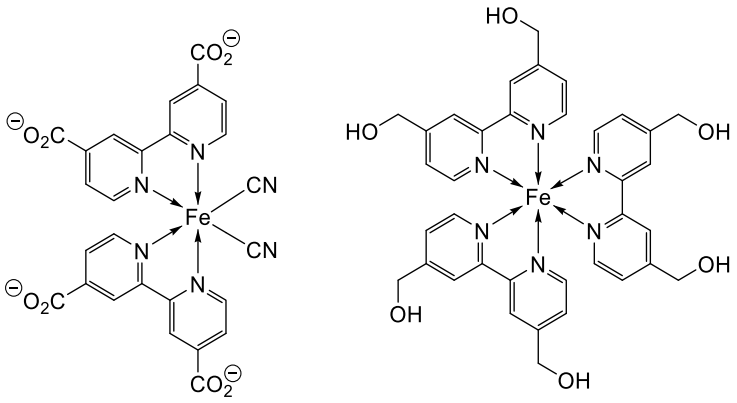

Figure 15: Best two iron complexes reported as catholytes.

2.6.2.5. TEMPO derivatives

TEMPO is a stable nitroxyl radical designed to have stability, contrary to the typical notion associated with radicals. Its four methyl groups prevent attacks on the two-center three-electron N-O bond. Additionally, it lacks an α-position hydrogen atom, which would lead to disproportionation and the formation of hydroxylamine and nitrone compounds.[170] The presence of these methyl groups prevents their substitution with larger substituents, as it could result in homolytic cleavage of the C-N bond, generating a nitroso compound and alkyl radical.

TEMPO has been used as a catholyte in non aqueous systems, undergoing reversible one-electron oxidation to form the oxoammonium cation.[171] Since TEMPO is insoluble in water, various hydrophilic groups such as hydroxy, (TEMPOL)[102] sulfate,[172] and trimethyl ammonium (TMA)[155] have been attached to the 4-position of TEMPO to enhance its solubility in water. The derivative 4-TMA-TEMPO was coupled with methyl viologen in a highly concentrated (2 M) RFB, demonstrating a cell potential of 1.4 V and nearly full capacity retention. This family of compounds offers advantages such as extremely high redox potential (0.8-1.1 V *vs* SHE) and high solubility (>2 M). However, there are also significant disadvantages. TEMPOL derivatives are prone to degradation via disproportionation in acidic media and ring-opening of the oxoammonium cation in basic media.[90] Furthermore, these derivatives exhibit high crossover, which contributes to capacity decay.

To address this issue, Schubert *et al.* attempted to mitigate the problem by developing combi-molecules where the TEMPO moiety was attached to different anolyte moieties such as phenazine and methyl viologen (Figure 16).[173,174] While the phenazine-based combi-molecule showed almost full capacity retention, its poor kinetics resulted in low energy efficiencies. In the case of the methyl viologen-based combi-molecule, its poor solubility necessitated the addition of a non-

aqueous cosolvent (20 vol.% of ethylene carbonate). However, rapid capacity decay was observed due to pH changes caused by the formation of hydroxylamine (TEMPO-NOH) during battery charging.

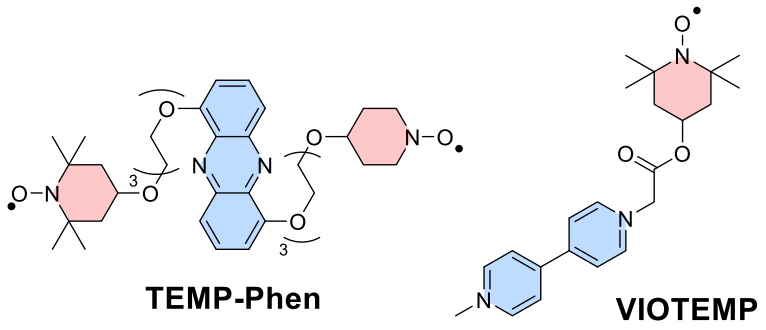

Figure 16: Two combi-molecules reported by Schubert *et al* matching the TEMPO core with the phenazine and viologen backbone.

Leo Liu *et al.* [175] introduced a new generation of TMA-TEMPO derivatives last year, making these candidates more stable and soluble in water. They replaced one of the methyl groups in the trimethyl ammonium moiety with a propyl ammonium substituent (N_2-TEMPO). This modification increased the repulsion between molecules, enhancing the stability of the new derivative. This strategy showed no capacity decay over 400 cycles when using 0.5 M of the redox-active material (RAM), making it one of the most stable catholytes to date. However, when the RAM concentration was increased to 1 M, the battery exhibited a 10% capacity loss due to volume changes between the electrolytes.

In another strategy, they replaced the trimethyl ammonium moiety with acetylamino and trimethyl ammonium (TMAAcNH-TEMPO).[176] This modification resulted in a solubility of 4.3 M, enabling high-energy-density AORFB. When coupled with $(NPr)_2V$ as the anolyte, TMAAcNH-TEMPO showed low capacity decay of 0.346%/day over 40 days. The introduction of the trimethylammonium and acetamido groups effectively suppressed the ring-opening side reaction and crossover, which are the main causes of capacity decay (Figure 17). These works represent the best TEMPO derivatives to date. However, the low compatibility of TEMPO radicals with the membrane and the high-capacity decay in high-concentration batteries still require further investigation to address these issues.

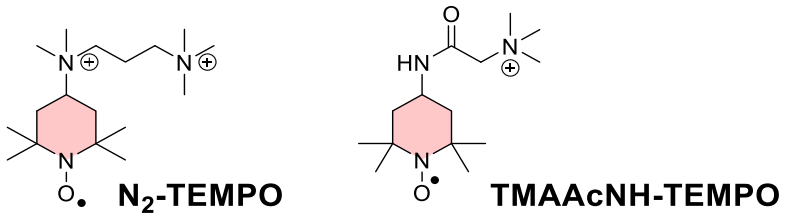

Figure 17: New generation of TEMPO derivatives show the best results of the family so far.

In summary, the vast majority of the organic redox active materials can be ascribed to one of these families. The range of potentials that each family of compounds provides are summarized in Figure 18.

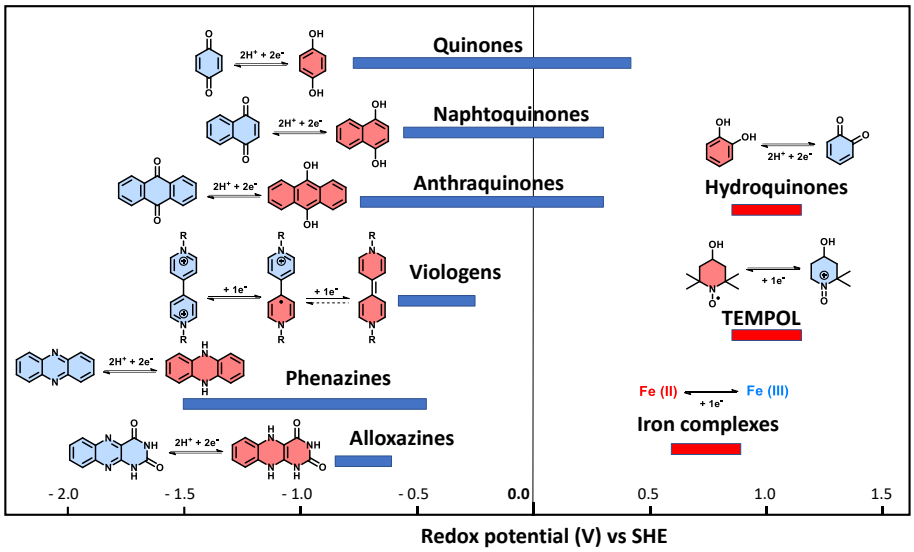

Figure 18: Redox potential ranges for each family described above.

Since the beginning of this thesis, no organic redox active material (RAM) has shown comparable results to VRFB. Therefore, the development and study of new organic RAM need to be thoroughly investigated and evaluated. This thesis is part of the HIGREEW project (Affordable High-performance Green Redox Flow Batteries), which aims to design, develop, and validate an advanced redox flow battery based on a new water-soluble, low-cost organic electrolyte. The focus is on developing an electrolyte that is compatible with optimized low-resistance membranes and fast electrode kinetics, aiming for high energy density and long service life.

The primary task of our group in this project has been the selection and modification of commercial ion exchange membranes to meet the project requirements. This thesis primarily focuses on the development of aqueous organic RFB. Therefore, it will highlight the main characteristics, thermodynamic considerations, and kinetics during battery operation. The aim is to provide a useful introduction to the complex and fascinating field of RFB.

2.7. Computational chemistry and DFT calculations in RFB

As a branch of theoretical chemistry, computational chemistry utilizes computer simulations to solve various chemistry problems. By incorporating methods from theoretical chemistry into computer programs, it becomes possible to calculate the structures, interactions, and properties of molecules. There are several methods available in computational chemistry, including *ab initio*, semiempirical, and

density functional theory (DFT). The choice of method depends on factors such as computational cost (time) and the desired level of accuracy in the results. Each method has its own characteristics, advantages, and disadvantages, which will be described in the next Section: Experimental and Theoretical procedures.

DFT calculations have garnered significant attention due to their ability to provide accurate results for large systems while consuming relatively less computational time. DFT calculations have become one of the most valuable tools for chemists to understand and predict the behavior of different compounds. With a strong interest in developing aqueous organic redox flow batteries (AORFB), the use of DFT calculations has become imperative due to the vast chemical space offered by organic chemistry. In this regard, DFT can guide the synthesis of organic compounds by predicting important properties such as solubility, redox potentials, and stability, among others.[103,156,177,178] High-throughput screening techniques can further accelerate the synthesis of promising candidates based on the most important characteristics of redox active materials (RAM).[179,180]

DFT calculations serve not only as a screening tool for RAM but also play a crucial role in addressing stability issues, which is another major concern in RFB. By understanding the electrochemical properties of compounds, side reactions can be identified and avoided through appropriate substituent patterns. The stability of different compounds has been analyzed by studying charge distribution,[181] geometric distribution,[115] acidity,[117] orbital density,[157] and the effect of additives.[182] Additionally, important electrochemical parameters such as the kinetics of the redox process based on Marcus theory can be studied.[183] If the redox process involves significant structural changes between the oxidized and reduced states, the kinetics of the process may be compromised.[184]

DFT calculations also allow for the study of the interaction between organic molecules and ion exchange membranes, providing insights into the potential issue of crossover in the battery.[105] The volume of the RAM and the choice of substituents can help mitigate this phenomenon. Furthermore, aggregation formation, which can compromise battery performance by reducing the solubility of the redox-active material, has been investigated using DFT and Molecular Dynamics (MD) simulations.[185]

This is just a brief introduction to highlight the usefulness of density functional theory (DFT) calculations in the context of RFB. In this thesis, DFT calculations have been employed as a means to gain insight into and optimize the designed redox active materials (RAM) developed throughout the past three years (**Chapter 1** and **3**).

2.8. HIGREEW project

HIGREEW is a research and innovation project that aims to design, develop, and validate an advanced redox flow battery based on a new water-soluble, low-cost organic electrolyte. The battery will be compatible with an optimized low-resistance membrane and fast electrode kinetics to ensure long service life. The key objectives of the project are to create an environmentally sustainable battery with high energy and power density, maximize lifetime and efficiency, and minimize costs.

The HIGREEW project began four years ago in November 2019 and involves 10 organizations from six different countries: CIC energigune, Gamesa Electric, Universidad Autónoma de Madrid, Siemens Gamesa (Spain), CNRS (France), C-TECH (United Kingdom), University of West Bohemia, PinFlow Energy Storage (Czech Republic), Uniresearch (Netherlands), and Fraunhofer ICT (Germany).

During the first half of the project, the focus was on the technical aspects. CIC Energigune, in collaboration with a student from UAM, developed the organic electrolyte. Different organic catholytes and anolytes were synthesized, and their electrochemical properties were analyzed for implementation in a Redox Flow Battery. Simultaneously, our group was responsible for selecting, characterizing, and modifying various commercial Ion Exchange Membranes. Since the commercial membranes showed high permeation for organic redox-active materials, different modifications such as *in situ* polymerization and Layer-by-Layer deposition were developed and optimized to reduce permeability while minimizing increased resistance. Additionally, in France, CNRS studied the compatibility of the redox-active materials with carbon felts and determined the best activation method (thermal, chemical, etc.).

The second part of the project is now nearing completion, where all the components have been assembled in an initial stack to demonstrate their performance in an RFB. The system setup, optimization, and validation have been developed in collaboration between C-TECH, Pinflow Energy Storage, Gamesa Electric, and Fraunhofer ICT.

Through this project, knowledge regarding a complete RFB system, not just single-cells, has been acquired. Typically, universities focus on experiments related to single-cells due to their simplicity and lower cost of setup. However, after these initial trials, scale-up through stacks, which allow for the storage of larger amounts of energy (from kWh to MWh), is carried out by companies. Therefore, this project has provided the student with a closer perspective on the final battery product.

2.9. References

(1) Dresselhaus, M. S.; Thomas, I. L. Alternative Energy Technologies. **2001**, *414*.

(2) Sternberg, A.; Bardow, A. Power-to-What? – Environmental Assessment of Energy Storage Systems. *Energy Environ. Sci.* **2015**, *8*, 389–400. https://doi.org/10.1039/C4EE03051F

(3) Yang, Z.; Zhang, J.; Kintner-Meyer, M. C. W.; Lu, X.; Choi, D.; Lemmon, J. P.; Liu, J. Electrochemical Energy Storage for Green Grid. *Chem. Rev.* **2011**, *111*, 3577–3613. https://doi.org/10.1021/cr100290v

(4) International Energy Outlook 2019.

(5) Mitali, J.; Dhinakaran, S.; Mohamad, A. A. Energy Storage Systems: A Review. *Energy Storage and Saving* **2022**, *1*, 166–216. https://doi.org/10.1016/j.enss.2022.07.002

(6) Dunn, B.; Kamath, H.; Tarascon, J.-M. Electrical Energy Storage for the Grid: A Battery of Choices. *Science* **2011**, *334*, 928–935. https://doi.org/10.1126/science.1212741

(7) Hossain, E.; Faruque, H.; Sunny, Md.; Mohammad, N.; Nawar, N. A Comprehensive Review on Energy Storage Systems: Types, Comparison, Current Scenario, Applications, Barriers, and Potential Solutions, Policies, and Future Prospects. *Energies* **2020**, *13*, 3651. https://doi.org/10.3390/en13143651

(8) Fan, L.; Tu, Z.; Chan, S. H. Recent Development of Hydrogen and Fuel Cell Technologies: A Review. *Energy Reports* **2021**, *7*, 8421–8446. https://doi.org/10.1016/j.egyr.2021.08.003

(9) Mousavi G, S. M.; Faraji, F.; Majazi, A.; Al-Haddad, K. A Comprehensive Review of Flywheel Energy Storage System Technology. *Renewable and Sustainable Energy Reviews* **2017**, *67*, 477–490. https://doi.org/10.1016/j.rser.2016.09.060

(10) Bazdar, E.; Sameti, M.; Nasiri, F.; Haghighat, F. Compressed Air Energy Storage in Integrated Energy Systems: A Review. *Renewable and Sustainable Energy Reviews* **2022**, *167*, 112701. https://doi.org/10.1016/j.rser.2022.112701

(11) Kumar, N.; Kim, S.-B.; Lee, S.-Y.; Park, S.-J. Recent Advanced Supercapacitor: A Review of Storage Mechanisms, Electrode Materials, Modification, and Perspectives. *Nanomaterials* **2022**, *12*, 3708. https://doi.org/10.3390/nano12203708

(12) Kurzweil, P. Gaston Planté and His Invention of the Lead–Acid Battery—The Genesis of the First Practical Rechargeable Battery. *Journal of Power Sources* **2010**, *195*, 4424–4434. https://doi.org/10.1016/j.jpowsour.2009.12.126

(13) Sparacino, A. R.; Reed, G. F.; Kerestes, R. J.; Grainger, B. M.; Smith, Z. T. Survey of Battery Energy Storage Systems and Modeling Techniques. In *2012 IEEE Power and Energy Society General Meeting*; IEEE: San Diego, CA, 2012; pp 1–8. https://doi.org/10.1109/PESGM.2012.6345071

(14) Zhang, S.: Guo, W.: Yang, F.: Zheng, P.: Qiao, R.: Li, Z. Recent Progress in Polysulfide Redox-Flow Batteries. *Batteries Supercaps* **2019**, *2*, 627-637. https://doi.org/10.1002/batt.201900056

(15) Reddy, M. V.; Mauger, A.; Julien, C. M.; Paolella, A.; Zaghib, K. Brief History of Early Lithium-Battery Development. *Materials* **2020**, *13*, 1884. https://doi.org/10.3390/ma13081884

(16) Usiskin, R.; Lu, Y.; Popovic, J.; Law, M.; Balaya, P.; Hu, Y.-S.; Maier, J. Fundamentals, Status and Promise of Sodium-Based Batteries. *Nat Rev Mater* **2021**, *6* (11), 1020–1035. https://doi.org/10.1038/s41578-021-00324-w

(17) Faggioli, E.; Rena, P.; Danel, V.; Andrieu, X.; Mallant, R.; Kahlen, H. Supercapacitors for the Energy Management of Electric Vehicles. **1999**.

(18) Bolund, B.; Bernhoff, H.; Leijon, M. Flywheel Energy and Power Storage Systems. *Renewable and Sustainable Energy Reviews* **2007**, *11*, 235–258. https://doi.org/10.1016/j.rser.2005.01.004

(19) Wang, Y.; Liu, C.; Pan, R.; Chen, Z. Modeling and State-of-Charge Prediction of Lithium-Ion Battery and Ultracapacitor Hybrids with a Co-Estimator. *Energy* **2017**, *121*, 739–750. https://doi.org/10.1016/j.energy.2017.01.044

(20) Chen, Y.; Kang, Y.; Zhao, Y.; Wang, L.; Liu, J.; Li, Y.; Liang, Z.; He, X.; Li, X.; Tavajohi, N.; Li, B. A Review of Lithium-Ion Battery Safety Concerns: The Issues, Strategies, and Testing Standards. *Journal of Energy Chemistry* **2021**, *59*, 83–99. https://doi.org/10.1016/j.jechem.2020.10.017

(21) Goodenough, J. B.; Park, K.-S. The Li-Ion Rechargeable Battery: A Perspective. *J. Am. Chem. Soc.* **2013**, *135* (4), 1167–1176. https://doi.org/10.1021/ja3091438

(22) Ibrahim, H.; Ilinca, A.; Perron, J. Energy Storage Systems—Characteristics and Comparisons. *Renewable and Sustainable Energy Reviews* **2008**, *12*, 1221–1250. https://doi.org/10.1016/j.rser.2007.01.023

(23) Ke, X.; Prahl, J. M.; Alexander, J. I. D.; Wainright, J. S.; Zawodzinski, T. A.; Savinell, R. F. Rechargeable Redox Flow Batteries: Flow Fields, Stacks and Design Considerations. *Chem. Soc. Rev.* **2018**, *47*, 8721–8743. https://doi.org/10.1039/C8CS00072G

(24) Arévalo-Cid, P.; Dias, P.; Mendes, A.; Azevedo, J. Redox Flow Batteries: A New Frontier on Energy Storage. *Sustainable Energy Fuels* **2021**, *5*, 5366–5419. https://doi.org/10.1039/D1SE00839K

(25) Li, X.; Zhang, H.; Mai, Z.; Zhang, H.; Vankelecom, I. Ion Exchange Membranes for Vanadium Redox Flow Battery (VRB) Applications. *Energy Environ. Sci.* **2011**, *4*, 1147. https://doi.org/10.1039/c0ee00770f

(26) Ghimire, P. C.; Bhattarai, A.; Lim, T. M.; Wai, N.; Skyllas-Kazacos, M.; Yan, Q. In-Situ Tools Used in Vanadium Redox Flow Battery Research—Review. *Batteries* **2021**, *7*, 53. https://doi.org/10.3390/batteries7030053

(27) Li, M.; Odom, S. A.; Pancoast, A. R.; Robertson, L. A.; Vaid, T. P.; Agarwal, G.; Doan, H. A.; Wang, Y.; Suduwella, T. M.; Bheemireddy, S. R.; Ewoldt, R. H.; Assary, R. S.; Zhang, L.; Sigman, M. S.; Minteer, S. D. Experimental Protocols for Studying Organic Non-Aqueous Redox Flow Batteries. *ACS Energy Lett.* **2021**, *6*, 3932–3943. https://doi.org/10.1021/acsenergylett.1c01675

(28) Yao, Y.; Lei, J.; Shi, Y.; Ai, F.; Lu, Y.-C. Assessment Methods and Performance Metrics for Redox Flow Batteries. *Nat Energy* **2021**, *6*, 582–588. https://doi.org/10.1038/s41560-020-00772-8

(29) Wagner, N.; Gülzow, E. Change of Electrochemical Impedance Spectra (EIS) with Time during CO-Poisoning of the Pt-Anode in a Membrane Fuel Cell. *Journal of Power Sources* **2004**, *127*, 341–347. https://doi.org/10.1016/j.jpowsour.2003.09.031

(30) Zheng, Q.; Xing, F.; Li, X.; Ning, G.; Zhang, H. Flow Field Design and Optimization Based on the Mass Transport Polarization Regulation in a Flow-through Type Vanadium Flow Battery. *Journal of Power Sources* **2016**, *324*, 402–411. https://doi.org/10.1016/j.jpowsour.2016.05.110

(31) Kwabi, D. G.; Ji, Y.; Aziz, M. J. Electrolyte Lifetime in Aqueous Organic Redox Flow Batteries: A Critical Review. *Chem. Rev.* **2020**, *120*, 6467–6489. https://doi.org/10.1021/acs.chemrev.9b00599.

(32) Liu, Y.; Chen, Q.; Zhang, X.; Ran, J.; Han, X.; Yang, Z.; Xu, T. Degradation of Electrochemical Active Compounds in Aqueous Organic Redox Flow Batteries. *Current Opinion in Electrochemistry* **2022**, *32*, 100895. https://doi.org/10.1016/j.coelec.2021.100895

(33) Wei, L.; Zhao, T. S.; Xu, Q.; Zhou, X. L.; Zhang, Z. H. In-Situ Investigation of Hydrogen Evolution Behavior in Vanadium Redox Flow Batteries. *Applied Energy* **2017**, *190*, 1112–1118. https://doi.org/10.1016/j.apenergy.2017.01.039

(34) Prifti, H.; Parasuraman, A.; Winardi, S.; Lim, T. M.; Skyllas-Kazacos, M. Membranes for Redox Flow Battery Applications. *Membranes* **2012**, *2*, 275–306. https://doi.org/10.3390/membranes2020275

(35) Viswanathan, V.; Crawford, A.; Stephenson, D.; Kim, S.; Wang, W.; Li, B.; Coffey, G.; Thomsen, E.; Graff, G.; Balducci, P.; Kintner-Meyer, M.; Sprenkle, V. Cost and Performance Model for Redox Flow Batteries. *Journal of Power Sources* **2014**, *247*, 1040–1051. https://doi.org/10.1016/j.jpowsour.2012.12.023

(36) Chen, D.; Kim, S.; Sprenkle, V.; Hickner, M. A. Composite Blend Polymer Membranes with Increased Proton Selectivity and Lifetime for Vanadium Redox Flow Batteries. *Journal of Power Sources* **2013**, *231*, 301–306. https://doi.org/10.1016/j.jpowsour.2013.01.007

(37) Xi, J.; Wu, Z.; Qiu, X.; Chen, L. Nafion/SiO2 Hybrid Membrane for Vanadium Redox Flow Battery. *Journal of Power Sources* **2007**, *166*, 531–536. https://doi.org/10.1016/j.jpowsour.2007.01.069

(38) Mao, X. SPES/PVDF Binary Membrane as an Alternative Proton Exchange Membrane in Vanadium Redox Flow Battery Application. *J. Wuhan Univ. Technol.-Mat. Sci. Edit.* **2018**, *33*, 1428–1432. https://doi.org/10.1007/s11595-018-1986-6

(39) Hudak, N. S.; Small, L. J.; Pratt, H. D.; Anderson, T. M. Through-Plane Conductivities of Membranes for Nonaqueous Redox Flow Batteries. *J. Electrochem. Soc.* **2015**, *162*, A2188–A2194. https://doi.org/10.1149/2.0901510jes

(40) Tung, S. on; Fisher, S. L.; Kotov, N. A.; Thompson, L. T. Nanoporous Aramid Nanofibre Separators for Nonaqueous Redox Flow Batteries. *Nat Commun* **2018**, *9*, 4193. https://doi.org/10.1038/s41467-018-05752-x

(41) Kreuer, K.-D.; Jannasch, P. A Practical Method for Measuring the Ion Exchange Capacity Decrease of Hydroxide Exchange Membranes during Intrinsic Degradation. *Journal of Power Sources* **2018**, *375*, 361–366. https://doi.org/10.1016/j.jpowsour.2017.07.106

(42) Vega, J. A.; Chartier, C.; Mustain, W. E. Effect of Hydroxide and Carbonate Alkaline Media on Anion Exchange Membranes. *Journal of Power Sources* **2010**, *195*, 7176–7180. https://doi.org/10.1016/j.jpowsour.2010.05.030

(43) Nagarale, R. K.; Gohil, G. S.; Shahi, V. K. Recent Developments on Ion-Exchange Membranes and Electro-Membrane Processes. *Advances in Colloid and Interface Science* **2006**, *119*, 97–130. https://doi.org/10.1016/j.cis.2005.09.005

(44) Pujiastuti, S.; Onggo, H. Effect of Various Concentration of Sulfuric Acid for Nafion Membrane Activation on the Performance of Fuel Cell; Bandung, Indonesia, 2016; p 060006. https://doi.org/10.1063/1.4941639

(45) Jiang, B.; Yu, L.; Wu, L.; Mu, D.; Liu, L.; Xi, J.; Qiu, X. Insights into the Impact of the Nafion Membrane Pretreatment Process on Vanadium Flow Battery Performance. *ACS Appl. Mater. Interfaces* **2016**, *8*, 12228–12238. https://doi.org/10.1021/acsami.6b03529

(46) Nayak, P. K.; Yang, L.; Brehm, W.; Adelhelm, P. From Lithium-Ion to Sodium-Ion Batteries: Advantages, Challenges, and Surprises. *Angew. Chem. Int. Ed.* **2018**, *57*, 102–120. https://doi.org/10.1002/anie.201703772

(47) Kim, K. J.; Park, M.-S.; Kim, Y.-J.; Kim, J. H.; Dou, S. X.; Skyllas-Kazacos, M. A Technology Review of Electrodes and Reaction Mechanisms in Vanadium Redox Flow Batteries. *J. Mater. Chem. A* **2015**, *3*, 16913–16933. https://doi.org/10.1039/C5TA02613J

(48) Tsai, H.-M.; Yang, Shin-Yi; Ma, C.-C. M.; Xie, X. Preparation and Electrochemical Properties of Graphene-Modified Electrodes for All-Vanadium Redox Flow Batteries. *Electroanalysis* **2011**, *23*, 2139–2143. https://doi.org/10.1002/elan.201100181

(49) Wang, X.; Li, W.; Chen, Z.; Waje, M.; Yan, Y. Durability Investigation of Carbon Nanotube as Catalyst Support for Proton Exchange Membrane Fuel Cell. *Journal of Power Sources* **2006**, *158*, 154–159. https://doi.org/10.1016/j.jpowsour.2005.09.039

(50) Park, S.; Popov, B. N. Effect of a GDL Based on Carbon Paper or Carbon Cloth on PEM Fuel Cell Performance. *Fuel* **2011**, *90*, 436–440. https://doi.org/10.1016/j.fuel.2010.09.003

(51) Kaneko, H.; Nozaki, K.; Wada, Y.; Aoki, T.; Negishi, A.; Kamimoto, M. Vanadium Redox Reactions and Carbon Electrodes for Vanadium Redox Flow Battery. *Electrochimica Acta* **1991**, *36*, 1191–1196. https://doi.org/10.1016/0013-4686(91)85108-J

(52) Rychcik, M.; Skyllas-Kazacos, M. Evaluation of Electrode Materials for Vanadium Redox Cell. *Journal of Power Sources* **1987**, *19*, 45–54. https://doi.org/10.1016/0378-7753(87)80006-X

(53) Sun, B.: Skyllas-Kazacos, M. Modification of graphite electrode materials for vanadium redox flow battery application—I. Thermal treatment. *Electrochimica Acta* ***1992***, 37, *1253*–1260. https://doi.org/10.1016/0013-4686(92)85064-R

(54) Sun, B.; Skyllas-Kazacos, M. Chemical Modification of Graphite Electrode Materials for Vanadium Redox Flow Battery Application—Part II. Acid Treatments. *Electrochimica Acta* **1992**, *37*, 2459–2465. https://doi.org/10.1016/0013-4686(92)87084-D

(55) Sun, B.; Skyllas-Kazakos, M. Chemical Modification and Electrochemical Behaviour of Graphite Fibre in Acidic Vanadium Solution. *Electrochimica Acta* **1991**, *36*, 513–517. https://doi.org/10.1016/0013-4686(91)85135-T

(56) Xing, F.; Liu, T.; Yin, Y.; Bi, R.; Zhang, Q.; Yin, L.; Li, X. Highly Active Hollow Porous Carbon Spheres@Graphite Felt Composite Electrode for High Power Density Vanadium Flow Batteries. *Adv Funct Materials* **2022**, *32*, 2111267. https://doi.org/10.1002/adfm.202111267

(57) Li, Y.; Yang, S.; Zhao, Y.; Mubarak, N.; Xu, M.; Ihsan-Ul-Haq, M.; Zhao, T.; Chen, Q.; Kim, J.-K. Deciphering the Exceptional Kinetics of Hierarchical Nitrogen-Doped Carbon Electrodes for High-Performance Vanadium Redox Flow Batteries. *J. Mater. Chem. A* **2022**, *10*, 5605–5613. https://doi.org/10.1039/D2TA00324D

(58) Zhang, X.; Zhang, D.; Xu, Z.; Zhang, K.; Zhang, Y.; Jing, M.; Liu, L.; Zhang, Z.; Pu, N.; Liu, J.; Yan, C. A Pioneering Melamine Foam-Based Electrode via Facile Synthesis as Prospective Direction for Vanadium Redox Flow Batteries. *Chemical Engineering Journal* **2022**, *439*, 135718. https://doi.org/10.1016/j.cej.2022.135718

(59) Lv, Y.; Yang, C.; Wang, H.; Zhang, J.; Xiang, Y.; Lu, S. Antimony-Doped Tin Oxide as an Efficient Electrocatalyst toward the VO^{2+} /VO_2^{+} Redox Couple of the Vanadium Redox Flow Battery. *Catal. Sci. Technol.* **2020**, *10*, 2484–2490. https://doi.org/10.1039/C9CY01793C

(60) Wang, W. H.; Wang, X. D. Investigation of Ir-Modified Carbon Felt as the Positive Electrode of an All-Vanadium Redox Flow Battery. *Electrochimica Acta* **2007**, *52*, 6755–6762. https://doi.org/10.1016/j.electacta.2007.04.121

(61) García-Alcalde, L.; González, Z.; Barreda, D.; Rocha, V. G.; Blanco, C.; Santamaría, R. Unraveling the Relevance of Carbon Felts Surface Modification during Electrophoretic Deposition of Nanocarbons on Their Performance as Electrodes for the VO2+/VO2+ Redox Couple. *Applied Surface Science* **2021**, *569*, 151095. https://doi.org/10.1016/j.apsusc.2021.151095

(62) Tang, L.; Leung, P.; Xu, Q.; Mohamed, M. R.; Dai, S.; Zhu, X.; Flox, C.; Shah, A. A. Future Perspective on Redox Flow Batteries: Aqueous versus Nonaqueous Electrolytes. *Current Opinion in Chemical Engineering* **2022**, *37*, 100833. https://doi.org/10.1016/j.coche.2022.100833

(63) Gong, K.; Fang, Q.; Gu, S.; Li, S. F. Y.; Yan, Y. Nonaqueous Redox-Flow Batteries: Organic Solvents, Supporting Electrolytes, and Redox Pairs. *Energy Environ. Sci.* **2015**, *8*, 3515–3530. https://doi.org/10.1039/C5EE02341F

(64) Kowalski, J. A.; Su, L.; Milshtein, J. D.; Brushett, F. R. Recent Advances in Molecular Engineering of Redox Active Organic Molecules for Nonaqueous Flow Batteries. *Current Opinion in Chemical Engineering* **2016**, *13*, 45–52. https://doi.org/10.1016/j.coche.2016.08.002

(65) Shinkle, A. A.; Pomaville, T. J.; Sleightholme, A. E. S.; Thompson, L. T.; Monroe, C. W. Solvents and Supporting Electrolytes for Vanadium Acetylacetonate Flow

Batteries. *Journal of Power Sources* **2014**, *248*, 1299–1305. https://doi.org/10.1016/j.jpowsour.2013.10.034

(66) Shin, S.-H.; Yun, S.-H.; Moon, S.-H. A Review of Current Developments in Non-Aqueous Redox Flow Batteries: Characterization of Their Membranes for Design Perspective. *RSC Adv.* **2013**, *3*, 9095. https://doi.org/10.1039/c3ra00115f

(67) Singh, V.; Kim, S.; Kang, J.; Byon, H. R. Aqueous Organic Redox Flow Batteries. *Nano Res.* **2019**, *12* (9), 1988–2001. https://doi.org/10.1007/s12274-019-2355-2

(68) Gentil, S.; Reynard, D.; Girault, H. H. Aqueous Organic and Redox-Mediated Redox Flow Batteries: A Review. *Current Opinion in Electrochemistry* **2020**, *21*, 7–13. https://doi.org/10.1016/j.coelec.2019.12.006

(69) Fischer, P.; Mazúr, P.; Krakowiak, J. Family Tree for Aqueous Organic Redox Couples for Redox Flow Battery Electrolytes: A Conceptual Review. *Molecules* **2022**, *27*, 560. https://doi.org/10.3390/molecules27020560

(70) Skyllas-Kazacos, M.; Rychcik, M.; Robins, R. G.; Fane, A. G.; Green, M. A. New All-Vanadium Redox Flow Cell. *J. Electrochem. Soc.* **1986**, *133*, 1057–1058. https://doi.org/10.1149/1.2108706

(71) Lourenssen, K.; Williams, J.; Ahmadpour, F.; Clemmer, R.; Tasnim, S. Vanadium Redox Flow Batteries: A Comprehensive Review. *Journal of Energy Storage* **2019**, *25*, 100844. https://doi.org/10.1016/j.est.2019.100844

(72) Yuan, Z.; Yin, Y.; Xie, C.; Zhang, H.; Yao, Y.; Li, X. Advanced Materials for Zinc-Based Flow Battery: Development and Challenge. *Adv. Mater.* **2019**, *31* (50), 1902025. https://doi.org/10.1002/adma.201902025

(73) Zhang, H.; Sun, C.; Ge, M. Review of the Research Status of Cost-Effective Zinc–Iron Redox Flow Batteries. *Batteries* **2022**, *8*, 202. https://doi.org/10.3390/batteries8110202

(74) Anon. NASA Redox Storage System Development Project Calendar Year 1982. *NASA Technical Memorandum* **1983**.

(75) Yang, D.-S.; Lee, J. Y.; Jo, S.-W.; Yoon, S. J.; Kim, T.-H.; Hong, Y. T. Electrocatalytic Activity of Nitrogen-Doped CNT Graphite Felt Hybrid for All-Vanadium Redox Flow Batteries. *International Journal of Hydrogen Energy* **2018**, *43*, 1516–1522. https://doi.org/10.1016/j.ijhydene.2017.11.145

(76) He, Z.; Liu, L.; Gao, C.; Zhou, Z.; Liang, X.; Lei, Y.; He, Z.; Liu, S. Carbon Nanofibers Grown on the Surface of Graphite Felt by Chemical Vapour Deposition for Vanadium Redox Flow Batteries. *RSC Adv.* **2013**, *3*, 19774. https://doi.org/10.1039/c3ra22631j

(77) Shen, Y.; Xu, H.; Xu, P.; Wu, X.; Dong, Y.; Lu, L. Electrochemical Catalytic Activity of Tungsten Trioxide- Modified Graphite Felt toward VO2+/VO2+ Redox Reaction. *Electrochimica Acta* **2014**, *132*, 37–41. https://doi.org/10.1016/j.electacta.2014.03.107

(78) Xiang, Y.; Daoud, W. A. Cr2O3-Modified Graphite Felt as a Novel Positive Electrode for Vanadium Redox Flow Battery. *Electrochimica Acta* **2018**, *290*, 176–184. https://doi.org/10.1016/j.electacta.2018.09.023

(79) Xiang, Y.; Daoud, W. A. Binary $NiCoO_2$-Modified Graphite Felt as an Advanced Positive Electrode for Vanadium Redox Flow Batteries. *J. Mater. Chem. A* **2019**, *7*, 5589–5600. https://doi.org/10.1039/C8TA09650C

(80) Tsai, H.-M.; Yang, S.-J.; Ma, C.-C. M.; Xie, X. Preparation and Electrochemical Activities of Iridium-Decorated Graphene as the Electrode for All-Vanadium Redox Flow Batteries. *Electrochimica Acta* **2012**, *77*, 232–236. https://doi.org/10.1016/j.electacta.2012.05.099

(81) Suárez, D. J.; González, Z.; Blanco, C.; Granda, M.; Menéndez, R.; Santamaría, R. Graphite Felt Modified with Bismuth Nanoparticles as Negative Electrode in a Vanadium Redox Flow Battery. *ChemSusChem* **2014**, *7*, 914–918. https://doi.org/10.1002/cssc.201301045

(82) Zhang, W.; Xi, J.; Li, Z.; Zhou, H.; Liu, L.; Wu, Z.; Qiu, X. Electrochemical Activation of Graphite Felt Electrode for VO2+/VO2+ Redox Couple Application. *Electrochimica Acta* **2013**, *89*, 429–435. https://doi.org/10.1016/j.electacta.2012.11.072

(83) Skyllas-Kazacos, M.; Kazacos, M. State of Charge Monitoring Methods for Vanadium Redox Flow Battery Control. *Journal of Power Sources* **2011**, *196*, 8822–8827. https://doi.org/10.1016/j.jpowsour.2011.06.080

(84) Lopez-Atalaya, M.; Codina, G.; Perez, J. R.; Vazquez, J. L.; Aldaz, A. Optimization Studies on a Fe/Cr Redox Flow Battery. *Journal of Power Sources* **1992**, *39*, 147–154. https://doi.org/10.1016/0378-7753(92)80133-V

(85) Thaller, H. L. US 3996064. **1976**.

(86) Hagedorn, N. H.; Thaller, H. L. NASA-TEM-82854 Design Flexibility of Redox Flow Systems. **1982**.

(87) Bradley, C. S. US 312802. **1885**.

(88) Eustace, D. J. US 4064324. **1977**.

(89) Eustace, D. J. Bromine Complexation in Zinc-Bromine Circulating Batteries. *J. Electrochem. Soc.* **1980**, *127*, 528–532. https://doi.org/10.1149/1.2129706

(90) Winsberg, J.; Hagemann, T.; Janoschka, T.; Hager, M. D.; Schubert, U. S. Redox-Flow Batteries: From Metals to Organic Redox-Active Materials. *Angew. Chem. Int. Ed.* **2017**, *56*, 686–711. https://doi.org/10.1002/anie.201604925

(91) Ding, Y.; Zhang, C.; Zhang, L.; Zhou, Y.; Yu, G. Molecular Engineering of Organic Electroactive Materials for Redox Flow Batteries. *Chem. Soc. Rev.* **2018**, *47*, 69–103. https://doi.org/10.1039/C7CS00569E

(92) Zhong, F.; Yang, M.; Ding, M.; Jia, C. Organic Electroactive Molecule-Based Electrolytes for Redox Flow Batteries: Status and Challenges of Molecular Design. *Front. Chem.* **2020**, *8*, 451. https://doi.org/10.3389/fchem.2020.00451

(93) Milshtein, J. D.; Barton, J. L.; Carney, T. J.; Kowalski, J. A.; Darling, R. M.; Brushett, F. R. Towards Low Resistance Nonaqueous Redox Flow Batteries. *J. Electrochem. Soc.* **2017**, *164*, A2487–A2499. https://doi.org/10.1149/2.0741712jes

(94) Tseng, T.-M.; Huang, R.-H.; Huang, C.-Y.; Hsueh, K.-L.; Shieu, F.-S. A Kinetic Study of the Platinum/Carbon Anode Catalyst for Vanadium Redox Flow Battery. *J. Electrochem. Soc.* **2013**, *160*, A690–A696. https://doi.org/10.1149/2.073304jes

(95) Zhou, X.; Zhang, X.; Mo, L.; Zhou, X.; Wu, Q. Densely Populated Bismuth Nanosphere Semi-Embedded Carbon Felt for Ultrahigh-Rate and Stable Vanadium Redox Flow Batteries. **2020**, *16*, 190733–1907343. https://doi.org/10.1002/smll.201907333

(96) Xu, Q.; Zhao, T. S.; Zhang, C. Effects of SOC-Dependent Electrolyte Viscosity on Performance of Vanadium Redox Flow Batteries. *Applied Energy* **2014**, *130*, 139–147. https://doi.org/10.1016/j.apenergy.2014.05.034

(97) Geoffroy, I.; Willmann, P.; Mesfar, K.; Carré, B.; Lemordant, D. Electrolytic Characteristics of Ethylene Carbonate–Diglyme-Based Electrolytes for Lithium Batteries. *Electrochimica Acta* **2000**, *45*, 2019–2027. https://doi.org/10.1016/S0013-4686(99)00431-4

(98) Wiberg, C.; Carney, T. J.; Brushett, F.; Ahlberg, E.; Wang, E. Dimerization of 9,10-Anthraquinone-2,7-Disulfonic Acid (AQDS). *Electrochimica Acta* **2019**, *317*, 478–485. https://doi.org/10.1016/j.electacta.2019.05.134

(99) Wei, X.; Xu, W.; Huang, J.; Zhang, L.; Walter, E.; Lawrence, C.; Vijayakumar, M.; Henderson, W. A.; Liu, T.; Cosimbescu, L.; Li, B.; Sprenkle, V.; Wang, W. Radical Compatibility with Nonaqueous Electrolytes and Its Impact on an All-Organic Redox Flow Battery. *Angew. Chem. Int. Ed.* **2015**, *54*, 8684–8687. https://doi.org/10.1002/anie.201501443

(100) Nolte, O.; Volodin, I. A.; Stolze, C.; Hager, M. D.; Schubert, U. S. Trust Is Good, Control Is Better: A Review on Monitoring and Characterization Techniques for Flow

Battery Electrolytes. *Mater. Horiz.* **2021**, *8*, 1866–1925. https://doi.org/10.1039/D0MH01632B

(101) Curzons, A. D.; Constable, D. C.; Cunningham, V. L. Solvent Selection Guide: A Guide to the Integration of Environmental, Health and Safety Criteria into the Selection of Solvents. *Clean Technologies and Environmental Policy* **1999**, *1*, 82–90. https://doi.org/10.1007/s100980050014

(102) Liu, T.; Wei, X.; Nie, Z.; Sprenkle, V.; Wang, W. A Total Organic Aqueous Redox Flow Battery Employing a Low Cost and Sustainable Methyl Viologen Anolyte and 4-HO-TEMPO Catholyte. *Adv. Energy Mater.* **2016**, *6*, 1501449. https://doi.org/10.1002/aenm.201501449

(103) Hu, B.; DeBruler, C.; Rhodes, Z.; Liu, T. L. Long-Cycling Aqueous Organic Redox Flow Battery (AORFB) toward Sustainable and Safe Energy Storage. *J. Am. Chem. Soc.* **2017**, *139*, 1207–1214. https://doi.org/10.1021/jacs.6b10984

(104) Hu, B.; Liu, T. L. Two Electron Utilization of Methyl Viologen Anolyte in Nonaqueous Organic Redox Flow Battery. *Journal of Energy Chemistry* **2018**, *27*, 1326–1332. https://doi.org/10.1016/j.jechem.2018.02.014

(105) DeBruler, C.; Hu, B.; Moss, J.; Luo, J.; Liu, T. L. A Sulfonate-Functionalized Viologen Enabling Neutral Cation Exchange, Aqueous Organic Redox Flow Batteries toward Renewable Energy Storage. *ACS Energy Lett.* **2018**, *3*, 663–668. https://doi.org/10.1021/acsenergylett.7b01302

(106) Hu, B.; Tang, Y.; Luo, J.; Grove, G.; Guo, Y.; Liu, T. L. Improved Radical Stability of Viologen Anolytes in Aqueous Organic Redox Flow Batteries. *Chem. Commun.* **2018**, *54*, 6871–6874. https://doi.org/10.1039/C8CC02336K

(107) Bird, C. L.; Kuhn, A. T. Electrochemistry of the Viologens. *Chem. Soc. Rev.* **1981**, *10*, 49. https://doi.org/10.1039/cs9811000049

(108) DeBruler, C.; Hu, B.; Moss, J.; Liu, X.; Luo, J.; Sun, Y.; Liu, T. L. Designer Two-Electron Storage Viologen Anolyte Materials for Neutral Aqueous Organic Redox Flow Batteries. *Chem* **2017**, *3*, 961–978. https://doi.org/10.1016/j.chempr.2017.11.001

(109) Luo, J.; Hu, B.; Debruler, C.; Liu, T. L. A π-Conjugation Extended Viologen as a Two-Electron Storage Anolyte for Total Organic Aqueous Redox Flow Batteries. *Angew. Chem. Int. Ed.* **2018**, *57*, 231–235. https://doi.org/10.1002/anie.201710517

(110) Lv, X.-L.; Sullivan, P.; Fu, H.-C.; Hu, X.; Liu, H.; Jin, S.; Li, W.; Feng, D. Dextrosil-Viologen: A Robust and Sustainable Anolyte for Aqueous Organic Redox Flow Batteries. *ACS Energy Lett.* **2022**, *7*, 2428–2434. https://doi.org/10.1021/acsenergylett.2c01198

(111) Jin, S.; Fell, E. M.; Vina-Lopez, L.; Jing, Y.; Michalak, P. W.; Gordon, R. G.; Aziz, M. J. Near Neutral PH Redox Flow Battery with Low Permeability and Long-Lifetime Phosphonated Viologen Active Species. *Adv. Energy Mater.* **2020**, *10*, 2000100. https://doi.org/10.1002/aenm.202000100

(112) Liu, Y.; Goulet, M.-A.; Tong, L.; Liu, Y.; Ji, Y.; Wu, L.; Gordon, R. G.; Aziz, M. J.; Yang, Z.; Xu, T. A Long-Lifetime All-Organic Aqueous Flow Battery Utilizing TMAP-TEMPO Radical. *Chem* **2019**, *5*, 1861–1870. https://doi.org/10.1016/j.chempr.2019.04.021

(113) Wu, W.; Wang, A. P.; Luo, J.; Liu, T. L. A Highly Stable, Capacity Dense Carboxylate Viologen Anolyte towards Long-Duration Energy Storage. *Angew Chem Int Ed* **2023**, *62*. https://doi.org/10.1002/anie.202216662

(114) Hu, M.; Wu, W.; Luo, J.; Liu, T. L. Desymmetrization of Viologen Anolytes Empowering Energy Dense, Ultra Stable Flow Batteries toward Long-Duration Energy Storage. *Advanced Energy Materials* **2022**, *12*, 2202085. https://doi.org/10.1002/aenm.202202085

(115) Huang, J.; Yang, Z.; Murugesan, V.; Walter, E.; Hollas, A.; Pan, B.; Assary, R. S.; Shkrob, I. A.; Wei, X.; Zhang, Z. Spatially Constrained Organic Diquat Anolyte for

Stable Aqueous Flow Batteries. *ACS Energy Lett.* **2018**, *3*, 2533–2538. https://doi.org/10.1021/acsenergylett.8b01550

(116) Burešová, Z.; Klikar, M.; Mazúr, P.; Mikešová, M.; Kvíčala, J.; Bystron, T.; Bureš, F. Redox Property Tuning in Bipyridinium Salts. *Front. Chem.* **2021**, *8*, 631477. https://doi.org/10.3389/fchem.2020.631477

(117) Sánchez-Castellanos, M.; Flores-Leonar, M. M.; Mata-Pinzón, Z.; Laguna, H. G.; García-Ruiz, K. M.; Rozenel, S. S.; Ugalde-Saldívar, V. M.; Moreno-Esparza, R.; Pijpers, J. J. H.; Amador-Bedolla, C. Theoretical Exploration of 2,2′-Bipyridines as Electro-Active Compounds in Flow Batteries. *Phys. Chem. Chem. Phys.* **2019**, *21*, 15823–15832. https://doi.org/10.1039/C9CP03176F

(118) Kurreck, H.; Huber, M. Model Reactions for Photosynthesis—Photoinduced Charge and Energy Transfer between Covalently Linked Porphyrin and Quinone Units. *Angew. Chem. Int. Ed. Engl.* **1995**, *34*, 849–866. https://doi.org/10.1002/anie.199508491

(119) Scott, D. T.; Mcknight, D. M.; Blunt-Harris, E. L.; Kolesar, S. E.; Lovley, D. R. Quinone Moieties Act as Electron Acceptors in the Reduction of Humic Substances by Humics-Reducing Microorganisms. *Environ. Sci. Technol.* **1998**, *32*, 2984–2989. https://doi.org/10.1021/es980272q

(120) Quan, M.; Sanchez, D.; Wasylkiw, M. F.; Smith, D. K. Voltammetry of Quinones in Unbuffered Aqueous Solution: Reassessing the Roles of Proton Transfer and Hydrogen Bonding in the Aqueous Electrochemistry of Quinones. *J. Am. Chem. Soc.* **2007**, *129*, 12847–12856. https://doi.org/10.1021/ja0743083

(121) Wedege, K.; Dražević, E.; Konya, D.; Bentien, A. Organic Redox Species in Aqueous Flow Batteries: Redox Potentials, Chemical Stability and Solubility. *Sci Rep* **2016**, *6*, 39101. https://doi.org/10.1038/srep39101

(122) Xu, Y.; Wen, Y.; Cheng, J.; Yanga, Y.; Xie, Z.; Cao, G. Novel Organic Redox Flow Batteries Using Soluble Quinonoid Compounds as Positive Materials. *2009 World Non-Grid-Connected Wind Power and Energy Conference*; IEEE: Nanjing, China, 2009; 1–4. https://doi.org/10.1109/WNWEC.2009.5335870

(123) Drazevic, E.; Szabo, C.; Konya, D.; Lund, T.; Wedege, K.; Bentien, A. Investigation of Tetramorpholinohydroquinone as a Potential Catholyte in a Flow Battery. *ACS Appl. Energy Mater.* **2019**, *2*, 4745–4754. https://doi.org/10.1021/acsaem.9b00351

(124) Yang, X.; Garcia, S.; Janoschka, T.; Kónya, D.; Hager, M.; Schubert, U. Novel, Stable Catholyte for Aqueous Organic Redox Flow Batteries: Symmetric Cell Study of Hydroquinones with High Accessible Capacity. *Molecules* **2021**, *26*, 3823. https://doi.org/10.3390/molecules26133823

(125) Hoober-Burkhardt, L.; Krishnamoorthy, S.; Yang, B.; Murali, A.; Nirmalchandar, A.; Prakash, G. K. S.; Narayanan, S. R. A New Michael-Reaction-Resistant Benzoquinone for Aqueous Organic Redox Flow Batteries. *J. Electrochem. Soc.* **2017**, *164*, A600–A607. https://doi.org/10.1149/2.0351704jes

(126) Yang, B.; Hoober-Burkhardt, L.; Wang, F.; Surya Prakash, G. K.; Narayanan, S. R. An Inexpensive Aqueous Flow Battery for Large-Scale Electrical Energy Storage Based on Water-Soluble Organic Redox Couples. *J. Electrochem. Soc.* **2014**, *161*, A1371–A1380. https://doi.org/10.1149/2.1001409jes

(127) Yang, Z.; Tong, L.; Tabor, D. P.; Beh, E. S.; Goulet, M.-A.; De Porcellinis, D.; Aspuru-Guzik, A.; Gordon, R. G.; Aziz, M. J. Flow Batteries: Alkaline Benzoquinone Aqueous Flow Battery for Large-Scale Storage of Electrical Energy *Adv. Energy Mater.* **2018**, *8*, 1870034. https://doi.org/10.1002/aenm.201870034

(128) Wang, C.; Yang, Z.; Wang, Y.; Zhao, P.; Yan, W.; Zhu, G.; Ma, L.; Yu, B.; Wang, L.; Li, G.; Liu, J.; Jin, Z. High-Performance Alkaline Organic Redox Flow Batteries Based on 2-Hydroxy-3-Carboxy-1,4-Naphthoquinone. *ACS Energy Lett.* **2018**, *3*, 2404–2409. https://doi.org/10.1021/acsenergylett.8b01296

(129) Gerhardt, M. R.; Tong, L.; Gómez-Bombarelli, R.; Chen, Q.; Marshak, M. P.; Galvin, C. J.; Aspuru-Guzik, A.; Gordon, R. G.; Aziz, M. J. Anthraquinone Derivatives in

Aqueous Flow Batteries. *Adv. Energy Mater.* **2017**, *7*, 1601488. https://doi.org/10.1002/aenm.201601488

(130) Huskinson, B.; Marshak, M. P.; Suh, C.; Er, S.; Gerhardt, M. R.; Galvin, C. J.; Chen, X.; Aspuru-Guzik, A.; Gordon, R. G.; Aziz, M. J. A Metal-Free Organic–Inorganic Aqueous Flow Battery. *Nature* **2014**, *505*, 195–198. https://doi.org/10.1038/nature12909

(131) Lin, K.; Chen, Q.; Gerhardt, M. R.; Tong, L.; Kim, S. B.; Eisenach, L.; Valle, A. W.; Hardee, D.; Gordon, R. G.; Aziz, M. J.; Marshak, M. P. Alkaline Quinone Flow Battery. *Science* **2015**, *349*, 1529–1532. https://doi.org/10.1126/science.aab3033

(132) Amini, K.; Kerr, E. F.; George, T. Y.; Alfaraidi, A. M.; Jing, Y.; Tsukamoto, T.; Gordon, R. G.; Aziz, M. J. An Extremely Stable, Highly Soluble Monosubstituted Anthraquinone for Aqueous Redox Flow Batteries. *Adv Funct Materials* **2023**, 2211338. https://doi.org/10.1002/adfm.202211338

(133) Wu, M.; Jing, Y.; Wong, A. A.; Fell, E. M.; Jin, S.; Tang, Z.; Gordon, R. G.; Aziz, M. J. Extremely Stable Anthraquinone Negolytes Synthesized from Common Precursors. *Chem* **2020**, *6*, 1432–1442. https://doi.org/10.1016/j.chempr.2020.03.021

(134) Ji, Y.; Goulet, M.; Pollack, D. A.; Kwabi, D. G.; Jin, S.; Porcellinis, D.; Kerr, E. F.; Gordon, R. G.; Aziz, M. J. A Phosphonate-Functionalized Quinone Redox Flow Battery at Near-Neutral PH with Record Capacity Retention Rate. *Adv. Energy Mater.* **2019**, *9*, 1900039. https://doi.org/10.1002/aenm.201900039

(135) Kerr, E. F.; Tang, Z.; George, T. Y.; Jin, S.; Fell, E. M.; Amini, K.; Jing, Y.; Wu, M.; Gordon, R. G.; Aziz, M. J. High Energy Density Aqueous Flow Battery Utilizing Extremely Stable, Branching-Induced High-Solubility Anthraquinone near Neutral PH. *ACS Energy Lett.* **2023**, *8*, 600–607. https://doi.org/10.1021/acsenergylett.2c01691

(136) Huang, S.; Zhang, H.; Salla, M.; Zhuang, J.; Zhi, Y.; Wang, X.; Wang, Q. Molecular Engineering of Dihydroxyanthraquinone-Based Electrolytes for High-Capacity Aqueous Organic Redox Flow Batteries. *Nat Commun* **2022**, *13*, 4746. https://doi.org/10.1038/s41467-022-32424-8

(137) Goulet, M.-A.; Tong, L.; Pollack, D. A.; Tabor, D. P.; Odom, S. A.; Aspuru-Guzik, A.; Kwan, E. E.; Gordon, R. G.; Aziz, M. J. Extending the Lifetime of Organic Flow Batteries via Redox State Management. *J. Am. Chem. Soc.* **2019**, *141*, 8014–8019. https://doi.org/10.1021/jacs.8b13295

(138) Tong, L.; Jing, Y.; Gordon, R. G.; Aziz, M. J. Symmetric All-Quinone Aqueous Battery. *ACS Appl. Energy Mater.* **2019**, *2*, 4016–4021. https://doi.org/10.1021/acsaem.9b00691

(139) Hollas, A.; Wei, X.; Murugesan, V.; Nie, Z.; Li, B.; Reed, D.; Liu, J.; Sprenkle, V.; Wang, W. A Biomimetic High-Capacity Phenazine-Based Anolyte for Aqueous Organic Redox Flow Batteries. *Nat Energy* **2018**, *3*, 508–514. https://doi.org/10.1038/s41560-018-0167-3

(140) Lin, K.; Gómez-Bombarelli, R.; Beh, E. S.; Tong, L.; Chen, Q.; Valle, A.; Aspuru-Guzik, A.; Aziz, M. J.; Gordon, R. G. A Redox-Flow Battery with an Alloxazine-Based Organic Electrolyte. *Nat Energy* **2016**, *1*, 16102. https://doi.org/10.1038/nenergy.2016.102

(141) Orita, A.; Verde, M. G.; Sakai, M.; Meng, Y. S. A Biomimetic Redox Flow Battery Based on Flavin Mononucleotide. *Nat Commun* **2016**, *7*, 13230. https://doi.org/10.1038/ncomms13230

(142) Chen, S.; Hossain, M. S.; Foss, F. W. Organocatalytic Dakin Oxidation by Nucleophilic Flavin Catalysts. *Org. Lett.* **2012**, *14*, 2806–2809. https://doi.org/10.1021/ol3010326

(143) de Gonzalo, G.; Smit, C.; Jin, J.; Minnaard, A. J.; Fraaije, M. W. Turning a Riboflavin-Binding Protein into a Self-Sufficient Monooxygenase by Cofactor Redesign. *Chem. Commun.* **2011**, *47*, 11050. https://doi.org/10.1039/c1cc14039f

(144) Lindén, A. A.; Johansson, M.; Hermanns, N.; Bäckvall, J.-E. Efficient and Selective Sulfoxidation by Hydrogen Peroxide, Using a Recyclable Flavin−[BMIm]PF_6 Catalytic System. *J. Org. Chem.* **2006**, *71*, 3849–3853. https://doi.org/10.1021/jo060274q

(145) Orita, A.; Verde, M. G.; Sakai, M.; Meng, Y. S. A Biomimetic Redox Flow Battery Based on Flavin Mononucleotide. *Nat Commun* **2016**, *7*, 13230. https://doi.org/10.1038/ncomms13230

(146) Hong, J.; Lee, M.; Lee, B.; Seo, D.-H.; Park, C. B.; Kang, K. Biologically Inspired Pteridine Redox Centres for Rechargeable Batteries. *Nat Commun* **2014**, *5*, 5335. https://doi.org/10.1038/ncomms6335

(147) Chu, C.; Kwon, B. W.; Lee, W.; Kwon, Y. Effect of Temperature on the Performance of Aqueous Redox Flow Battery Using Carboxylic Acid Functionalized Alloxazine and Ferrocyanide Redox Couple. *Korean J. Chem. Eng.* **2019**, *36*, 1732–1739. https://doi.org/10.1007/s11814-019-0374-z

(148) Chang, D.; Kim, Y.; Jung, S. Comprehensive Study of the Performance of Alkaline Organic Redox Flow Batteries as Large-scale Energy Storage Systems. *Int J Energy Res* **2019**, *43*, 4449–4458. https://doi.org/10.1002/er.4573

(149) Wang, R.; Okajima, T.; Kitamura, F.; Kawauchi, S.; Matsumoto, N.; Thiemann, T.; Mataka, S.; Ohsaka, T. Catalytic Reduction of O_2 by Pyrazine Derivatives. *J. Phys. Chem. A* **2004**, *108*, 1891–1899. https://doi.org/10.1021/jp036024k

(150) Winsberg, J.; Stolze, C.; Muench, S.; Liedl, F.; Hager, M. D.; Schubert, U. S. TEMPO/Phenazine Combi-Molecule: A Redox-Active Material for Symmetric Aqueous Redox-Flow Batteries. *ACS Energy Lett.* **2016**, *1*, 976–980. https://doi.org/10.1021/acsenergylett.6b00413

(151) Wang, C.; Li, X.; Yu, B.; Wang, Y.; Yang, Z.; Wang, H.; Lin, H.; Ma, J.; Li, G.; Jin, Z. Molecular Design of Fused-Ring Phenazine Derivatives for Long-Cycling Alkaline Redox Flow Batteries. *ACS Energy Lett.* **2020**, *5*, 411–417. https://doi.org/10.1021/acsenergylett.9b02676

(152) Pang, S.; Wang, X.; Wang, P.; Ji, Y. Biomimetic Amino Acid Functionalized Phenazine Flow Batteries with Long Lifetime at Near-Neutral PH. *Angew Chem Int Ed* **2021**, *60*, 5289–5298. https://doi.org/10.1002/anie.202014610

(153) Lai, Y. Y.; Li, X.; Liu, K.; Tung, W.-Y.; Cheng, C.-F.; Zhu, Y. Stable Low-Cost Organic Dye Anolyte for Aqueous Organic Redox Flow Battery. *ACS Appl. Energy Mater.* **2020**, *3*, 2290–2295. https://doi.org/10.1021/acsaem.9b01735

(154) Xu, J.; Pang, S.; Wang, X.; Wang, P.; Ji, Y. Ultrastable Aqueous Phenazine Flow Batteries with High Capacity Operated at Elevated Temperatures. *Joule* **2021**, *5*, 2437–2449. https://doi.org/10.1016/j.joule.2021.06.019

(155) Janoschka, T.; Martin, N.; Hager, M. D.; Schubert, U. S. An Aqueous Redox-Flow Battery with High Capacity and Power: The TEMPTMA/MV System. *Angew. Chem. Int. Ed.* **2016**, *55*, 14427–14430. https://doi.org/10.1002/anie.201606472

(156) Beh, E. S.; De Porcellinis, D.; Gracia, R. L.; Xia, K. T.; Gordon, R. G.; Aziz, M. J. A Neutral PH Aqueous Organic–Organometallic Redox Flow Battery with Extremely High Capacity Retention. *ACS Energy Lett.* **2017**, *2*, 639–644. https://doi.org/10.1021/acsenergylett.7b00019

(157) Zeng, Y. K.; Zhao, T. S.; An, L.; Zhou, X. L.; Wei, L. A Comparative Study of All-Vanadium and Iron-Chromium Redox Flow Batteries for Large-Scale Energy Storage. *Journal of Power Sources* **2015**, *300*, 438–443. https://doi.org/10.1016/j.jpowsour.2015.09.100

(158) Waters, S. E.; Robb, B. H.; Marshak, M. P. Effect of Chelation on Iron–Chromium Redox Flow Batteries. *ACS Energy Lett.* **2020**, *5*, 1758–1762. https://doi.org/10.1021/acsenergylett.0c00761

(159) Luo, J.; Sam, A.; Hu, B.; DeBruler, C.; Wei, X.; Wang, W.; Liu, T. L. Unraveling PH Dependent Cycling Stability of Ferricyanide/Ferrocyanide in Redox Flow Batteries. *Nano Energy* **2017**, *42*, 215–221. https://doi.org/10.1016/j.nanoen.2017.10.057

(160) High Solubility Iron Hexacyanides. US Patent US9929425B2, Filed Februaty 20,2014, and Granted March 27, 2018.
(161) Luo, J.; Hu, B.; Debruler, C.; Bi, Y.; Zhao, Y.; Yuan, B.; Hu, M.; Wu, W.; Liu, T. L. Unprecedented Capacity and Stability of Ammonium Ferrocyanide Catholyte in PH Neutral Aqueous Redox Flow Batteries. *Joule* **2019**, *3*, 149–163. https://doi.org/10.1016/j.joule.2018.10.010
(162) Zhao, Z.; Zhang, B.; Schrage, B. R.; Ziegler, C. J.; Boika, A. Investigations Into Aqueous Redox Flow Batteries Based on Ferrocene Bisulfonate. *ACS Appl. Energy Mater.* **2020**, *3*, 10270–10277. https://doi.org/10.1021/acsaem.0c02259
(163) Chen, Q.; Li, Y.; Liu, Y.; Sun, P.; Yang, Z.; Xu, T. Designer Ferrocene Catholyte for Aqueous Organic Flow Batteries. *ChemSusChem* **2021**, *14*, 1295–1301. https://doi.org/10.1002/cssc.202002467
(164) Daum, P. H.; Enke, C. G. Electrochemical Kinetics of the Ferri-Ferrocyanide Couple on Platinum. *Anal. Chem.* **1969**, *41*, 653–656. https://doi.org/10.1021/ac60273a007
(165) Hawthorne, K. L.; Wainright, J. S.; Savinell, R. F. Studies of Iron-Ligand Complexes for an All-Iron Flow Battery Application. *J. Electrochem. Soc.* **2014**, *161*, A1662–A1671. https://doi.org/10.1149/2.0761410jes
(166) Gong, K.; Xu, F.; Grunewald, J. B.; Ma, X.; Zhao, Y.; Gu, S.; Yan, Y. All-Soluble All-Iron Aqueous Redox-Flow Battery. *ACS Energy Lett.* **2016**, *1*, 89–93. https://doi.org/10.1021/acsenergylett.6b00049
(167) Ferrere, S.; Gregg, B. A. Photosensitization of TiO_2 by $[Fe^{II}$ (2,2'-Bipyridine-4,4'-Dicarboxylic Acid)$_2$ $(CN)_2]$: Band Selective Electron Injection from Ultra-Short-Lived Excited States. *J. Am. Chem. Soc.* **1998**, *120*, 843–844. https://doi.org/10.1021/ja973504e
(168) Li, X.; Gao, P.; Lai, Y.-Y.; Bazak, J. D.; Hollas, A.; Lin, H.-Y.; Murugesan, V.; Zhang, S.; Cheng, C.-F.; Tung, W.-Y.; Lai, Y.-T.; Feng, R.; Wang, J.; Wang, C.-L.; Wang, W.; Zhu, Y. Symmetry-Breaking Design of an Organic Iron Complex Catholyte for a Long Cyclability Aqueous Organic Redox Flow Battery. *Nat Energy* **2021**, *6*, 873–881. https://doi.org/10.1038/s41560-021-00879-6
(169) Gao, J.; Amini, K.; George, T.Y.; Jing, Y.; Tsukamoto, T.; Xi, D.; Gordon, R. G.; Aziz, M. J. A High Potential, Low Capacity Fade Rate Iron Complex Posolyte for Aqueous Organic Flow Batteries. *Adv. Energy Mater.* **2022**, *12*, 2202444–2202457. https://doi.org/10.1002/aenm.202202444
(170) Book: Nitroxide Radicals: Properties, Synthesis and Applciations. In *Stable Radicals: Fundamentals and Applied Aspects of Odd-Electron Compounds*; 2010; Vol. 12, pp 173–229.
(171) Soule, B.; Hyodo, F.; Matsumoto, K.; Simone, N.; Cook, J.; Krishna, M.; Mitchell, J. The Chemistry and Biology of Nitroxide Compounds. *Free Radical Biology and Medicine* **2007**, *42*, 1632–1650. https://doi.org/10.1016/j.freeradbiomed.2007.02.030
(172) Winsberg, J.; Stolze, C.; Schwenke, A.; Muench, S.; Hager, M. D.; Schubert, U. S. Aqueous 2,2,6,6-Tetramethylpiperidine- *N*-Oxyl Catholytes for a High-Capacity and High Current Density Oxygen-Insensitive Hybrid-Flow Battery. *ACS Energy Lett.* **2017**, *2*, 411–416. https://doi.org/10.1021/acsenergylett.6b00655
(173) Winsberg, J.; Stolze, C.; Muench, S.; Liedl, F.; Hager, M. D.; Schubert, U. S. TEMPO/Phenazine Combi-Molecule: A Redox-Active Material for Symmetric Aqueous Redox-Flow Batteries. *ACS Energy Lett.* **2016**, *1*, 976–980. https://doi.org/10.1021/acsenergylett.6b00413
(174) Janoschka, T.; Friebe, C.; Hager, M. D.; Martin, N.; Schubert, U. S. An Approach Toward Replacing Vanadium: A Single Organic Molecule for the Anode and Cathode of an Aqueous Redox-Flow Battery. *ChemistryOpen* **2017**, *6*, 216–220. https://doi.org/10.1002/open.201600155

(175) Hu, B.; Hu, M.; Luo, J.; Liu, T. L. A Stable, Low Permeable TEMPO Catholyte for Aqueous Total Organic Redox Flow Batteries. *Advanced Energy Materials* **2022**, *12*, 2102577. https://doi.org/10.1002/aenm.202102577

(176) Fan, H.; Wu, W.; Ravivarma, M.; Li, H.; Hu, B.; Lei, J.; Feng, Y.; Sun, X.; Song, J.; Liu, T. L. Mitigating Ring-Opening to Develop Stable TEMPO Catholytes for PH-Neutral All-Organic Redox Flow Batteries. *Adv Funct Materials* **2022**, *32*, 2203032. https://doi.org/10.1002/adfm.202203032

(177) Ghule, S.; Dash, S. R.; Bagchi, S.; Joshi, K.; Vanka, K. Predicting the Redox Potentials of Phenazine Derivatives Using DFT-Assisted Machine Learning. *ACS Omega* **2022**, *7*, 11742–11755. https://doi.org/10.1021/acsomega.1c06856

(178) Kucharyson, J. F.; Cheng, L.; Tung, S. O.; Curtiss, L. A.; Thompson, L. T. Predicting the Potentials, Solubilities and Stabilities of Metal-Acetylacetonates for Non-Aqueous Redox Flow Batteries Using Density Functional Theory Calculations. *J. Mater. Chem. A* **2017**, *5* (26), 13700–13709. https://doi.org/10.1039/C7TA01285C

(179) Cheng, L.; Assary, R. S.; Qu, X.; Jain, A.; Ong, S. P.; Rajput, N. N.; Persson, K.; Curtiss, L. A. Accelerating Electrolyte Discovery for Energy Storage with High-Throughput Screening. *J. Phys. Chem. Lett.* **2015**, *6*, 283–291. https://doi.org/10.1021/jz502319n

(180) de la Cruz, C.; Molina, A.; Patil, N.; Ventosa, E.; Marcilla, R.; Mavrandonakis, A. New Insights into Phenazine-Based Organic Redox Flow Batteries by Using High-Throughput DFT Modelling. *Sustainable Energy Fuels* **2020**, *4*, 5513–5521. https://doi.org/10.1039/D0SE00687D

(181) Griffin, J. D.; Pancoast, A. R.; Sigman, M. S. Interrogation of 2,2′-Bipyrimidines as Low-Potential Two-Electron Electrolytes. *J. Am. Chem. Soc.* **2021**, *143*, 992–1004. https://doi.org/10.1021/jacs.0c11267

(182) Oldenburg, F. J.; Bon, M.; Perego, D.; Polino, D.; Laino, T.; Gubler, L.; Schmidt, T. J. Revealing the Role of Phosphoric Acid in All-Vanadium Redox Flow Batteries with DFT Calculations and *in Situ* Analysis. *Phys. Chem. Chem. Phys.* **2018**, *20*, 23664–23673. https://doi.org/10.1039/C8CP04517H

(183) Hashemi, A.; Peljo, P.; Laasonen, K. Understanding Electron Transfer Reactions Using Constrained Density Functional Theory: Complications Due to Surface Interactions. *J. Phys. Chem. C.* **2023**, *127*, 3398–3407. https://doi.org/10.1021/acs.jpcc.2c06537

(184) Lv, Y.; Liu, Y.; Feng, T.; Zhang, J.; Lu, S.; Wang, H.; Xiang, Y. Structure Reorganization-Controlled Electron Transfer of Bipyridine Derivatives as Organic Redox Couples. *J. Mater. Chem. A* **2019**, *7*, 27016–27022. https://doi.org/10.1039/C9TA08910A

(185) Xiang, Z.; Li, W.; Wan, K.; Fu, Z.; Liang, Z. Aggregation of Electrochemically Active Conjugated Organic Molecules and Its Impact on Aqueous Organic Redox Flow Batteries. *Angew Chem Int Ed* **2023**, *62*. https://doi.org/10.1002/anie.202214601

3. General objectives of the Doctoral Thesis

3. General objectives of the Doctoral Thesis

Energy storage is a critical pillar of modern societies, providing a vital solution to address contemporary challenges faced by our communities. As we strive to transition towards more sustainable and environmentally friendly practices, the integration of renewable energies into the electrical grid and the reduction of CO_2 emissions have become imperatives in combatting climate change and its far-reaching effects. In this context, energy storage technologies play a pivotal role, enabling the efficient capture, storage, and utilization of renewable energy sources while providing stability and reliability to the grid.

To facilitate these essential transitions, the European Union has been at the forefront of supporting numerous research projects dedicated to advancing energy storage technologies.

The HIGREEW project, within which this thesis is situated, holds a particular significance in the realm of energy storage research. The primary objective of this project is to advance and validate an aqueous organic redox flow battery system. Redox flow batteries offer unique advantages for large-scale energy storage, providing scalability, high energy density, and enhanced safety compared to traditional battery technologies. As part of the HIGREEW project, our research group has been diligently engaged in selecting, characterizing, and modifying commercial ion exchange membranes. These membranes are integral components of the redox flow battery, facilitating the efficient transport of ions between the positive and negative electrolytes. Additionally, our efforts are dedicated to developing new organic electrolytes to replace the current vanadium electrolyte, which aligns with the overall goals of the project.

In this context, the objectives of this research are centered around the critical role of energy storage in modern societies, aiming to address pressing challenges and support sustainable practices. Specifically, the objectives are:

1. Develop and validate an aqueous organic redox flow battery as a key energy storage technology for enabling the seamless transition from fossil fuels to renewable energies.

2. Select, characterize, and modify commercial ion exchange membranes to enhance their performance and suitability for use in redox flow batteries.

3. Utilize the research group's expertise in organic synthesis to develop and comprehend organic redox active materials, with a focus on optimizing their electrochemical properties, solubility, and stability within the battery environment.

4. Evaluate the performance and behavior of various organic redox active materials in redox flow batteries under different conditions to identify promising candidates for practical applications.
5. Employ Density Functional Theory (DFT) calculations to gain mechanistic insights into the redox reactions and ion transport processes occurring within the battery system, providing a deeper understanding of the underlying mechanisms.
6. Contribute to advancing energy storage technology and promoting a sustainable future by harnessing the potential of organic redox active materials and their applications in redox flow batteries.

4. Experimental and theoretical procedures

4. Experimental and theoretical procedures

4.1. Electrochemical techniques

This thesis has mainly focused on understanding Aqueous Organic Redox Flow Batteries and developing new anolytes based on viologen and triazine chemistry. As RFB are Electrochemical Energy Storage Devices, the primary characterization techniques employed are electrochemical. However, chemical characterization has also been conducted. Below, it is provided a brief description of the most common characterization techniques for organic redox active materials and redox flow batteries.

4.1.1. Characterization of Redox Active Materials

4.1.1.1 Cyclic voltammetry and Linear Sweep Voltammetry

Cyclic Voltammetry (CV) is one of the most well-known and powerful techniques for the rapid characterization of electroactive molecular species. CV provides information about the redox process without the need for complex systems or sophisticated mathematical transformations. However, the interpretation of CV results is not always straightforward due to the influence of various processes, including chemical reactions coupled to the redox process,[1] ohmic resistance,[2] double-layer capacitance,[3] and electrode effects, among others.[4,5]

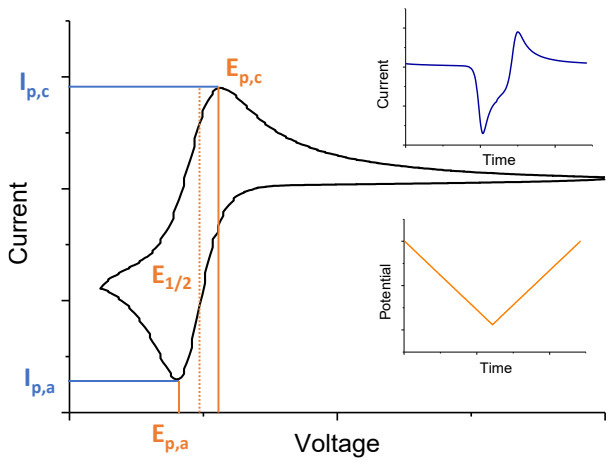

Figure 1: Schematic representation of Cyclic Voltammetry.

Cyclic Voltammetry is performed using a three-electrode setup, which includes a working electrode (where the electrochemical event of interest occurs), a counter electrode (to complete the electric circuit with the working electrode), and a reference electrode (a nonpolarizable electrode with a well-known and stable equilibrium potential used as a reference point for measuring the potential applied

to the working electrode). A potentiostat is used to incrementally increase the potential (the energy of electrons in the electrode) until a specific current flows between the working and counter electrodes.

If only a single linear scan is performed, the technique is referred to as Linear Sweep Voltammetry (LSV). In cases where electrochemically reversible redox processes involve freely diffusing redox species, the peak current follows the Randles-Sevcik equation:

$$I_p = 0.4463nFAc\sqrt{\frac{nFvD}{RT}} \quad (1)$$

In the equation, I_p represents the peak current (mA/cm^2), n is the number of electrons involved in the redox reaction, F is the Faraday constant, A is the electrode surface area (cm^2), c is the molar concentration (mol/cm^3), v is the scan rate (V/s), and D is the diffusion coefficient of the consumed molecule in the electrode (cm^2/s). This equation allows for the calculation of the diffusion coefficients of the prepared redox active materials. It's worth noting that slight differences may be observed in irreversible processes. For electrode-absorbed species, the peak current exhibits a linear dependence on the scan rate.[6]

Furthermore, cyclic voltammetry (CV) can be used to study the reversibility of the redox process under investigation. It is important to understand that electrochemical irreversibility does not imply that the redox process cannot be reversed, but rather that it does not occur within the timescale of the experiment. Various approaches exist to assess reversibility, with Matsuda and Ayabe introducing the reversibility parameter, λ, which in this context refers to the balance between electrode kinetics and the timescale of the CV experiment.[7] From an analytical perspective, "*electrochemical reversibility*" implies that the surface concentrations of the reduced species ($c_{red,S}$ (t)) and oxidized species ($c_{ox,S}$ (t)) adhere to the Nernst equation at all times. Consequently, reversible systems should exhibit a close-to-unity relationship between the anodic peak current ($I_{p,a}$) and cathodic peak current ($I_{p,c}$).

In reversible redox processes, the current is primarily limited by diffusional mass transport, whereas in irreversible processes, the charge-transfer kinetics become the limiting factor. Quasireversible systems exhibit intermediate behavior, influenced by both charge transfer and mass transport phenomena.

For reversible redox processes, the peak potentials and peak separation remain independent of the scan rate, consistent with the Randles-Sevcik equation (as shown in equation 1). Conversely, in irreversible systems, the peak potential and peak separation increase (in absolute value) with higher scan rates.[8]

1. Reversible redox process: $\Delta E_p = \frac{57}{n}\ mV$

2. Quasireversible redox process: $\Delta E_p \leq \frac{200}{n}\ mV$
3. Irreversible redox process: $\Delta E_p \geq \frac{200}{n}\ mV$

In this thesis, almost all the examples studied exhibited a reversible or quasireversible redox behavior. Cyclic voltammetry measurements were conducted using a 5-neck cell with a Glassy carbon working electrode (6.1204.300 from Metrohm) of 3.0 mm diameter. Platinum (Pt) was utilized as the counter electrode (CE), and an Ag|AgCl electrode (3 M KCl) was employed as the reference electrode (RE) for all electrochemical measurements. Rotating disk electrode (RDE) experiments were performed using a Metrohm Autolab Motor Controller. Both cyclic voltammetry (CV) and RDE tests were carried out utilizing an Autolab electrochemical system II PGSTAT30 potentiostat.

4.1.1.2. Rotatory Disk Electrode (RDE)

Hydrodynamic voltammetry techniques, such as Rotating Disk Electrode (RDE) voltammetry, are widely employed for determining the kinetic constants and diffusion coefficients of the studied redox processes. In an RDE setup, a planar working electrode, typically made of glassy carbon, is rotated at a specific angular velocity (ω) in radians per second to induce convection at the electrode surface. As a result, mass transfer does not follow the Randles-Sevcik model, and instead of peaks, a plateau of constant current is observed at high overpotentials. This limiting current can be described using the Levich equation:

$$I_{lim} = 0.620nFAcD^{2/3}v^{-1/6}\omega^{1/2} \quad (2)$$

In the Levich equation, ν represents the kinematic viscosity of the electrolyte in cm^2/s, and ω denotes the angular rotation velocity.

Additionally, the Koutecky-Levich model enables us to establish a relationship between the measured current and the combined contributions of the kinetic activity and mass transport of the reactants. This model provides insights into the relative importance of these two factors in determining the observed current response.

$$\frac{1}{I_m} = \frac{1}{I_k} + \frac{1}{I_{MT}} \quad (3)$$

In the RDE setup, the I_{MT} = I_{lim} can be modeled using the Levich equation:

$$\frac{1}{I_m} = \frac{1}{I_k} + \frac{1}{0.62nFAD^{2/3}v^{-1/6}c\cdot\omega^{1/2}} \quad (4)$$

The kinetic current can be modeled by the Butler Volmer equation as:

$$\log i_K = \log nFC_oAk_o + \frac{\alpha nF\eta}{2.303RT} \quad (5)$$

where $k_o$is the standard rate constant (cm/s), α the charge transfer coefficient (dimensionless), and η is the overpotential defined as E – E_{eq} (V)

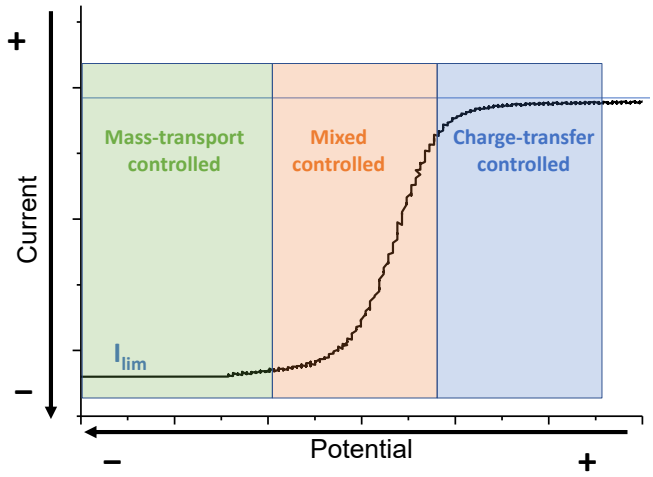

Figure 2: Schematic representation of LSV and the different regions for a reduction process.

By utilizing the Koutecky-Levich equation, it becomes possible to estimate the diffusion coefficient and kinetic constant of the redox process under investigation. Typically, organic redox active materials exhibit diffusion coefficients in the range of 10^{-6} cm^2/s and kinetic constants around 10^{-3} cm/s.

Another method commonly used in the literature for determining these parameters is the Nicholson equation.[8] However, it is worth noting that this method has not been employed in the present thesis and is therefore excluded from the analysis.

Rotating disk electrode measurements were recorded using the same experimental setup as employed in cyclic voltammetry.

4.1.1.3. Solubility

The UV-Vis absorption spectroscopy can be utilized to determine the concentration of a given solution containing organic redox active materials. According to the Lambert-Beer law, the absorbance of light is directly proportional to the concentration of the absorbing species in the solution. By measuring the absorbance of the solution at a specific wavelength in the UV-Vis range and applying the Lambert-Beer law, it becomes possible to quantify the concentration of the redox active material in the solution. This method provides a straightforward and widely used approach for determining the concentration of various compounds in solution:

$$A = \varepsilon l c \qquad (6)$$

In the Lambert-Beer law equation, *A* represents the absorbance, which reflects the relationship between the initial intensity of light and the intensity after passing through the sample (measured in arbitrary units). The molar absorption coefficient, ε, quantifies how strongly a molecule absorbs light at a specific wavelength (measured in $M^{-1} \cdot cm^{-1}$). The optical path length, *l*, denotes the distance the light travels through the sample (measured in cm). Lastly, *c* represents the concentration of the absorbing species in the solution (measured in M).

To determine the solubilities of the different prepared anolytes, UV-Vis spectroscopy was employed using a PerkinElmer Lambda 365 instrument. Calibration curves were previously obtained for all the compounds. An aliquot of the saturated solution of each derivative was diluted until the absorption of the sample matched the corresponding calibration curve. By multiplying the concentration obtained from the sample interpolation by the corresponding dilution factor, the maximum solubility of the compounds was calculated.

4.1.1.4. Nuclear Magnetic Resonance Spectroscopy

Nuclear Magnetic Resonance (NMR) spectroscopy is a powerful tool extensively used by organic chemists to elucidate, characterize, and confirm the structures of compounds. NMR spectroscopy relies on the presence of a magnetic field generated by a magnet within the instrument. This magnetic field causes different atoms within a sample to become aligned. In an organic molecule, protons can align in two distinct orientations: parallel to the magnetic field or antiparallel to it. These two orientations are not energetically equivalent, meaning that it requires a certain amount of energy to transition from one state to the other. When an organic molecule is introduced into the NMR magnet, and the energy of the magnetic field is gradually increased, the sample absorbs part of the magnetic field energy based on the chemical behavior of each proton within the molecule. This absorption of energy provides information about the nature of the protons in the organic molecule, effectively creating a unique fingerprint for each molecule.

This simplified explanation provides a general overview of the underlying principle of NMR spectroscopy. It showcases how the technique exploits the behavior of protons, allowing chemists to obtain valuable structural information about organic compounds.

In this thesis, NMR spectroscopy has been employed to characterize all the compounds utilized and synthesized. Both ^{1}H (proton) and ^{13}C (carbon) NMR spectroscopy have been conducted on all the prepared compounds. The purpose of these NMR measurements is to verify the organic structure of the compounds and confirm that the synthesized or received products are indeed the desired ones.

Figure 3: NMR magnets at the UAM (SIdI, Servicio Interdepartamental de Investigación) facilities.

4.1.2 Characterization of Ion Exchange Membranes (IEM)

4.1.2.1. Membrane pretreatment

In this thesis, the membranes under investigation were conditioned by immersing them in a solution of the appropriate supporting electrolyte. This process aimed to charge the membranes with the desired counterion. Commercially obtained membranes often contain unwanted counterions, such as iodine or methanesulfonate, which can potentially interfere with the subsequent electrochemical analysis. To mitigate this issue, the membranes were soaked in a solution of the desired supporting electrolyte. The soaking process was carried out at room temperature for a duration of 24 hours. By immersing the membranes in the supporting electrolyte solution, the undesired counter-ions were effectively exchanged with the desired counter-ions, ensuring the suitability of the membranes for the subsequent electrochemical studies.

4.1.2.2. Water uptake

Ion Exchange Membranes consist of a hydrophobic matrix containing dispersed hydrophilic groups. These hydrophilic groups, along with the pores and cavities within the membrane, have the ability to absorb water molecules.[9] This water absorption leads to an increase in the mass of the ion exchange membrane. To ensure the mechanical integrity of the membrane, it is important that the water uptake does not exceed a certain limit. Typically, the water uptake of an IEM should not exceed 30%. If the water uptake exceeds this threshold, the mechanical properties of the membrane may be compromised.[10]

To determine the water uptake of the membranes in this study, a series of steps were carried out. First, the membranes underwent pretreatment, after which they were washed with deionized (DI) water. Subsequently, the membranes were dried

in a vacuum oven at 60 °C and 100 mbar for a duration of 24 hours using a Memmert Vacuum drying oven VO. The weight of the membranes was then measured. Following the drying process, the membranes were hydrated by immersing them in DI water for 24 hours. After removing the excess water from the surface of the membranes using tissue paper, the membranes were weighed again. The water uptake of the membranes was calculated by comparing the weight before and after hydration:

$$Water\ uptake\ (WU) = \frac{w_w - w_d}{w_d} \cdot 100 \quad (7)$$

w_w represents the weight of the hydrated membrane, while w_d represents the weight of the dried membrane. To accurately measure the weights, we utilized a precision balance with a precision of 0.01 mg. This high-precision balance ensured accurate and reliable measurements of the membrane weights, enabling precise calculation of the water uptake percentage.

4.1.2.3. Swelling ratio

Due to the hydration of the IEM, a restructuring occurs within the hydrophobic matrix, resulting in swelling of the membrane in all three dimensions.[9] This observation strongly suggests that a membrane with an exceptionally high water uptake has the potential to compromise its mechanical stability. To calculate the degree of swelling we use the following equation:

$$Swelling\ Ratio\ (SR) = \frac{l_w - l_d}{l_d} \cdot 100 \quad (8)$$

where l_w represents the length of the hydrated membrane in one of the dimensions, and l_d represents the length of the dried membrane. The lengths of the membranes were measured using a caliper (Sparkfun TOL-10997) and a micrometer (Mitutoyo).

4.1.2.4. Ion Exchange Capacity

The Ion Exchange Capacity (IEC) is a measure of the ion-exchange group content in a membrane. As a result, the properties of the membrane, such as conductivity, water uptake, and swelling ratio, are intrinsically linked to the IEC. The IEC is typically expressed as the ratio of milliequivalents of exchangeable ions per unit weight of the dry membrane.

$$Ion\ Exchange\ Capacity\ (IEC) = \frac{n_{displaced\ counter-ion}}{w_d} \quad (9)$$

A UV-Vis spectrophotometer (PerkinElmer, Lambda 365) was utilized to measure the ion-exchange capacity (IEC), employing different methodologies based on the cationic or anionic characteristics of the ion-exchange membrane (IEM). The procedures for CEM and AEM were as follows:

For Cation Exchange Membranes (CEM):

1. The membrane was soaked in 0.01 M HCl to remove impurities, followed by rinsing with deionized (DI) water to prevent excess acid on the membrane surface.
2. Subsequently, the membrane was immersed in a 1 M NaCl solution, and the quantification of IEC was conducted using UV-Vis spectroscopy.
3. To determine the number of displaced protons, a linear regression was generated using various standard solutions containing phenolphthalein (pink color). This method assesses the decrease in absorption resulting from the addition of the released protons to an equimolar NaOH solution containing phenolphthalein. This approach provides a more reliable value compared to standard titration methods.

For Anion Exchange Membranes (AEM):

1. The membrane was soaked in a 1 M $NaNO_3$ solution instead of 0.01 M HCl, as in the case of CEM.
2. Afterward, the membrane was washed with DI water and immersed in a NaCl solution.
3. The number of displaced nitrate ions was determined using a similar method as with CEM, involving the construction of a linear regression with various nitrate ion solutions using the UV-Vis spectrophotometer.
4. The utilization of the UV-Vis spectrophotometer (PerkinElmer, Lambda 365) in these methodologies enabled accurate measurement of the ion-exchange capacity, contributing valuable insights into the characteristics and performance of both cationic and anionic ion-exchange membranes.

4.1.2.5. Ion conductivity

As mentioned above, ion conductivity depends on the number of ion exchange groups present in the structure. The increase in ionic conductivity would reduce ohmic losses, leading to higher power densities.[11] The most commonly used method to determine through-plane ion conductivity is Electrochemical Impedance Spectroscopy (EIS). In the high-frequency region, the intercept with the abscissa represents the resistance of the membrane (R). Thus, σ was determined using an AUTOLAB equipment (PGSTAT 302 N) connected to a Frequency Response Analyzer (FRA) and monitored with NOVA software in the frequency range of 10^6–1 Hz using an amplitude perturbation wave of 10 mV. This alternating current (AC) technique involves perturbing a magnitude (current or voltage, GEIS or PEIS, respectively) over a range of frequencies. After collecting the impedance data, the data can be fitted to various circuit models to identify the individual contributions to the total impedance (charge transfer resistance, mass transport, electrode process, etc.). The pretreated membranes were cleaned with

DI water before conducting ion conductivity testing. σ was calculated using equation 10:

$$\sigma = \frac{l}{R \cdot A} \quad (10)$$

where l is the thickness of the dried membrane (cm), R is the resistance of the membrane (Ohm), and A is the area of the membrane (cm^2).

4.1.2.6. Membrane permeability

Regarding the relevance of crossover in RFB, the capacity of the device may potentially be compromised due to possible self-discharge processes and side reactions. Crossover refers to the migration of redox active species through the ion exchange membrane. Typically, crossover occurs through the pores, channels, and imperfections of the ion exchange membrane, making it challenging to completely eliminate. The presence of charged ion-exchange groups can either enhance or reduce crossover through the Donnan effect, which involves the interaction with other charged species. This effect allows the passage of oppositely charged species while preventing the approach of species with the same charge. Cation exchange membranes (CEM) possess negatively charged ion-exchange groups, which favor the passage of positively charged species while repelling negatively charged species.

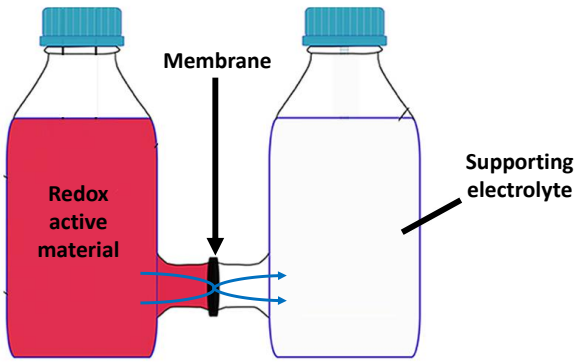

Figure 4: Schematic representation of a diffusion cell or H-cell.

Permeability measurements of the corresponding redox active materials were performed using a diffusional cell. In this setup, a $4cm^2$ membrane sample was placed between two diffusion half-cells. One compartment contained a solution of the redox active material and the supporting electrolyte, while the other compartment was filled with a solution of only the supporting electrolyte. Both solutions were continuously stirred to prevent the formation of concentration gradients on the membrane surface. However, it should be noted that this method neglects the influence of the electric field and flow. To account for these factors, permeability measurements were also conducted under operando conditions. The

permeation in the deficient compartment was periodically checked using a UV-Vis spectrophotometer and calculated based on Fick's law (equation 11):

$$V_B \frac{dC_B(t)}{dt} = \frac{AP}{l}\left(C_A - C_B(t)\right) \quad (11)$$

where C_B is the deficiency side and C_A the enriched one (mol/cm^3). In the same way, V_B is the volume of electrolyte in the deficiency side, A is the area of the diffusion cell (cm^2), P is the permeability (cm^2/s), and l is the thickness of the membrane (cm). Thus, permeability (P) can be calculated as:

$$P = \frac{V_B l}{At} \ln\left(\frac{C_A}{C_A - C_B}\right) \quad (12)$$

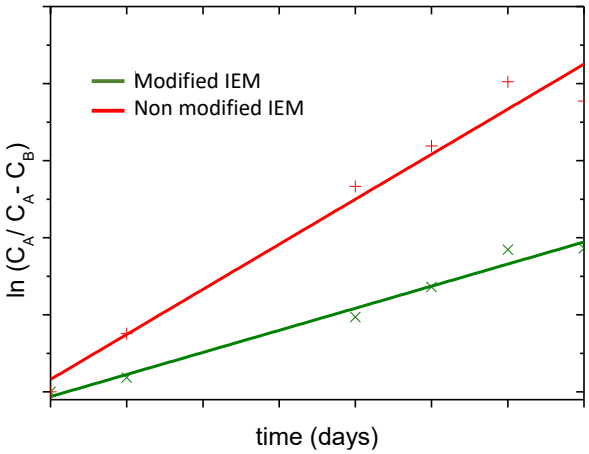

Figure 5: Schematic representation of one permeability plot.

4.1.2.7. Membrane modification

Membrane modifications can play a crucial role in achieving the goals set for HIGREEW by reducing the permeation of active species while preserving battery performance. Based on the results obtained, it has been identified that permeability is the most critical aspect to be addressed in the membranes being explored for them to be suitable in RFB. By improving the membrane's ability to restrict the passage of active species, it is possible to enhance the efficiency and overall performance of the battery system. Along this line, two different strategies have been explored:

1. *In situ polymerization*. This method involves conducting polymerization directly on the surface of a membrane to block its channels and pores. The UAM group has significant expertise in the field of membrane modifications. Leveraging this expertise, our efforts have focused on the use of commercial membranes in combination with two specific polymers, namely polyaniline and polypyrrole. These choices were made based on considerations of scalability and economic viability. Commercial

membranes were used to test the two monomeric materials, aniline and pyrrole, with varying polymerization times, in order to identify the most suitable option that fulfills the requirements of HIGREEW.

For the *polymerization of pyrrole*, the preactivated membrane was soaked in a solution consisting of a 1:1 mixture of pyrrole (0.1 M) and H_2SO_4 (0.1 M) for a duration of 2 minutes (or 6 minutes if a longer polymerization is desired). Following this, the membrane was immersed in another solution containing the oxidant (either $FeCl_3 \cdot 6H_2O$ or $Na_2S_2O_8$) for 6 minutes (or 18 minutes in the case of long polymerization). Afterward, the membranes were rinsed with deionized water and stored in a 1 M NaCl solution to ensure complete removal of any residual oxidizing agents. The volume of the solutions used depends on the size of the membrane being modified. For instance, when modifying a 4x4 cm membrane, 25 mL of each solution was utilized.

For the *polymerization of aniline*, the preactivated membrane was soaked in a solution containing a 1:1 ratio of aniline (1 M) and HCl (1 M) for 1 minute (or 3 minutes for longer polymerization). Subsequently, the membrane was immersed in another solution containing the oxidant ($Na_2S_2O_8$) for 3 minutes (or 9 minutes for long polymerization). Following this, the membranes were rinsed with deionized (DI) water and stored in a 1 M NaCl solution to ensure complete removal of chemicals. The volume of the solutions depended on the size of the membrane being modified. For instance, when a 4x4cm membrane was modified, 25 mL of each solution was used.

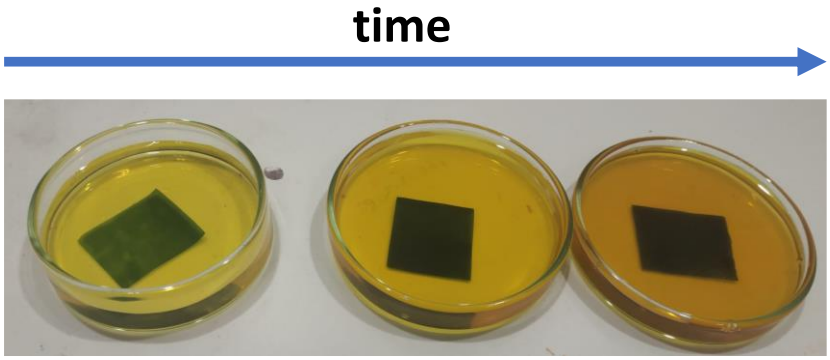

Figure 6: Representation of the polymerization of PPy on IEM over time.

2. In the *Layer-by-Layer (LbL) deposition method*, the preactivated membrane was immersed in a solution of the opposite charged polymer: If the membrane is a Cation Exchange Membrane (CEM), we start with the positively charged polymer. Conversely, if it is an Anion Exchange Membrane (AEM), we start with the negatively charged polymer. In our

study, we utilized PEI (branched, average molecular weight ~25000, Sigma Aldrich, Germany) as the positively charged polymer and Nafion ionomer (Nafion perfluorinated resin solution, 5% mass in lower aliphatic alcohols and water, 1100EW; Sigma-Aldrich, Germany) as the negatively charged polymer. The positive solution consisted of 0.1% mass of PEI in ultrapure water, while the negative solution contained 0.1% mass of Nafion ionomer in ultrapure water. The membranes were sequentially immersed in the PEI solution placed in a Petri dish for 5 minutes, thoroughly rinsed with ultrapure water, immersed in the Nafion solution placed in a Petri dish for another 5 minutes, and subsequently rinsed with ultrapure water. The modified membranes were then stored in the desired supporting electrolyte.

4.2. Battery set up

The single-cell setup used in this thesis is illustrated in Figure 7 and 8.

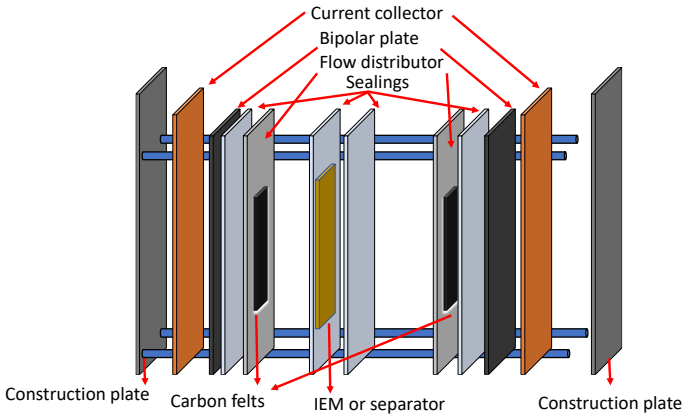

Figure 7: Schematic representation of each component of a single-cell.

To assemble the cell and ensure there is no leakage, the following steps should be followed:

1. Begin by placing the end plate with the insulating plate on the appropriate stand for cell assembly. This will allow for the insertion of the remaining components and the tightening of the cell using a wrench and torque key.
2. Insert the copper current collector.
3. Insert the bipolar plate, which is a carbon-polymer composite.
4. Insert the seal for the bipolar plate.
5. Insert the first flow frame.
6. Insert the first felt electrode.
7. Insert the first seal for the membrane.
8. Insert the membrane, ensuring there is at least a 1 cm overlay of the active zone on each side to prevent leakage.
9. Place the second seal for the membrane.
10. Insert the second flow frame.
11. Insert the second felt electrode.
12. Insert the seal for the bipolar plate.
13. Insert the second bipolar plate.
14. Insert the copper current collector.

15. Put the end plate in position.
16. Insert the eight screws, including washers. From the bottom, add the nuts along with washers. Tighten the screws by hand until they start to resist.
17. Use a wrench and torque key to tighten all the screws up to 8 N·m. Double-check to ensure that all screws are tightened to 8 N·m.
18. The lab-cell is now ready to be connected to liquid tanks and electronics.

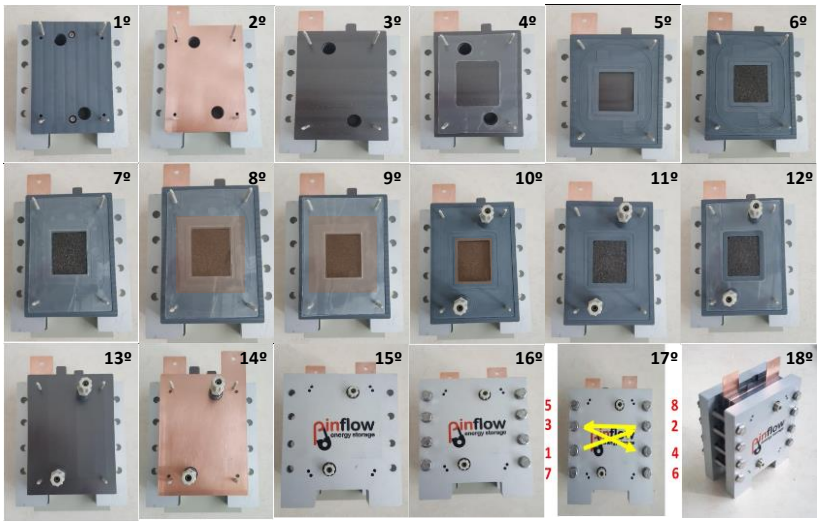

Figure 8: Step by step representation of the setup of the battery

After the cell has been assembled, it is important to cover all tubing connections with Teflon to prevent leakage and avoid O_2 permeation. The tubing is then connected to the vessels and peristaltic pumps. The supporting electrolyte is circulated through the cell for 30 minutes as a preconditioning step for the ion exchange membrane or separator. This process also helps to verify the absence of possible leaks.

Once the preconditioning step is complete, the supporting electrolyte is removed from the cell, and each electrolyte is placed in its respective vessel. The actual electrolyte is pumped through the cell for another 30 minutes. At this stage, the system is placed inside a homemade glovebox. The impedance is then measured to ensure that the membrane has been fully acclimated. The impedance should not exceed 5 Ohm·cm^2.

Following the impedance measurement, the electrolyte is purged with Ar for 30 minutes to remove any traces of O_2 present in the system. Subsequently, the electrolyte is flowed through the cell for an additional 30 minutes to ensure complete exclusion of any remaining O_2. Finally, the glovebox is purged with Ar for 30-40 minutes to eliminate any O_2 permeation from the system.

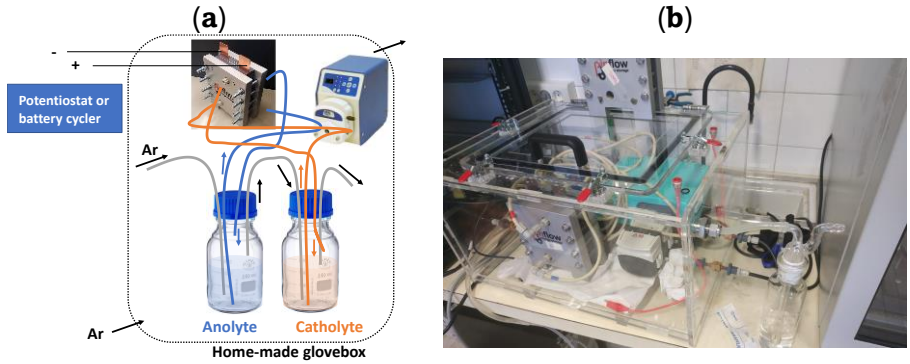

Figure 9: (a): Schematic representation of the glovebox with peristaltic pump, single-cell, tanks, and piping. (b): picture of the assembled system.

4.3. Battery testing

Once the battery has been set up, it is important to characterize the performance of each component under different methods and conditions. This characterization helps understand the behavior of the individual components and their influence on overall battery performance. Here are some methods and conditions commonly used for component characterization:

4.3.1. Galvanostatic cycling (and potential holding)

As expected, the quality of a battery is determined by its ability to be charged and discharged continuously without losing or significantly changing its properties. The most common method to assess battery performance involves charging and discharging the battery using a battery cycler at a constant current density until the desired voltage cut-off is reached. By plotting voltage versus time or capacity (mAh) versus voltage, the voltage evolution provides valuable information about the battery's performance.

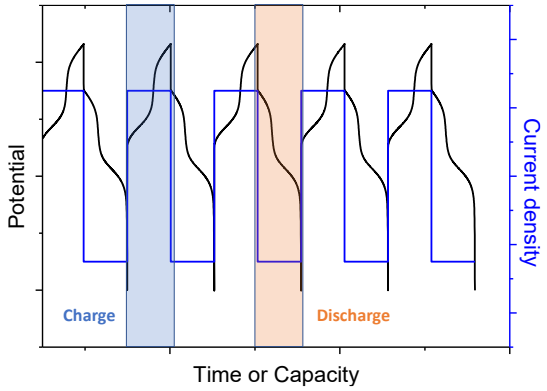

Figure 10: Schematic representation of the Potential and Current density *vs* Time (or Capacity) for a galvanostatic cycling.

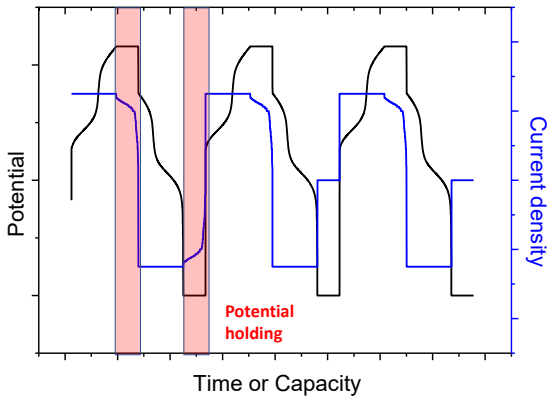

Figure 11: Schematic representation of the Potential and Current density *vs* Time (or Capacity) for a galvanostatic cycling with a potentiostatic holding.

At the initial stage, the voltage increases considerably due to electrode polarization. Subsequently, a plateau is reached, which exhibits a slight slope due to the presence of ohmic resistance. Finally, the voltage begins to increase again due to mass transport resistance.

During galvanostatic cycling, various parameters such as coulombic efficiency, voltage efficiency, energy efficiency, capacity decay (versus cycle or time), and capacity utilization can be determined. This method is commonly employed to evaluate system performance as these parameters provide valuable information about the overall performance of the system.

This method can be slightly modified by incorporating a constant voltage hold at the end of the galvanostatic cycling. In this modification, the upper and lower cut-off voltages are maintained until the current density decreases to extremely low values. This modification enables the utilization of a higher battery capacity since the current density only decreases when all the reactants in the electrolyte have been charged or discharged.

4.3.2. Polarization curves

Polarization curves have been widely used to identify and quantify primary losses, mainly kinetic activation, ohmic polarization, and mass transport limitations.[12] In the case of RFB, this method has been extensively studied as it provides information about the resistance of the entire system and the power of the battery. It is important to measure polarization curves when the electrolyte is at a specific state of charge. There are two methods commonly used for measuring polarization curves:

1. *Linear Sweep Voltammetry*: This method involves applying a linear scan of current density while measuring the corresponding voltage (see **Chapter 1** on Results and discussion). One challenge with this method is that the state

of charge of the electrolyte may change during the charging and discharging process, leading to deviations from linearity.

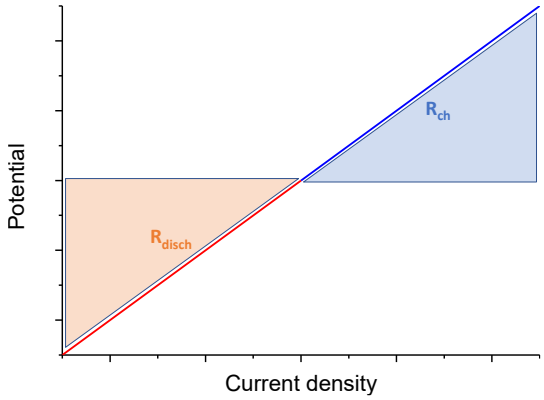

Figure 12: Schematic representation of Linear Sweep Voltammetry.

2. *Point-by-point method*. This method involves applying a specific current density for a given time, followed by a holding time to stabilize the system, and then applying the opposite current density to return the system to its initial state of charge. Using this method, lower deviations are expected since the system maintains the state of charge after each charge-discharge cycle. The current density is increased until it reaches a point where the polarization and mass transport become too high, resulting in a loss of linearity, or until the achieved potential exceeds the safety range (see **Chapter 3** on results and discussion).

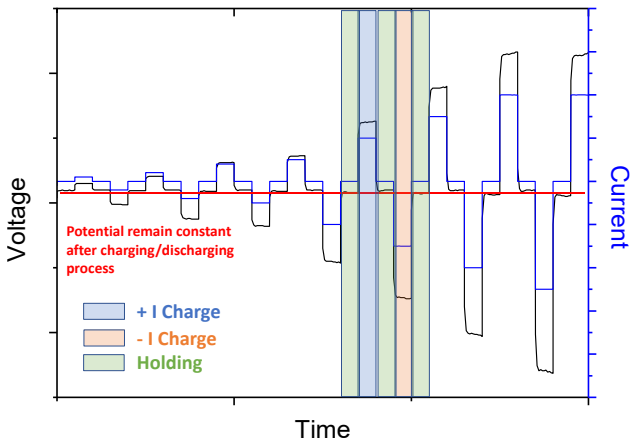

Figure 13: Schematic representation of point-by-point polarization curve.

4.3.3. Electrochemical Impedance Spectroscopy

In addition to CV, EIS (Electrochemical Impedance Spectroscopy) is one of the most commonly used techniques, although it is also one of the most complex ones. EIS is an AC (alternating current) technique that is performed at a fixed potential or current (Potentiostatic and Galvanostatic EIS, respectively). In this technique, the frequency of a specified amplitude is swept through various orders of magnitude.[13]

The data obtained from EIS can be plotted using the Nyquist representation, which comprises a real x-axis (Z´) and an imaginary (-Z´´) y-axis. By fitting this data to an appropriate equivalent circuit, important resistances can be calculated, such as R_s (solution resistance), R_{mem} (membrane resistance), R_{ct} (charge transfer resistance), etc.[14] The ASR (Area-Specific Resistance) can be obtained from this plot where the imaginary component is zero, representing the resistance of the entire system.[15]

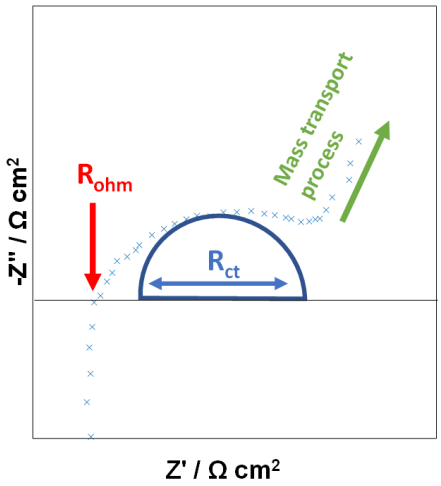

Figure 14: Schematic representation of Electrochemical Impedance Spectroscopy.

In a battery, it is crucial to prevent an increase in system resistance. Such an increase in resistance can occur due to various factors, including the adsorption or deposition of species onto the electrodes or membranes, a loss in the ionic conductivity of the system, and other similar factors. Therefore, it is important to ensure that the impedance before and after cycling remains similar, indicating that the battery has been functioning properly throughout the entire experiment.

4.4. DFT calculations

Computational chemistry is a field dedicated to solving chemical problems using specialized software and computational power. It provides a powerful tool for calculating various properties of chemical systems. With computational chemistry, we can compute optimized geometries in different phases, relative energies, dipolar moments, polarizabilities, NMR coupling constants, and intermolecular interactions. The availability of software programs like Gaussian has significantly simplified the utilization of computational chemistry techniques.

Theoretical calculations can be performed for systems in different phases, including liquids, solids, and gases, in both ground and excited states. There is a diverse range of models and methods available to calculate the energy and structure of the system. The choice of the appropriate theoretical method depends on the specific problem and the level of accuracy required.

Computational calculations in chemistry can be broadly divided into classical mechanics and quantum mechanics approaches.[16,17] Classical mechanics methods, such as molecular dynamics, simulate the motion of atoms and molecules using classical force fields. Quantum mechanics methods, on the other hand, employ quantum mechanical principles to describe the electronic structure and properties of molecules. In the following scheme, the different theoretical methods used in computational chemistry are illustrated, along with their main characteristics.

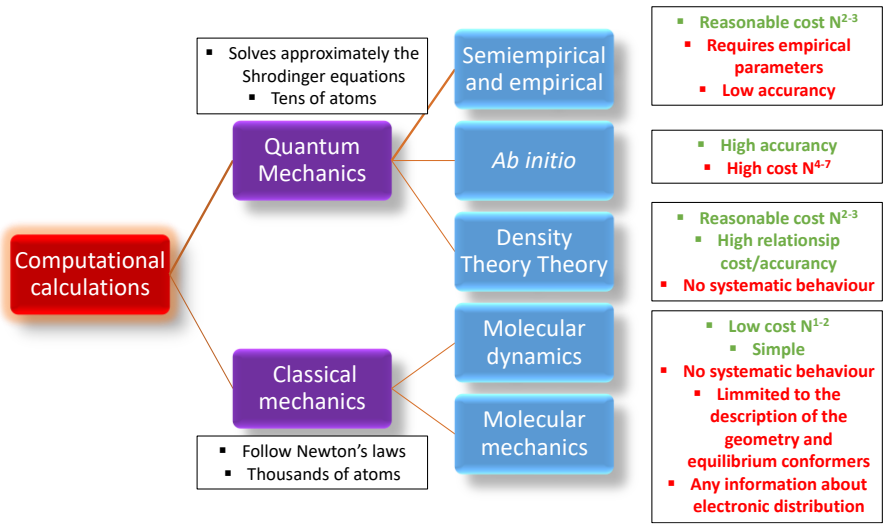

Figure 15: Scheme of the different computational methods with their main advantages and disadvantages.

The work presented in this thesis primarily relies on DFT (Density Functional Theory) calculations. However, a brief introduction to quantum and classical mechanics is provided as follows:

- *Classical mechanics*: This method applies the principles of classical physics to describe molecules in terms of bonded atoms that deviate from ideal geometries due to non-bonded Van der Waals and Coulomb interactions.
- *Quantum mechanics*: In this method, the behavior of electrons is explicitly taken into account under two main approximations: *ab initio* (explicit electrons) and Density Functional Theory (DFT, electronic density).

4.4.1. The time-dependent Schrödinger equation

Since the thesis mainly focuses on DFT calculations, let's provide a short introduction to Density Functional Theory (DFT). But before that, it's essential to understand the main fundamentals of quantum mechanics, particularly the time-dependent Schrödinger equation:

$$\hat{H}(R,r,t)\psi(R,r,t) = E\psi(R,r,t) \quad (13)$$

The molecular Hamiltonian, denoted as $\hat{H}$, depends on the coordinates of nuclei (R), electronic coordinates (r), and time (t), and the wave function (ψ) depends on the same parameters. The energy of the system is denoted by E.

In the language of linear algebra, the Schrödinger equation can be viewed as an eigenvalue equation. The wave function ψ is an eigenfunction of the Hamiltonian operator $\hat{H}$, and the corresponding eigenvalue E represents the energy of the system associated with that wave function. The stationary state with the lowest energy is known as the ground state.

For stationary systems, where time dependence is not considered, we can work with the time-independent version of the Schrödinger equation, known as the stationary Schrödinger equation. This equation allows us to find the eigenvalues and eigenfunctions of the system, providing information about the energy levels and wave functions associated with different states.

In the context of molecular systems, the Hamiltonian operator $\hat{H}$ can be constructed as the sum of various terms:

$$\hat{H} = T_n + T_e + V_{nn} + V_{ee} + V_{ne} \quad (14)$$

Where T_n and T_e are the kinetic contribution of nuclei and electrons, respectively, and V_{nn}, V_{ee}, and V_{ne} are the potential energy function between nuclei (repulsion), electrons (repulsion) and nuclei-electrons (attraction).

The stationary Schrödinger equation can be exactly solved only for the Hydrogen atom and hydrogen-like atoms (systems with one electron). For multiple-electron systems, approximations are necessary. One commonly used approximation is the Born-Oppenheimer approximation, which treats the nuclei and electrons separately due to the large mass difference. This simplifies the problem by

decoupling their motions. However, it's important to acknowledge that the Born-Oppenheimer approximation has limitations and is an approximation.

$$\hat{H}^{tot} = \hat{H}^{nuc} + \hat{H}^{elec} \quad (15)$$

$$\hat{H}^{nuc} = T_n + V_{nn} \quad (16)$$

$$\hat{H}^{elec} = T_e + V_{ee} + V_{ne} \quad (17)$$

In the stationary Schrödinger equation, the movement of electrons around fixed nuclei can be considered (with the kinetic contribution of nuclei equal to zero). The calculated energy depends on the positions of the nuclei, which is particularly useful for optimizing the molecular geometry. Thus, the stationary Schrödinger equation can be divided into two parts: the nuclear part and the electronic part:

$$\hat{H}^{nuc}(R)\psi^{nuc}(R) = E^{nuc}\psi^{nuc}(R) \quad (18)$$

$$\hat{H}^{elec}(R,r)\psi^{elec}(R,r) = E^{elec}\psi^{elec}(R,r) \quad (19)$$

It is important to note that in the Born-Oppenheimer approximation, the nuclear contribution remains constant as the kinetic contribution is zero and the nucleus-nucleus potential is fixed due to the stationary nuclei. However, the electronic part of the equation includes the nuclei coordinates since the solution parametrically depends on the positions of the nuclei.

In computational methods, the Schrödinger equation is typically solved for a given set of nuclear positions to calculate the system's energy. The positions of the nuclei are then altered, and the equation is solved again, generating energy values for different nuclear configurations. This process allows for the construction of the Potential Energy Surface (PES), which represents the relationship between energy and nuclear positions.

For methods based on the Born-Oppenheimer approximation, the electron-electron interaction (V_{ee}), also known as electronic correlation, poses the most challenging aspect. Approximate methods are employed to address the issue of electronic correlation. The quality of the Schrödinger equation solution depends on two main factors:

1. The method used: This pertains to the description of the Hamiltonian employed to account for electronic correlation and calculate energy and other properties. This encompasses the treatment of electronic correlation within the *N*-electron space.

2. The set of wavefunctions: These describe the space in which the electrons move, including the choice of monoelectronic space or active electron space.

By considering both the appropriate method and the suitable set of wavefunctions, accurate solutions to the Schrödinger equation can be obtained, enabling the calculation of energy and other properties of the system.

4.4.2. Plausible solutions of the Schrodinger equation

There are different methods to solve the Schrödinger equation, and two common approaches are described below. These methods provide approximations to determine the electronic structure and properties of molecular systems.

1. Simplifying the Hamiltonian: One approach involves simplifying the Hamiltonian by disregarding the electron-electron interaction potential V_{ee}. In this case, the Hamiltonian is described as the sum of N monoelectronic operators $\hat{h}\,(r)$, where N represents the number of electrons and r is the position vector. The monoelectronic operator includes the electronic kinetic energy T_e and the nuclei-electron interaction potential energy V_{ne}.

   $$\hat{h}\,(r) = T_e + V_{ne}$$

   The wavefunction is then expressed as the product of the monoelectronic functions $\varphi_i(r)$, which depend only on the coordinates of individual electrons.

   $$\psi = \prod_{i=1}^{n} \varphi_i(r) \qquad (20)$$

2. Hartree-Fock method: Another approach is the Hartree-Fock method, where the Hamiltonian retains the electron-electron interaction potential V_{ee}. The Hamiltonian is represented by the monoelectronic operator, called the Fock operator, which includes the $\hat{h}\,(r)$ term and the Hartree-Fock potential $V^{HF}\,(r)$ accounting for the electron-electron interaction.

   $$\hat{F} = \hat{h}\,(r) + V^{HF}\,(r) \qquad (21)$$

   In the Hartree-Fock method, the N-electron system is replaced by an equivalent monoelectronic system, where each electron experiences an average repulsion potential created by the other (N-1) electrons. The total wavefunction $\Phi^{HF}$is built using the Slater determinant, ensuring that it is antisymmetric to satisfy the Pauli exclusion principle.

   $$\Phi^{HF}(1,\ldots,N) = \left(\frac{1}{\sqrt{N!}}\right) \begin{vmatrix} \varphi_1(1) & \cdots & \varphi_N(1) \\ \vdots & \ddots & \vdots \\ \varphi_1(N) & \cdots & \varphi_N(N) \end{vmatrix} \qquad (22)$$

   Here, φ_i(r) represents the orthonormal monoelectronic functions, and $\left(\frac{1}{\sqrt{N!}}\right)$ is the normalization constant.

   The determination of the monoelectronic functions $\varphi_i(r)$ is achieved using the variational method. It involves starting with a trial function ψ_{test}dependent on $\varphi_i(r)$ and the Hamiltonian. The energy is then optimized by varying the coefficients C_i^p, which leads to changes in $\varphi_i(r)$. The goal is to find the trial wavefunction ψ_{test} with the minimum energy.

4.4.3. Monoelectronic functions $\varphi_i(r)$

Monoelectronic functions $\varphi_i(r)$ are defined as linear combinations of atomic orbitals χ_p, using the concept of Linear Combination of Atomic Orbitals (LCAO):

$$\varphi_i(r) = \sum_{p=1}^{N_{bas}} C_i^p \chi_p \quad (23)$$

Where $N_{bas}$is the number of atomic orbitals, and χ_p and $C_i^p$are the coefficients.

Solving equation (23) involves solving a system of linear equations. Roothan demonstrated that introducing $\varphi_i(r)$ into the following matrix equation is obtained:[18]

$$\hat{F}C = \varepsilon SC \quad (24)$$

Here, C is the matrix of coefficients C_i^p, S is the matrix of overlap integrals, and ε represents the matrix of energies.

The challenge lies in selecting the appropriate functions χ_p that accurately represent the shape of the atomic orbitals. There are a few options available:[19]

1. Slater orbitals: These orbitals provide an accurate description of the shape of the orbitals. However, their integration is more complex due to the presence of the term *exp(-ξr)*.
2. Gaussian functions: Gaussian functions are not as accurate as Slater orbitals, but their integration is more straightforward due to the presence of the term *exp(-αr²)*. If only a single function is used, it is called a primitive Gaussian. However, when multiple functions (linear combinations of Gaussians) are employed, they are referred to as contracted Gaussian functions.

The choice between Slater orbitals and Gaussian functions depends on the specific requirements of the calculation, balancing accuracy and computational efficiency.

4.4.4. Basis sets

The selection of functions is commonly referred to as a basis set, which is a set of functions that describe the space in which electrons can move. The choice of basis set is crucial as it influences the accuracy of the results. Different basis sets have different dimensions and play a role in the quality of the calculations.

Here are some common types of basis sets:

1. Minimum basis: This type includes the same number of functions as the number of orbitals in the system. While providing qualitative results, they may not capture all the details accurately. The dimension of the basis set is the same for all elements in the same row of the periodic table. An example is the Slater-type orbital (STO) basis, where each atomic orbital is represented by a single Gaussian function.

2. Extended basis: Extended basis sets, such as double-zeta (DZ), add additional functions to each orbital, allowing for the expansion and contraction of valence orbitals to consider the anisotropy of the system. Examples include the 6-31G and 3-21G basis sets.
3. Polarized basis: In systems with polarized bonds, basis sets centered solely on the atom may not be adequate. Polarized basis sets allow for the study of electron movements away from the nuclear positions, capturing the effects of polar bonds. Examples include the 6-31G(d,p) and 6-31G(d) basis sets.
4. Diffuse basis: Diffuse basis sets are useful for capturing electron movements over larger distances. They are particularly important for studying long-range interactions like hydrogen bonding or van der Waals interactions. An example is the 6-31+G(d,p) basis set.

- *Basis sets: an example*

Let´s use 6-311++G**, one of the Gaussian basis set, used in this Thesis, as an example. This basis set includes multiple types of functions, such as polarization and diffuse functions, to provide a more accurate representation of electron behavior in the system.

6-311++G**

6: The core orbitals of the atoms are described by a single contracted Gaussian function. This means that for each core orbital, there is a linear combination of six primitive Gaussian functions.

311: The valence orbitals of the atoms are described by three contracted Gaussian functions. Specifically, there are three different sets of primitive Gaussians used: one set with three primitives, another set with one primitive, and a final set with one primitive. These primitive Gaussians are combined in a linear combination to represent each valence orbital.

++: Diffuse functions are included for both heavy atoms and hydrogen atoms. This indicates that additional diffuse Gaussian functions are used to describe the electron density distribution for these atoms. The first "+" denotes the diffuse functions for heavy atoms, while the second "+" represents the diffuse functions for hydrogen atoms.

*****: Polarized functions are used for both heavy atoms and hydrogen atoms. The first "*" *signifies the presence of polarized Gaussian functions for heavy atoms, and the second* "*" indicates the presence of polarized Gaussian functions for hydrogen atoms. These polarized functions allow for a more accurate representation of the electron density near the nuclei.

By incorporating diffuse and polarized functions, the 6-311++G** basis set provides a more comprehensive description of the electronic behavior, especially for heavy atoms and hydrogen atoms, in the system under study.

4.4.5. Optimization of the coefficients. The Self-consistent Field (SCF) method

After selecting the appropriate basis functions, the next step is to optimize the coefficients C_i^p in order to minimize the energy of the system under study. This process, known as the Self-consistent Field (SCF) method, aims to iteratively solve the Hartree-Fock equation.

The SCF method starts with an initial geometry of the system and a chosen basis set of atomic orbitals. The program then solves the Hartree-Fock equations and performs a convergence test to assess the energy achieved. The coefficients are adjusted iteratively until a minimum energy is obtained. It is important to note that under the variational approximation, the calculated energy (E) will always be higher or equal to the true energy (E_{real}). The goal is to approach the real energy as closely as possible by improving the optimization of the coefficients.

This iterative resolution of the Hartree-Fock equation allows computational calculations to proceed, continuously refining the description of the electronic structure and energy of the system.[20]

4.4.6. The Hartree-Fock (HF) method

Here is a concise outline of the steps followed by the Hartree-Fock method to solve the equations, for which successive iterations are needed to refine the solution until convergence is achieved.

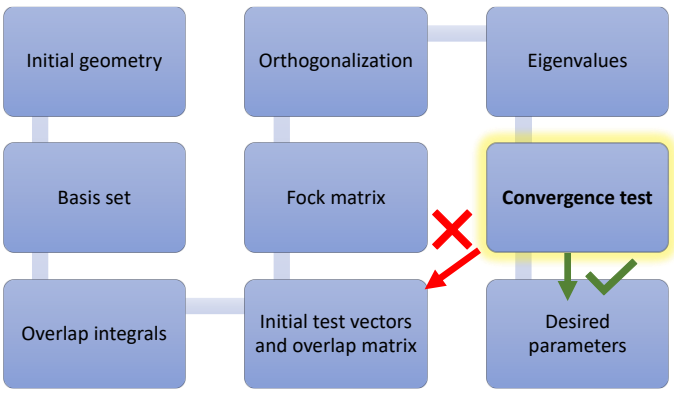

Figure 16: Outline of the steps followed by the Hartree-Fock method.

In the pursuit of achieving the optimized structure and minimum energy of a molecule, two processes must converge:

1. The first process involves optimizing the energy for a fixed geometry using the variational method. This optimization focuses on finding the optimal coefficients that result in the minimum energy for the given molecular geometry.
2. The second process involves scanning the atomic coordinates of the molecule to find the geometry that corresponds to the minimum eigenvalue (energy).

- *The HF method: limitations*

Despite its usefulness, the Hartree-Fock (HF) method has certain limitations. It treats electron interactions as an averaged potential and describes wavefunctions as products of monoelectronic functions. Consequently, the HF method tends to produce infinitely long bond distances. Additionally, the use of an averaged potential leads to potential holes, causing electrons with different spins to be placed at the same position and resulting in artificially short bond distances.

To address these limitations and obtain more accurate results, it is necessary to incorporate correlation effects. Various methods have been developed to include correlation effects, such as post-Hartree-Fock methods (e.g., MPn, which stands for Møller-Plesset perturbation theory) and density functional theory (DFT).

Post-Hartree-Fock methods introduce corrections to the HF wavefunction through perturbation theory, allowing for a more accurate description of electron correlation. DFT, on the other hand, employs the electron density as the fundamental quantity and uses exchange-correlation functionals to capture electron correlation effects.

These alternative methods, beyond HF, provide more reliable results by accounting for electron correlation and addressing the limitations of the HF method.

4.4.7. Density Functional Theory

As the majority of calculations in this thesis utilized Density Functional Theory (DFT), a brief description of this theory is provided.[21]

DFT provides an efficient and practical framework for investigating the electronic structure and properties of molecules and materials by utilizing the electronic density and functionals to compute the system's energy. Due to the high computational cost and limitations of *ab initio* calculations, alternative methods were explored for studying medium to small-sized systems. DFT emerged as a more cost-effective approach, describing the electronic density $\rho(r)$ instead of individual electrons. By focusing on the electronic distribution in three-dimensional space, DFT reduces the problem of n electrons to a three-dimensional representation, rather than the $3n$ dimensions required for the wavefunction ψ.

The fundamental concept of DFT involves calculating the system's energy, denoted as $E_{exact}[\rho]$, as a functional that depends on the electronic density $\rho(r)$. This functional also incorporates other functionals, which account for the exchange-correlation effects among electrons:

$$E_{exact}[\rho] = T[\rho] + V_{ne}[\rho] + V_{ee}[\rho] \quad (25)$$

where $T[\rho]$ represents the electronic kinetic energy functional, $V_{ne}[\rho]$ is the nuclei-electron potential functional, and $V_{ee}[\rho] = J[\rho] + K[\rho]$ denotes the electron-electron potential functional. Here, $J[\rho]$ corresponds to the Coulomb interaction functional, while $K[\rho]$ represents the exchange functional.

Similarly to how the wavefunction in the Hartree-Fock method was described based on atomic orbitals, J. Sham introduced the concept of the electronic density as a function of molecular orbitals:[22]

$$\rho(r) = \sum_{i=1}^{n} \varphi_i^*(r)\varphi_i(r) \quad (26)$$

where n is the number of orbitals.

By applying the variational principle to the functions $\varphi_i(r)$, the Kohn-Sham (KS) equations are derived.:

$$E^{KS}[\rho] = T^{KS}[\rho] + {E_V}^{KS}[\rho] + {E_J}^{KS}[\rho] + {E_{XC}}^{KS}[\rho] \quad (27)$$

T^{KS} represents the kinetic energy term associated with the movement of electrons, ${E_V}^{KS}$ accounts for the potential energy arising from the interactions between the nucleus-electron and nucleus-nucleus, ${E_J}^{KS}[\rho]$ represents the electron-electron Coulombic energy, and ${E_{XC}}^{KS}$ denotes the exchange-correlation energy. Similar to the Hartree-Fock (HF) equations, the KS equations involve the determination of the electronic density [ρ] through the optimization of coefficients. This is achieved by constructing a Slater determinant using the orbitals $\varphi_i(r)$.

DFT calculations have been extensively employed in various systems, yielding reliable results. However, a limitation of DFT calculations lies in the inclusion of empirical values, which can impact the obtained results. To address this limitation, different methods such as B3LYP, M062X, and B97D3 have been developed. In this thesis, a comparison was conducted among the B3LYP, M062X, and B97D3 methods for bipyridinium systems but, all three methods yielded similar results in this particular study.

Describing the appropriate functional, particularly the Exchange-correlation functional $E_{XC}[\rho]$, which captures the electronic correlation interactions, is one of the most challenging tasks in DFT calculations. Various approximations exist for calculating the exchange-correlation energy:

- Local Density Approximation (LDA): This approximation assumes a homogeneous electronic density $\rho(r)$. However, it is far from reality as actual molecules exhibit energy density fluctuations.

- Non-Local Density Approximation (NLDA): This approach improves upon the LDA by incorporating corrections based on the electronic density gradient. It aims to provide a closer representation of real systems.
- Hybrid Functionals: This is a more recent approach that combines terms from both DFT exchange and exact exchange. The exchange-correlation energy is defined as a mixture of the Non-Local and Local Density Approximations.

Selecting the most suitable approximation for the studied system, particularly the Exchange-correlation functional, is crucial for obtaining accurate results in DFT calculations.

4.5. Chemicals and instruments

Unless otherwise noted, reagents and materials were purchased from commercial suppliers and used without further purification. Air sensitive reactions were conducted under inert atmosphere making use of previously dried argon gas. Rotary evaporator was used for the removal of solvents under reduced pressure. Purity of final compounds was assessed by ^{1}H NMR. Final materials were dried under vacuum prior to be used.

Monodimensional and/or bidimensional Nuclear Magnetic Resonance (NMR) proton and carbon spectra were recorded at 300 MHz for ^{1}H NMR and 75.5 MHz for ^{13}C NMR at 25 °C on a 300 MHz spectrometer using dimethylsulfoxide-*d6* (DMSO-*d6*) and D2O as solvents and Me_4Si as internal standard. Chemical shifts (δ) are reported in ppm relative to residual solvent signals (dimethylsulfoxide-d6 2.50 ppm for ^{1}H NMR, 39.5 ppm for ^{13}C NMR; D2O 4.79 ppm for ^{1}H NMR) and coupling constants (*J*) in hertz (Hz). The data are represented as follows: chemical shift (ppm), multiplicity (s = singlet, d = doublet, t = triplet, q = quartet, m = multiplet or unresolved, bs = broad signal) coupling constant(s) (*J*), integration. ^{13}C NMR spectra were recorded with ^{1}H decoupling.

A 4 cm^2 active area single-cell from Pinflow was used to achieve all the most of the battery results using in the following set up: two copper current collector plates, two composite bipolar plates (carbon-polyolefin), graphite felts electrodes (SGL GFD 4.6 EA) four sheets of gasket (flat, polyolefin) and the corresponding membrane previously soaked for 24 h in the supporting electrolyte. A Watson Marlow 323 peristaltic pump was used to circulate electrolyte through the system at a flow rate of 40 mL/min. The reservoirs were purged with Argon (99.999%) for 30 minutes to avoid the presence of O_2 before cycling it. The whole system was placed inside a homemade glovebox which was purged with Argon (same quality) for another 30 minutes. The battery measurements were recorded using a Biologic multichannel potentiostatic/galvanostatic coupled to an impedance module BSC-815. In the case of the triazine anolyte, it was used a 5 cm^2 active area home-made

flow cell with flat flow fields using two composite bipolar plates (carbon-polyolefin), graphite felts electrodes (SGL GFD 4.6 EA) compressed to 3 mm, two sheets of gasket (expanded Teflon) and Nafion 212® from Dupont. A Chonry BT600M peristaltic pump was calibrated with Masterflex,C-Flex tubbing (Cole-Parmer). The whole system was placed in a glovebox MBRAUN ([O_2] <1 ppm) to avoid the presence of oxygen during cycling. For battery measurements, a LANHE Battery tester 400 W was used.

4.6. Synthesis and cycling details of 2,2'-bipyridines 1-8

2,2'-bipyridine derivatives were synthesized by introduction of alkyl substituents at *N,N'* atoms through a straightforward procedure, either by regular heating in a solvent-free process (Method A) or in a microwave-assisted process (Method B). The corresponding derivatives were next subjected to anion exchange procedure using IRA-900 chloride form resin. NMR spectra can be found in *Annex A*

RDE were conducted using a Metrohm Autolab Motor Controller. Both CV and RDE tests were performed using an Autolab electrochemical system II PGSTAT30 potentiostat. RDE analysis can be found in *Annex A*. The solubilities were measured using an UV−Vis spectrophotometer (PerkinElmer, Lambda365). And the spectra as well the analysis can be found in *Annex A*.

The cell was galvanostatically charged/discharged at room temperature using a Biologic multichannel potenciostatic-galvanostaic coupled to an impedance module BSC-815 in the voltage range of 0–1.57 V for the compound **2** and 0–1.67 V for the compound **4** at current density of 100 mA/cm^2. When the cutoff potentials were reached the cell was further charged/discharged applying a constant voltage as defined by the cut off limits until the current density decreased below 12.5 mA/cm^2. This method was applied to ensure that both experiments have reached the desired state of charge making the results comparable. Note that a potentiostatic electrochemical impedance spectroscopy (EIS) of both systems were measured before and after cycling, showing in all the cases similar resistance (≈2.5 Ω cm^2). The impedance before and after cycling as well as the evolution of the coulombic, voltage and energy efficiencies and discharge capacity over cycling for compound **2** and **4** can be found in the *Annex A*.

Geometries were optimized using IEF-PCM methodology at B3LYP/6-311++G(d,p) level of theory and can be found in *Annex A*

METHOD A: 2,2′-bipyridine derivatives were synthesized following already reported literature procedures. A solution of 2,2′-bipyridine (1 Eq) in the corresponding dibromoalkane (2–23 Eq) was refluxed for 16 h, during which a precipitate accumulated. The reaction was cooled down to room temperature and the solid was filtered and washed with acetone and hexanes. The solid was then subjected to anion exchange procedure using IRA-900 chloride form resin and

water was evaporated under reduced pressure on a rotary evaporator. The final compound was dried under vacuum to afford the desired 2,2-bipyridine.

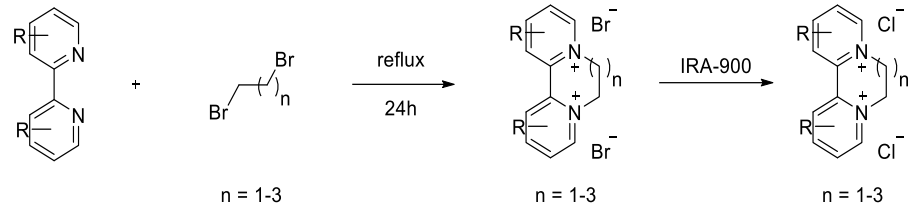

Figure 17: Synthetic route towards 2,2'-bipyridine under conventional heating conditions

METHOD B: To a microwave vial equipped with a magnetic bar (for microwave reactor), 2,2'-bipyridine (1 Eq), the corresponding dibromoalkane (1.3–4 Eq) and acetonitrile were added. The vial was sealed and placed in the microwave reactor. The appearance of a solid indicated the formation of the product. The solid was filtered and washed with acetonitrile to ensure the elimination of the dibromoalkane excess and was then subjected to anion exchange procedure using IRA-900 chloride form resin. Water was evaporated under reduced pressure on a rotary evaporator. Before characterization, the product was dried at 65 °C in the oven.

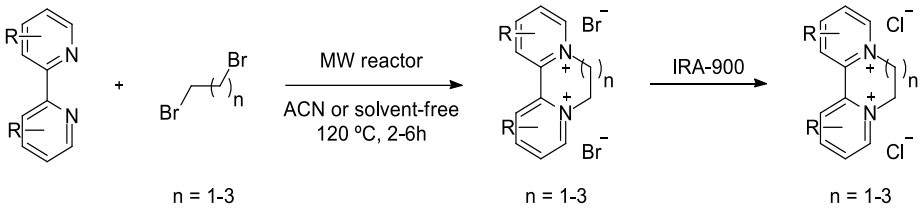

Figure 18: Microwave reaction for the synthesis of 2,2'-bipyridine derivatives.

6,7-dihydrodipyrido[1,2-a:2'1'-c]pyrazine-5,8-diium bromide (**1**)

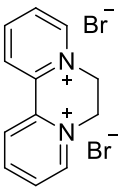

Method A: The title product was obtained from 2,2'-bipyridine (1 g, 6.40 mmol, 1 eq) and 1,2-dibromoethane (1.11 mL, 12.80 mmol, 2 eq). 92% yield (2.0 g, 5.89 mmol), pale brown solid. **Method B:** The title product was obtained from 2,2'-bipyridine (4 g, 25.54 mmol, 1 eq) and 1,2-dibromoethane (24 g, 25.6 mmol, 4 eq) in ACN (0.55 M) for 6h. 50% yield (0.816 g, 3.2 mmol), pale orange solid. Spectroscopic data were in good agreement with those reported in the literature.[23] H NMR (300 MHz, D_2O) δ 9.31 – 9.23 (m, 2H), 9.07 – 8.99 (m, 2H), 8.99 – 8.93 (m, 2H), 8.44 (ddd, J = 7.7, 6.0, 1.6 Hz, 2H), 5.40 (s, 4H). ^{13}C NMR (75 MHz, D_2O) δ 148.37 (s), 147.12 (s), 139.68 (s), 130.75 (s), 128.35 (s), 52.40 (s).

7,8-dihydro-6H-dipyrido[1,2-A:2'-1'-c][1,4]diazepine-5,9-diium bromide (**2**)

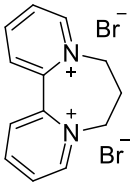

Method A: The title product was obtained from 2,2'bipyridine (1 g, 6.40 mmol, 1 eq) and 1,3-dibromopropane (7.5 mL, 73.6 mmol, 11.5 eq). 80% yield (1.83 g, 5.12 mmol), pale brown solid. **Method B:** The title product was obtained from 2,2'-bipyridine (4 g, 25.5 mmol, 1 eq) and 1,3-dibromopropane (6.56 g, 32.5 mmol, 1.3 eq) for 2h. 99% yield (6.81 g, 25.2 mmol), pale yellow solid. Spectroscopic data were in good agreement with those reported in the literature.[24] ^{1}H NMR (300 MHz, D_2O) δ 9.35 – 9.26 (m, 2H), 8.97 (td, *J* = 8.0, 1.4 Hz, 2H), 8.62 – 8.52 (m, 2H), 8.47 (ddd, *J* = 7.8, 6.1, 1.5 Hz, 2H), 5.11 (dt, *J* = 14.4, 3.9 Hz, 2H), 4.61 (dt, *J* = 14.3, 9.4 Hz, 2H), 3.03 (ddd, *J* = 9.4, 7.5, 4.1 Hz, 2H). ^{13}C NMR (75 MHz, D_2O) δ 148.20 (s), 147.60 (s), 143.83 (s), 131.69 (s), 131.26 (s), 56.12 (s), 30.32 (s).

6,7,8,9-tetrahydrodipyrido[1,2-a:2',1'-c][1,4]diazocine-5,10-diium bromide (**3**)

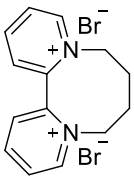

The title product was obtained following **Method B** from 2,2'-bipyridine (0.523 g, 3.35 mmol, 1 eq) and 1,4-dibromobutane (5.29 g, 24.5 mmol, 4 eq) in 6 mL of ACN for 6h. 50% yield (0.5 g, 1.175 mmol), colourless solid. Spectroscopic data were in good agreement with those reported in the literature.[25] ^{1}H NMR (300 MHz, D_2O) δ 9.66 (dd, *J* = 6.2, 1.4 Hz, 1H), 9.15 (td, *J* = 7.9, 1.4 Hz, 1H), 8.82 – 8.67 (m, 2H), 5.22 (dd, *J* = 14.6, 6.4 Hz, 1H), 4.60 – 4.46 (m, 1H), 2.74 (td, *J* = 11.1, 6.7 Hz, 1H), 2.62 – 2.44 (m, 1H).^{13}C NMR (75 MHz, D_2O) δ 148.13, 147.95, 143.81, 132.20, 132.01, 59.83, 27.02.

3,11-dimethyl-7,8-dihydro-6H-dipyrido[1,2-a:2',1'-c][1,4]diazepine-5,9-diium bromide (**4**)

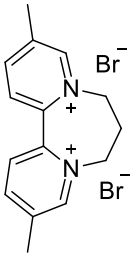

Method A: The title product was obtained from 5,5'-dimethyl-2,2'-bipyridyl (1 g, 5.42 mmol, 1 eq) and 1,3-dibromopropane (12.7 mL, 124.8 mmol, 23 eq). 87% yield (1.82 g, 4.71 mmol), pale brown solid. **Method B:** The title product was obtained from 5,5'-dimethyl-2,2'-bipyridine (1 g, 6.4 mmol, 1 eq) and 1,3-dibromopropane (5.17 g, 24.5 mmol, 4 eq) for 6h. 84% yield (1.754 g, 5.376 mmol), pale brown solid. Spectroscopic data were in good agreement with those reported in the literature.[24] ^{1}H NMR (300 MHz, D_2O) δ 9.13 (d, *J* = 1.9 Hz, 2H), 8.74 (ddd, *J* = 8.2, 1.9, 0.9 Hz, 2H), 8.37 (d, *J* = 8.2 Hz, 2H), 5.00 (d, *J* = 14.5 Hz, 2H), 4.62 – 4.46 (m, 2H), 3.05 – 2.89 (m, 2H), 2.73 (d, *J* = 0.7 Hz, 6H). ^{13}C NMR (75 MHz, D_2O) δ 147.98 (s), 147.27 (s), 143.52 (s), 141.11 (s), 130.61 (s), 55.91 (s), 30.25 (s), 17.99 (s).

2,12-dimethyl-7,8-dihydro-6H-dipyrido[1,2-a:2',1'-c]diazepine-5,9-diium bromide (**5**)

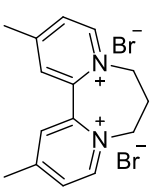

Method A: The title product was obtained from 4,4'-dimethyl-2,2'-bipyridyl (1 g, 5.42 mmol, 1 eq) and 1,3-dibromopropane (12.7 mL, 124.8 mmol, 23 eq). 91% yield (1.63 g, 4.93 mmol), pale brown solid. **Method B:** The title product was obtained from 4,4'-dimethyl-2,2'-bipyridine (1 g, 6.4 mmol, 1 eq), 1,3-dibromopropane (5.17 g, 24.5 mmol, 4 eq) for 3h. 78% yield (1.61 g, 4.93 mmol), pale orange solid. Spectroscopic data were in good agreement with those reported in the literature.[24] ^{1}H NMR (300 MHz, D_2O) δ 9.03 (d, *J* = 6.3 Hz, 2H), 8.34 (d, *J* = 2.0 Hz, 2H), 8.22 (ddd, *J* = 6.3, 2.0, 0.8 Hz, 2H), 4.99 (dt, *J* = 14.6, 3.9 Hz, 2H), 4.48 (dt, *J* = 14.4, 9.3 Hz, 2H), 2.93 (ddd, *J* = 9.6, 7.5, 4.2 Hz, 2H), 2.83 (s, 6H). ^{13}C NMR (75 MHz, D_2O) δ 163.24 (s), 146.16 (s), 143.01 (s), 131.98 (s), 131.10 (s), 55.17 (s), 29.96 (s), 21.75 (s).

2,12-dimethoxy-7,8-dihydro-6H-dipyrido[1,2-a:2',1'-c][1,4]diazepine-5,9-diium bromide (**6**)

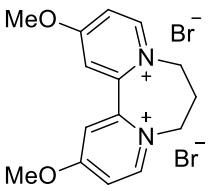

The title product was obtained following **Method A** from 4,4'-dimethoxy-2,2'-bipyridyl (1 g, 4.62 mmol, 1 eq) and 1,3-dibromopropane (10.83 mL, 106.26 mmol, 23 eq). 93% yield (1.80 g, 4.30 mmol), pale brown solid. ^{1}H NMR (300 MHz, D_2O) δ 8.52 (d, *J* = 7.2 Hz, 2H), 7.44 (d, *J* = 2.8 Hz, 2H), 7.27 (dd, *J* = 7.2, 2.8 Hz, 2H), 4.79 (s, 6H), 4.64 (dt, *J* = 14.9, 3.8 Hz, 2H), 4.23 (ddd, *J* = 14.7, 10.0, 8.3 Hz, 2H), 2.66 (ddt, *J* = 7.1, 5.0, 2.8 Hz, 2H). ^{13}C NMR (75 MHz, D_2O) δ 174.76, 146.52, 145.44, 118.90, 116.65, 52.86, 29.17.

2,12-dicarboxy-7,8-dihydro-6H-dipyrido[1,2-a:2',1'-c][1,4]diazepine-5,9-diium bromide (**7**)

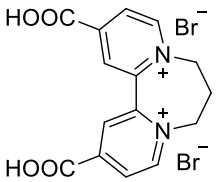

The title product was obtained following **Method A** from 2,2'-bipyridil-4,4-dicarboxylic acid (0.2 g, 0.82 mmol, 1 eq) and 1,3-dibromopropane (1.92 mL, 18.83 mmol, 23 eq). TEA (0.23 mL, 1.64 mmol, 2 eq) was subsequently added to the reaction mixture. 24% yield (0.09 g, 0.196 mmol), orange solid. ^{1}H NMR (300 MHz, DMSO-d_6) δ 9.68 (d, *J* = 6.1 Hz, 2H), 8.90 – 8.79 (m, 4H), 5.24 (dt, *J* = 13.6, 3.9 Hz, 2H), 4.62 (dt, *J* = 13.6, 9.2 Hz, 2H), 2.85 (d, *J* = 11.8 Hz, 2H).^{13}C NMR (75 MHz, DMSO-d_6) δ 163.15, 149.21, 146.51, 144.45, 131.53, 129.99, 55.59, 30.54.

2,3-dihydro-1H-[1,4]diazepino[1,2-a:4,3-a']diquinoline-4,17-diium bromide (**8**)

The title product was obtained following **Method A** from 2,2'-biquinoline (0.5 g, 1.95 mmol, 1 eq) and 1,3-dibromopropane (4.6 mL, 44.9 mmol, 23 eq). 10% yield (0.085 g, 0.185 mmol), yellow solid. ^{1}H NMR (300 MHz, D_2O) δ 9.60 (dd, *J* = 8.7, 2.6 Hz, 2H), 8.78 (d, *J* = 9.2 Hz, 2H), 8.71 – 8.57 (m, 4H), 8.51 (ddd, *J* = 9.0, 7.1, 1.8 Hz, 2H), 8.24 (t, *J* = 7.6 Hz, 2H), 5.96 (d, *J* = 15.4 Hz, 2H), 4.65 – 4.46 (m, 2H), 3.23 (s, 2H). ^{13}C NMR (75 MHz, D_2O) δ 149.92, 147.43, 139.67, 138.92, 131.91, 131.72, 131.33, 124.55, 118.06, 50.33, 30.34.

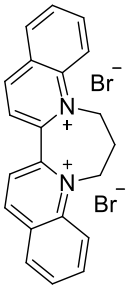

4.7. Cycling of $Na_4[Fe(CN)_6]$ and AQDS systems.

$Na_4[Fe(CN)_6]$ and AQDS compounds were used as redox-active materials for battery performance without any purification and were purchased from Sigma-Aldrich. Nafion® 212 was used as the exchange membrane and purchased from the Fuel Cell store. Membrane pretreatment was used considering the well-established reported methodology for Nafion®. For battery evaluation, the cell was galvanostatically charged/discharged at room temperature in the voltage range of 0–1.1 V at various current densities (20, 40, 60, 80 and 100 mA/cm^2, 5 cycles) and cycled for 100 cycles at 80 mA/cm^2. The battery was also evaluated considering the effects of pH ranging from 4, 7 and 10. The cell was first charged to 50% SOC, and load curves were carried out to obtain the area-specific resistance at the given conditions. In this process, a current density scan of 1 mA/cm^2 was applied until the desired current cut-off ±125 mA/cm^2 was reached. Extra information about the battery cycling results can be found in *Annex A*.

4.8. Synthesis and cycling details of (SPr_3)4TpyTz.

4-cyanopyridine, sodium hydroxide, propane sultone, and dimethyl-formamide (DMF) chlorohydric acid were purchased from Sigma-Aldrich and used without further purification. NMR spectra as well as RDE analysis, solubilities calibration plots and optimized geometries coordinates can be found in *Annex A*.

The home-made flow cell with flat flow fields was setup using two composite bipolar plates (carbon-polyolefin), graphite felts electrodes (SGLGFD4.6 EA, used as received and compressed to 3 mm), two sheets of gasket (expanded, Teflon), and Nafion 212 ® membrane from Dupont. The active area of the cell was 5 cm^2. A Chonry BT600M peristaltic pump was calibrated with Masterflex C-Flex tubbing (Cole-Parmer) and used to circulate the electrolyte through the system at a flow rate of 60 mL/min. The reservoirs and the cell were placed inside a glovebox purged with nitrogen (MBRAUN). After circulating the electrolyte for 30 min, the

initial resistance of the system was determined using impedance spectroscopy with a BioLogic SP-300 potentiostat. For battery measurements, a LANHE Battery Tester 400W was used. The cell was galvanostatically charged/discharged at room temperature in different voltage ranges (each cut off can be found in the footnote of each figure) at different current densities (20, 40, 60, 80, and 100 mA/cm^2, 5 cycles) and cycled for several cycles at 60 mA/cm^2. The polarization curves were measured point-by-point by applying a current of +1 mA/cm2during10, 10 s resting, and 10 s at−1 mA/cm2, so the SOC is expected to do not change during the experiment.

TPT was synthesized basic catalyzed triazine formation from nitrile according to literature.[26]

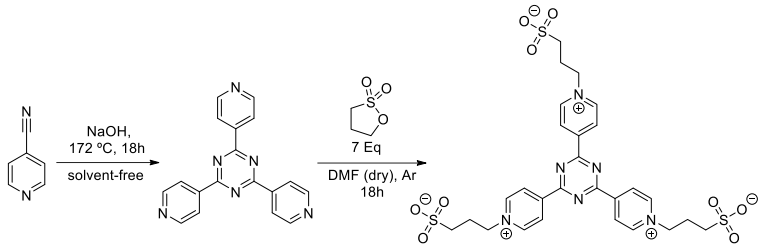

Figure 19: Synthetic route towards 2,2'-bipyridine under conventional heating conditions

2,4,6-tri(pyridin-4-yl)-1,3,5-triazine

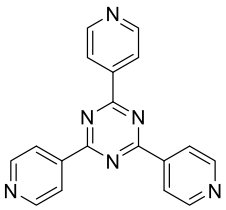

30 g of 4-cyanopyridine (288.2 mmol, 3Eq) were placed in a 100 mL round bottom flask and heated to 172 °C. Once the whole solid gets liquid, 0.912 g of powdered NaOH (22.8 mmol, ≈0.1 Eq) were added in small portions. The resulting mixture was stirred 18 h until all the liquid become pale solid. The solid was dissolved using concentrated HCl aqueous solution 50 mL and sonicated for 30 minutes at room temperature. After that, the solution was neutralized using 6 M aqueous solution of NaOH until pH 7. The white product was purified by redissolving it in 10 mL of concentrated HCl aqueous solution and neutralized using 6 M aqueous solution of NaOH to achieve the desired product. The white powder was cleaned using 3 x 50 mL of acetone and finally with 50 mL of water, achieving 19 g of the pale white solid (60.8 mmol, 63.3%). Spectroscopic data were in good agreement with those reported in the literature.[23] ^{1}H NMR (300 MHz, $CDCl_3$) δ 8.95 (s, 6H), 8.57 (s, 6H).

3,3',3''-((1,3,5-triazine-2,4,6-triyl)tris(pyridine-1-ium-4,1-diyl))tris(propane-1-sulfonate)

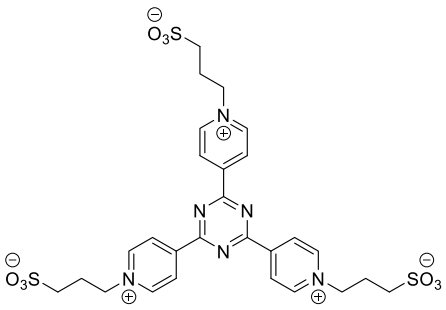

2 g of TPT (6.4 mmol, 1 Eq) and 9 g of 1,3-propanesultone (73.7 mmol 4 Eq) were dissolved in 50 mL of DMF and heated to reflux for 18 h in a 250 mL round bottom flask. After this time, a brown pale solid appears in the bottom of the flask. The solution was cooled until reach room temperature to ensure the precipitation of all the product. The solid was filtered using a Buchner funnel and washed with cool DMF and acetone. The solid was purified by dissolving it in water and precipitating using MeOH. So, 3.6 g of the pure product (5.3 mmol, 82.8%) was achieved as a brown pale solid. ^{1}H NMR (300 MHz, D_2O) δ 9.40 (d, J = 6.2 Hz, 6H), 9.32 (d, J = 7.1 Hz 2H), 5.01 (t, J = 7.4 Hz, 6H), 3.11 (t, J = 7.2 Hz, 6H), 2,63 (p, J = 7.2 Hz, 6H) ^{13}C NMR (75 MHz, D_2O) δ 169.5 (s), 149.7 (s), 146.0 (s), 127.5 (s), 60.4 (s), 47.0 (s). 26.2 (s).

NOTE: Additional information can be found in Annex A about NMR spectra, RDE analysis, solubilities spectra and analysis, optimized geometries coordinates, cell testing.

4.9. References:

(1) Nicholson, R. S.; Shain, I. Theory of Stationary Electrode Polarography. Single Scan and Cyclic Methods Applied to Reversible, Irreversible, and Kinetic Systems. *Anal. Chem.* **1964**, *36*, 706–723. https://doi.org/10.1021/ac60210a007

(2) Charoen-amornkitt, P.; Suzuki, T.; Tsushima, S. Ohmic Resistance and Constant Phase Element Effects on Cyclic Voltammograms Using a Combined Model of Mass Transport and Equivalent Circuits. *Electrochimica Acta* **2017**, *258*, 433–441. https://doi.org/10.1016/j.electacta.2017.11.079

(3) Montella, C. LSV/CV Modelling of Electrochemical Reactions with Interfacial CPE Behaviour, Using the Generalised Mittag–Leffler Function. *Journal of Electroanalytical Chemistry* **2012**, *667*, 38–47. https://doi.org/10.1016/j.jelechem.2011.12.010

(4) Bieniasz, L. K. Automatic Solution of Integral Equations Describing Electrochemical Transients under Conditions of Internal Cylindrical Diffusion. *Journal of Electroanalytical Chemistry* **2013**, *700*, 30–39. https://doi.org/10.1016/j.jelechem.2013.04.010

(5) Bieniasz, L. K. Automatic Simulation of Electrochemical Transients at Cylindrical Wire Electrodes, by the Adaptive Huber Method for Volterra Integral Equations.

Journal of Electroanalytical Chemistry **2011**, *662* (2), 371–378. https://doi.org/10.1016/j.jelechem.2011.09.01

(6) Elgrishi, N.; Rountree, K. J.; McCarthy, B. D.; Rountree, E. S.; Eisenhart, T. T.; Dempsey, J. L. A Practical Beginner's Guide to Cyclic Voltammetry. *J. Chem. Educ.* **2018**, *95* (2), 197–206. https://doi.org/10.1021/acs.jchemed.7b00361

(7) Matsuda, H.; Ayabe, Y. Zur Theorie der Randles-Sevčikschen Kathodenstrahl-Polarographie. *Zeitschrift für Elektrochemie, Berichte der Bunsengesellschaft für physikalische Chemie* **1955**, *59*, 494–503. https://doi.org/10.1002/bbpc.19550590605

(8) Wang, H.; Sayed, S. Y.; Luber, E. J.; Olsen, B. C.; Shirurkar, S. M.; Venkatakrishnan, S.; Tefashe, U. M.; Farquhar, A. K.; Smotkin, E. S.; McCreery, R. L.; Buriak, J. M. Redox Flow Batteries: How to Determine Electrochemical Kinetic Parameters. *ACS Nano* **2020**, *14*, 2575–2584. https://doi.org/10.1021/acsnano.0c01281

(9) Zawodzinski, T. A.; Derouin, C.; Radzinski, S.; Sherman, R. J.; Smith, V. T.; Springer, T. E.; Gottesfeld, S. Water Uptake by and Transport Through Nafion® 117 Membranes. *J. Electrochem. Soc.* **1993**, *140*, 1041–1047. https://doi.org/10.1149/1.2056194

(10) Nagarale, R. K.; Gohil, G. S.; Shahi, V. K. Recent Developments on Ion-Exchange Membranes and Electro-Membrane Processes. *Advances in Colloid and Interface Science* **2006**, *119*, 97–130. https://doi.org/10.1016/j.cis.2005.09.005

(11) Sun, C.; Zhang, H. Investigation of Nafion Series Membranes on the Performance of Iron-chromium Redox Flow Battery. *Int J Energy Res* **2019**, er.4875. https://doi.org/10.1002/er.4875

(12) Aaron, D.; Tang, Z.; Papandrew, A. B.; Zawodzinski, T. A. Polarization Curve Analysis of All-Vanadium Redox Flow Batteries. *J Appl Electrochem* **2011**, *41*, 1175–1182. https://doi.org/10.1007/s10800-011-0335-7

(13) Book: Barsoukov, E.; Macdonald, R. *Impedance Spectroscopy: Theory, Experiment, and Applications*; John Wiley & Sons, Inc, 2018

(14) Paul, D. K.; McCreery, R.; Karan, K. Proton Transport Property in Supported Nafion Nanothin Films by Electrochemical Impedance Spectroscopy. *J. Electrochem. Soc.* **2014**, *161*, F1395–F1402. https://doi.org/10.1149/2.0571414jes

(15) Ashraf Gandomi, Y.; Aaron, D.; Nolan, Z.; Ahmadi, A.; Mench, M. Direct Measurement of Crossover and Interfacial Resistance of Ion-Exchange Membranes in All-Vanadium Redox Flow Batteries. *Membranes* **2020**, *10*, 126. https://doi.org/10.3390/membranes10060126

(16) Book: Hehre, W. J. *A Guide to Molecular Mechanics and Quantum Chemical Calculations*; Wavefunction, Inc: Irvine, CA, 2003.

(17) Book: Cramer, C. J. *Essentials of Computational Chemistry: Theories and Models*, 2nd Edition.; Wiley: Chichester, 2015.

(18) Roothaan, C. C. J. New Developments in Molecular Orbital Theory. *Rev. Mod. Phys.* **1951**, *23*, 69-89. https://doi.org/10.1103/RevModPhys.23.69

(19) Slater, J. C. Atomic Shielding Constants. *Phys. Rev.* **1930**, *36*, 57–64. https://doi.org/10.1103/PhysRev.36.57

(20) Head-Gordon, M.; Pople, J. A. A Method for Two-electron Gaussian Integral and Integral Derivative Evaluation Using Recurrence Relations. *The Journal of Chemical Physics* **1988**, *89*, 5777–5786. https://doi.org/10.1063/1.455553

(21) Barone, V.; Alessandrini, S.; Biczysko, M.; Cheeseman, J. R.; Clary, D. C.; McCoy, A. B.; DiRisio, R. J.; Neese, F.; Melosso, M.; Puzzarini, C. Computational Molecular Spectroscopy. *Nat Rev Methods Primers* **2021**, *1*, 38. https://doi.org/10.1038/s43586-021-00034-1

(22) Kohn, W.; Sham, L. J. Self-Consistent Equations Including Exchange and Correlation Effects. *Phys. Rev.* **1965**, *140*, A1133–A1138. https://doi.org/10.1103/PhysRev.140.A1133

(23) Huang, J.; Yang, Z.; Murugesan, V.; Walter, E.; Hollas, A.; Pan, B.; Assary, R.S.; Shkrob, I.A.; Wei, Z.; Zhang, Z. Spatially Constrained Organic Diquat Anolyte for Stable Aqueous Flow Batteries. *ACS Energy Lett.* **2018**, *3*, 2533-2538. https://doi.org/10.1021/acsenergylett.8b01550

(24) Xiao, Y.; Chu, L.; Sanakis, Y.; Liu, P. P. Revisiting the IspH Catalytic System in the Deoxyxylulose Phosphate Pathway: Achieving High Activity. *J. Am. Chem. Soc.* **2009**, *131*, 9931-9933. https://doi.org/10.1021/ja903778d

(25) Okura, I.; Kita, T.; Aono, S.; Kaji, N.; Yamada, A. Photoinduced Hydrogen Evolution Using Bipyridinium Salts as Electron Carrier. *Inorg. Chem.* **1985**, *24*, 451-452. https://doi.org/10.1021/ic00198a001

(26) Huang, J.; Hu, S.; Yuan, X.; Xiang, Z.; Huang, M.; Wan, K.; Piao, J.; Fu, Z.; Liang, Z. Radical Stabilization of a Tripyridinium–Triazine Molecule Enables Reversible Storage of Multiple Electrons. *Angew Chem Int Ed* **2021**, *60*, 20921–20925. https://doi.org/10.1002/anie.202107216

5. Results and discussion

5. Results and Discussion

5.1. HIGREEW project

After the introduction of Redox Flow Batteries and the need to develop them in order to ease the implementation of renewable energies into the electrical grid among other applications, European Commission has funded different research projects with the goal to develop a new efficient Redox Flow Battery that could substitute/complement the state-of-the-art (Vanadium RFB). This is the context in which the HIGREEW Project and this PhD are framed. The main reason is that almost all the available Vanadium in the earth is controlled by China government. Furthermore, the scarce availability of vanadium and the high demand of the steel industry make the cost of vanadium too volatile and unpredictable. So, the European research projects are focused on substituting the vanadium as the main redox active material for other organic molecules, copper, hydrogen-bromine, lignin-based redox active materials. The design of a Redox Flow Battey is not an easy task cause the wide variety of components and parameters influencing the high efficiency of the device's performance. For this reason, these projects have been developed by a consortium of universities and private companies which each partner will be in charge of development and optimization of one component. This is a way to merge different experts on each component trying to optimize the performance of the final battery. Here a brief outline of HIGREEW's partners and tasks can be found:

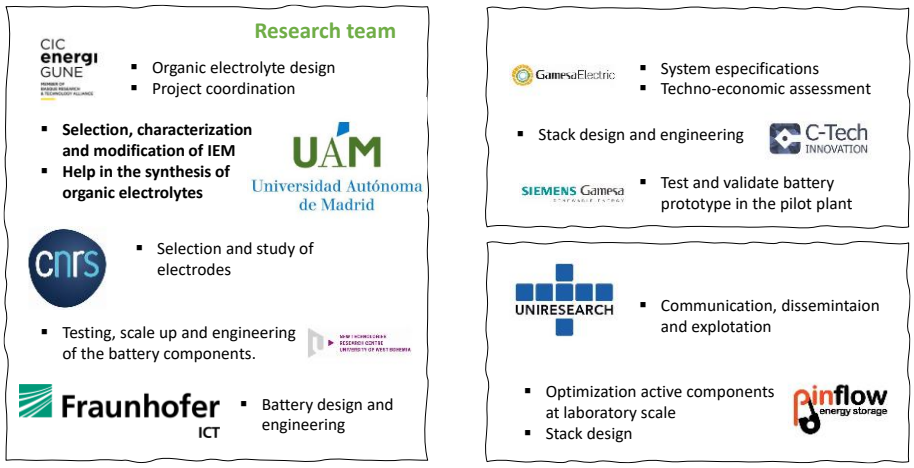

Figure 1: Partners and their main tasks of the HIGREEW project.

UAM team was in charge of the selection, characterization and modification of commercial Ion Exchange Membranes. Furthermore, the team helped in the synthesis, characterization, and test organic electrolytes. Finally, once the organic redox active materials, the membrane and the electrodes were selected, the final battery was tested by all the research teams to corroborate the performance of the battery at different conditions.

5. Results and discussion

This thesis will be divided in three part: i) Synthesis and characterization of different organic redox active materials for neutral aqueous flow batteries (**Chapter 1**), ii) The characterization, selection and modification of different commercial IEM (**Chapter 2**) and iii) Test the studied materials in single-cell corroborating their performance in a battery (**Chapter 3**).

Chapter 1: Organic electrolyte

5.2. Organic electrolytes

It has been introduced the huge variety of organic redox active materials families that have been studied in the literature. As the project aim to develop a neutral aqueous system, viologens seem to be the more effective RAM in neutral pH based on the low redox potential, high-solubility, and fast electrokinetics.[1,2,3] Furthermore, the redox reaction is not proton coupled so, the pH should be constant during the battery operation making the system more stable. The synthesis is quite simple or straightforward which is mandatory since if the RAM works properly, it will be used in large scale (> kg scale). Another advantage of the neutral pH is related to the containers and other components like the membrane, electrodes, bipolar plates and tubbing stability since could be compromised on very aggressive electrolytes. So, 4,4'-bipyridinium salts have been widely studied in the literature decreasing the opportunity for new derivatives.[4,5,6,7,8] On the other hand, 2,2-bipyridinium salts have been poorly studied. To the best of our knowledge only a few examples of 2,2-bipyridinium or bipyridines salts have been considered.[9,10,11]

5.2.1. 2,2-bipyridinium salts as anolyte for RFB.

Diquat herbicides act by inhibition of the electron transfer chain in photosystem I (protein complex that uses light energy to catalyze the transfer of electrons) of the plants by accepting the transferred electrons suggesting a clear redox activity of 2,2-bipridinium derivatives.[12] Despite this, few examples have been studied as anolyte for aqueous redox flow batteries. Zhang *et al* [10] demonstrate the redox activity of 5 different 2,2'-bipyridine electrolytes trying to understand the structural parameters effect. Furthermore, they studied the degradation mechanism of the reduced species trying to stabilize it and afford a stable anolyte for RFB. Here for the first time, they suggest that both nitrogen atoms must be linked to achieve reversible redox process, otherwise the process become completely irreversible.

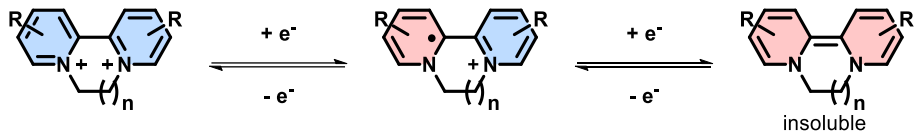

Figure 2: Redox reaction of 2,2'-bipyridinium salts.

As it can be observed, 2,2'-bipyridinium salts behave as viologens derivatives, the first reduction leads to a stable radical cation that can be delocalized through both aromatic rings stabilizing the product (Figure 2). A second reduction afford a completely neutral molecule which is insoluble in water making the redox process irreversible.

Bures *et al* [9] also studied different 2,2'-, 3,3'- and 4,4'-bipyridinium salts with sulfonate alkyl chains. From this study, a poor reversibility of the 3,3'-bipyridinium salts have been observed after the reduction due to the poor delocalization of the radical cation afforded. Again, linked 2.2'-bipyridinium salts (**1e** in their work) is presenting the best redox behavior. In this sense, we would like to study the effect of the dihedral angles between the two pyridinium rings by changing the length of the alkyl chain which link both nitrogen atoms.

2,2'-bipyridine derivatives were synthesized by introduction of alkyl substituents at *N,N'* atoms followed by an anion exchange step through a straightforward procedure either by regular (Method A) or microwave-assisted (Method B) heating in a solvent-free process. So, the six, seven and eight-membered rings of the 2,2'-bipyridinium salts have been prepared and studied (**1**, **2** and **3,** see Figure 3 and 4).

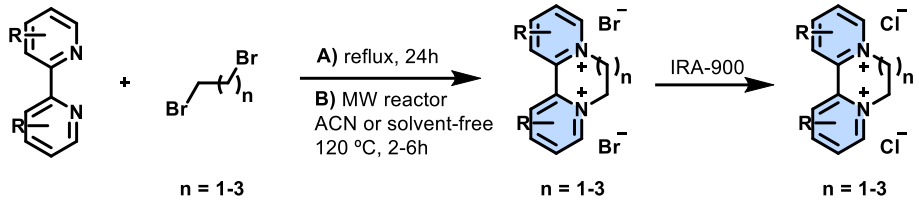

Figure 3: Synthesis methods to prepare the different bipyridinium salts.

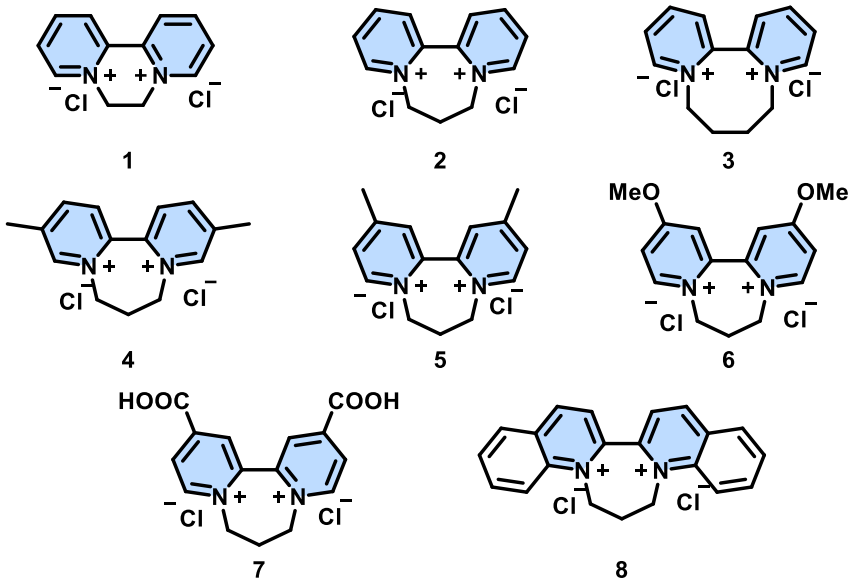

Figure 4: Eight redox active materials prepared and studied.

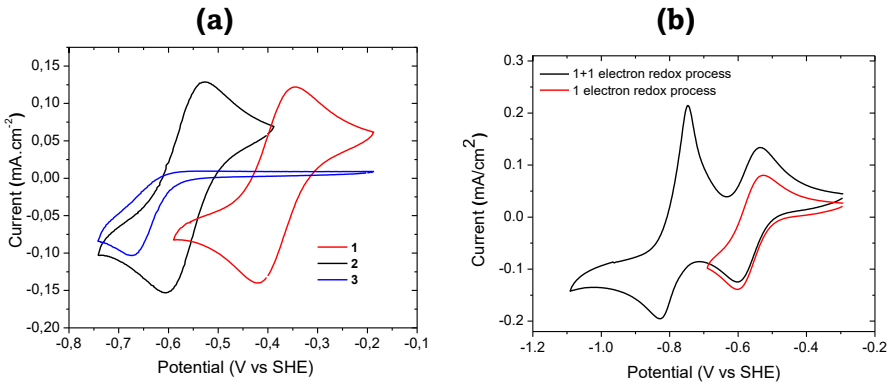

Figure 5: (a) Cyclic voltammetry at 50 mV/s scan rate of compounds **1-3**. (b) Cyclic voltammetry at 50 mV/s of compound **2** reaching two electrons. All the compounds were tested at 1 mM in 1 M NaCl solution at room temperature.

From the CV analysis, we can see clearly that the dihedral angle between two pyridinium rings play a vital role (Figure 5a). Furthermore, Zhang *et al* [10] demonstrated that the unlinked methyl diquat shows an irreversible redox process due to the complete alternation between both aromatic rings. Note that all the compounds present two redox processes (Figure 5b) like it has been reported previously for viologen (and 2,2'-bipyridine derivatives) but just the first represent a fast reversible process.[13,14,15] Interestingly, reversible reduction process of 7-membered ring derivative **2** is observed at a significantly low redox potential when compared to diquat **1** (ΔV = 0.18 V). On the contrary, the redox process of 8-membered ring derivative **3** is completely irreversible and therefore, it was discarded as a candidate. We can expect that higher atoms of carbon in the ring will lead to higher dihedral angle, so, the eight-membered ring show an irreversible redox behavior. If the dihedral angle is too high, the delocalization of the afforded radical cation is inhibited and side reactions (probably protonation) of the reduced species makes the process chemically irreversible. One way to demonstrate this hypothesis is to calculate the structural parameters. Using one of the most reliable tools of chemist, DFT calculations, two key parameters (dihedral angle and C_{ipso}-$C'_{ipso'}$ distance between both aromatic rings) were calculated. C_{ipso}-$C'_{ipso'}$ bond could let us understand how much sp^2 character present between both aromatics rings. So, as shorter is the C_{ipso}-C'_{ipso} bond distance more sp^2 character present and higher delocalization between the aromatics rings is expected. In the same way, as shorter is the dihedral angle, more planar disposition between the two aromatic rings which lead to higher delocalization of the generated radical and as consequence higher stability (Figure 6).

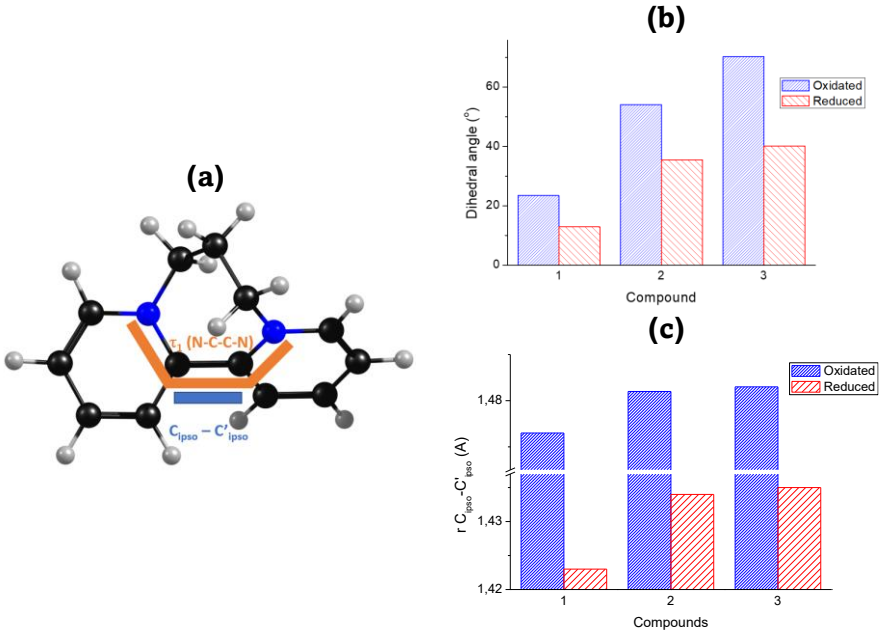

Figure 6: (a) Dihedral angle (orange) and C_{ipso}-C_{ipso}' distance (blue) (b) Variation of dihedral angle (c) and C_{ipso}-C_{ipso}' distance for compounds **1-3.**

As we suspected increasing the number of atoms in the ring increase the dihedral angle and the distance between both aromatic rings what explain the poorer delocalization. So, the irreversible behavior of compound **3** can be explained by the lack of stabilization and delocalization along both aromatic rings. It is noteworthy that the dihedral angles decrease considerably in the reduced form due to the need of this stabilization of the radical via delocalization.

As the six-membered ring derivatives have been studied by Zhang *et al* [10] showing high-capacity decay we focus our efforts on developing a family of seven-membered ring bipyridinium salts bearing different substituents (Compounds **2** and **4-8,** see Figure 4). These seven membered rings present higher dihedral angle that could avoid the intermolecular interaction as well as should present bigger volumes (loss of planarity) which could lead to lower crossover through the membrane. Substituents has been grafted in the bipyridinium core to understand their electronic effect in the redox behavior as well as in the structural parameters. One advantage of these bipyridinium salts is the simple and efficient synthesis that could enhance their implementation in RFB.

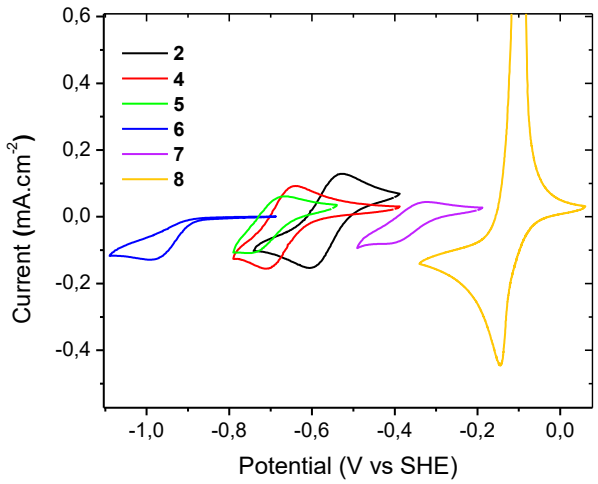

Figure 7: Cyclic voltammograms at 50 mV/s of Compound **2** and **4-8.** All the compounds were tested at 1 mM in 1 M NaCl solution at room temperature.

We can see clearly that Electron Donating Groups in the *para* position turn the redox process completely irreversible as well as shift the redox potential to lower values (compound **7**). It makes sense, since as higher is the electronic density in the bipyridinium core more challenging is going to be introduce an electron. On the other hand, Electron Withdrawing Groups shift the redox potential to higher values due to the opposite argument (compound **6**). Soft EDG as the methyl group (compounds **4** and **5**) enhance the redox potential without affecting the reversibility of the redox process. Regarding the methyl substituent, *meta* and *para* position effect can be depicted (Figure 7). The substitution placed in the para position presents a more significant influence on the redox potential as it can be expected due to the radical delocalization. Here we have found a special case, compound **8** present a very particular redox behavior. A sharp peak was observed in the cyclic voltammogram suggesting the deposition/adsorption of material on the electrode surface. One way to demonstrate this theory is by plotting the current *vs* the square root of the scan rate. If linearity is followed, it suggests that redox species are diffusion controlled. On the other hand, if there is no linearity, the redox process does not freely diffuse (Figure 8).

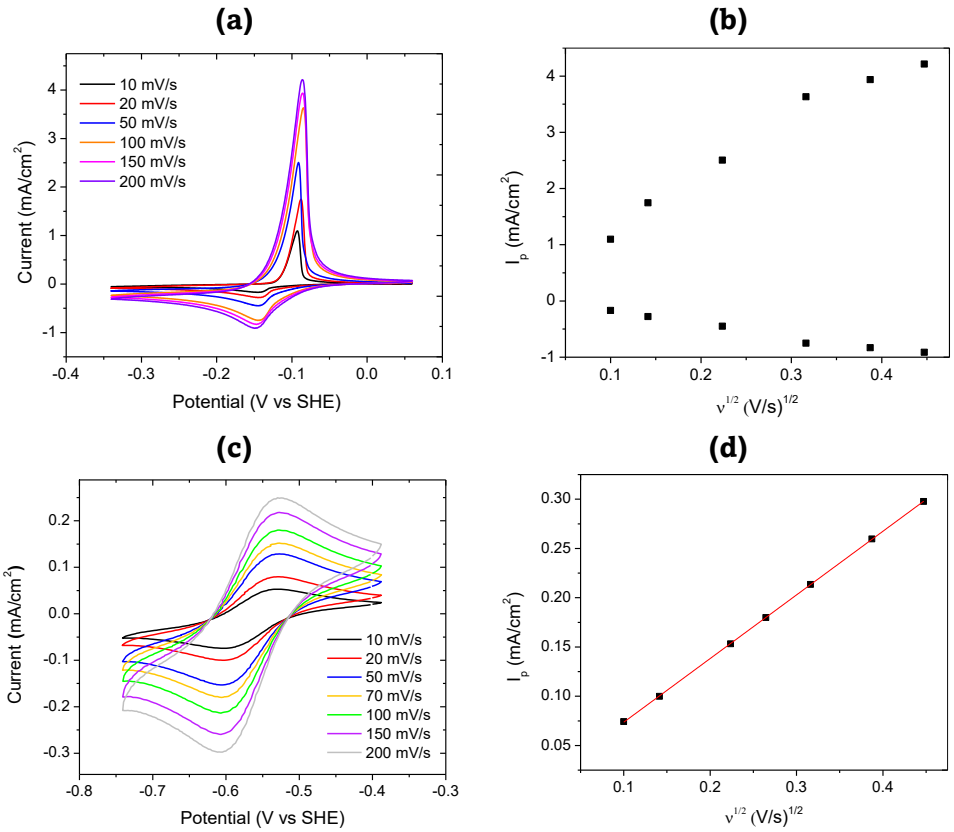

Figure 8: Comparison of CV of compound **8** (adsorption phenomena, (a) and **2** (free-diffusion process, (c). Plot of current peak *vs* square root of the scan rate. Non-linear behavior for compound **8** (b) and linear behavior for compound **2** (d). All the compounds were tested at 1 mM in 1 M NaCl solution at room temperature.

Compound **2** present a clear diffusion-controlled redox behavior showing no change in the redox potential, while increase the scan rate of the CV measurements, Furthermore, when plotting the current peak *vs* square root of the scan rate we can see a clear linearity in the plot. On the other hand, compound **8** present some deviation in the redox potential when increase the scan rate of the CV measurements. Besides, the non-linearity of the current peak *vs* square root of the scan rate indicates an adsorption or deposition phenomena.[16] This phenomenon could be explained by the stronger interactions of the extended π-system within the glassy carbon electrode used in these measurements.

It has been reported that the redox potential can be estimated using the energies of the oxidated and reduced state of RAM calculated from the DFT calculation.[17,18,19] Here, we thought that could be easy to calculate the redox potential. Furthermore, the main goal of this work was developing an efficient method that would allow chemists to predict the battery performance of RAM before synthesizing them. So, the redox potentials were calculated following the following Hess diagram and equation (Scheme 1 and equations 1 and 2):

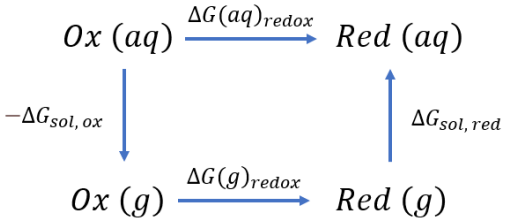

Scheme 1: Born-Haber cycle for the redox potential calculation.

$$\Delta G(aq)_{redox} = \Delta G(g)_{redox} + \Delta G_{sol,\ red} - \Delta G_{sol,\ ox} \quad (1)$$

$$\Delta G(aq)_{redox} = -FE_{redox}{}^{o} \quad (2)$$

Being $\Delta G(g)_{redox} = \Delta G(g)_{red} - \Delta G(g)_{ox}$, $\Delta G_{sol,\ ox} = \Delta G(aq)_{ox} - \Delta G(g)_{ox}$ and $\Delta G_{sol,\ red} = \Delta G(aq)_{red} - \Delta G(g)_{red}$ (KJ/mol).

The redox potential must be corrected to the standard hydrogen electrode potential ΔSHE (-4,43 V). Other relativistic and geometry correction could be considered although it is out of the scope of this work.

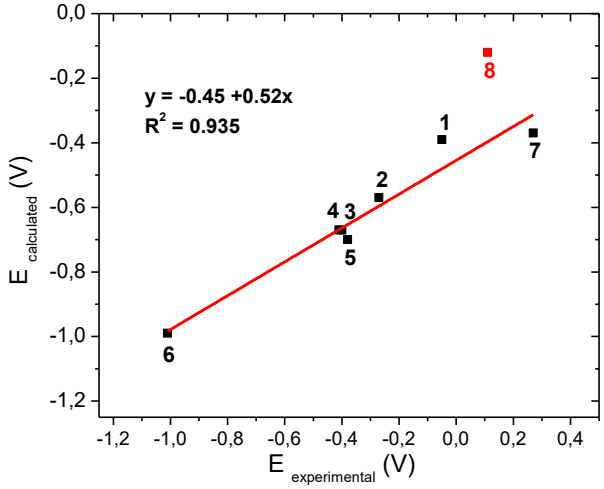

Figure 9: Correlation between the predicted and experimental redox potential for compounds **1** to **8**.

So, the redox potential of the different bipyridinium salts have been precisely calculated showing just one exception, compound **8**. That could be explained due to the higher redox potential of biquinoline which is attributed to the extended aromatic structure and could not be accurately predicted by Hess's Law. Knowing that the Hess's Law uses the energies of the optimized geometries in aqueous and gas phases, the low solubility of compound **8** could lead to some deviations in the

calculated redox potential (red dot in Figure 9). Furthermore, the adsorption of compound **8** could significantly vary the redox potential of the RAM.

Table 1: Main parameters for the bipyridinium salts.

RAM	Form	$E_{1/2}$ exp*	$E_{1/2}$ calc*	τ_1 (°)	r C_{ipso}-C'_{ipso} (A)	D (cm^2/s)	k (cm/s)	λ (eV)	Solubility (M)
1	Ox	-0.39	-0.05	23.5	1.473	$7.24 \cdot 10^{-6}$	$1.54 \cdot 10^{-2}$	0.064	2.4
	Red			12.9	1.423				
2	Ox	-0.57	-0.27	54.0	1.482	$4.13 \cdot 10^{-6}$	$6.14 \cdot 10^{-3}$	0.143	2.8
	Red			35.5	1.434				
3	Ox	-0.67	-0.40	70.2	1.483	n.r	n.r	0.287	---
	Red			40.1	1.435				
4	Ox	-0.67	-0.41	53.4	1.479	$4.46 \cdot 10^{-6}$	$4.42 \cdot 10^{-3}$	0.132	2.2
	Red			35.1	1.434				
5	Ox	-0.70	-0.38	53.4	1.483	$5.59 \cdot 10^{-6}$	$1.58 \cdot 10^{-3}$	n.d	2.6
	Red			35.1	1.433				
6	Ox	-0.99	-1.01	53.5	1.484	n.r	n.r	n.r	---
	Red			37.7	1.441				
7	Ox	-0.37	0.27	54.1	1.482	$3.02 \cdot 10^{-6}$	$2.88 \cdot 10^{-2}$	n.d	---
	Red			38.5	1.445				
8	Ox	-0.12	0.11	53.6	1.487	n.s	n.s	n.s	<0.1
	Red			34.1	1.440				

* V *vs* SHE, n. r: not reversible, n. d.: not determined, n. s.: not soluble

The water solubility is an important property considering the potential application of these materials as anolytes in RFB. The molar water solubility of 2,2'-bipyridynium compounds was measured by UV/Vis spectroscopy (see Table 1). The higher solubility of the 7-membered ring **2** (2.8 M) when compared to diquat, **1** (2.4 M), may be attributed to the lower planarity and higher polarity conferred by the longer alkyl linker bridging nitrogen atoms. By contrast, the solubility of substituted bipyridinium salts **4**, **5** and **8** confirmed the relevance of both the nature of the substituents and the disposition of them in the core structure. Thus, methyl substituents in *meta*- and *para*- positions have opposite effect on solubility. Worth noting, *para*-substituted bipyridinium compound showed higher solubility, up to 2.6 M. Nevertheless, the substitution of pyridine rings by more hydrophobic quinoline rings led to a dramatic drop on water solubility (< 0.1 M). The latter is in good agreement with the hypothesis of material deposition on electrode surface during cyclic voltammetry experiment for compound **8**. The more hydrophobic character of compound **8** and the potentially stronger π-π interactions shall explain the lower water solubility.

After corroborating the redox activity and the solubility of the bipyridinium salts and be able to reproduce a key parameter such as the redox potential, the next step is determined the kinetic constants and diffusion coefficients of the redox reaction. A promising redox active material should present efficient electrokinetics otherwise high mass-transport and activation resistances will be expected in the redox flow battery. The electron transfer rate (k) and diffusion coefficients (D) were determined experimentally from linear sweep voltammograms (LSV) using a rotating disk electrode (RDE) and calculated through the Koutecky-Levich and

Levich equations, respectively (Experimental and theoretical procedures). As it can be commented before only the first redox process is reversible and do not present any adsorption or precipitation of the redox active material, for this reason, just the kinetic constants and diffusion coefficients of the first electron (n = 1) for compounds that are reversible has been studied. Thus, the electron-transfer rate constants obtained were $1.54 \cdot 10^{-2}$ and $6.14 \cdot 10^{-3}$ cm/s for compounds **1** and **2**, respectively. On the other hand, the substituents on the aromatic ring did not lead to significant changes on the reaction kinetics. (Compound **4** and **5** showed similar kinetics and diffusion values as compound **2**).

With the target to use DFT calculations to predict the electrochemical behavior of redox active materials and trying to predict this tendency in the kinetics of the redox process, the Marcus theory appears as an interesting approach. Marcus theory describes the kinetic of reactions where significant structural changes do not take place.[15] Scanning the reaction coordinate (the parameter which change along the reaction) the energy of the starting material (in our case the oxidated form) and the final product (reduced state) is calculated at each point. So, the Marcus parameter can be calculated and as higher is this value slower are the kinetics cause the product and the reagent are far in energy. This theory is based on higher Marcus parameter (or energy distance between both states) implying bigger reorganization and as consequence slower kinetic of the process. As it has been depicted in Table 1 there is a significant change in the dihedral angle between the oxidized and reduced state. For this reason, the dihedral angle was selected as the reaction coordinate for the redox process (C_{ipso}-C'_{ipso} distance could be used too). Here, in Figure 10 an example of the energies at different values of the dihedral angle for both states as well as how the Marcus parameter was calculated is shown:

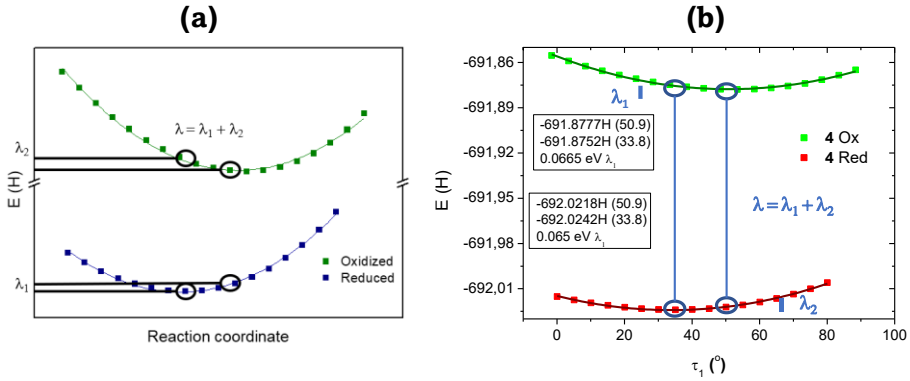

Figure 10: (a) Schematic representation of the Marcus parameter calculation (b) example of the curves obtained for the compound **4** when the dihedral angle was scanning.

From this study, the Marcus parameters for the bipyridines with different number of atoms in the ring **1**, **2** and **3** have been calculated (Table 1). We can see clearly that the theory fix with the experimental results, **1** present the fastest kinetic and also the lowest Marcus parameter. Then **2**, present medium kinetics and Marcus

parameters and the slowest bipyridinium **3** show the highest Marcus value. Seven-membered ring bipyridinium salts present similar structural parameters and as consequence almost equal kinetic constants. Trying to corroborate this trend, the Marcus parameter of compound **4** was calculated and compared to **2.** We can see that both redox active materials present almost the same kinetic constant and Marcus parameters. The prediction of the redox potential and the kinetic constant cheer us up to create a method that can predict the stability of the RAM. Usually, the stability of the redox active materials is tested using a symmetric or a single-cell (coupled with another component). This kind of experiments are expensive due to the use of expensive ion exchange membranes, bipolar plates, electrodes (typically carbon felts), sealing materials, peristaltic pumps, hermetic cells, and glovebox (or a system that prevents the oxygen penetration into the system). Taking this on mind, the idea to be able to know the stability of the RAM before assembly the cell and test it appears like an interesting approach that could save money and time.

Since the stability of viologen and mostly all of the organic anolytes are related with the reactivity of reduced species, the delocalization of the cation radical is going to be a key parameter in this issue. The main degradation pathway reported to the 2,2'-bipyridinium salts is the proton catalyzed disproportionation so, as higher is the delocalization more difficult will be the degradation.[10] The structural parameters have showed that for all the seven-membered ring derivatives are almost equal so any information can be extracted from this part. The electronic effect of the substituents must play a role in the delocalization of the generated radical. The study of the Natural Bond Orbitals and charge distribution delocalization along both aromatic rings could shed light on this issue.

- *Natural Bond Orbitals delocalization*:

Analyzing the interactions between different NBO[20] of the reduced species allows to understand how the charge is allocated along the structure. More than 10000 interactions between orbitals have been studied in some derivatives. Therefore, the different interactions between orbitals which involve the two aromatic rings let us estimate the delocalization of the reduced species.

Table 2: Sum of the delocalization interactions between the NBO between both aromatic rings.

Molecules	Interactions (Kcal/mol)	Normalized Degree of delocalization***
1	157	1.02
2	154	1
3	130	0.84
4	11317	73.49
5	1777	11.54
6	99	0.64

7	2942	19.10
8	119312	774.75

***The degree of delocalization is the normalized interaction to compound **2** at the B3LYP level of theory.

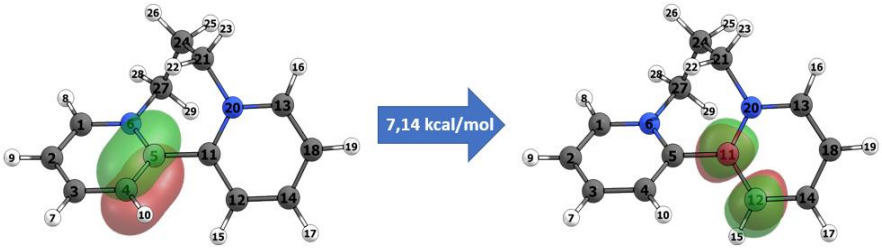

Figure 11: Example of one NBO delocalization between aromatic rings for the compound **2**.

Based on the analysis of the Natural Bond Orbitals of the reduced species, a comparison of the electronic delocalization for the different bipyridinium derivatives was performed (Figure 11, Table 2). As it can be seen in Figure 13, derivatives **1**, **2** and **3** show similar electronic delocalization, being higher as shorter the bridge is (**1** ≈ **2** > **3**). Thus, the higher delocalization forecasted by NBO analysis fits with the previously calculated structural parameters, as the dihedral angle and the interring bond distance as well as the experimental results. When focusing on the role of substituents, it could be observed that substituents which do not allow delocalization present lower interactions, for example strong EDG in **6** inhibits the delocalization between the two aromatic rings. The expansion of aromaticity (compound **8**) significantly enhances the delocalization because of the increased number of interactions. In principle, this higher level of interactions should correspond to a more stable reduced form. However, the mismatch between theoretical and experimental outcome may be explained by the low water solubility of compound **8.** The addition of a methyl group also enhances the delocalization between the two aromatics moieties (**4** and **5**). The methyl group acts as a weak donor substituent enhancing the NBO interactions between the two aromatic rings. When the focus is put on the *para* position, it could be observed that higher electron withdrawing character of the substituent enhances the delocalization between the aromatic rings (compound **7**).

- *Charge distribution analysis:*

The analysis of the charge distribution along the different atoms in both redox states serves for a better understanding of the delocalization in the rings. As expected, the reduced species have more negative charges that the oxidized ones because of the charge provided by the new introduced electron. Here, the interesting point is to know how different these aromatic rings are (an example of

the equation used is shown in Equation 3). Higher differences between homologous carbons of each ring mean lower delocalization between both rings.[21]

$$\Delta\Delta\, charge = |\Delta Charge\ (Red - Ox)_{C2} - \ \Delta Charge\ (Red - Ox)_{C2'}| \quad (3)$$

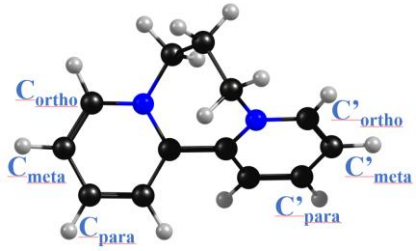

Figure 12: Representative example of the carbons on which the charges distribution has been studied.

The influence of the interring delocalization on the stability of the reduced radical has been reinforced by the study of the charge distribution which show how the electron in the reduced form has been allocated.[11] The difference between the change in each carbon of the aromatic ring (*ortho-*, *meta-* and *para-* relative positions to the nitrogen of the pyridine, Figure 12) when comparing oxidized and reduced forms define the symmetric or nonsymmetric distribution between both aromatic rings. By comparing this distribution between two aromatic rings, it can be determined if the charge has been allocated in both aromatic rings or preferentially in one of them, making both rings different (Table 3). In this study different population analysis has been compared considering their strengths and weaknesses: Mulliken,[22] Hirshfeld,[23] and Atom Dipole Correction Hirshfeld (ADCH).[24] While Mulliken analysis is a well extended method it is not ideal for practical applications due to the poor reproducibility of observable properties such as molecular dipole moment, a very high basis dependence and occasionally meaningless results. On the contrary, Hirshfeld analysis leads to qualitatively consistent results with the general chemical concepts, and it is insensitive to the size of the wavefunction, and the applicability of the Hirshfeld population is not constrained by the type of wavefunction. The con of this method is that the charges are always too small and the poor reproducibility of observable quantities because the Hirshfeld population completely ignores atomic dipole moments. In this sense, the Atomic Dipole Corrected Hirshfeld (ADCH) analysis takes into account the atomic dipole moment and the charges achieved are significantly higher.

Table 3: Mulliken, Hirshfeld and Atomic Dipole Corrected Hirshfeld (ADCH) charge variations in the redox process between the homologous C and C' (without hydrogens summed into heavy atoms).

|ΔΔ charge| C(Red→Ox) →C'(Red→Ox)				
Molecules	**Position**	**Mulliken**	**Hirshfeld**	**ACDH**
1	*Ortho*	0	0	0
	Meta	0	0	0
	Para	0	0	0
2	*Ortho*	1E-6	0	1.61E-4
	Meta	1E-6	0	4.90E-5
	Para	2.4E-6	0	2.15E-4
3	*Ortho*	1E-6	5E-6	1.14E-3
	Meta	3E-6	1E-6	6.72E-3
	Para	1.3E-5	6E-6	8.87E-3
4	*Ortho*	2.70E-3	6.2E-5	2.15E-3
	Meta	6.76E-3	1.8E-5	4.50E-3
	Para	1.16E-4	1.1E-6	5.84E-3
5	*Ortho*	6.53E-4	5E-6	0.99E-4
	Meta	3.63E-4	5E-6	1.73E-4
	Para	1.1E-4	6E-6	3.83E-4
6	*Ortho*	7.53E-2	5.89E-3	2.47E-2
	Meta	7.88E-2	8.52E-4	0.28
	Para	9.14E-2	3.7E-3	2.73E-2
7	*Ortho*	0.239	4.07E-4	6.24E-2
	Meta	0.0567	4.03E-3	0.14
	Para	0.273	6.89E-4	0.25
8	*Ortho*	5.33E-4	1.5E-5	8.97E-4
	Meta	6.04E-4	1E-5	1.11E-2
	Para	9.1E-5	3E-6	1.63E-2

The three analysed methods lead to similar trends when comparing bipyridinium derivatives, see Table 3 for more details. The ADCH method was selected. If the bipyridinium derivative presents high delocalization, the difference in the charge distribution should be low. For example, compounds **1** and **2** show almost negligible difference between the charge distribution for both aromatic rings. The compound **3** shows higher differences, which is aligned with previous predictions based on the higher dihedral angle and resultant lower delocalization. When turning into the study of the effect of the substituents, similarly to what has been observed in the NBO analysis, the introduction of strong EDG or EWG has a detrimental effect on the interactions or interring delocalization as evidenced by

the significant differences between aromatic rings in terms of charge allocation determined for compounds **6** and **7**. Compounds **8**, which according to NBO analysis show an increase number of interring interactions present a lower interring delocalization that the non-substituted pyridinium homologue. A preferential delocalization within the quinoline ring is therefore expected for compound **8**, which according to delocalization predicted in the NBO and charge analysis could be a highly stable active material. However, it is discarded based on its poor solubility. Finally, the methyl group **4** and **5** show quite similar charge distribution between the two pyridine rings. Again, mild EDG seem to somehow promote further interactions between rings and charge delocalization. Thus, high stability for the cation radical reduced species is foreseen for those bipyridinium derivatives.

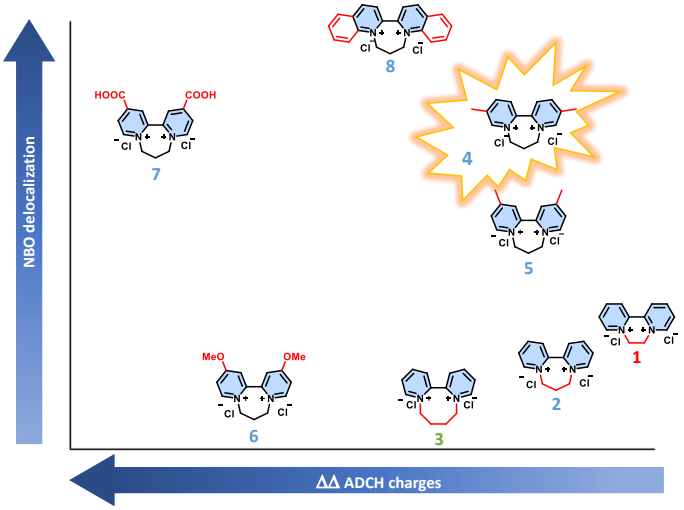

Figure 13: Illustrative figure evaluating the contribution of the NBO delocalization and the ADCH charge distribution.

Charge analysis have been proposed as a powerful tool that combined with NBO and structural analysis, provide deeper understanding on the stability of these compounds. Note that Figure 13 shows, in a representative way, the contribution of NBO delocalization and the ADCH (most chemically meaningful of the three studied methods) charge distribution to the stability of the bipyridinium derivatives and serves as a plausible guidance in the selection of a good candidate for a potential RFB. Thereby, by considering both contributions, bipyridine derivatives with high delocalization are expected to render more stable electrolytes due to the high stabilization of the cation radical.

Encourage by the computational studies, compound **4** was selected for the preparation and testing of electrolytes for AORFB. Therefore, based on the given theoretical predictions, single-cell tests were addressed to corroborate the stability of its reduced form. These experiments will be discussed in **Chapter 3**: Single-cell experiments.

5.2.2. Triazine derivatives for multiple electron storage.

The relatively low standard cell potential (1.26 V for all-Vanadium RFB) compared to other batteries like the Li-ion battery (showing a cell voltage up to 3.85 V) and solubility representing low amount of redox active materials in a huge matrix of solvent (up to 2 M in the case of anolytes and 4~5 M in the case of catholytes) compared with the electrodes materials (used in other batteries) are the main responsible for the low energy density of RFB. For these reasons, there is a clear trend to develop systems which allow to increase the energy density. By developing new RAM with higher redox potential, higher solubility and more electrons involved in the redox reactions the energy of RFB could be enhanced. That last strategy has been employed with quinones based electrolytes, but these materials consume and release protons during the operation of the battery Proton Coupled Electron Transfer, PCET). Regarding viologens, the use of two electrons have been pursued but lead to higher capacity decay.[5,26,21] Lately, an interesting approach has been developed by Liang *et al*, where a new aqueous soluble triazine derivative has been reported. This new triazine anolyte has been able to store up to three electrons in neutral pH in single-cell. Furthermore, the use of bigger RAM could help to solvent one of the major concerns of RFB, the crossover. This new triazine-pyridinium derivative benefits the delocalization between the pyridinium rings as well as the triazine core stabilizing the radical species during the reduction. The problem of this last derivative is the tedious synthetic route followed with various ion exchange steps to increase the solubility of intermediates.[27] For this reason we thought a zwitterionic alternative that could store multiple-electron and be afforded by a simple synthesis (Figure 14). This is something that must keep on mind, the development of efficient RAM must follow simple synthetic routes or procedures since the preparation complex molecules cannot compete with vanadium electrolyte price (V_2O_5 typically between 5 to 10 $/kg).

(a)

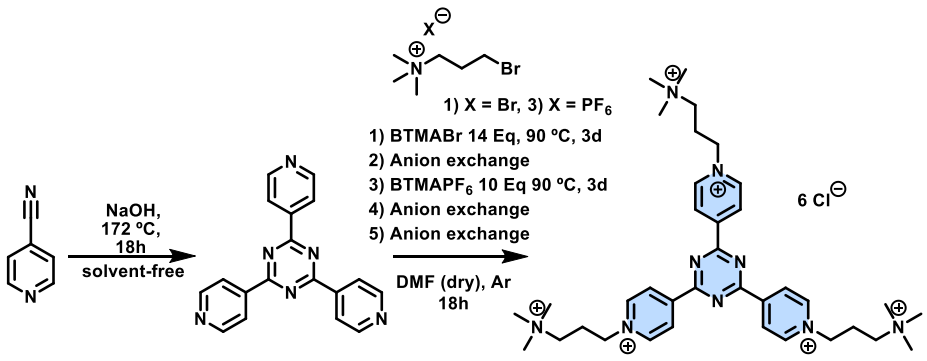

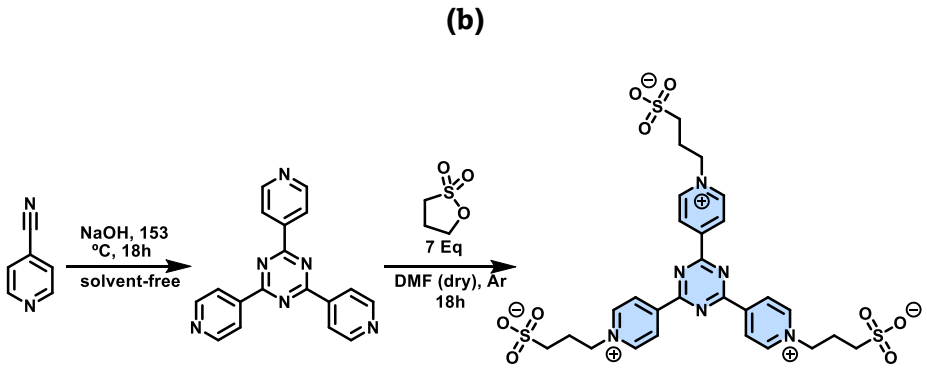

Figure 14: (a) Reported synthesis for the synthesis of the first triazine anolyte. (b) Synthesis of **(SPr)$_3$4TpyTz.**

The prepared compound exhibits three reversible redox processes at -0.47 V, -0.62 V and -0.82 V *vs* Ag|AgCl (3 M KCl) (Figure 15a). In the cyclic voltammetry (CV) measurement the peak separation of the first process is scan rate independent, but peak separation for the second and third process increases with increasing scan rate. Therefore, the first process can be considered reversible, while the other two are quasi-reversible. That suggest that the kinetic of the second and third redox process could be compromised. The Differential Pulse Voltammogram (DPV) (Figure 15) shows three reduction peaks where the two redox processes at less negative potentials correspond to single-electron reduction. By contrast, at more negative potential the peak of the DPV has double the current, indicating two-electron reduction, as shown in Figure 15b.

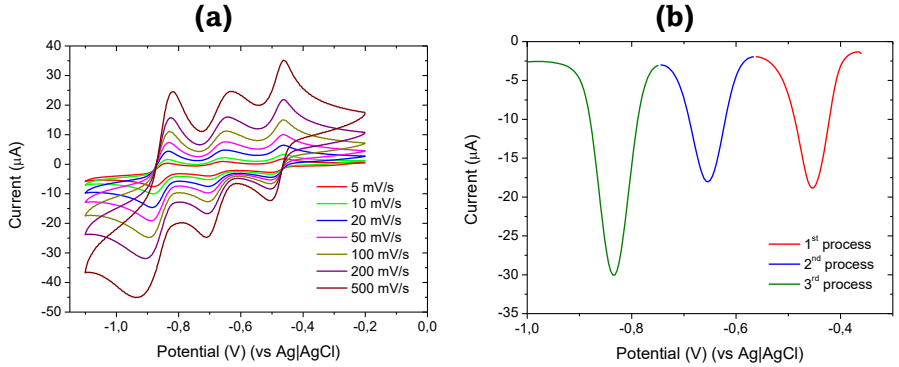

Figure 15: (a) CV at different scan rates and (b) DPV using 1 mM of **(SPr)$_3$4TpyTz** in 1 M KCl**.**

Table 4: Redox potential, kinetic constants, and diffusion coefficient for each redox process.

	E (V) *vs* Ag|AgCl (3 M KCl)	k (cm/s) · 10^{-3}	D (cm^2/s) ·10^{-6}
1st process	-0.47	19.60	1.95
2nd process	-0.62	2.32	1.53
3rd process	-0.82	0.16	0.56

Again, the diffusion coefficients and the kinetic rate constants of each reversible process were studied using Linear Sweep Voltammetry (LSV) on a glassy carbon rotating disk electrode (RDE) (Table 4). As expected, based on CVs, the first process has faster kinetics than the two others which have showed a quasireversible behavior on CV. The solubility was determined by UV/Vis spectroscopy showing a high solubility of 0.94 M in 1 M KCl. Interestingly, the solubility of the triazine anolyte depends significantly on the presence of enough amount of supporting electrolyte. The anolyte is almost completely insoluble in water at become more soluble when potassium chloride is added (Figure 16). This behavior has been observed for other zwitterionic species like for examples the proteins, *salt in* effect.[28] One way to understand why the molecule is almost completely insoluble without the presence of salt could be the interaction between the sulfonate group with the pyridinium core losing the solubilizing power.

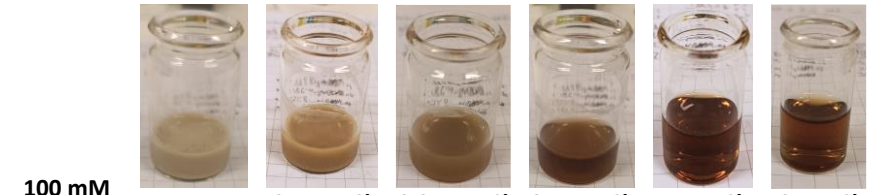

Figure 16: Pictures of the solution 100 mM of **$(SPr)_3$4TpyTz** with different concentrations of KCl.

This interaction was also observed in the NOESY NMR spectra where a correlation between the alkylic chain and the pyridinium protons can be observed (Figure 17 highlighted in the red). This interaction has been also observed for the sulfonated viologen reported by Leo Liu.[29] They developed a rod-shaped viologen which decrease the permeability through the IEM, increase the redox potential and higher stability by grafting methyl into the pyridinium core to avoid this interaction.

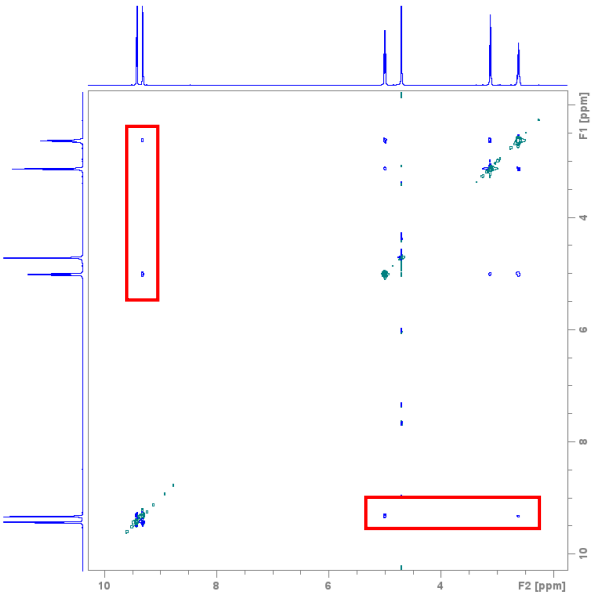

Figure 17: NOESY spectra of **(SPr)$_3$4TpyTz** in 1 M KCl D_2O.

The same NMR experiment was repeated using different supporting electrolyte like NH_4Cl, urea (H-bond between the ammonium and sulfonate could avoid the intermolecular interaction), LiCl (smaller cation) NaCl (more oxophilic cation) but in all the cases the cross-peaks signals appear.

Another possibility could be the intermolecular interaction between the sulfonate group and the pyridinium core of different molecules. Other molecules like the naphthalene diimide derivative suffered aggregation and it was corroborated by NMR.[30] The self-association for the NDI derivative lead to a concentration dependent of the chemical shift from ^{1}H NMR. In order to check if there is some kind of aggregation the NMR at different concentrations were recorded. Any peak shift was observed so it suggests that there is any aggregate (Figure 18).

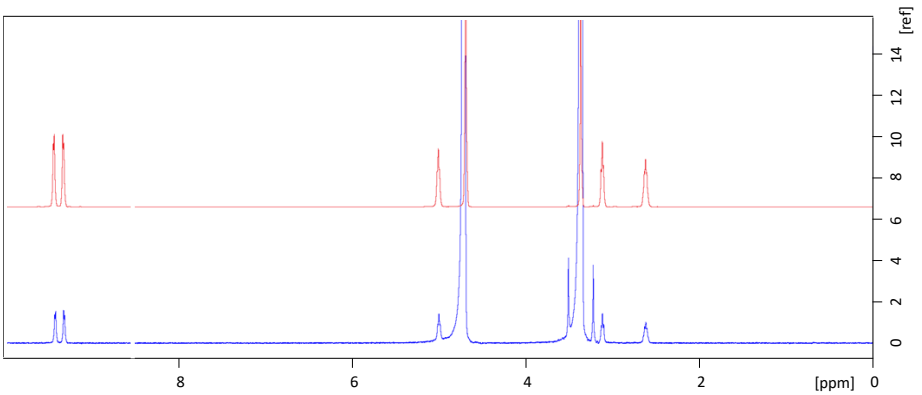

Figure 18: ^{1}H NMR of **(SPr)$_3$4TpyTz** at different concentrations 1 mM and 50 mM in D_2O.

As the fast kinetics and high diffusion coefficients are matched with the high solubility initial evaluation of the molecule is promising and the performance should be tested in single-cell and will be discussed in **Chapter 3**.

In **Chapter 1**, we conducted the development and characterization of new bipyridinium salts as potential anolytes for redox flow batteries. These highly water-soluble (>2 M) and non-planar bipyridinium salts were chosen as a case study to establish and validate a computational predictive model. This model successfully predicts their stability and potential application as active materials in AORFB. An initial theoretical-experimental characterization of selected bipyridines allowed us to examine the effect of ring size, geometry, and electron density on the physico-chemical properties of the materials. Notably, the NBO and ADCH charge analyses proved to be essential tools in understanding the stability of the reduced species, particularly in terms of electronic delocalization and the significance of molecular design in determining the stability of the electrolyte for AORFB.

Herein, we have achieved one of the most challenging approaches – multiple-electron storage for viologen derivatives in neutral pH, which can significantly enhance their capacity and energy density. The primary obstacle for multiple-electron storage lies in the stability of radical intermediates. The synthesis of **(SPr)$_3$4TpyTz** was achieved through a highly atom-economic, short, and cost-effective route. The triazine anolyte is a promising anolyte not just based on the fast kinetics, high diffusion and high solubility, but its ability to store multiple electrons. Furthermore, it has undergone in-depth study using DFT calculations to gain insights into the intermolecular interactions responsible for the formation of insoluble aggregates.

All in all, these anolytes will be tested in single-cell to show their promising characteristics and could open the door to new derivatives.

Chapter 2: Ion Exchange Membranes

The characterization, selection and modification of different IEM has been addressed in this chapter. This is a quite complex task since all the commercial IEM are protected, which means that information on their chemical composition is scarce. A first step is a strong characterization of these where all the key characteristics of IEM must be studied before modification and always keeping in mind that these materials must be operational for a 5 kW stack as set in the HIGREEW Project.

5.3. Ion Exchange Membrane characterization

Different cationic and anionic IEM as well as separators were selected as candidate materials. Each kind of material could provide different characteristics which can provide advantages or disadvantages. It is expected that Cationic Exchange Membranes provide higher conductivity due to the high ionic mobility of the cations, but at the same time the size of the cations must be taken into account because higher crossover of positively charged species may appear as for example occurs with vanadium ions.[31] On the other hand, AEM should provide lower crossover but higher resistance (due to the lower mobility of the anions compared to cations). Ceramic porous separators instead of any IEM could be taken into consideration. These materials allow the pass of small ions/molecules through their pores but can inhibiting the pass of bigger molecules. This last option should present high conductivity, low costs but any selectivity due to the lack of functional groups that can distinguish among cations or anions.

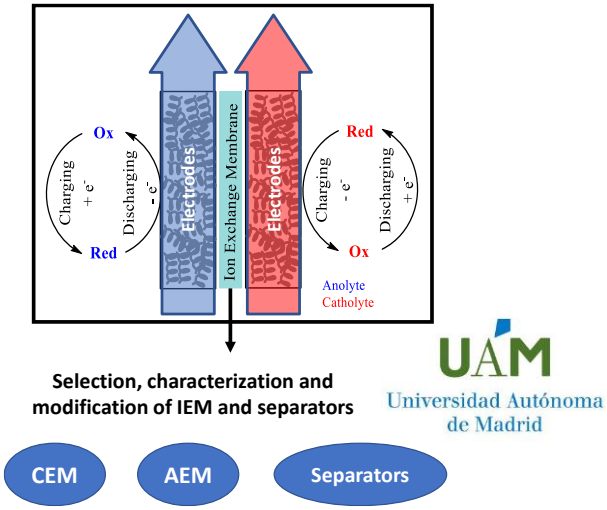

Figure 19: Schematic representation of the role of the IEM and the main tasks of the UAM team in the HIGREEW project.

The first step carried out in this PhD was to characterize all these materials by determining the main parameters that affect their performance in the RFB: IEC, SR, WU, σ... Furthermore, the permeabiliy and interaction between the redox active material and the membrane should be evaluated by analyzing the cross-

mixing of these species (inherently linked with the durability of the system). Further characterization regarding membrane morphology and other physics chemical analysis were performed. Note that at the beginning of the project, where this PhD has been developed, requirements were set for all components, being "MUST requirements" which must be fulfilled, and the expected values initially proposed to accomplish are the "HIGREEW requirements".

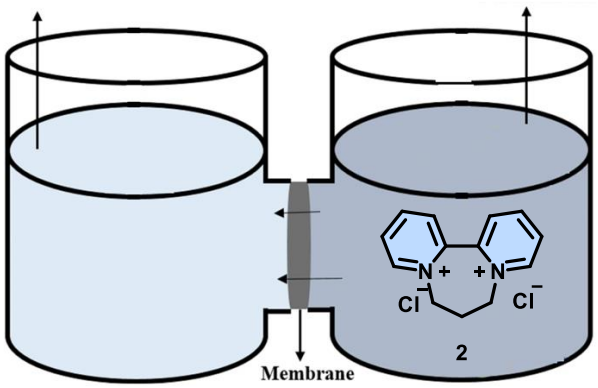

Figure 20: Schematic representation of the permeability test using H-cell and Compound **2** as active material (both tanks have solution with the same supporting electrolyte).

Table 5: UAM measurements of physicochemical properties of some commercial materials.

Membrane	**FAA-3-50**	**FAA-3-PE-30**	**FAPQ-330**	**E-620(K)-PE**	**E-630(K)**	**FS-930**	**FS-950**
Provider	Fumatech BWT	Fumatech BWT	Fumatech BWT	Fumatech BWT	Fumatech BWT	Fumatech BWT	Fumatech BWT
Price (€/m²)	481	481	760	401	401	1122	1122
Type (Counter-ion)	AEM (Cl^-)	AEM (Cl^-)	AEM (Cl^-)	CEM (Na^+)	CEM (Na^+)	CEM (Na^+)	CEM (Na^+)
Thickness (µm)	45.0	23.0	26.0	19.0	34.0	34.0	52.0
WU (%)	15.6	17.1	21.0	47.5	19.6	0	15.8
SR (%)	<30	<30	<30	<30	~30	<30	<30
IEC (mmol/g)*	1.9	1.1	1.0	2.8*	1.5	2.1	1.5
Conductivity (mS/cm)	1.1	0.3	1.7	0.8	2.6	1.9 (>70)	2.2
Permeabiity (cm^2/s) Compound 2	1.26E-10	5.41E-10	1.42E-8	2.39E-8	3.43E-8	1.31E-8	2.49E-10

*Too high values could compromise the mechanical stability.

Table 6: (Continuation) UAM measurements of physicochemical properties of some commercial materials.

Membrane	E98-15S	E87-05S	FAAM-40	AP-40	AM-40	Sample A	Sample B	Sample C
Provider	Solvay	Solvay	Fumatech BWT	Fumatech BWT	Fumatech BWT	Amer-Sil	Amer-Sil	Amer-Sil
Price (€/m²)	2700	2650	1022	1000	1033			
Type (Counter-ion)	CEM (Na^+)	CEM (Na^+)	PBI-membrane (none)	PBI-membrane (none)	PBI-membrane (none)	Separator (none)	Separator (none)	Separator (none)
Thickness (μm)	168.0	62.0	42.0	40.0	46.0	365.0	398.0	385.0
WU (%)	4.4	3.7	6.5	9.6	6.7	76.1	74.3	79.6
SR (%)	<30	<30	<30	<30	<30	<30	<30	<30
IEC (mmol/g)*	831*	2.4	---	---	---	---	---	---
Conductivity (mS/cm)	5.0	6.6	$>10^{-2}$	$>10^{-2}$	$>10^{-2}$	28.8	18.5	16.7
Permeability (cm^2/s) Compound 2	6.15E-8	1.21E-8	8.02E-9	2.83E-13	3.20E-13	4.79E-7	≈10E-7	≈10E-7
Median pore size (μm)	---	---	---	---	---	0.07	0.04	0.05

*Too high values could compromise the mechanical stability.

Note: Red color: out of MUST and HIGREEW requirements. Orange color: properties with the minimum requirements but not the desirable (fulfill MUST requirements). Green color: fulfill with the MUST and HIGREEW requirements.

Based on their conductivity and permeability *vs* Compound **2** active material, the membranes and separators were classified into four groups. Compound **2** was selected as based material to evaluate the crossover due to the simple synthesis and the positively charged core.

- Group 1. Those with good conductivity and low crossover (< 2% in 7 days for the Compound **2**): FAA-3-50, FAA-3-30-PE (AEM) and FS-950 (CEM) fulfill the HIGREEW and/or MUST requirements.
- Group 2. Those with good conductivity and high crossover (> 25% in 7 days for the Compound **2**): FAPQ-330 (AEM), FS-930, E-620(K)PE, E-630K, E98-15S and E87-05S (CEM) are susceptible to be employed as starting materials where different modifications could avoid their high crossover without affecting their electrochemical properties.
- Group 3. consisted of FAAM-40, AM-40 and AP-40 membranes, which were not considered at this moment because of their low conductivity shown (they do not accomplish with the MUST and HIGREEW requirements). Regarding this last group, increase the conductivity of an IEM is a quite complicated task. Incorporating new functional groups into

the polymeric matrix requires complex techniques, so these membranes were discarded.

- Group 4. Amer-Sil separators (Sample A, B and C) were also evaluated. Using the DFT optimized geometries of Compound **2**, the volume was calculated. By comparing the size of hydrated electroactive material and the pore size in Amer-Sil separators (medium pore size 300000 times higher than organic molecule), the high crossover observed in the H-cells could be explained by. Therefore, the separators are not able to avoid the crossover of the electrolytes between the two tanks. In addition, the fragility of these can jeopardize the stability of the battery, although the low price is in their favor. Separators neither fulfill the HIGREEW and MUST requirements in terms of permeability and they were discarded too.

Based on the obtained results, membrane materials were selected bearing in mind the permeability and conductivity bounded values defined in the HIGREEW project and the provider budget. Finally, costs were also considered for the preselection. In case of AEM, FAA-3-50 and FAA-3-PE-30 were the most promising candidates in light of their low permeation to Compound **2** ($1.26 \cdot 10^{-10}$ and $5.41 \cdot 10^{-10}$ cm^2/s) and medium conductivity (1.1 and 0.3 mS/cm). Regarding CEM, E98-15S, E87-05S, FS-950 and E-630(K) showed higher conductivity values (5.0, 6.6, 2.2 and 2.6 mS/cm, respectively) despite having greater permeability values than AEM due to the Donnan effect contribution established between the positive charges of Compound **2** and the negative charges of the CEM. It is worth mentioning that FS-950 showed lower permeability values *vs* Compound **2** in comparison with the rest of the CEM. However, it showed the lowest ion conductivity when compared to the rest of CEM. Concerning the high cost of Aquivion membranes from Solvay (E98-15S and E87-05S), E-630(K) was selected as an alternative candidate. Thereby, two AEM (FAA-3-50 and FAA-3-PE-30) and two CEM (FS-950 and E-630(K)) were preselected as substrates for modifications and for evaluation at flow cell level.

5.3.1. Modification strategies

Crossover is one of the main problems of Redox Flow Batteries. In cases such as all Vanadium RFB where symmetric electrolyte is used, this issue can be mitigated, but it still plays a vital role due to the imbalance in the state of charge between the two electrolytes. This problem can lead to hydrogen/oxygen evolution among other problems, but can be easily solved by rebalancing both tanks, which is why several papers have focused their work on this type of process.[32] Typically, Aqueous Organic RFB used asymmetric electrolytes where the effect of the crossover becomes irreversible. By the cross mixing of redox active materials, the rebalancing is not a solution anymore and the separation of both materials represent a challenging task. So, the capacity of the device may potentially be compromised due to possible self-discharge processes and side reactions. Therefore, membrane modifications can help to achieve the HIGREEW targets

reducing the permeation of the active species persevering the battery performance. In view of obtained results, permeability has been identified as one of the most critical point to be addressed in explored membranes to make them suitable for application of RFB. In this case, two different strategies have been explored:

5.3.1.1 *In situ* polymerization.

This method consists of an *in situ* polymerization on the surface of the membranes to block their channels and pores (Figure 21 and 22). We need to think that all IEM present pores, channels and imperfections that enhance the undesired crossover. It is important to note that the modification process needs to be simple because if successful it should be used to modify all the IEM for the 5kW-stack (around 10 m^2 of IEM). These polymerizations are interesting in terms of scalability and economic viability. Two polymers (polyaniline and polypyrrole) and two different times of polymerization were the focus of the study based on previous experience of the research group in IEM for fuel cells.[33]

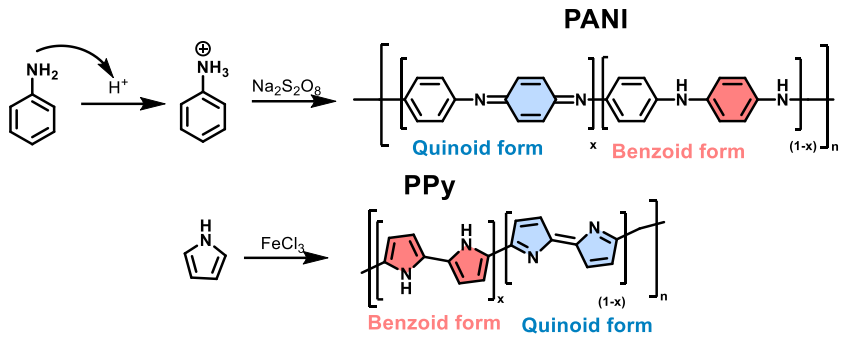

Figure 21: Membrane *in situ* modification reactions and main structures present in the PPy and PANI.

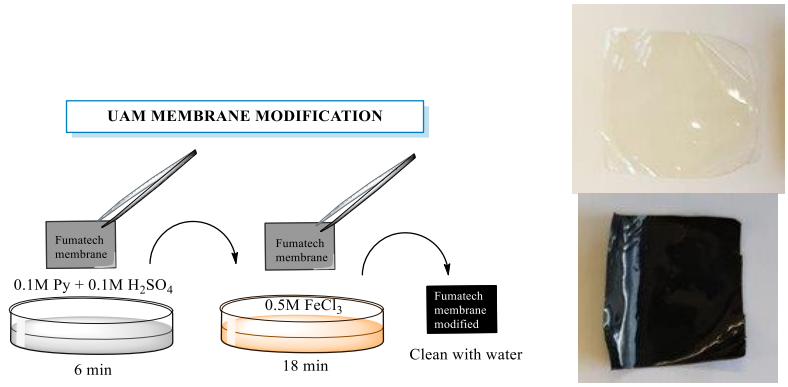

Figure 22: Schematic representation of the modification procedure. () Example of pre- and post-treatment modification of a piece of E-630(K) membrane.

Two monomeric (aniline and pyrrole) were tested at different conditions of polymerization on membranes to reach the best one according to HIGREEW requirements. Short and long polymerization times were tested. The selected membrane for screening was the E98-15S (Solvay) because the high crossover of the pristine material could help to discern between the two materials and the two polymerization times.

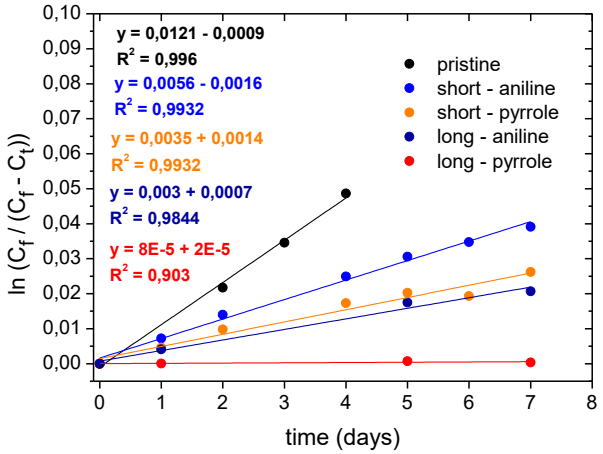

Figure 23: Permeability test using different monomers (aniline and pyrrole) at different polymerization times using compound **2** as active material.

From this study, it was observed that deeper polymerizations decreased the permeability of Compound **2** more than short polymerizations time (see Figure 23). Furthermore, it seems that the polypyrrole is able to block more efficiently the pores, channels and imperfections than the polyaniline in these conditions.

Table 7: Permeability results of the membrane E98-15S with the different treatments.

Membrane	P (cm²/s)	Crossover (%)
E98-15S	1,21E-08	9,6 (4 days)
E98-15S aniline short polymerization	5,58E-09	7,9 (7days)
E98-15S pyrrole short polymerization	3,49E-09	5,5 (7 days)
E98-15S aniline long polymerization	2,99E-09	4,4 (7 days)
E98-15S pyrrole long polymerization	7,98E-11	<1% (7days)

Although the aniline monomer is cheaper than pyrrole, better results and more homogenous membranes were achieved with the polypyrrole modification. As can

be seen in Table 7, deep polymerization of the pyrrole on the membranes provided the best results.

The effect of this optimized polymerization on the permeability of Compound **2** and TEMPOL (used as plausible catholyte for the HIGREEW project) as electrolyte was evaluated in the selected membranes. As detailed in Table 8, it was observed that the modification successfully reduced the permeation of Compound **2** and TEMPOL through the selected membranes.

Table 8: Physicochemical properties of the modified selected membranes.

Membrane		**FAA-3-50-PPy**	**FAA-3-PE-30-PPy**	**FS-950-PPy**	**E-630(K)-PPy**
Type (Counter-ion)		AEM (Cl^-)	AEM (Cl^-)	CEM (Na^+)	CEM (Na^+)
Thickness (µm)		45.0	23.0	52.0	34.0
WU (%)		6.6	0.8	3.2	6.1
SR (%)		<30	<30	<30	<30
IEC (mmol/g)		2.3	2.0	0.4	0.9
Conductivity (mS/cm)		3.8	1.5	5.3	3.5
Permeability (cm^2/s) Compound 2	**Pristine**	1.26E-10	5.41E-10	2.49E-10	3.43E-8
	Modified	3.46E-10	1.39E-10	7.11E-11	1.45E-10
Permeability (cm^2/s) TEMPOL	**Pristine**	1.92E-8	6.88E-9	9.60E-9	1.21E-10
	Modified	6.29E-11	6.18E-11	3.06E-9	9.66E-11

Note: Red color: out of MUST and HIGREEW requirements. Orange color: properties with the minimum requirements but not the desirable. Green color: fulfill with the MUST and HIGREEW requirements.

Before study any change in membrane properties, the first step is to characterize the modified membranes by trying to understand the nature of the new materials. Thus, a quick initial characterization using the FTIR spectroscopy was recorded trying to observe any difference before and after the modification as shown in Figure 24. Note that commercially available membranes are protected materials so, just few information about their composition is depicted in the specifications. The peak intensities around 1460 (–CH_2 δ), 1303 (– CH_3 δ) and 2900 cm^{-1} (C–H st) are found in both AEM suggesting a similar monomer composition (Figure 24b and 24d). The presence of these bands implies hydrocarbon polymeric chains. The absorption band around 3400 cm^{-1} can be assigned to the presence of –NH group and/or the membrane humidity. This peak could correlate with the absorption band around 1188 cm^{-1} (C–N) suggesting that ion fixed groups attached on the polymeric chains could be ammonium-type groups.

Absorption peak that arises at a frequency below 3000 cm^{-1} in FAA-3-50 and more intense, in FAA-3-PE-30 is due to the stretching vibration of the –C–H bond. Such slightly differences are probably caused by distinction of incorporating polyethylene (PE) as a reinforcement in the membrane. Absorption peaks at around 1601 cm^{-1} can be related to –C=C– and/or –C=O groups.

In case of CEM, both membranes FS-950 and E-630(K) showed similar composition to N117 membrane since characteristic peaks at frequencies around 1203-1147, 1078, 624 and 510 cm^{-1} were attributed to CF_2, $–SO_3H$, C–H and C–F groups.[34] These groups merge perfectly with the Nafion polymers (PTFE and the sulfonic groups). As well as the absorption peak around 3400 cm^{-1} which is due to the presence of –OH group. By contrast, the absorption peaks found in E-630(K) below 3000 cm^{-1} and between 1595 and 1470 cm^{-1} revealed that E-630(K) membrane is not fully fluorinated polymer membrane as is the case of FS-950 (Nafion-like). According to FTIR spectra all the characteristic peaks are present in the membrane, revealing the presence of sulfonic-type functional groups in CEM.

The infrared absorption spectra of the modified membranes show noticeable differences compared to pristine membranes at regions around 1700 – 1520 cm^{-1} and 990 – 890 cm^{-1} (highlighted in squares). Besides, in case of FAA-3-PE-30 overlapped bands around 2950 – 2840 cm^{-1} and 740 – 640 cm^{-1} were observed after the membrane modification. There is a strong relationship between the oxidation degree and the observed vibrational modes with the properties of the semiconductor polymer and therefore the membrane properties.

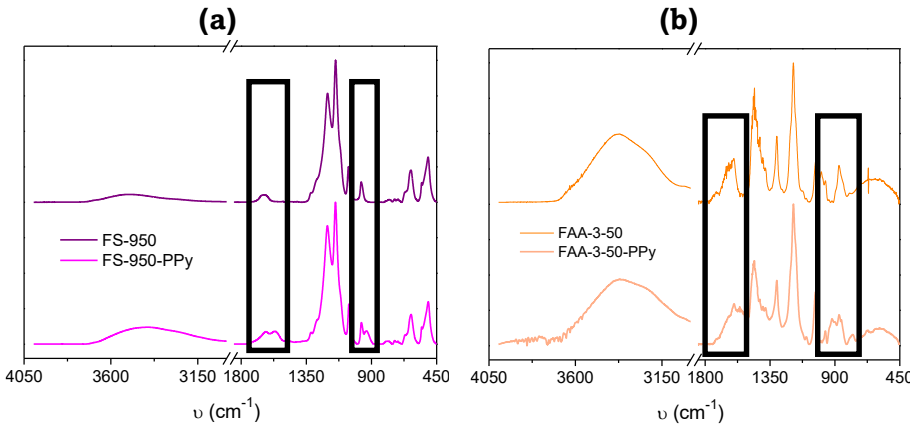

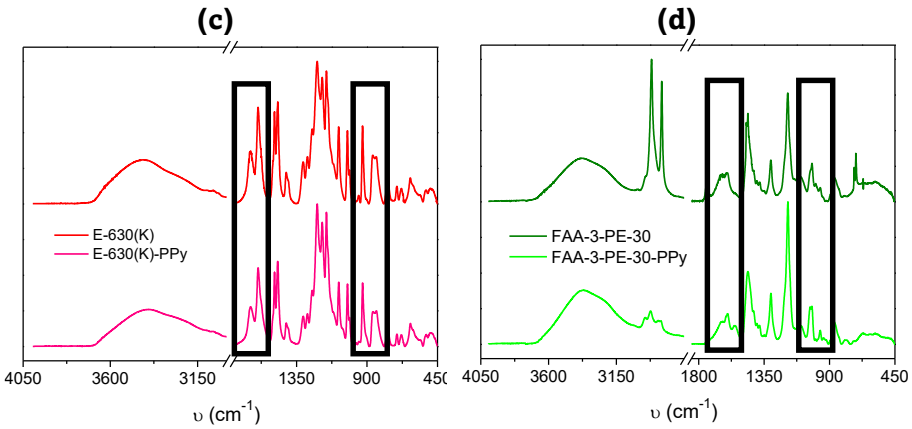

Figure 24: FTIR spectra before and after the PPy modification of CEM (a) FS950 and (c) E-630(K) and AEM (b) FAA-3-50 and (d) FAA-3-PE-30 .

After that, trying to understand how deep the modification was and where is present the polypyrrole we thought that SEM/EDX could show us the distribution of polypyrrole along the initial structure of IEM. The surface morphology of the membranes is rather important since modifying their microstructure will determine the transport of the ions as well as the membrane properties.[35,36] The micro-phase morphology (both surface and cross-section) of representative membranes was characterized by scanning electron microscopy (SEM). As it is shown in the Figure 25 the modification changed from a smooth surface to a rough surface without increasing the membrane thickness.

The elemental composition of the modified membranes was investigated by energy-dispersive X-ray spectroscopy (EDX). Qualitative analysis results show: i) nitrogen as indicator of the presence of polypyrrole molecules especially for CEM (AEM usually present ammonium groups) and ii) occluded iron as initiator of the pyrrole polymerization are present throughout all membranes including the surface and inside the membranes as shown in Figure 25. This is confirmed by the relative quantitative intensity profiles (see Table 9). The nature of the IEM affects the composition found since a different chemical environment is found when performing the modification. This fact may explain the differences found (i) membrane color appearance, being the CEM the opaquest; and (ii) iron contents between CEM and AEM, being the last one which shows the lowest content. The higher attractive electrostatic force existing between the anionic groups in CEM membranes and Fe^{3+} supports the results. It is worth mentioning that all the membranes were soaked in supporting electrolyte for 24 h to enhance the desorption of iron atoms form the modified membrane. After that, no significant desorption of iron was observed.

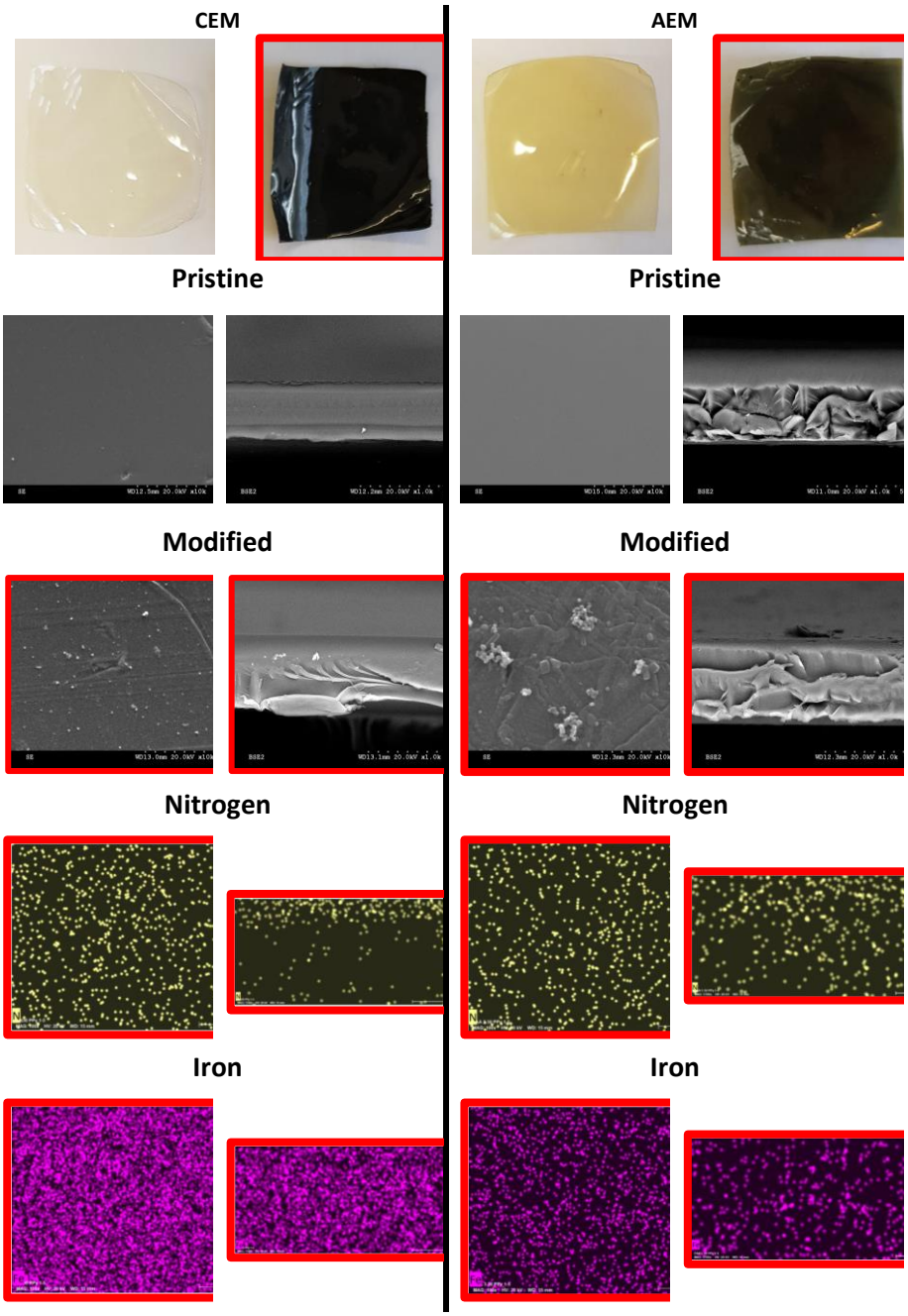

Figure 25: Membrane morphology of representative membranes. CEM: E-630(K) (left) *vs* E-630(K)-PPy (right). AEM: FAA-3-50 (left) *vs* FAA-3-50-PPy (right). SEM/EDX mapping of nitrogen and iron.

Table 9: Surface EDX analysis of the modified membranes.

Samples	Membrane type	Iron content (%)	Nitrogen content (%)
FS-950-PPy	CEM	5.30%	10.34%
E-630(K)-PPy	CEM	3.46%	2.24%
FAA-3-50-PPy	AEM	0.16%	1.91%
FAA-3-PE-30-PPy	AEM	1.27%	5.08%

The next step is study how the modification has altered the properties of IEM. The differences found in physicochemical properties between pristine and modified membranes are listed in Table 10. Usually, membranes absorb water depending on the hydrophilicity of the ionic fixed groups attached in the polymeric chains and the nature of backbone polymer. On one hand, larger amounts of water uptake would compromise the mechanical properties of the membrane materials.[37,38] On the other hand, lower values of WU would increase the resistivity of the material decreasing the energy density of the battery device.

Table 10: Physicochemical properties of pristine and modified membranes.

Samples	Thickness (μm)	WU (%)	Contact angle (°)	Ion conductivity [c] (mS cm^{-1})	IEC (mmol g^{-1})
FS-950	52.0	15.8	84.8 ± 2.0	2.2	1.5
FS-950-PPy		3.2	93.4 ± 1.0	5.3	0.4
E-630(K)	34.0	19.6	70.2 ± 2.0	2.6	1.1
E-630(K)-PPy		6.1	81.4 ± 2.2	3.5	0.9
FAA-3-50	45.0	15.6	85.3 ± 3.9	1.1	1.9
FAA-3-50-PPy		6.6	96.5 ± 0.9	3.8	2.3
FAA-3-PE-30	23.0	17.1	70.0 ± 2.8[a] / 81.0 ± 2.2[b]	0.3	1.1
FAA-3-PE-30-PPy		0.8	80.1 ± 2.0[a] / 80.4 ± 2.7[b]	1.5	2.0

[a] Face area non-containing PE as a reinforcement.

[b] Face area containing PE as a reinforcement.

[c] Conductivity measurements were performed in a two-chambers cell set-up under flowing wetted air at 30 °C.

All pristine commercial membranes presented suitable values of water uptake for battery operation (15.6–19.6%). By contrast, after the modification however, it decreases significantly, as expected. The introduction of a new hydrophobic polymer, PPy, decrease the hydrophilicity of the new material. This fact can be corroborated by analyzing the contact measurements, these are included in Table 10. The contact angle is modeled according to Young's equation (Equation (1)) where θ is the contact angle, γ_{SV} , γ_{SL} and γ_{LV} are the solid, solid-liquid and liquid surface free energies, respectively. Higher values of contact angles represent more hydrophobic surfaces. So, the presence of PPy in the membrane's surface increased the contact angle by approximately 10° in all cases (Figure 26).

Therefore, the surface of the pristine membranes became more hydrophobic after modification, impeding water diffusion inside the membrane due to the presence of hydrophobic PPy. It is worth mentioning that FAA-3-PE-30 possess two different faces, one non-containing a PE reinforcement and the opposite containing the PE. When analyzing both faces, the hydrophilicity of the membrane area without reinforcement significantly reduced, whereas in the other side containing the PE, it remained unaltered, perhaps due to high hydrophobicity of the PE or poor interaction between the PE and PPy.

$$\gamma^{SV} = \gamma^{SL} + \gamma^{LV}\cos(\theta) \quad (4)$$

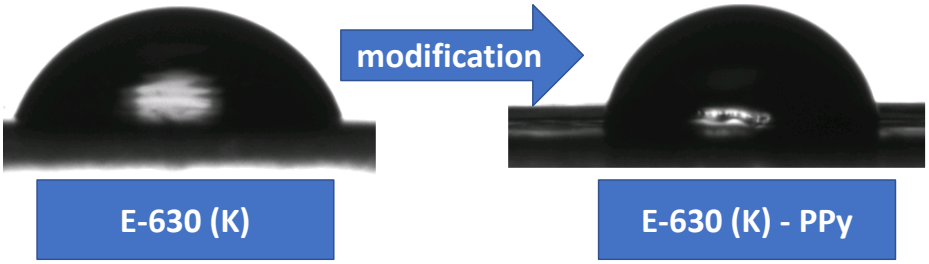

Figure 26: Increase in the contact angle after the membrane modification.

Ion conductivity is one of the fundamental parameters of this kind of materials since directly affects the energy density of RFB. Different cations or anions can be exchanged depending on the nature of the membrane. The different mobility of ions will affect the conductivity of the material. In this work, both CEM, FS-950 and E-630(K), exchange sodium ions and σ_{Na^+} has been calculated 2.2 mS/cm and 2.6 mS/cm, respectively. However, when analyzing AEM a lower chloride conductivity σ_{Cl^-} was found in FAA-3-PE-30 (0.3 mS/cm) when compared with FAA-3-50 (1.1 mS/cm). This result could be ascribed to the presence of the PE reinforcement. Reinforcement plays an important role when considering ion conductivity of the membrane materials since implies the increasing of non-conducting regions in the polymeric matrix, although on the other hand it improves the mechanical properties.

As described earlier, introducing a new polymeric material to the IEM results in a decrease in its hydrophilicity. One might assume that this would also lead to a decrease in ion conductivity. However, after the modification was made, all membranes showed an increase in conductivity, from 0.3-2.6 to 1.5-5.3 mS cm^{-1}. This increase was attributed to the formation of different structural PPy molecules within the ion exchange membrane, which was confirmed by infrared and diffuse reflectance analyses. Polypyrrole has been shown to exhibit significant ion conductivity in its oxidized state, with higher degrees of oxidation resulting in higher conductivity levels.[39] The defects in the π-electron system, such as polarons

and bipolarons (Figure 27), act as positive charge centers that facilitate the conduction of mobile counter-ions in the polymer. Therefore, using PPy as an ionomer in our membranes offers a double benefit by reducing the permeation of active species while increasing ion conductivity. Furthermore, during the modification, some iron ions got occluded that can contribute to increase the ionic conductivity in the modified membranes.

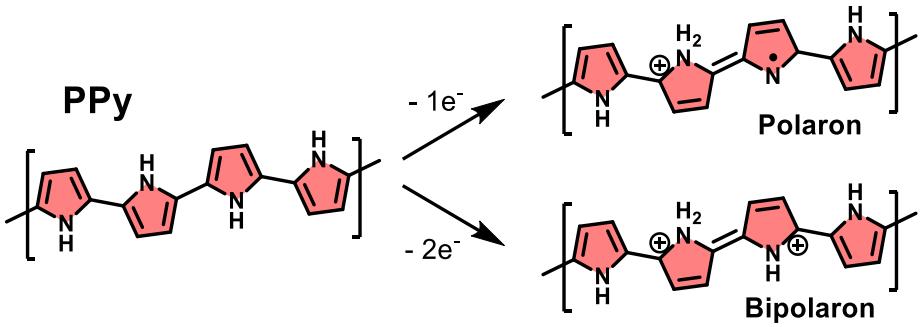

Figure 27: Oxidated states (polaron and bipolaron) of the PPy.

However, this measurement was performed in a static cell without continuous flow of electrolyte. When comparing the conductivity obtained from the two-chamber and flow battery devices, pristine membranes showed a significant increase, from 0.54 to 4.39 mS cm^{-1}, respectively. In contrast, the conductivity increase in modified membranes was only 1.6 times, from 0.85 to 1.33 mS cm^{-1}, respectively. Both membranes increased their conductivity due to the greater supply of the electrolyte solution through their microstructure. However, the modified membranes had lower conductivity because their pores and cavities were partially filled with PPy. Therefore, the incorporation of PPy as an ionomer in modified membranes has a different contribution depending on the cell conditions. However, the proposed modification allows us to reduce the cross-mixing of organic redox-active species (see Table 8), which could lead to significant losses of capacity and reduced performance in battery systems during prolonged periods of operation.

PPy could act as a semiconductor, in this sense to corroborate the insulating behavior of the modified membranes, a pristine and modified membranes (FS-950 *vs* FS-950-PPy e.g.) were dried at 60 °C during 24 h and the electronic conductivity measured at these conditions was $1.6 \cdot 10^{-4}$ and $1.7 \cdot 10^{-4}$ mS cm^{-1}, respectively. This values can only belong to the electronic contribution ensuring that modification does not enhance it.

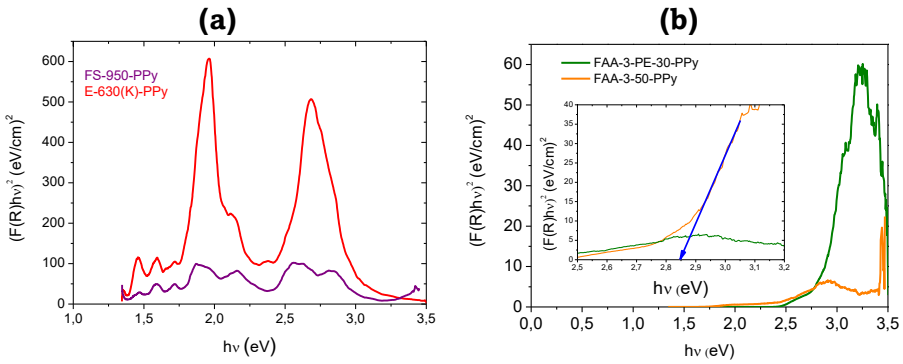

Figure 28: DR spectra of modified membranes CEM (a) and AEM (b), detail of GAP calculation for FAA-3-PE-30-PPy membrane is provided in the insert).

The ion-exchange capacity (IEC) represents the amount of ion fixed groups that possess the material, which determine the conductivity and therefore with the transport properties of the material. The highest values of IEC were obtained with the thickest membranes both anionic (FAA-3-50 with 1.9 mmol g^{-1}) and cationic (FS-950 with 1.5 mmol g^{-1}) whereas the thinnest ones both with 1.1 mmol g^{-1} in FAA-3-PE-30 and E-630(K). All these materials are chemically different and transport properties as well as their microstructural phase may be different one from each other. Nevertheless, it is worth mentioning that anion exchange membranes with highly values of IEC usually become unstable depending on the pH media. AEM typically present ammonium group as active group, these groups on basic media con suffer different degradation (Hoffman elimination, α-elimination…).[40,41] In this work, the values of IEC obtained were quite good for the battery purposes working at neutral pH. However, when performing the modification two different behaviors were obtain depending on the type of ion exchange membrane. In CEM the IEC values decreased (FS-950-PPy and E-630(K)-PPy down to 0.4 and 0.9 mmol g^{-1}, respectively) whereas in AEM the IEC values were increased (FAA-3-50-PPy and FAA-3-PE-30-PPy up to 2.3 and 2.0 mmol g^{-1}, respectively). In this sense, negatively charged membranes (CEM) may interact with oxidized PPy molecules decreasing the IEC by electrostatic interaction generating a kind of bipolar membrane because PPy contains positive charged structures. On the other hand, positively charged membranes (AEM) the increasing of IEC could be related to the incorporation of more positive charges along the polymeric matrix in form of polypyrrole (polaron and bipolarons). It is worth mentioning that the iron retained in the membranes may influence since can interact electrostatically as well. This fact could be explained by Diffuse Reflectance (DR) since show the relationship between different oxidized PPy species.

Using the FTIR spectroscopy, different oxidation degree can be detected, and they can be explained by the polaron – bipolaron model structures, widely used to explain the properties of conducting polymers.[42] These PPy oxidized species present excess holes and therefore, creates a p-type semiconductor. They are

produced by oxidation with $FeCl_3$. The assignment of the vibrational bands of polarons and bipolarons[43,44] is well known and arises around 1620 cm^{-1} (quinoid fragment) whereas the reduced form of PPy arises around 1560 cm^{-1} (benzoid fragment). Both bands correspond to $\nu_{c=c}$ assignment. Additionally, bands around 925 cm^{-1} (quinoid fragment) and 990 cm^{-1} (benzoid fragment) correspond to ν_{c-H} assignment and are well observed in Figure 24. By integration of these band areas and comparing their relationship, it is possible to determine the oxidation degree of the corresponding modified membranes (see Table 11). These values were calculated by the deconvolution of the bands (quinoid and benzoid fragments) between the modified and pristine membrane spectra. FS-950-PPy and FAA-3-PE-30-PPy showed high level of oxidation being the FAA-3-PE-30-PPy the most oxidized (≈72% of oxidation) whereas in case of FAA-3-50-PPy was the lowest (≈37%). In case of E-630(K)-PPy was not possible to estimate due to overlapping of bands. However, higher oxidation degree does not necessarily imply larger amount of positive charges of PPy, since they evolve towards the formation of neutral double bonds and therefore, lose their electronic properties.[45]

Table 11: Estimated values obtained from FTIR (degree of oxidation) and DR (absorption maximum and band gap energies) spectra of the modified membranes.

Samples	Membrane type	Estimated oxidation degree (%)	Absorption max. energies (eV)	Estimated band gap (eV)
FS-950-PPy	CEM	60%	1.8 and 2.5	1.75 and 2.40
E-630(K)-PPy	CEM	--	2.0 and 2.7	1.75 and 2.50
FAA-3-50-PPy	AEM	37%	2.1 and 2.9	1.75 and 2.35
FAA-3-PE-30-PPy	AEM	72%	2.8 and 3.2	2.45 and 2.85

Diffuse reflectance (DR) allows to determine the neutral – polaron – bipolaron transitions in the modified membranes as shown in Table 11 and Figure 28. The different band gap energies from DR show the coexistence of the vibrational bands associated to quinoid and benzoid fragments. According to literature,[12] high band gap transitions (above 3.2 eV) indicate lower oxidation degree whereas lower values (below 1.5 eV) point to elevated oxidation degree. As a general conclusion, no electronic conductor properties would be expected in any modified membrane based on the high electronic transitions observed. In fact, electronic transitions below 1 eV are typical in a good semiconductor material.

Further investigation about the transport phenomena of these new modified materials using the two-phase model which consider IEM as an heterophase system (gel and interstitial phases) was developed by our research group. So, the effect of the modification from the microstructural point of view was studied.

5.3.1.2 Interfacial polymerization (layer-by-layer LbL).

Trying to find an alternative modification and based on the ionic charge of IEM, Layer-by-Layer (LbL) polymerization emerges as a plausible option. The LbL deposition is a convenient and efficient surface modification routine for charged polymeric matrix (like IEM). By dipping the charged matrix alternatingly with positively charged polymer (polyethyleneimine (PEI)), and negatively charged polymer (Nafion). Then, a bilayer structure is built up on the substrate (Figure 29), which could avoid the cross mixing of the active species like the PPy attached to the IEM. Wittstock *et al*[46] describe a modified Nafion membrane with different number of bilayers. The modified membranes present a greater values of proton conductivity *vs* vanadium permeation $\frac{\sigma_{H^+}}{P_{V^{2+}}}$. Seeing the promising results, membrane E97-05S membrane was selected to evaluate this strategy for neutral organic RFB incorporating 5, 10 and 20 bilayers of PEI and Nafion. Initially, modified membranes presented higher values of conductivity (10-20% higher) and the modification was characterized by the appearance of the characteristic IR signals of the different deposited layer of polymers. E87-05S is a Nafion type membrane, so is partially/fully fluorinated, so, it shows absorption peaks related with the C-F bond (ν_a C-F ~1200 cm^{-1}, ν_s C-F ~1150 cm^{-1}), C-O-C ($\nu_{a/s}$ C-O-C ~985-970 cm^{-1}) and S-O bond) ν_s S-O ~1060 cm^{-1}). The modified membrane present signals typical from C-H bond signals (ν_a C-H ~2930 cm^{-1}, ν_s C-H ~2815 cm^{-1}, δ C-H ~1469 cm^{-1}) and N-H bond (δ C-H ~1585 cm^{-1}) meaning that the PEI polymer has been adhered to the membrane surface. The Nafion membrane is not visible since the pristine membrane present Nafion monomers in their own structure. Despite it could be an interesting approach, the low compatibility showed between the membrane and the redox active material (evidence of Compound **2** decomposition when the crossover was analysed) as well as the detachment of the bilayers in aqueous solution led us to discard this methodology after making different approaches. Wittstock *et al*[46] also observed some kind of detachment/interaction between the modified membranes and the vanadium electrolyte. Layer-by-Layer modification represent an appealing strategy to modify IEM since the conductivity is not decreased and the permeability of RAM can be reduced. At this point it has not been implemented because the poor stability of the bilayers attached to the membrane. Long terms experiments need to be investigated to corroborate the feasibility of this strategy.

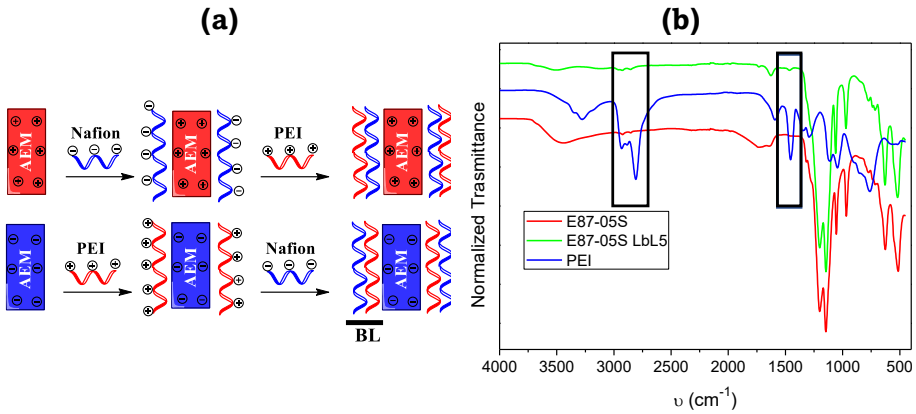

Figure 29: (a) Schematic representation of the Layer-by-Layer deposition method. Main polymers. (b) modification in the FTIR spectra of the studied membrane.

In this **Chapter 2**, a strong background of commercially available membranes has been acquired dividing a set of membranes in four groups based on their electrochemical response. Trying to improve their performance two modification strategies have been studied *in situ* polymerization (aniline and pyrrole) and Layer-by-Layer. The first strategy using pyrrole as the precursor lead to better results in terms of permeability. So, the permeability of Compound **2** and TEMPOL has been significantly reduced. PPy based modified membranes have been studied trying to understand how the incorporation of a new material affect intp the ionic conductivity, hydrophilicity of the new material, electrical conductivity and into the membrane ion transport properties. Despite the efforts employed in this method HIGREEW consortium decided to discard these modified membranes because of the increase in the resistance of the system using the modified membranes. The second strategy was not useful due to the poor compatibility of the modified membranes with the organic electrolytes as well as the complex and tedious modification process. All in all, since HIGREEW project is required to develop a 5 kW stack the use of modified membranes was discarded as a consequence of the immature research field of modified membranes for long term experiments.

Chapter 3: Single-cell results

In the previous chapter of this PhD, different organic electrolytes have been synthetized and electrochemically characterized and several Ion Exchange Membranes have been characterized and modified. Now we moved to check the performance of these materials in single-cell showing their applicability in an actual redox flow battery.

5.4. Main characterization techniques and components effects in single-cell using AQDS and $Na_4[Fe(CN)_6]$.

Along this thesis, different parameters of RFB have been depicted and explained but the reality is that batteries are a multi-component and multivariant system where each component or parameter can play a role. Few examples in the literature have tried to explain the basic concepts. The first examples where the basic concepts of RFB where described appeared in 2019:

1) Anders Bentien *et al* developed an educational paper where the basic concepts of the battery were depicted. In this paper, a laboratory practice was developed using the anthraquinone (AQDS) and bromine chemistry. This contribution is not talking about "flow batteries" but could be as the first example where efforts were put through explain the basic concepts of batteries. This example could serve as an initial step where the charging and discharging cycles as well as the coulombic, voltage and energy efficiencies are described.[47]

2) Latter in 2021, Maria Skyllas Kazacos *et al* developed a paper where the tools employed in the Vanadium RFB were introduced. This work is a more complex explanation of the fundamentals (battery components, redox reactions, efficiencies description) but describes the influence of the resistance, the use of different current densities in the RFB performance. More important are the description of polarization curves and the electrochemical impedance spectroscopy where the influence of each resistance is described.[48] Furthermore, other experimental issues as the use of flow fields, reference electrodes, pressure drop, the state of charge monitoring method and their influence in the battery performance were successfully described. This marvelous work let understand RFB from the bottom (basic concepts) to the top (the role of each component and the experimental techniques used). So, other works where the experimental protocols for non-aqueous systems[49] and studies such the electrolyte degradation or the crossover were highlighted.[2]

The first part of this chapter is focused on study the influence of different experimental parameters such as: the electrolytes pH, the O_2 presence, the membrane pretreatment and the capacity limiting side, showing the meaning of relevant electrochemical techniques (load curve measurements, electrochemical impedance spectroscopy and charge-discharge cycling tests). In this sense, using a very well-known redox active materials (AQDS as anolyte and $Na_4[Fe(CN)_6]$ as catholyte), membrane (Nafion 212®), carbon felts (SGL 4.6 EA) the single-cell tests were set up being sure about the starting point.

The redox activity and reversibility of the redox active materials must be corroborated by Cyclic Voltammetry (CV) technique is very suitable for such a study (Figure 30, see *Experimental and theoretical procedures* for more information regarding the basic concepts or the experimental set up). It seems clear that both electrolytes are active and reversible based on the criteria of reversibility. Anthraquinone derivatives suffer a Proton Coupled Electron Transfer (PCET), so the concentration of protons in the electrolyte will play a vital role. In this case the redox reactions involved in the battery are as follows (Figure 31):

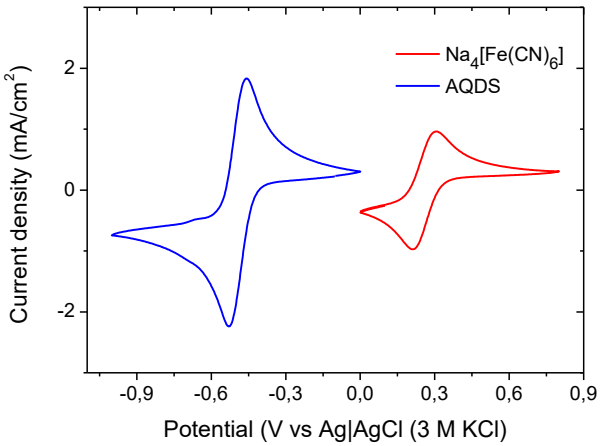

Figure 30: Cyclic voltagramms of 10 mM od AQDS in 1 M NaCl

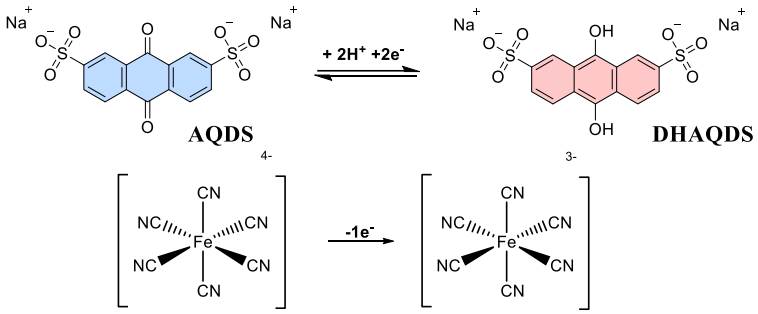

Figure 31: Electrochemical reaction of AQDS and ferrocyanide in the RFB.

The Nernst equation for the AQDS system is given by (Equation 5):

$$E = E^{o} - \frac{RT}{nF}\ln\frac{[AQDS]\cdot[H^{+}]^{2}}{[DHAQDS]} \qquad (5)$$

The redox potential where AQDS will be reduced to $AQDSH_2$ will be affected by the protons concentration in the electrolyte, so, the CV must be studied at different pH (Figure S35 in *Annex A*) in order to plot the Pourbaix diagram which provide information about the redox mechanism (Figure 32). This is the first problem that

can be faced if the electrolyte is unbuffered. When the redox reaction takes place consuming protons, the pH in the vicinity of the electrode will change deviating the results. For this reason, the use of buffered electrolytes will be important.

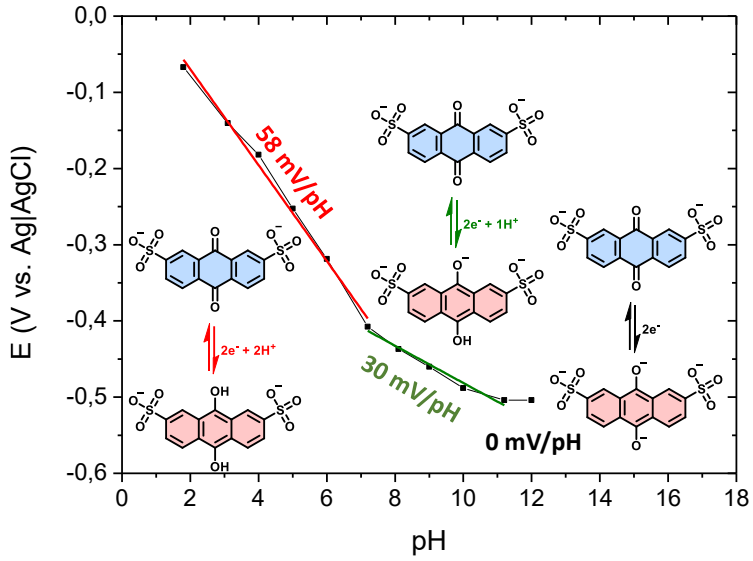

Figure 32: Pourbaix diagram of the AQDS. Reaction mechanism at different pH.

From the Pourbaix diagram (Figure 32), three zones can be identified clearly, i) pH below 7 (red line) with slope around 58 mV/unit pH suggesting that the number of electrons and protons consumed in the redox reaction are equal. That means that the reduced hydroquinone is completely protonated, ii) from pH 7 to 11 (green line) the slope is around 29 mV/unit pH meaning that the double of electrons than protons are consumed in the redox reaction, which means that one of the OH from the reduced hydroquinone is deprotonated, iii) finally, at pH above 11 (black line) the hydroquinone afforded after the redox reaction is completely deprotonated, so any protons are consumed in the redox reaction making the redox potential independent of the pH of the electrolyte.

Once the redox reactions have been studied, we check the kinetic constants and the diffusion coefficients of each derivative using the hydrodynamic electrochemical techniques (Figure 33). We used a Rotatory Disk Electrode (RDE) as a working electrode to diffuse constantly redox active material through the electrode surface (information in the *Experimental and theoretical procedures*). The diffusion coefficients were determined by Levich equation and they are $3.99 \cdot 10^{-6}$ and $4.38 \cdot 10^{-6}$ cm^2/s for AQDS and $Na_4[Fe(CN)_6]$, respectively. Using the Koutecky-Levich plot and the Tafel plot the kinetic constant for both redox active materials have been determined by extrapolated to infinite rates; $9.96 \cdot 10^{-3}$ and $7.99 \cdot 10^{-3}$ cm/s was obtained for AQDS and $Na_4[Fe(CN)_6]$, respectively.[50] (RDE analysis can be found in *Annex A*). From these studies we can corroborate that both RAM present

suitable kinetics otherwise, the redox flow battery will show an increase resistance to mass transport and electrode activation.

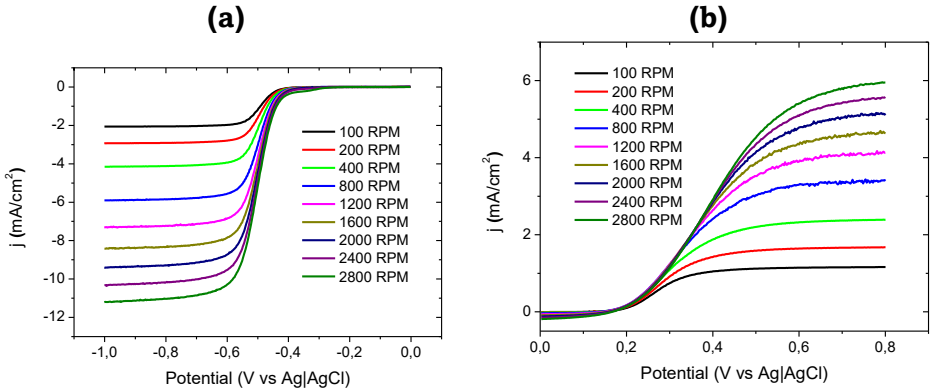

Figure 33: RDE experiments for (a) AQDS and (b) $Na_4[Fe(CN)_6]$.

Another important characteristic is the solubility of the RAM, even if a RAM shows really good reversibility and kinetics without a good solubility their applicability in redox flow batteries will be compromised. Solubility determines the theoretical volumetric charge capacity of the electrolyte as given in Equation 6. It indicates the amount of charge that can be stored in a certain volume of electrolyte. UV-Vis calibration curves can be found in *Annex A*. It depends on the number of electrons, *n*, that participate in the redox process, the active material molecular mass *M* and mass *m*, Faraday's constant *F* and the tank volume *V*. The most used unit to express the volumetric capacity is Ah/L. The volumetric energy density includes the voltage displayed (*U* at open circuit potential) between the utilized couples and the volumetric capacity (*Q*), thus is measured in Wh/L (Equation 7).

$$Q = \frac{m \cdot n \cdot \mathrm{F}}{M \cdot V} \tag{6}$$

$$\mathrm{E} = \mathrm{Q} \cdot \mathrm{U} \tag{7}$$

The solubility of the sodium ferrocyanide and the sodium AQDS is around 0.5 M in neutral pH, which could lead to maximum volumetric capacities of 26.8 Ah/L for AQDS.[19]

This first characterization of the redox materials has given enough information to elucidate the conditions where the battery should work as initial step. After that, using commercial and well described components (i.e., ion-exchange membranes and carbon felts) the RFB can be set up (see the Supporting Information). Now, by showing different RFB testing cases, we will research about the dependence of RFB polarization on the pH of the electrolytes, anolyte chemical degradation due to O_2 permeation, membrane pretreatment effects on the battery's performance

and capacity-limiting side effects. Additional information about the battery cycling results can be found in *Annex A*.

5.4.1. Effect of pH

The pH of the electrolyte's solutions is a determinant parameter. In these cases, the pH changes caused by the reaction, can modify the mechanism of the redox reactions, and therefore the cell potential (see Figure 32) and ultimate the whole performance of the battery.[51] The same battery was tested under different initial pH: pH 4, 7 and 10. The capacity comparison over 100 cycles will be discussed below. Here we demonstrate how the difference in the pH supporting electrolyte can influence fundamental battery parameters such as the cell voltage, the stability of the redox active materials and the resistance of the cell.

The ASR of the cell has been determined showing up changes because the different ionic conductivity of the supporting electrolytes. The resistances were determined from EIS and load curve (LC) measurements at different SOC and the results are summarized in Table 12 and Figure 34. The linear current sweep was selected because the measurement is shorter and the influence of O_2 can be minimized (the measurements have been performed outside of the glovebox so longer experiments leads to bigger effect of the oxygen in that case). So, from the linear part of the LC, the resistance R_{charge}, $R_{discharge}$ including ohmic, charge transfer and mass transport polarization of both electrodes can be determined (Figure 34).

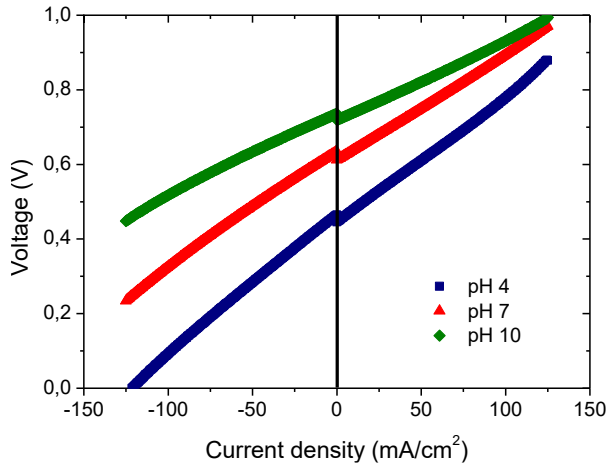

Figure 34: Load curves measured at 50% SOC at different pH. 0.08 M AQDS in 1 M buffer solution *vs* 0.2 M $Na_4[Fe(CN)_6]$ in 1 M buffer solution, using pretreated Nafion 212® membrane. Scan rate: 1 mA/cm^2·s

From LC, small deviation from linearity and differences between R_{charge} and $R_{discharge}$ probably due to the changes in the SOC of the electrolyte can be seen. In agreement with the achieved resistances, we can conclude that at 50% SOC (Table 12); the system undergoes an activation upon the charging decreasing the ohmic

ASR when compared to 0% SOC. Also, in all cases the R_{charge} is always higher than the $R_{discharge}$. The resistance of the cell is intrinsically linked to the ionic conductivity of the electrolytes (Table 12). When carbonate buffer is used for electrolytes at pH 10, the ionic conductivity is the highest and the cell resistance is the lowest (Green colour). But in the case of acetate buffer at pH 4 the ionic conductivities of both electrolytes are very low, so the cell resistance increases. Comparing the contribution of the ohmic resistance at 50% SOC with the resistance of the discharging process on each pH studied we can conclude that higher ionic conductivity of the electrolytes leads to lower contribution of the membrane to the total cell resistance. Note that the charge transfer resistance and the mass transport resistance could also change with the different composition of the electrolytes.

Table 12: Open cell voltage, resistance at different SOC, ion conductivity of the different electrolytes, energy efficiencies and capacity decay at different pH.

Parameter	Unit	pH 4		pH 7		pH 10	
U_{cell}	V	0.455		0.624		0.728	
R_{ohm} (0% SOC)	Ohm·cm^2	1.91		1.87		1.58	
R_{ohm} (50% SOC)	Ohm·cm^2	1.93		1.85		1.54	
R_{disch} (50% SOC)	Ohm·cm^2	3.83		3.21		2.30	
R_{charge} (50% SOC)	Ohm·cm^2	3.51		2.87		2.19	
R_{ohm} (50% Soc)/R_{disch}	-	50.4		57.6		67.0	
Ionic conductivity	mS/cm	21.2 (A)	41,9 (C)	21.2 (A)	54.7 (C)	41.9 (A)	54.7 (C)
Energy efficiencies	%	12.2		34.1		53.4	
Capacity decay	%Q_{theo}/ h	-0.21		-0.10		-0.38	

Note: (A) is for the ionic conductivity of the anolyte and (C) for the catholyte. The coulombic, voltage, energy efficiencies and the capacity evolution in 100 cycles at 100 mA/cm^2 for each battery can be found in *Annex A* (Figure S39-41 and Table S1).

Regarding the U_{cell}, it corresponds to the values measured at the OCV at 50% SOC. The redox potential of AQDS decreases at higher pH values (Figure 32) and consequently, the battery OCV increases. Higher pH values of the electrolytes establish a higher OCV which can be observed in LC at 0 mA/cm^2 (black line, Figure 34). In terms of voltage and energy efficiencies, the battery showing the highest cell ASR is the one using electrolyte at pH 4 (lowest ionic conductivity) and therefore it provides the lowest efficiencies. On the other hand, the battery at pH 10 present the highest ionic conductivity and consequently the highest voltage and energy efficiencies. The stability of the redox active materials is truly affected by the environment of the electrolyte. An analysis of capacity fade during the long cycling shows clear differences between the three studied pH. The battery at pH

10 shows the highest capacity decay per hour and could be because of the low stability of the ferrocyanide in basic media.[55] The battery at pH 7 is the most long-stable, the redox active materials are more stable in less aggressive solutions showing a notably low-capacity decay.

The role of the supporting electrolyte and the comparison of the different resistances contributing to the resistance of the whole system have been analyzed. Furthermore, the stability of the RAM and the effect in the battery performance have been showed being the neutral pH the most stable media, although the basic media which present the highest conductivity also present the lowest resistance.

5.4.2. Effect of oxygen

Almost all published work on aqueous organic redox flow batteries have been evaluated inside a glovebox due to the detrimental influence of oxygen on battery efficiency and stability, as it imbalances the SOC of battery´s electrolytes and lowers CE. The solubility of O_2 at room temperature in water is approximately 0.25 mM. Thus, the charge imbalance of the system exposed to O_2 depends on how much O_2 dissolves in the system, the liquid-gas contact area, the concentration of electroactive species their reactivity with oxygen and the duration of the experiment.[56]

Herein we present three identical redox flow batteries (0.1 M AQDS in 1 M NaCl *vs* 0.1 M $Na_4[Fe(CN)_6]$ in 1 M NaCl, with pretreated Nafion 212® membrane, 40 mL/min electrolytes flow rate and operated at room temperature) exposed to different amounts of oxygen in atmosphere to evaluate its influence on RFB: the first RFB cell and electrolytes has not been purged by nitrogen, the second one has been purged and introduced in an home-made nitrogen-filled box ([O_2] <2% fraction molar) and the third one which has been operated in a commercial nitrogen filled glovebox ([O_2]<1ppm).

Firstly, the three systems should present similar initial resistance, (0.99-1.02 Ohm·cm^2), they have been charged-discharged at 20 mA/cm^2 up to the same cut-offs (1.1-0 V) during 5 cycles, The single-cell exposed to atmospheric O_2 concentration shows a clear disbalance between both electrolytes. This fact is supported by looking at Figure 35, black columns. Once the battery is fully charged (first filled black column, 63.0 mAh, 94% SOC), it reacts with the oxygen present in the electrolyte solution discharging the anolyte (first dashed black column, 39.0 mAh, 58.2% SOC), while the catholyte is fully charged. When the next discharging process starts, the capacity of the anolyte is lower than the catholyte, and then the capacity of the battery is limited by the amount of the reduced anolyte. So, if the single-cell is exposed to constant O_2 concentrations, O_2 permeates into the solution and continuously discharge the battery. When the battery is exposed to smaller amounts of O_2, such as in the home-made glovebox system (blue columns), the O_2 has big influence on the first cycle but when the O_2 present in the solution is consumed the effect is almost negligible because permeation is practically

suppressed. Finally, if we look at the results achieved when the battery is placed in an atmosphere without O_2 (commercial glovebox), the disbalance is negligible and no significant differences between charge and discharge process even in the first cycle were observed (green columns).

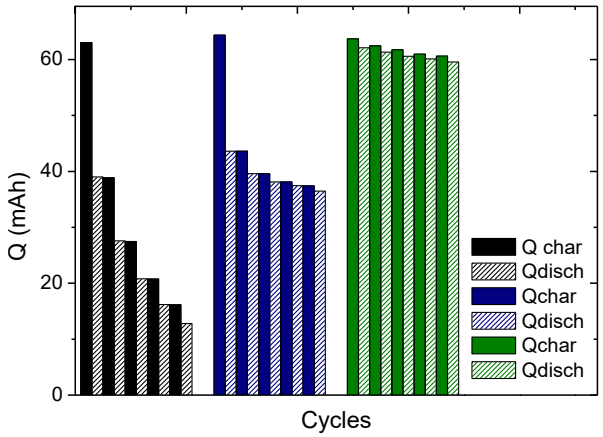

Figure 35: Comparison of the 5 first cycles at 20 mA/cm^2 for battery expose to different concentration of O_2. Black colour, single-cell exposes to atmospheric concentration of oxygen, blue colour, single-cell inside a home-made glovebox concentration <2% of O_2 and green colour, single-cell cycle inside a glovebox (<1% O_2). Filled columns and dashed column represent charge and dis-charge capacity, respectively. 0.1 M AQDS in 1 M NaCl *vs* 0.1 M $Na_4[Fe(CN)_6]$ in 1 M NaCl, using pretreated Nafion 212® membrane. The coulombic, voltage, energy efficiencies and the capacity evolution for each battery at different current densities can be found in *Annex A* (Table S2).

The detrimental effect of O_2 content on RFB performance has been demonstrated. The active species in anolyte is reduced during the charging, and this reduced form, if sensitive to oxygen, reacts with oxygen producing the oxygen radical anion and regenerating the oxidized form of the anolyte (see Figure 36) and consequently discharging the system. Aziz *et al.* reported the reaction of the reduced viologen generating uncharged viologen and hydroxide anions.[57]

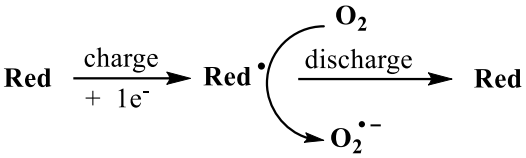

Figure 36: Schematic representation of the reaction between the anolyte and the oxygen.

Electrochemical oxygen reduction reaction (ORR) could be included with the consequent load consumption contributing to capacity losses due to faradaic imbalance, but considering the electrode material, pH of 7 and operating conditions it can be ruled out. Irreversible consumption of charge in the anolyte during the charging process causes that the anolyte does not to reach full charge

and consequently the discharge capacity will be limited, inhibiting the complete discharge of the catholyte, which cause SOC imbalance between both electrolytes. After highlighting the important effect of the O_2 in the battery performance, the next role of the membrane pretreatment will be discussed.

5.4.3. Effect of the membrane activation

The ion exchange membrane is responsible to close the internal circuit by allowing ions to pass between the electrode to preserve electroneutrality and prevents cross-mixing of the electrolytes.[58]

Nafion membranes® have been widely used due to their good mechanical and chemical properties, and good performance in different modes of operation in hydrated acidic environments. Nafion membrane, are generally pretreated before use to enhance the ionic conductivity, but this treatment also enhances the cross-mixing of RAM as demonstrated in the permeability study. Henceforth, we would like to show the advantages and disadvantages of this conditioning process, pointing out the importance of careful selection of both the right material and the pretreatment for a given system. By using the same configuration as in the previous section, the influence on RFB parameters was studied by comparing the membrane resistance determined by EIS at 0% SOC and the permeability results in both systems (Figure 37).

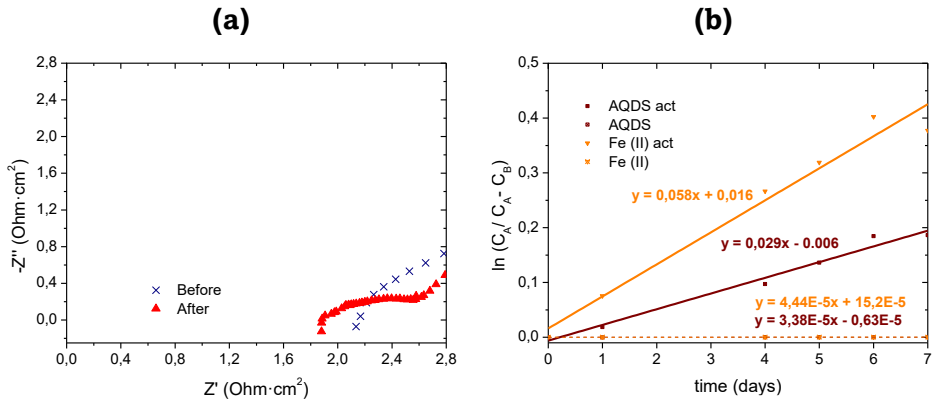

Figure 37: (a) Electrochemical impedance spectroscopy for both batteries in the high frequency region of the Nyquist plot. (b) Permeability evaluated from a H-cell using 100 mM of RAM in 1 M NaCl *vs* 1 M NaCl for one week.

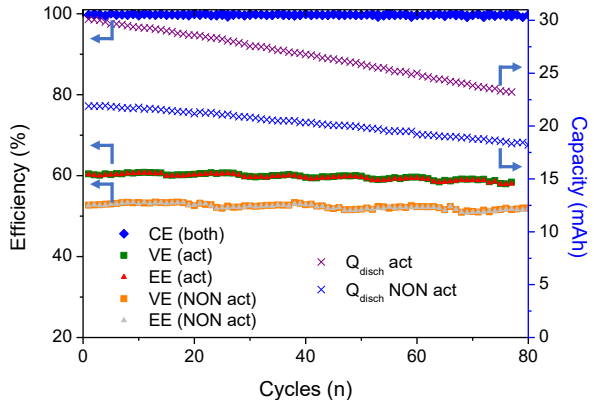

Figure 38: Comparison of the voltage and energy efficiencies for both batteries in 100 cycles at 100 mA/cm2. Coulombic efficiency (almost equal for both batteries), blue diamond. Voltage efficiency, green and orange square ($Na_4[Fe(CN)_6$ and AQDS as CLS, respectively). Energy efficiency, red and grey triangles ($Na_4[Fe(CN)_6$ and AQDS as CLS, respectively). Discharge capacity, blue and purple cross. ($Na_4[Fe(CN)_6$ and AQDS as CLS, respectively). 0.1 M AQDS in 1 M NaCl *vs* 0.1 M $Na_4[Fe(CN)_6]$ in 1 M NaCl, using pretreated and non-pretreated Nafion 212® membrane. The coulombic, voltage, energy efficiencies and the capacity evolution at different current densities for each battery can be found in *Annex A* (Table S3).

The comparison between cell resistance obtained by EIS before cycling, allow to compare the conductivity of the non-pretreated and pretreated membrane (see Figure 37a). The last one (blue crosses) shows a lower intercept with the Z' axis in the high frequency part of the EIS. During the boiling process, the membranes extend their polymeric structure resulting into a different internal conformation which makes the pores larger, and this may lead to more accessible ion-exchange groups, improving conductivity values (up to 53% higher in case of pretreated one comparing with the non-pretreated one). However, it also leads to increased cross-mixing of active species due to enhanced permeability. RAM permeability is a key parameter since limits the capacity of the battery and may alter also other parameters such as viscosity, stability and others. So, the permeabilities of redox active material have been carried out in a H-cell for each membrane being $1.7 \cdot 10^{-3}$ and $1.3 \cdot 10^{-6}$ cm^2/s for the $[Fe(CN)_6]^{4-}$ and $8.5 \cdot 10^{-4}$ and $9.9 \cdot 10^{-7}$ for the AQDS with the pretreated and non-treated membrane (Figure 37b, filled markers and non-filed markers, respectively). Both results are corroborated in the RFB set-up (Figure 38), despite both membranes show similar coulombic efficiencies, the higher resistance of the non-treated membrane led to lower voltage and energy efficiencies. The voltage and energy efficiencies using the pretreated membrane (Figure 38, green squares and red triangles, respectively) are around 10% higher than the VE and EE achieved with the non-pretreated membrane (Figure 38). Furthermore, comparing the capacity evolution over cycles (purple and blue crosses for the non-/pretreated membrane, respectively) lower capacity decay per hour (-0.33 *vs* -0.47 % Q_{theo}/h)

due to the lower permeability has been observed for the non-treated, when compared to the battery set with the pretreated membrane.

5.4.4. Effect of capacity limiting side

Even using the same redox couple, the performance of the battery will change if the catholyte or the anolyte is on the limiting capacity side. In this section, we study the different behavior if the catholyte (ferrocyanide, Figure 39a) or the anolyte (AQDS, Figure 39 b) are the limiting capacity side.

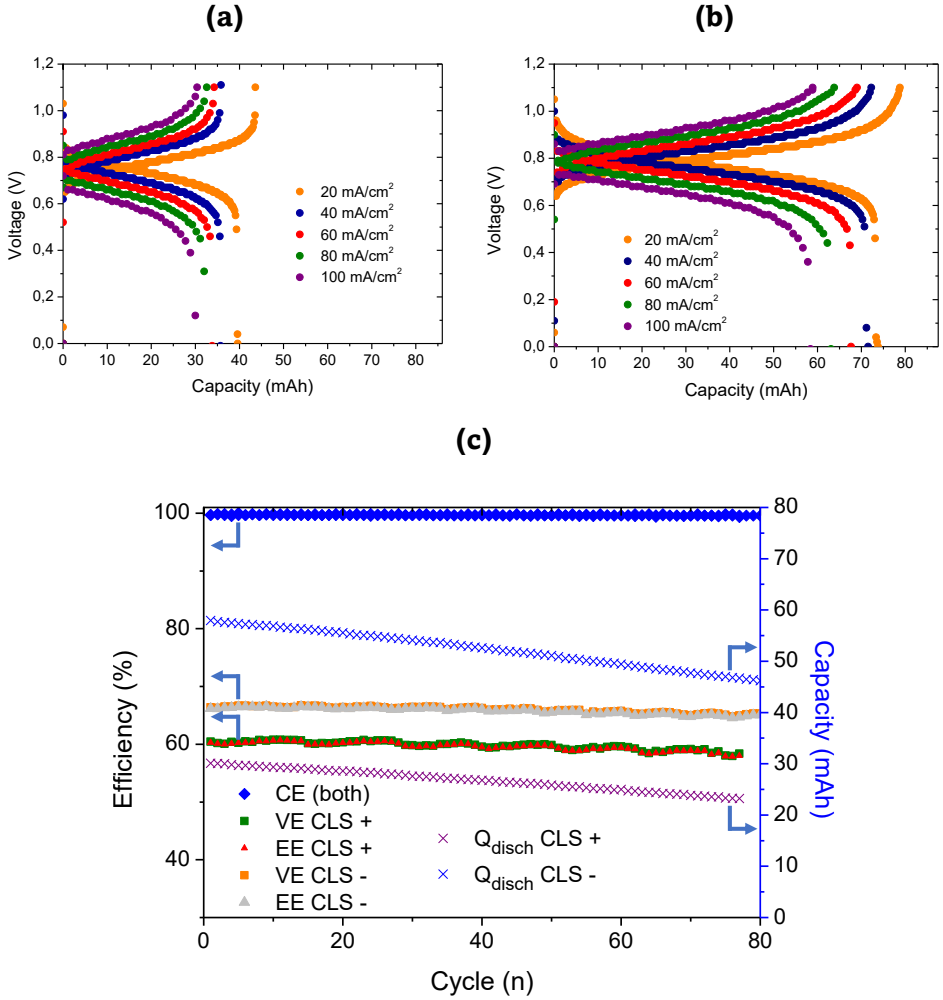

Figure 39: Comparison of charge/discharge profiles at different current densities (20, 40, 60, 80 and 100 mA/cm^2) for battery using different Capacity Limiting Side (CLS): (a) 0.1 M AQDS in 1 M NaCl *vs* 0.1 M $Na_4[Fe(CN)_6]$ in 1 M NaCl, (b) 0.08 M AQDS in 1 M NaCl *vs* 0.2 M $Na_4[Fe(CN)_6]$ in 1 M NaCl, using pretreated Nafion 212® membrane. (c) Comparison of the voltage and energy efficiencies for both batteries in 100 cycles at 100 mA/cm^2. Coulombic efficiency (almost equal for both batteries), blue diamond. Voltage efficiency,

green and orange square ($Na_4[Fe(CN)_6$ and AQDS as CLS, respectively). Energy efficiency, red and grey triangles ($Na_4[Fe(CN)_6$ and AQDS as CLS, respectively). Discharge capacity, blue and purple cross. ($Na_4[Fe(CN)_6$ and AQDS as CLS, respectively). The coulombic, voltage, energy efficiencies and the capacity evolution at different current densities for each battery can be found in *Annex A* (Table S4).

Both batteries show similar results in term of capacity fade, coulombic, voltage and energy efficiencies (Figure 39c) but is true that the capacity utilization is higher when the AQDS is the CLS compared when ferrocyanide is the CLS (67.5 *vs* 44.9%, respectively). The slightly higher capacity fade when AQDS (blue crosses) is the limiting side is due to the higher capacity utilization of the RAM (–0.18 *vs* –0.14% Q_{theo}/cycle, respectively). In this case the comparison of the loss of capacity per hour lead to opposite trend as a consequence of the different capacity on each experiment. Also, higher amounts of ferrocyanide provide a higher ionic conductivity, so higher efficiencies are expected.

As a brief summary, the experimental results of the same RFB set up but using different conditions have been used to highlight the main pitfalls. Furthermore, the effect of different parameters on the battery performance like the electrolyte pH, the O_2 presence, the membrane pretreatment and the capacity limiting have been discussed helping to understand the influence of the different variables on the behavior of RFB.

5.5. Testing of synthetized organic anolytes in single-cell.

5.5.1. Bipyridinium electrolytes

In the first part of the **chapter 1**, different bipyridinium salts has been synthetized, characterized, and studied. DFT calculation predicted the stability of each candidate based on the NBO and ADCH charge distribution analysis (Figure 40*). Following the study and based on the previous results reported by Bures *et al*,[9] the compound **1** serve as a starting point. If we analyze their results Compound **1** show a capacity decay of 26% within 50 cycles. In our study, Compound **1** and compound **2** should show similar results. The non-planarity, the lower redox potential compared to the six-membered ring (ΔV = 0.18 V) and the possibility of find a new promising anolyte that could avoid the degradation showed by compound **1** lead us to select compound **2** as the base material. First, the comparison between our results with compound **2** should show similar results than the reported by Bures *et al*. Second, compound **2** represent the core of the "optimized redox active material" compound **4**. So, both single-cells (compound **2** *vs* compound **4**) were studied in the same conditions (same membrane, catholyte, supporting material and conditions).

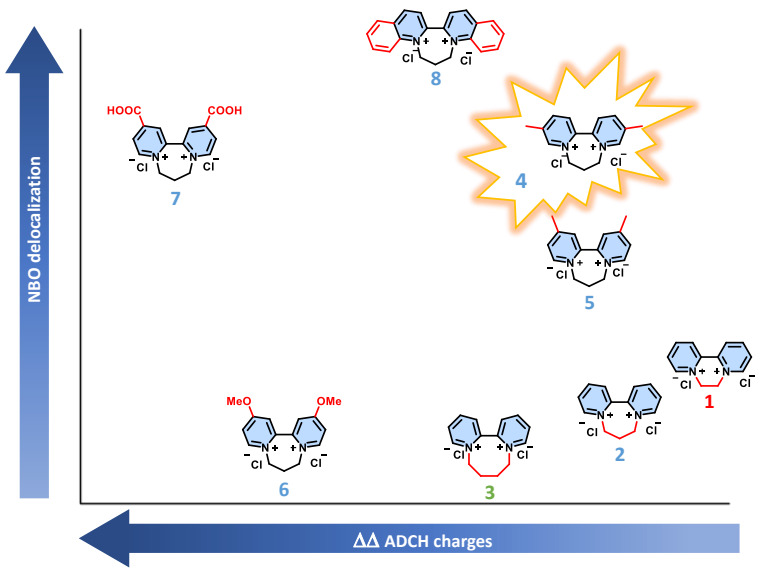

Figure 40: Illustrative figure evaluating the contribution of the NBO delocalization and the ADCH charge distribution. * Note Figure 40 is the same as Figure 13.

The evaluation of redox active materials along the literature has been done by different methods and the comparison of results is a hard task (Figure 41). Some research groups test all their results inside a glovebox where the effect of the O_2 can be neglected already mentioned and analyzed above. Galvanostatic charge/discharge (Figure 41a) and potentiostatic charge/discharge (Figure 41c) led to completely different results.[59,60] The use of the potentiostatic holding in the galvanostatic charging (Figure 41b) allow to access higher capacity utilization. The redox potential achieved on the electrochemical cell is an indicator of the SOC, so by using a voltage cut-off means that the SOC of the electrolyte is being limited. But the SOC reached in the electrochemical cell is not exactly the same than in the tanks. For this reason, when a potentiostatic holding is applied at the end of the galvanostatic cycling a specific SOC is reached for the whole electrolyte (in the cell and in the tanks). Finally, holding the battery at different state of charge show the reactivity of charged species (Figure 41d). For this reason, among the different possibilities, we select the galvanostatic cycling with the potentiostatic holding trying to access the maximum capacity in both redox active materials and being comparable the results despite this method usually lead to higher capacity decay.

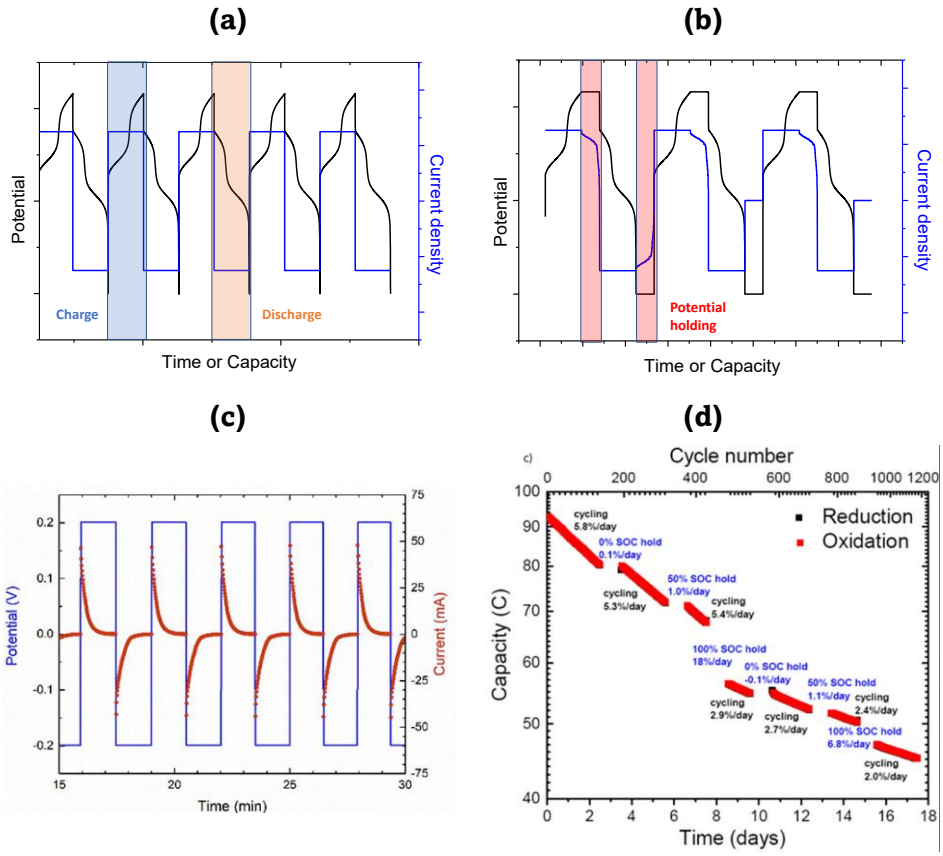

Figure 41: Different methods to charge/discharge a battery: (a) galvanostatic cycling at constant current, (b) Galvanostatic cycling + Potentiostatic holding (c) potentiostatic cycling (constant voltage) (d) Cycling pauses at different SOC (Source for both figures c and d in the down row: "Electrolyte Lifetime in Aqueous Organic Redox Flow Batteries: A Critical Review." Michael J. Aziz *et al. Chem. Rev.* **2020**, *120*, 6467).

On the basis of the results shown in DFT model, if the compounds **1, 2,** and **3** are compared, compound **3** should exhibit the worst results. We can explain this result since compound **3** present low ADCH charge distribution and NBO delocalization. Based on our DFT predicting model these results can be linked with a poor stability of the reduced specie. In this sense, this prediction match with the experimental results, compound **3** presented an irreversible behavior in CV. In the same way, compound **6** which is one of the worst redox active materials based on the prediction, also exhibit an irreversible behavior. Compound **7** and **8** has not been tested due to the poor reversibility and solubility showed in the previous characterization. At this point we can see that our model predicted the bad behavior of compound **3**, **6** and **8** (compound **7** could be a good candidate if its solubility was adequate). Analyzing Figure 40, it is expected that compound **2** should present similar results than compound **1** Since these compounds present similar ADCH charge distribution and NBO delocalization, so, same stability is

expected. At the same time, compounds **4** and **5** should present better behavior that the core structure (compound **2**). Besides, to corroborate the predicted stability of **4** over **2** by DFT analysis, both materials were integrated in a single-cell set-up subjected to repetitive charge-discharge cycles employing TEMPOL as reference catholyte material. Both tests were performed under comparable operating conditions, by using the same carbon felts as electrodes, membrane, electrolyte concentration and charge-discharge conditions (see the SI for detail information). The battery was charged and discharged at constant current and constant voltage ensuring that the anolyte reaches the desired SoC minimizing effect of overpotential. This methodology was proposed with the aim of comparing the stability of electrolytes which present differences in the electrochemical properties, such as redox potential, kinetic constant, and diffusion coefficient. Equally, to avoid the influence of the catholyte, an excess of TEMPOL was used.

First of all, the initial resistances of both systems have been checked to corroborate that both single-cells have been operated in the same conditions (Figure 42).

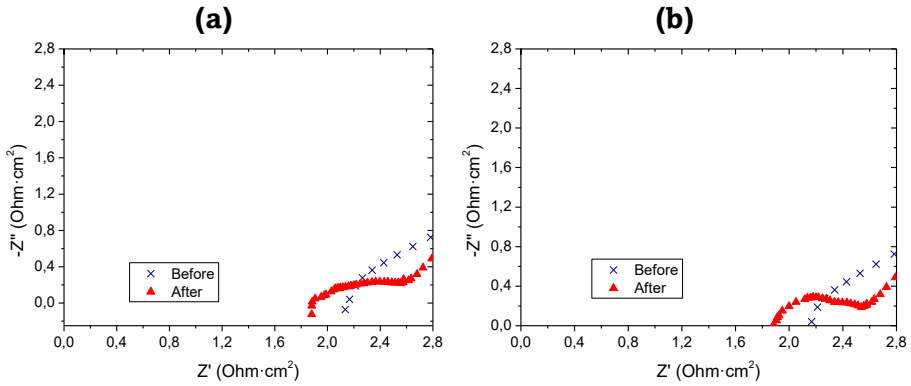

Figure 42: Electrochemical impedance spectroscopy before and after cycling (a) Compound **2** *vs* TEMPOL, (b) Compound **4** *vs* TEMPOL.

As the computational method predicted, compound **4** present significantly higher stability that compound **2** (Table 13 and Figure 43). Considering just the galvanostatic cycling, Compound **2** showed a capacity decay of 0.71%/cycle comparable with the reported one by Bures *et al* (0.52%/cycle) knowing that both systems has been evaluated differently (symmetric cell using galvanostatic cycling *vs* single-cell and galvanostatic cycling + potentiostatic holding). This first results proved that the compounds **1** and **2** present similar stability and that our predicting model was able to predict it. Furthermore, compound **4** showed better performance as expected showing a capacity decay of 0.35%/day reducing the capacity decay to the half and making us confident about the developed model. If we include the potentiostatic holding the difference is more significant, showing a capacity decay of 0.75%/day for the compound **2** compared to 0.16%/day of the compound **4**. Analyzing other parameters as the coulombic, voltage and energy

efficiencies, (Table 13) we can see clearly that both single-cells started with the same results in terms of efficiencies and capacity utilization. But after 100 cycles significant differences can be observed for compound **2** suggesting an increase in the cell polarization (decrease in the energy and voltage efficiencies). Furthermore, after few cycles we can see a new plateau in the cycling of compound **2** around voltage 0.4 - 0.6 V. This new plateau could be ascribed with the formation of new electroactive species that could be responsible of the high-capacity decay observed.

Table 13: Results of the single-cells tests performed with **2** and **4** as respective anolyte. Interval between the first and last efficiencies, capacity, capacity utilization and capacity decay.

RAM	CE (%)	VE (%)	EE (%)	$Q_{discharge}$ (mAh)	CU (%)	dQdis/dn (mAh)	d%Qdis/dn (%)
2	97.8-100.2	57.7-23.7	56.7-23.4	32.3-17.7	80.4-44.0	0.285	0.71
4	93.6-100.4	63.6-42.0	63.6-41.5	33.4-4.7	83.1-11,6	0.141	0.35

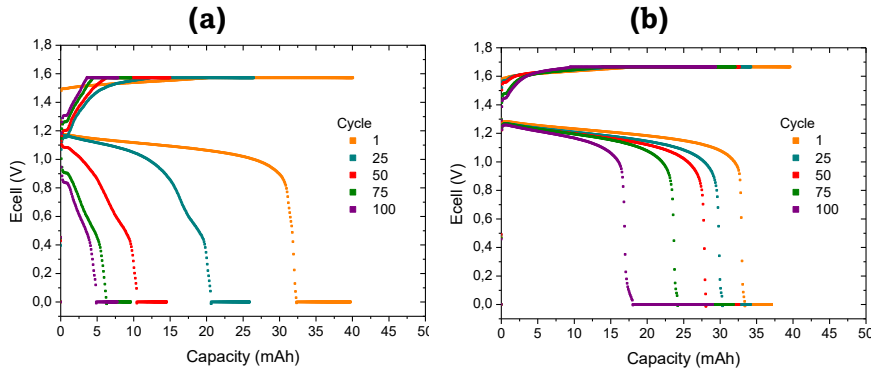

Figure 43: (a): Single-cell results using 0.1 M of **2** as anolyte *vs* 0.15 M of TEMPOL as catholyte, 100 cycles at room temperature, (b) Single-cell results using 0.1 M of **4** as anolyte *vs* 0.15 M of TEMPOL as catholyte, 100 cycles at room temperature.

5.5.2. Degradation of bipyridinium electrolytes

So, trying to shed light into this issue the charged and aged electrolyte were studied by NMR and UV-Vis spectroscopy. Zhang *et al* [10]described that the stability of diquat derivatives is closely associated with the proton catalyzed disproportionation of the charged species (Compound **2a**) affording the starting material (Compound **2**) and the totally reduced specie (Compound **2b**) which can suffer the prototanion (Compound **2c**) (Figure 44).

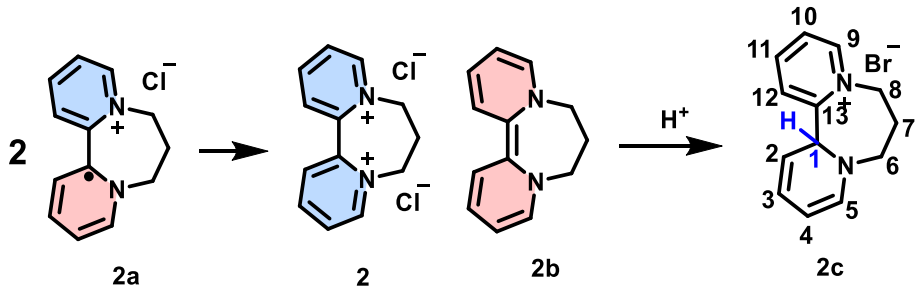

Figure 44: Proton catalyzed disproportionation of the charged species Compound **2a**.

The evaluation of charged electrolyte allowed to identify compounds **2b** and **2c**. Compound **2b** solution presents a band at 445 nm in UV-Vis (Figure 45) in agreement with radical reduced form.[61] Compound **2c** could be isolated from solution and fully characterized (*Annex A* Figures S35-S40). It was identified as a possible dead end out of the charge-discharge cycle.[62]

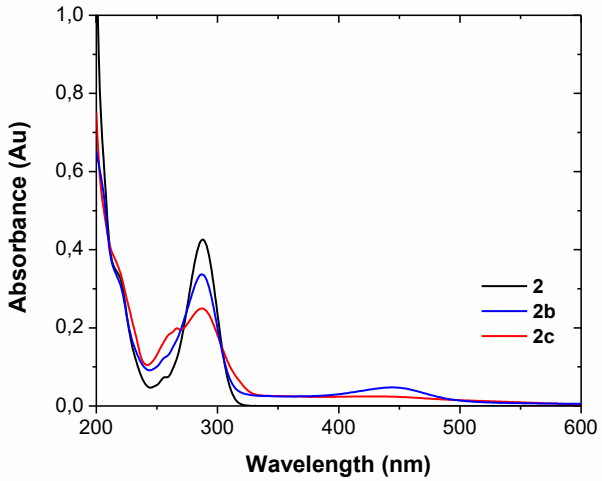

Figure 45: UV-Vis spectrum of compound **2, 2b** and **2c.**

Once that species in pristine **2** and charged electrolyte **2a** were identified and with the aim of understanding the underlying mechanism behind the capacity fade, the charged electrolyte was studied after cycling experiment, making again use of NMR and UV-Vis spectroscopy analyses. As it can be seen in the following NMR spectrum (Figure 46), additional signals could be identified, which differ from compound **2**, major product observed in the NMR spectrum, and from **2a** and **2c.** Broad signals are observed in the aromatic region (8-9.5 ppm) and a complex mixture of signals is as well identified at lower ppms. The broad signals in the NMR spectrum can be attributed to different issues: presence of radicals, insoluble species, agglomerates or polymers, etc. Insoluble species, agglomerates or

polymers may correlate with the lower performance observed and the observed semi-plateaus or plateaus in the charge-discharge profile.

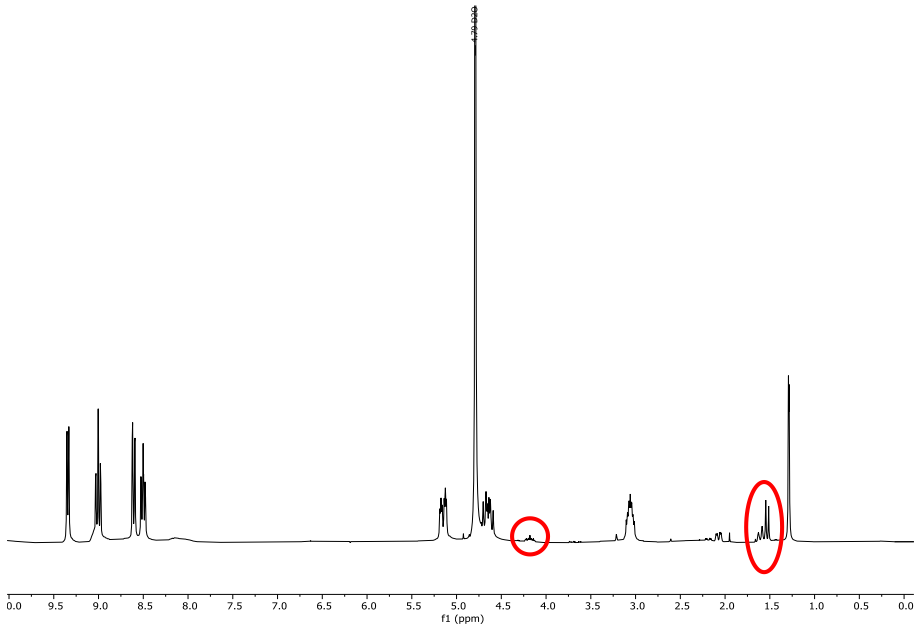

Figure 46: ^{1}H NMR spectrum of the electrolyte after cycling in which new signals are highlighted.

It should be noted that the UV-Vis spectrum of the cycled electrolyte displays a broad band (see Figure 45), which suggests the existence of additional species apart from already identified derivative **2**. Said additional species might be a π-system, such as derivative **2b** considering the wavelength of the absorption band. Thus, this would correlate with broad signals in the ^{1}H-NMR spectrum (> 8 ppm) rather than with signals at low ppms (figure 46).

The active material in solution was isolated for further characterization. As it can be seen in the gathered bidimensional ^{1}H-^{15}N HMBC spectrum (Figure 47a), three different N-containing systems could be identified. Due to the lack of correlation between the aromatic part of the ^{1}H NMR spectrum and the ^{15}N, formation of non-aromatic N-containing compounds can be envisaged. This would only be possible by loss of aromaticity on compound **2** upon subsequent multistep reduction or ring-opening. Those transformations would explain the loss of capacity considering the irreversible character of those transformations.

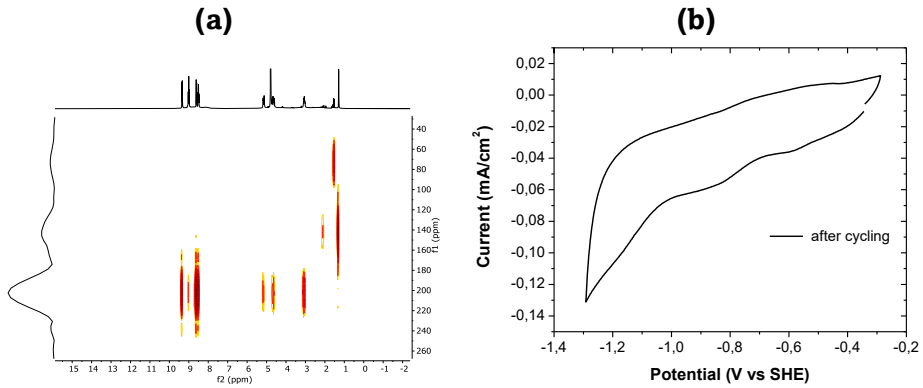

Figure 47: (a) Bidimensional ^{1}H-^{15}N HMBC spectrum for electrolyte after cycling. (b) Cyclic voltammogram of Compound **2b**.

To evaluate the redox activity of the isolated compound **2b**, a cyclic voltammetry of said compound was performed (Figure 47b). As the figure reflects, this compound is no longer a reversible redox active species.

Considering the performed experiments, it can be concluded that compound **2** is prone to undergo a protonation step after initial reduction, a compound that cannot longer be employed as reversible redox species. In addition, the presence of complex mixture of products in the cycled electrode also suggests that the capacity losses in the electrolyte can be ruled by the formation of side products.

The observed shoulder or plateaus in the charge-discharge profile might also correlate with the presence of species which present a redox activity but at different potential than pristine active material, compound **2**.

From this study we can conclude: i) different RAM based in diquat derivatives has been synthetized and electrochemically characterized. ii) A DFT method based on the NBO delocalization and the ADCH Mulliken distribution has been developed. iii) the experimental data has been used to corroborate the ability of the DFT method to predict the stability of the RAM.

5.5.3. Triazine electrolyte

In **Chapter 1** the new triazine-based anolyte has been synthetized and characterized, may represent an interesting candidate to increase the energy density due to four storable electrons, reasonable solubility, and redox potential. Now, the RFB results using this new anolyte are shown. The following experiments were developed during the PhD research stay in Turku University (Finland) under the supervision of Prof. Pekka Peljo.

The promising electrochemical properties studied and shown above encouraged testing the performance of **(SPr)$_3$4TpyTz** in a single-cell. To demonstrate the performance as new anolyte, a neutral-pH redox flow battery was assembled using 25 mM of **(SPr)$_3$4TpyTz** *vs* 125 mM $K_4[Fe(CN)_6]$ in 1 M KCl as positive electrolyte using Nafion 212® as ion exchange membrane. The battery was cycled galvanostatic at 60 mA/cm^2 at room temperature for 1000 cycles (11.7 days) with the cut-off potentials selected to access first and second reduction of the **(SPr)$_3$4TpyTz** (Figure 48). The achieved capacity of *ca*. 15 mAh corresponds to 74.6% of the theoretical capacity (20.1 mAh for two electrons storage). Deviations between the theoretical and the measured capacity are mainly attributed to the system resistance. In Figure 48, this battery shows a coulombic efficiency of 100% and voltage and energy efficiencies close to 75% in all cycles, which is comparable to the VRFB systems.[63] The capacity decay observed during cycling was -0.163 mAh/day which correspond to -1.08%/day respect the maximum capacity reached. The fluctuations in the capacity evolution during cycling could be ascribed to some drops on the vial walls. To the best of our knowledge, this compound represents one of the most stable systems reported in the literature and its synthesis is one of the cheapest and shortest.

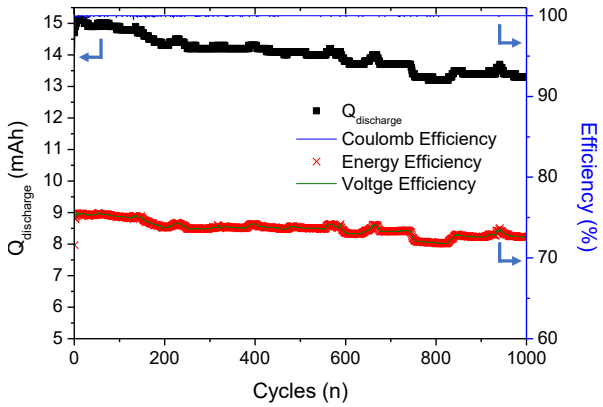

Figure 48: Galvanostatic cycling by using both electrons of **(SPr)$_3$4TpyTz** 25 mM in 1 M KCl and 100 mM $K_4[Fe(CN)_6]$ in 1 M KCl at 60 mA/cm^2 for 1000 cycles. Discharge capacity, coulombic, voltage and energy efficiencies evolution.

After these promising results provided by the battery at low concentrations, battery tests at higher concentrations were performed in the same conditions with 100 mM of **(SPr)$_3$4TpyTz** in 1 M KCl *vs* 300 mM of $K_4[Fe(CN)_6]$ in 1 M KCl. Once the battery started to be charged, after 15 cycles, the flow on the negative side was blocked due to the electrolyte precipitation, preventing further cycling. (Figure 49).

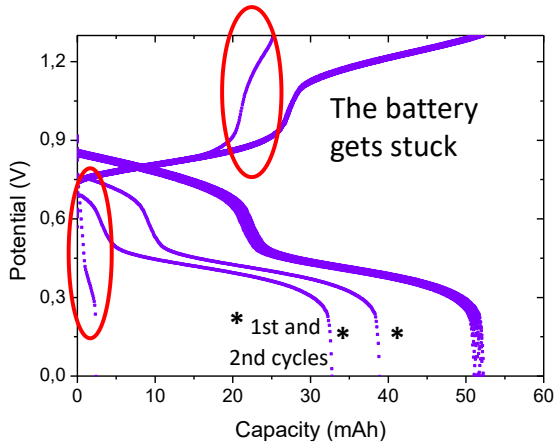

Figure 49: (a) E_{cell} *vs* Capacity plot at 60 mA/cm^2 for the battery (which get stuck in the 15th cycle) using 100 mM of **(SPr)$_3$4TpyTz** in 1 M KCl *vs* 300 mM $K_4[Fe(CN)_6]$ in 1 M KCl as electrolytes and N212® membrane.

After that, the electrolytes were analysed by ^{1}H NMR and CV. Both experiments demonstrate no degradation of the redox active material (Figure 50 and 51). Based on these results, it was speculated that the reduced state is not fully soluble while the battery is charging. By increasing the concentration of the reduced state, at some point the reduced state precipitates blocking the flow.

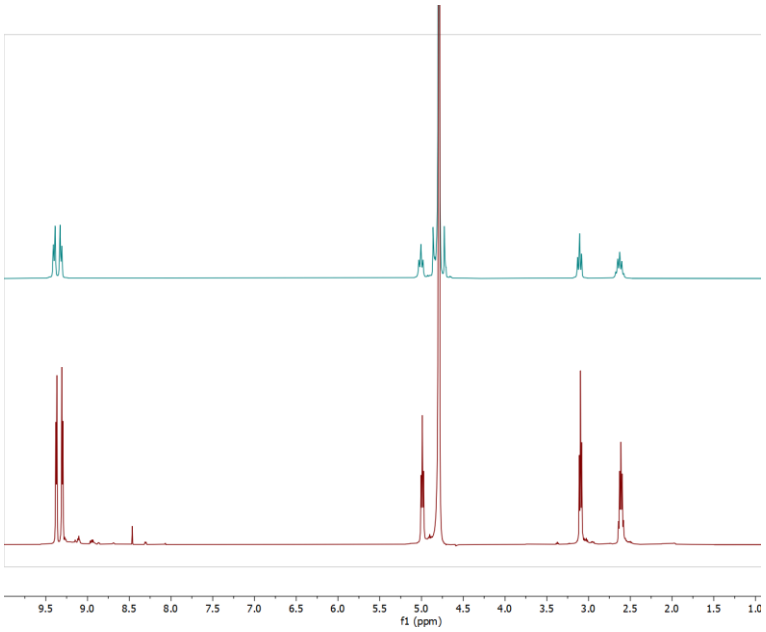

Figure 50: ^{1}H NMR spectra of anolyte 100 mM **(SPr)$_3$4TpyTz** in 1 M KCl after the battery gets stuck, measured in D_2O before (blue trace) and after stucking (red trace). The peaks with small intensity in the red spectra could be ascribed to the reduced form of the **(SPr)$_3$4TpyTz.**

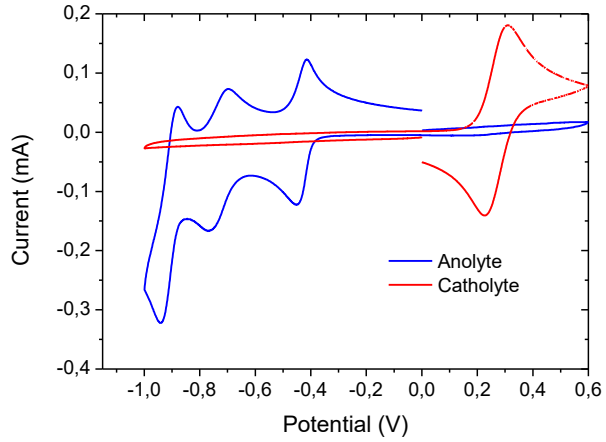

Figure 51: CV of anolyte 100 mM **(SPr)$_3$4TpyTz** in 1 M KCl and catholyte 100 mM $K_4[Fe(CN)_6]$ in 1 M of KCl after the battery gets stuck.

Some Density Functional Theory (DFT) calculations were employed to investigate the structure of the oxidized and reduced form of the **(SPr)$_3$4TpyTz** to deeply understand the effect of solubility (Figure 52). The geometric structures of both redox states were optimized using CAM-B3LYP/6-31G** level of theory with empirical dispersion correction (GD3BJ) and the implicit Solvent Model based on Density (SMD). As it can be observed in Figure 52a, the sulfonate group of the oxidized state is intramolecularly interacting with the pyridine of the triazine. This kind of interactions has been observed previously for sulfonated-viologen[29] and it has been corroborated by NOESY spectra (Figure 53). By contrast, in the reduced form, the sulfonate group is open and "free" to interact intermolecularly with the pyridine core of other molecules.

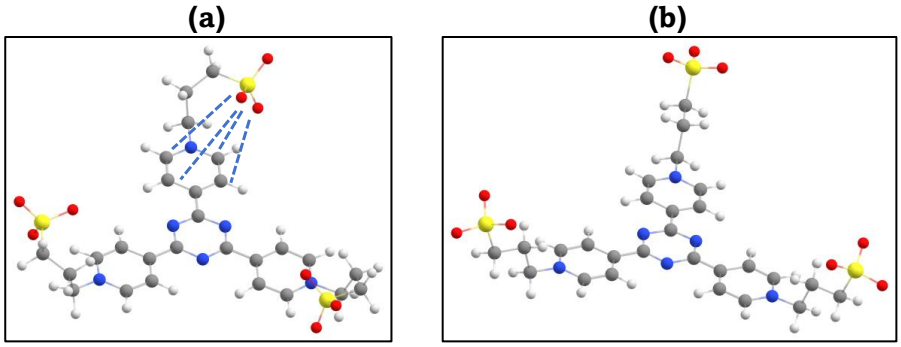

Figure 52: Optimized structures of the oxidized (a) and reduced (b) states of **(SPr)$_3$4TpyTz** at CAM-B3LYP/6-31G** level of theory.

This interaction of the oxidated state was also observed in the NOESY NMR spectra where a correlation between the alkylic chain and the pyridinium protons can be observed (Figure 53 highlighted in the red). This interaction has been also observed for the sulfonated viologen reported by Leo Liu.[24] They developed a rod-

shaped viologen which decrease the permeability through the IEM, increase the redox potential and higher stability by grafting methyl into the pyridinium core to avoid this interaction.

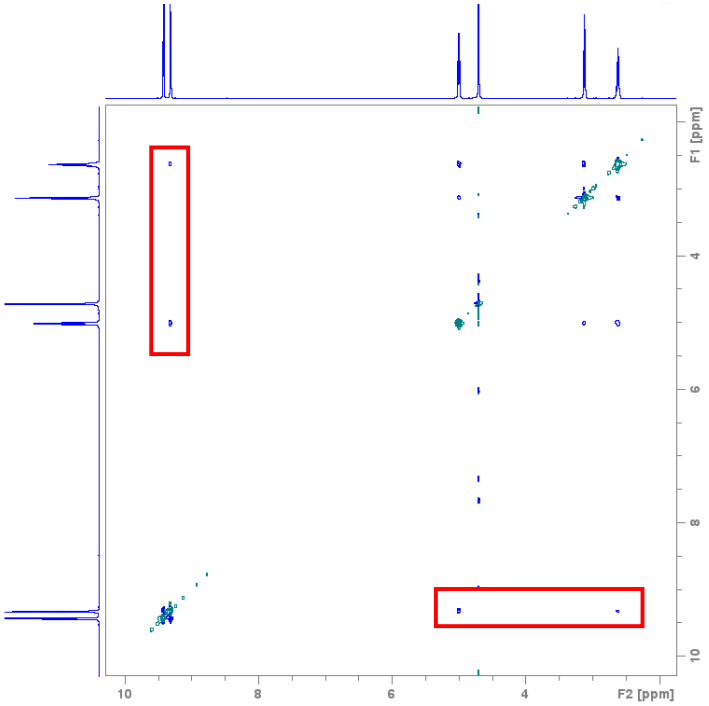

Figure 53: NOESY spectra of **$(SPr)_3$4TpyTz** in 1 M KCl D_2O.

The same NMR experiment was repeated using different supporting electrolyte like NH_4Cl, urea (H-bond between the ammonium and sulfonate could avoid the intermolecular interaction), LiCl (smaller cation) NaCl (more oxophilic cation) but in all the cases the cross-peaks signals appear.

Another possibility could be the intramolecular interaction between the sulfonate group and the pyridinium core of different molecules. Other molecules like the naphthalene diimide derivative suffered aggregation and it was corroborated by NMR spectroscopy. The self-association for the NDI derivative led to a concentration dependent of the chemical shift from ^1H NMR.[30] In order to check if there is some kind of aggregation the NMR at different concentrations were recorded. Any peak shift was observed so it suggests that there is any aggregate (Figure 54).

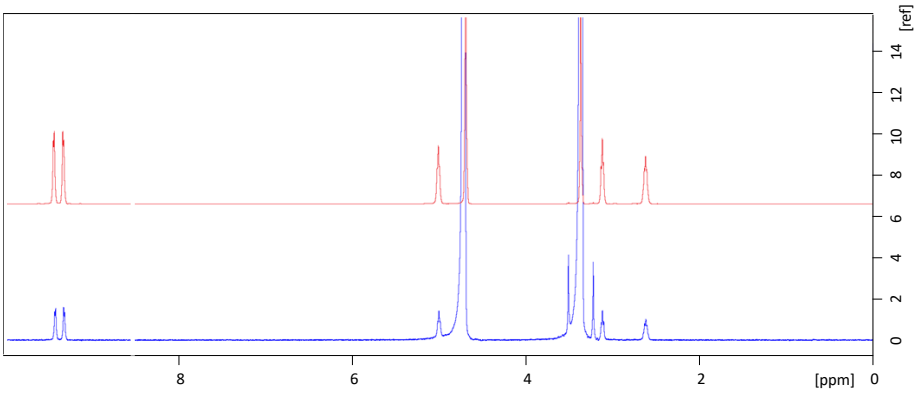

Figure 54: ^{1}H NMR of **(SPr)$_3$4TpyTz** at different concentrations 1 mM (blue trace) and 50 mM (red trace) in D_2O.

The possibility of this intermolecular interaction and the central symmetry which has been demonstrated that favours the formation of aggregates.[64] This fact may explain why the solubility of the reduced form can be compromised during charging. It has been reported that zwitterionic species solubility can be enhanced by increasing the salt concentration of the environment (salting in effect).[28] The solubility of the oxidized molecules is apparently not a problem as it was measured to be greater than 900 mM in 1 M KCl. Nevertheless, when the salt is removed, even the oxidized molecules are poorly soluble in water (< 100 mM in DI water, Figure 55).

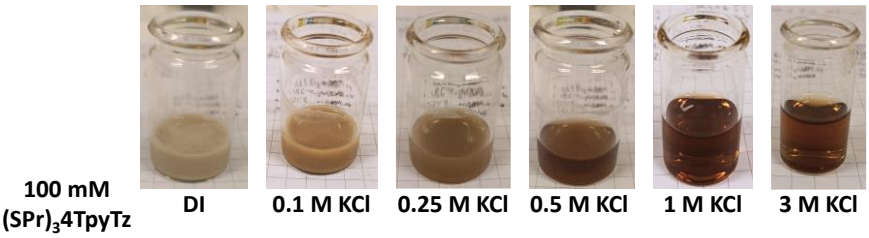

Figure 55: Pictures of the solution 100 mM of **(SPr)$_3$4TpyTz** with different concentrations of KCl.

All in all, it is evident that the salt is playing a vital role in the solubility of the triazine derivatives. The interaction between the zwitterionic species can lead to the formation of aggregates that becomes insoluble in water. By adding enough salt into the solution, these interactions can be avoided or at least lessened, enhancing the solubility. Furthermore, better solvation of the triazine molecules could lead in higher stability due to the hindered interaction between the molecules. In this sense, a plausible battery may work considering more concentrated supporting electrolyte solution. Thereby, a battery using 3 M KCl solution in the anolyte was tested (Figure 56).

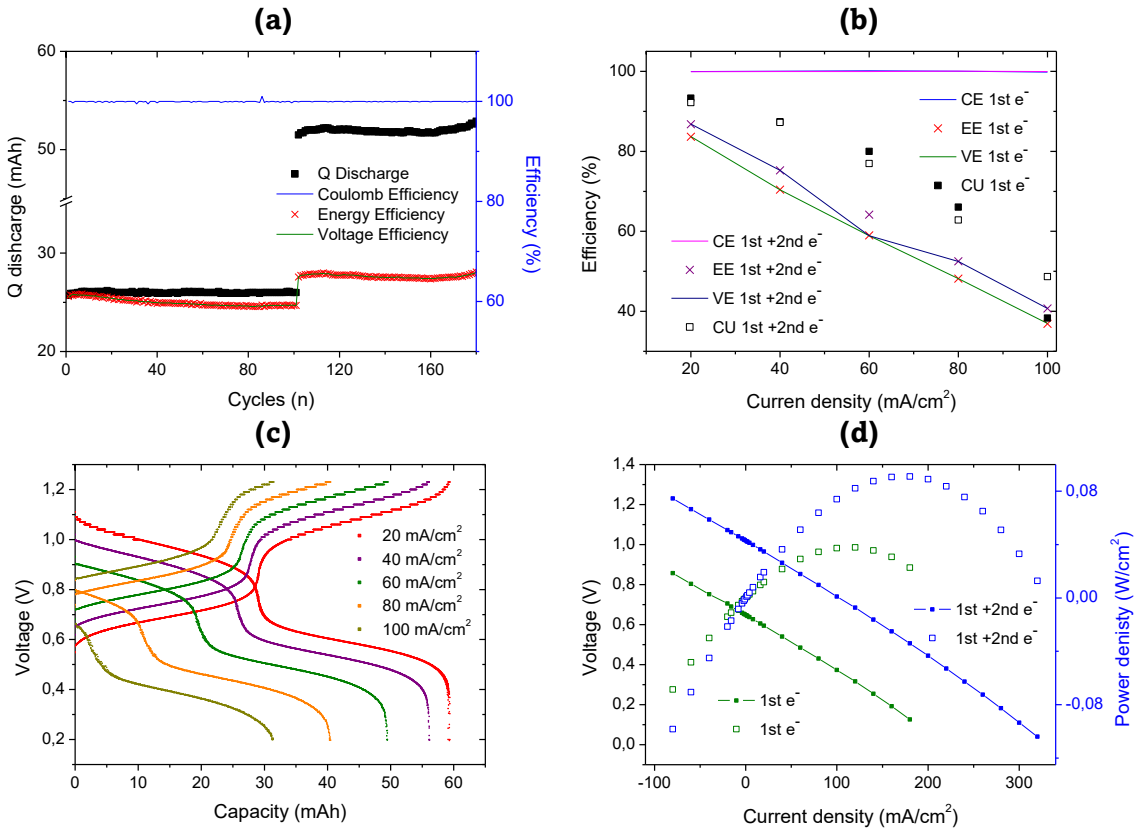

Figure 56: (a) Galvanostatic cycling of 100 mM of **(SPr)$_3$4TpyTz** in 3 M KCl *vs* 100 mM $K_4[Fe(CN)_6]$. Cycling a constant current reaching one (1-100 cyles) and two electrons (101-180 cycles) at 60 mA/cm^2 using 0.9 and 1.25 V upper cutoffs respectively and 0.2 V as lower cutoff. (b) Discharge capacity, coulombic, voltage and energy efficiencies evolution. (c) Charge-discharge capacity *vs* Voltage profile at different current densities (d) Polarization (line) and power density (scatter) curves for one and two electron battery at 50% SoC.

A flow cell with 12 mL of 0.1 M of **(SPr)$_3$4TpyTz** in 3 M KCl as anolyte and 50 mL of 0.1 M $K_4[Fe(CN)_6]$ in 1 M KCl as catholyte (0.2 M of electrons in the capacity limiting side (CLS)) was tested inside a glovebox. First, the cell was studied just analysing the first electron and then subsequently reach the second and the third electrons. Initially, the cell was galvanostatically charged at 60 mA/cm^2 with 0.9 V and 0.2 V as cut-offs for 100 cycles (Figure 56a, from cycle 1-100). The total discharge capacity was 26.11 mAh which correspond to 81.2% of the capacity utilization for one electron. Moreover, different current densities were tested (20, 40, 60, 80 and 100 mA/cm^2). In all currents, the coulombic efficiency was near 100%. The voltage and energy efficiencies range from 83.7 (lower current) to 36.9% (highest current). The capacity utilization reached 93.3 to 38.3% from the lowest to the highest current densities, respectively (Figure 56b)). All these results show that higher current densities lead to higher ohmic and mass transport resistances, increasing the overpotential. As the cut-off voltage was kept constant, the achieved SOC decreases with increasing current density.

After analysing the performance of the battery at different current densities, the system was charged to 50% SOC (with respect to the first electron of the anolyte) and the EIS experiments (*Annex A,* Figure S53), and the polarization curves were recorded (*Annex A,* Figure S54). From the polarization curve, the resistance of the whole system was calculated as 2.81 ohm·cm^2. A power density peak of 37.6 mW/cm^2 was achieved between 100 and 120 mA/cm^2. The cell was cycled 100 times suggesting a great stability showing no capacity decay over 18h. After that, the second electron was studied. First, the cell was cycled galvanostatically at the same current (60 mA/cm^2) but using 1.25 V and 0.2 V as cutoffs (Figure 56a from cycle 101 to 180). The total discharge capacity at this current was around 52 mAh which represents 76.9% of the capacity utilization. When cycled at different current densities, the coulombic efficiency was around 100%, the voltage and energy efficiencies range from 86.8 to 40.7% and the capacity utilization reached 92.2 (lowest current) and 48.7% (highest current) (Figure 56b). Subsequently, the system was theoretically charged to 50% SOC (with respect to the second electron of the anolyte) and the EIS experiments (*Annex A,* Figure S53) and the polarization curves were recorded (*Annex A,* Figure S55). A power density peak of 91.1 mW/cm^2 was achieved at 180 mA/cm^2. The modest power density would be increased in an optimized cell with a lower ohmnic resistance. The cell was cycled 80 times showing no capacity decay over 29h. Large multiple-electron storage materials typically have lower diffusion coefficients, but these bigger molecules could avoid the permeability through the ion exchange membrane which is one of the most limiting phenomena in RFB performance. The suppression of the crossover and the stability of the proposed triazine derivative place this work as a special redox active material which can work without showing any capacity decay over 3 days.

Finally, the third redox process was studied by increasing the upper cut-off to 1.5 V. This resulted in a completely capacity decay (Figure 57), and a significant increase in the pH of the electrolyte was observed (Table 14). In comparison, no pH change was observed if cycling was limited to 1st or 2nd reduction. Once the anolyte was analysed by ^{1}H NMR spectroscopy (Figure 58) completely change in the aromatic part can be observed. The main conclusion that can be extracted from the NMR analysis is that the new product has lose completely the symmetry of the triazine appearing different signals in the aromatic part (form 8 to 9 ppm). Low intensity signals appear between 6 and 7 ppm that can be ascribed to the protonated nitrogen atom. This fact is in good agreement with the proposed protonation reaction responsible of the pH change in the third redox process and, therefore, the observed capacity decay (Figure 59).

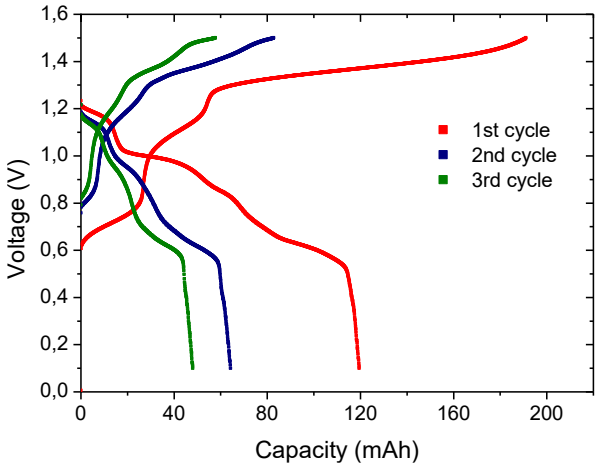

Figure 57: Galvanostatic cycling of battery 100 mM **(SPr)$_3$4TpyTz** in 3 M KCl *vs* 100 mM $K_4[Fe(CN)_6]$ in 1 M of KCl reaching third and fourth electron.

Table 14: Comparison of the initial pH and the pH after reaching the third redox process for the battery 100 mM **(SPr)$_3$4TpyTz** in 3 M KCl *vs* 100 mM $K_4[Fe(CN)_6]$ in 1 M of KCl.

	pH initial	**pH after 3rd process**
Anolyte	3.8	13.25
Catholyte	8.0	10.22

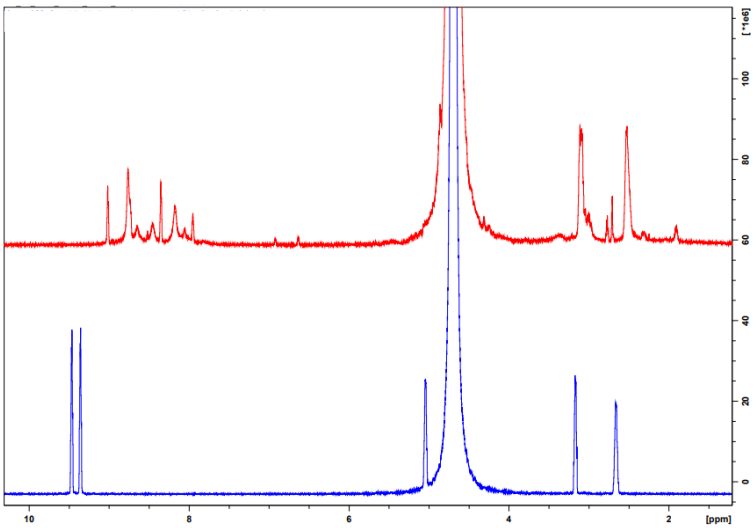

Figure 58: ^{1}H NMR of **(SPr)$_3$4TpyTz** before (blue trace) and after (red trace) cycling in D_2O.

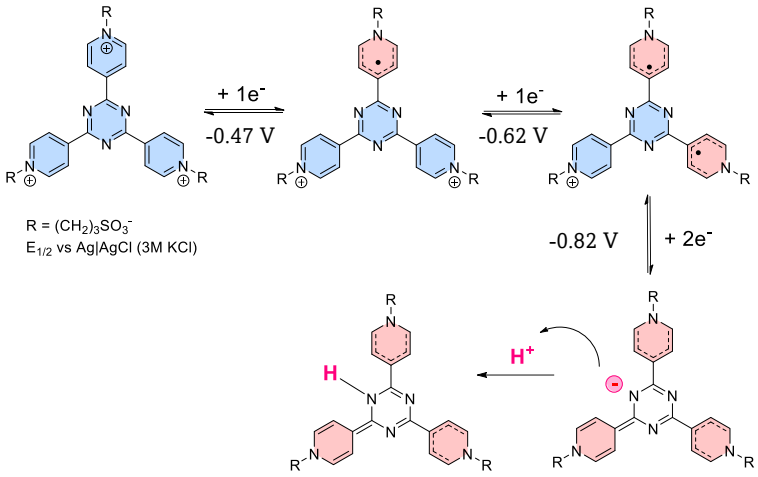

Figure 59: Proposed mechanism for each reduction step.

To understand the stable performance of the **(SPr)$_3$4TpyTz** we can focus on the mechanism of the redox reaction (Figure 59). The first reduction process reduces one of the pyridinium rings leading to a greatly stable radical delocalized throughout the whole structure. Second reduction process forms a biradical species which is in correlation with the mechanism proposed by Liang *et al.*[27] Finally, the third reduction process generates a negative charge in the N-atom of the triazine which gets protonated making the third process irreversible. This leads to a fast capacity decay observed if the third plateau is reached during charging, as well as a large decrease in the pH of the electrolyte (Figure 57 and Table 14). Triazine reported by Liang *et al* [25] could be reduced three times without significant adverse effects. This is most likely because all three pyridium groups are reduced before the triazine core. In our case it looks like the reduction of the triazine occurs with the potential range of the reduction of the last pyridinium, leading to high-capacity decay and the dramatic change in the pH after just 4 cycles.

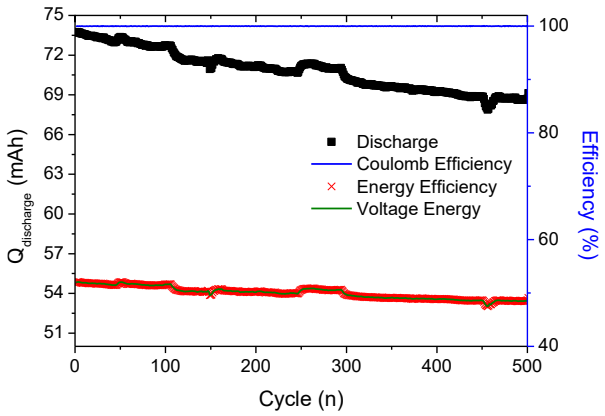

Figure 60: Galvanostatic cycling at 60 mA/cm^2 of 200 mM of **(SPr)$_3$4TpyTz** in 3 M KCl *vs* 300 mM $K_4[Fe(CN)_6]$ in 1 M KCl. Discharge capacity, coulombic, voltage and energy efficiencies evolution.

Finally, battery testing was carried out at higher concentration using 200 mM of **(SPr)$_3$4TpyTz** in 3 M KCl and 300 mM of $K_4[Fe(CN)_6]$ in 1 M of KCl (0.4 M of electrons in the negative CLS) (Figure 60). The battery was galvanostatically cycled for 500 cycles at 60 mA/cm^2 (14 days). The system shows a capacity decay of 4.47 mAh corresponding a capacity retention of 93.8% and a capacity decay of 0.012%/cycle or 0.44%/day (Figure 60). Both electrolytes were checked by CV ensuring that after 14 days no crossover was observed (Figure 61). Furthermore, impedance before and after cycling show a slightly increase in the resistance (20% higher) probably due to the formation of aggregates and their interaction with the IEM (*Annex A,* Figure S56). This capacity decay is ascribed to the precipitation of the triazine probably due to the change in the electrolyte composition because of the crossover of the potassium through the ion exchange membrane. This battery also shows slightly lower energy efficiency probably due to the higher concentration of the triazine leading to lower "free potassium" concentration, decreasing electrolyte conductivity and increasing the formation of triazine aggregates.

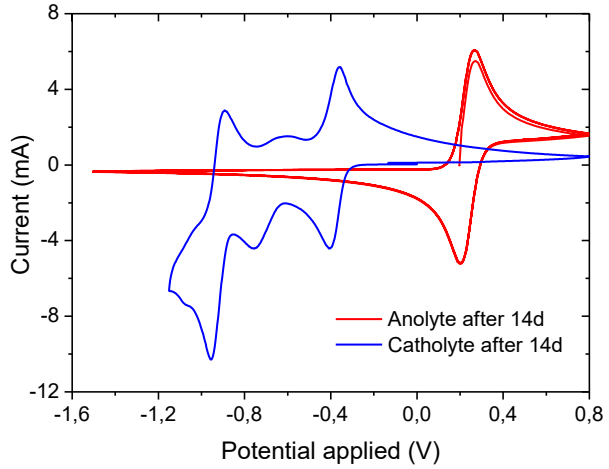

Figure 61: CV of anolyte 200 mM **(SPr)$_3$4TpyTz** in 3 M KCl and catholyte 300 mM $K_4[Fe(CN)_6]$ in 1 M of KCl after 14 days of battery cycling

This work represents one example where no capacity decay has been showed in the right composition of electrolyte, albeit at moderate concentrations of 100 mM. The larger triazine based anolyte is stable enough to store two electrons without any kind of degradation probably due to the high delocalization of the generated radicals into the pyridinium and triazine rings. Furthermore, the large size of this triazine derivative avoids crossover through the ion exchange membrane. The optimization of the electrolyte could enable the use of more concentrated solutions which could lead to a higher capacity for this system. To do this, the interaction

between the reduced state of **(SPr)$_3$4TpyTz** could be studied by Molecular Dynamics MD in order to understand how to avoid this interaction which precipitate the electrolyte at some SOC. Furthermore, the synthesis of new triazine derivatives where the central symmetry is avoided could avoid the formation of aggregates. This work opens the door to the synthesis of new triazine derivatives which are new candidates for multiple electron storage showing high stability during cycling.

Chapter 3 using a well-studied anthraquinone (AQDS)-based anolyte and $Na_4[Fe(CN)_6]$ catholyte chemistry, various characterization techniques for RFB are described. The chapter explores the influence of experimental parameters, such as electrolyte pH, O_2 presence, membrane pretreatment, and capacity limiting side, on battery performance. In addition, different electrochemical techniques, including load curve measurements, electrochemical impedance spectroscopy, and charge-discharge cycling tests, are introduced through this analysis.

Based on the predicting model results, we compared the cell performance of a seven-membered unsubstituted 2,2'-bipyridinium salt with the best candidate, the m-Me substituted analogue. The significantly superior performance of the selected anolyte validated the DFT protocol as an effective means to elucidate the performance of the prepared materials. This work demonstrates how DFT calculations can effectively guide synthesis across the vast chemistry space to identify candidates with optimum characteristics. As a result, chemists can save valuable resources, both time and money, by focusing their efforts on these "lead" compounds, which show promising potential as active materials for AORFB.

Finally, the new trispyridinium triazine anolyte efficiently stores two electrons under neutral conditions, without showing any capacity decay in suitable conditions. Additionally, further reduction of the triazine has been investigated, revealing significant capacity decay and changes in electrolyte pH. This observation has prompted us to suggest a mechanism for the reduction process. The successful development of this trispyridinium triazine anolyte with efficient multiple-electron storage capabilities represents a significant advancement in the field. The insights gained from DFT calculations and the understanding of reduction mechanisms are invaluable for optimizing and refining energy storage technologies for enhanced performance and stability.

5.6. References

(1) Kwabi, D. G.; Ji, Y.; Aziz, M. J. Electrolyte Lifetime in Aqueous Organic Redox Flow Batteries: A Critical Review. *Chem. Rev.* **2020**, *120*, 6467–6489. https://doi.org/10.1021/acs.chemrev.9b00599

(2) Fischer, P.; Mazúr, P.; Krakowiak, J. Family Tree for Aqueous Organic Redox Couples for Redox Flow Battery Electrolytes: A Conceptual Review. *Molecules* **2022**, *27*, 560. https://doi.org/10.3390/molecules27020560

(3) Singh, V.; Kim, S.; Kang, J.; Byon, H. R. Aqueous Organic Redox Flow Batteries. *Nano Res.* **2019**, *12*, 1988–2001. https://doi.org/10.1007/s12274-019-2355-2

(4) DeBruler, C.; Hu, B.; Moss, J.; Luo, J.; Liu, T. L. A Sulfonate-Functionalized Viologen Enabling Neutral Cation Exchange, Aqueous Organic Redox Flow Batteries toward Renewable Energy Storage. *ACS Energy Lett.* **2018**, *3*, 663–668. https://doi.org/10.1021/acsenergylett.7b01302

(5) DeBruler, C.; Hu, B.; Moss, J.; Liu, X.; Luo, J.; Sun, Y.; Liu, T. L. Designer Two-Electron Storage Viologen Anolyte Materials for Neutral Aqueous Organic Redox Flow Batteries. *Chem* **2017**, *3*, 961–978. https://doi.org/10.1016/j.chempr.2017.11.001

(6) Hu, M.; Wu, W.; Luo, J.; Liu, T. L. Desymmetrization of Viologen Anolytes Empowering Energy Dense, Ultra Stable Flow Batteries toward Long-Duration Energy Storage. *Advanced Energy Materials* **2022**, *12*, 2202085. https://doi.org/10.1002/aenm.202202085

(7) Wu, W.; Wang, A. P.; Luo, J.; Liu, T. L. A Highly Stable, Capacity Dense Carboxylate Viologen Anolyte towards Long-Duration Energy Storage. *Angew Chem Int Ed* **2023**, *62*. https://doi.org/10.1002/anie.202216662

(8) Lv, X.-L.; Sullivan, P.; Fu, H.-C.; Hu, X.; Liu, H.; Jin, S.; Li, W.; Feng, D. Dextrosil-Viologen: A Robust and Sustainable Anolyte for Aqueous Organic Redox Flow Batteries. *ACS Energy Lett.* **2022**, *7*, 2428–2434. https://doi.org/10.1021/acsenergylett.2c01198

(9) Burešová, Z.; Klikar, M.; Mazúr, P.; Mikešová, M.; Kvíčala, J.; Bystron, T.; Bureš, F. Redox Property Tuning in Bipyridinium Salts. *Front. Chem.* **2021**, *8*, 631477. https://doi.org/10.3389/fchem.2020.631477

(10) Huang, J.; Yang, Z.; Murugesan, V.; Walter, E.; Hollas, A.; Pan, B.; Assary, R. S.; Shkrob, I. A.; Wei, X.; Zhang, Z. Spatially Constrained Organic Diquat Anolyte for Stable Aqueous Flow Batteries. *ACS Energy Lett.* **2018**, *3*, 2533–2538. https://doi.org/10.1021/acsenergylett.8b01550

(11) Griffin, J. D.; Pancoast, A. R.; Sigman, M. S. Interrogation of 2,2′-Bipyrimidines as Low-Potential Two-Electron Electrolytes. *J. Am. Chem. Soc.* **2021**, *143*, 992–1004. https://doi.org/10.1021/jacs.0c11267

(12) Fuerst, E. P.; Norman, M. A. Interactions of Herbicides with Photosynthetic Electron Transport. *Weed. Sci.* **1991**, *39*, 458–464. https://doi.org/10.1017/S0043174500073227

(13) Heyrovsky, M. The Electroreduction of Methyl Viologen. *J. Chem. Soc., Chem. Commun.* **1987**, *24*, 1856–1857. https://doi.org/10.1039/C39870001856

(14) Liu, T.; Wei, X.; Nie, Z.; Sprenkle, V.; Wang, W. A Total Organic Aqueous Redox Flow Battery Employing a Low Cost and Sustainable Methyl Viologen Anolyte and 4-HO-TEMPO Catholyte. *Adv. Energy Mater.* **2016**, *6*, 1501449. https://doi.org/10.1002/aenm.201501449

(15) Lv, Y.; Liu, Y.; Feng, T.; Zhang, J.; Lu, S.; Wang, H.; Xiang, Y. Structure Reorganization-Controlled Electron Transfer of Bipyridine Derivatives as Organic Redox Couples. *J. Mater. Chem. A* **2019**, *7*, 27016–27022. https://doi.org/10.1039/C9TA08910A

(16) Elgrishi, N.; Rountree, K. J.; McCarthy, B. D.; Rountree, E. S.; Eisenhart, T. T.; Dempsey, J. L. A Practical Beginner's Guide to Cyclic Voltammetry. *J. Chem. Educ.* **2018**, *95*, 197–206. https://doi.org/10.1021/acs.jchemed.7b00361
(17) Ghule, S.; Dash, S. R.; Bagchi, S.; Joshi, K.; Vanka, K. Predicting the Redox Potentials of Phenazine Derivatives Using DFT-Assisted Machine Learning. *ACS Omega* **2022**, *7*, 11742–11755. https://doi.org/10.1021/acsomega.1c06856
(18) Kucharyson, J. F.; Cheng, L.; Tung, S. O.; Curtiss, L. A.; Thompson, L. T. Predicting the Potentials, Solubilities and Stabilities of Metal-Acetylacetonates for Non-Aqueous Redox Flow Batteries Using Density Functional Theory Calculations. *J. Mater. Chem. A* **2017**, *5*, 13700–13709. https://doi.org/10.1039/C7TA01285C
(19) Wedege, K.; Dražević, E.; Konya, D.; Bentien, A. Organic Redox Species in Aqueous Flow Batteries: Redox Potentials, Chemical Stability and Solubility. *Sci Rep* **2016**, *6*, 39101. https://doi.org/10.1038/srep39101
(20) Foster, J. P.; Weinhold, F. Natural Hybrid Orbitals. *J. Am. Chem. Soc.* **1980**, *102*, 7211–7218. https://doi.org/10.1021/ja00544a007
(21) Davidson, E. R.; Chakravorty, S. A Test of the Hirshfeld Definition of Atomic Charges and Moments. *Theoret. Chim. Acta* **1992**, *83*, 319–330. https://doi.org/10.1007/BF01113058
(22) Mulliken, R. S. Electronic Population Analysis on LCAO–MO Molecular Wave Functions. II. Overlap Populations, Bond Orders, and Covalent Bond Energies. *J. Chem. Phys.* **1955**, *23*, 1841–1846. https://doi.org/10.1063/1.1740589
(23) Hirshfeld, F. L. Bonded-Atom Fragments for Describing Molecular Charge Densities. *Theor. Chim. Acta.* **1977**, *44*, 129–138. https://doi.org/10.1007/BF00549096
(24) Lu, T.; Chen, F. Atomic Dipole Moment Corrected Hirshfeld Population Method. *J. Theor. Comput. Chem.* **2012**, *11*, 163–183. https://doi.org/10.1142/S0219633612500113
(25) Hu, B.; Liu, T. L. Two Electron Utilization of Methyl Viologen Anolyte in Nonaqueous Organic Redox Flow Battery. *Journal of Energy Chemistry* **2018**, *27*, 1326–1332. https://doi.org/10.1016/j.jechem.2018.02.014
(26) Luo, J.; Hu, B.; Debruler, C.; Liu, T. L. A π-Conjugation Extended Viologen as a Two-Electron Storage Anolyte for Total Organic Aqueous Redox Flow Batteries. *Angew. Chem. Int. Ed.* **2018**, *57* , 231–235. https://doi.org/10.1002/anie.201710517
(27) Huang, J.; Hu, S.; Yuan, X.; Xiang, Z.; Huang, M.; Wan, K.; Piao, J.; Fu, Z.; Liang, Z. Radical Stabilization of a Tripyridinium–Triazine Molecule Enables Reversible Storage of Multiple Electrons. *Angew Chem Int Ed* **2021**, *60*, 20921–20925. https://doi.org/10.1002/anie.202107216
(28) Blackman, L. D.; Gunatillake, P. A.; Cass, P.; Locock, K. E. S. An Introduction to Zwitterionic Polymer Behavior and Applications in Solution and at Surfaces. *Chem. Soc. Rev.* **2019**, *48*, 757–770. https://doi.org/10.1039/C8CS00508G
(29) Li, H.; Fan, H.; Hu, B.; Hu, L.; Chang, G.; Song, J. Spatial Structure Regulation: A Rod-Shaped Viologen Enables Long Lifetime in Aqueous Redox Flow Batteries. *Angew. Chem. Int. Ed.* **2021**, *60*, 26971–26977. https://doi.org/10.1002/anie.202110010
(30) Wiberg, C.; Owusu, F.; Wang, E.; Ahlberg, E. Electrochemical Evaluation of a Napthalene Diimide Derivative for Potential Application in Aqueous Organic Redox Flow Batteries. *Energy Technol.* **2019**, *7*, 1900843. https://doi.org/10.1002/ente.201900843
(31) Zhao, Z.; Zhang, B.; Schrage, B. R.; Ziegler, C. J.; Boika, A. Investigations Into Aqueous Redox Flow Batteries Based on Ferrocene Bisulfonate. *ACS Appl. Energy Mater.* **2020**, *3*, 10270–10277. https://doi.org/10.1021/acsaem.0c02259
(32) Poli, N.; Trovò, A.; Fischer, P.; Noack, J.; Guarnieri, M. Electrochemical Rebalancing Process for Vanadium Flow Batteries: Sizing and Economic Assessment. *Journal of Energy Storage* **2023**, *58*, 106404. https://doi.org/10.1016/j.est.2022.106404
(33) Escudero-Cid, R.; Montiel, M.; Sotomayor, L.; Loureiro, B.; Fatás, E.; Ocón, P. Evaluation of Polyaniline-Nafion ® Composite Membranes for Direct Methanol Fuel

Cells Durability Tests. *International Journal of Hydrogen Energy* **2015**, *40*, 8182–8192. https://doi.org/10.1016/j.ijhydene.2015.04.130

(34) Singh, R. K.; Kunimatsu, K.; Miyatake, K.; Tsuneda, T. Experimental and Theoretical Infrared Spectroscopic Study on Hydrated Nafion Membrane. *Macromolecules* **2016**, *49*, 6621–6629. https://doi.org/10.1021/acs.macromol.6b00999

(35) Melnikov, S.; Shkirskaya, S. Transport Properties of Bilayer and Multilayer Surface-Modified Ion-Exchange Membranes. *Journal of Membrane Science* **2019**, *590*, 117272. https://doi.org/10.1016/j.memsci.2019.117272

(36) Feng, C.; Li, Y.; Qu, K.; Zhang, Z.; He, P. Mechanical Behavior of a Hydrated Perfluorosulfonic Acid Membrane at Meso and Nano Scales. *RSC Adv.* **2019**, *9*, 9594–9603. https://doi.org/10.1039/C9RA00745H

(37) Kundu, S.; Simon, L. C.; Fowler, M.; Grot, S. Mechanical Properties of Nafion™ Electrolyte Membranes under Hydrated Conditions. *Polymer* **2005**, *46*, 11707–11715. https://doi.org/10.1016/j.polymer.2005.09.059

(38) Vandiver, M. A.; Caire, B. R.; Pandey, T. P.; Li, Y.; Seifert, S.; Kusoglu, A.; Knauss, D. M.; Herring, A. M.; Liberatore, M. W. Effect of Hydration on the Mechanical Properties and Ion Conduction in a Polyethylene-b-Poly(Vinylbenzyl Trimethylammonium) Anion Exchange Membrane. *Journal of Membrane Science* **2016**, *497*, 67–76. https://doi.org/10.1016/j.memsci.2015.09.034

(39) Ehrenbeck, C.; Jüttner, K. Ion Conductivity and Permselectivity Measurements of Polypyrrole Membranes at Variable States of Oxidation. *Electrochimica Acta* **1996**, *41*, 1815–1823. https://doi.org/10.1016/0013-4686(95)00500-5

(40) Vega, J. A.; Chartier, C.; Mustain, W. E. Effect of Hydroxide and Carbonate Alkaline Media on Anion Exchange Membranes. *Journal of Power Sources* **2010**, *195*, 7176–7180. https://doi.org/10.1016/j.jpowsour.2010.05.030

(41) Kreuer, K.-D.; Jannasch, P. A Practical Method for Measuring the Ion Exchange Capacity Decrease of Hydroxide Exchange Membranes during Intrinsic Degradation. *Journal of Power Sources* **2018**, *375*, 361–366. https://doi.org/10.1016/j.jpowsour.2017.07.106

(42) Andrieux, C. P.; Audebert, P.; Hapiot, P.; Saveant, J.-M. Identification of the First Steps of the Electrochemical Poiymerizatlon of Pyrroles by Means of Fast Potential Step Technlques. *J. Phys. Chem.* **1991**, *95*¸10158–10164. https://doi.org/10.1021/j100177a096

(43) Santos, M. J. L.; Brolo, A. G.; Girotto, E. M. Study of Polaron and Bipolaron States in Polypyrrole by in Situ Raman Spectroelectrochemistry. *Electrochimica Acta* **2007**, *52*, 6141–6145. https://doi.org/10.1016/j.electacta.2007.03.070

(44) Liu, Y.-C.; Hwang, B.-J. Identification of Oxidized Polypyrrole on Raman Spectrum. *Synthetic Metals* **2000**, *113*, 203–207. https://doi.org/10.1016/S0379-6779(00)00188-0

(45) Stejskal, J.; Trchová, M.; Bober, P.; Morávková, Z.; Kopecký, D.; Vrňata, M.; Prokeš, J.; Varga, M.; Watzlová, E. Polypyrrole Salts and Bases: Superior Conductivity of Nanotubes and Their Stability towards the Loss of Conductivity by Deprotonation. *RSC Adv.* **2016**, *6*, 88382–88391. https://doi.org/10.1039/C6RA19461C

(46) Grosse Austing, J.; Nunes Kirchner, C.; Komsiyska, L.; Wittstock, G. Layer-by-Layer Modification of Nafion Membranes for Increased Life-Time and Efficiency of Vanadium/Air Redox Flow Batteries. *Journal of Membrane Science* **2016**, *510*, 259–269. https://doi.org/10.1016/j.memsci.2016.03.005

(47) Arnbjerg, J.; Khataee, A.; Breitenbach, T.; Thøgersen, J.; Christiansen, S.; Gavlshøj Mortensen, H.; Bilde, M.; Frøhlich Hougaard, R.; Bentien, A. Battery Concepts in Physical Chemistry: Making Your Own Organic–Inorganic Battery. *J. Chem. Educ.* **2019**, *96*, 1465–1471. https://doi.org/10.1021/acs.jchemed.9b00090

(48) Ghimire, P. C.; Bhattarai, A.; Lim, T. M.; Wai, N.; Skyllas-Kazacos, M.; Yan, Q. In-Situ Tools Used in Vanadium Redox Flow Battery Research—Review. *Batteries* **2021**, *7*, 53. https://doi.org/10.3390/batteries7030053

(49) Li, M.; Odom, S. A.; Pancoast, A. R.; Robertson, L. A.; Vaid, T. P.; Agarwal, G.; Doan, H. A.; Wang, Y.; Suduwella, T. M.; Bheemireddy, S. R.; Ewoldt, R. H.; Assary, R. S.; Zhang, L.; Sigman, M. S.; Minteer, S. D. Experimental Protocols for Studying Organic Non-Aqueous Redox Flow Batteries. *ACS Energy Lett.* **2021**, *6*, 3932–3943. https://doi.org/10.1021/acsenergylett.1c01675

(50) Huskinson, B.; Marshak, M. P.; Suh, C.; Er, S.; Gerhardt, M. R.; Galvin, C. J.; Chen, X.; Aspuru-Guzik, A.; Gordon, R. G.; Aziz, M. J. A Metal-Free Organic–Inorganic Aqueous Flow Battery. *Nature* **2014**, *505*, 195–198. https://doi.org/10.1038/nature12909

(51) Wiberg, C.; Busch, M.; Evenäs, L.; Ahlberg, E. The Electrochemical Response of Core-Functionalized Naphthalene Diimides (NDI) – a Combined Computational and Experimental Investigation. *Electrochimica Acta* **2021**, *367*, 137480. https://doi.org/10.1016/j.electacta.2020.137480

(52) Yao, Y.; Lei, J.; Shi, Y.; Ai, F.; Lu, Y.-C. Assessment Methods and Performance Metrics for Redox Flow Batteries. *Nat Energy* **2021**, *6*, 582–588. https://doi.org/10.1038/s41560-020-00772-8

(53) Kwabi, D. G.; Lin, K.; Ji, Y.; Kerr, E. F.; Goulet, M.-A.; De Porcellinis, D.; Tabor, D. P.; Pollack, D. A.; Aspuru-Guzik, A.; Gordon, R. G.; Aziz, M. J. Alkaline Quinone Flow Battery with Long Lifetime at PH 12. *Joule* **2018**, *2*, 1894–1906. https://doi.org/10.1016/j.joule.2018.07.005

(54) Mazur, P.; Mrlik, J.; Charvat, J.; Pocedic, J.; Vrana, J.; Dundalek, J.; Kosek, J. A Complex Four-Point Method for the Evaluation of Ohmic and Faradaic Losses within a Redox Flow Battery Single-Cell. *MethodsX* **2019**, *6*, 534–539. https://doi.org/10.1016/j.mex.2019.03.007

(55) Fell, E. M.; De Porcellinis, D.; Jing, Y.; Gutierrez-Venegas, V.; Gordon, R. G.; Granados-Foncil, S.; Aziz, M. J. Long-Term Stability of Ferri-/Ferrocyanide as an Electroactive Component for Redox Flow Battery Applications: On the Origin of Apparent Capacity Fade. *J. Electrochem. Soc.* **2023** (accepted) https://doi.org/10.1149/1945-7111/ace936

(56) Páez, T.; Martínez-Cuezva, A.; Marcilla, R.; Palma, J.; Ventosa, E. Mitigating Capacity Fading in Aqueous Organic Redox Flow Batteries through a Simple Electrochemical Charge Balancing Protocol. *Journal of Power Sources* **2021**, *512*, 230516. https://doi.org/10.1016/j.jpowsour.2021.230516

(57) Beh, E. S.; De Porcellinis, D.; Gracia, R. L.; Xia, K. T.; Gordon, R. G.; Aziz, M. J. A Neutral PH Aqueous Organic–Organometallic Redox Flow Battery with Extremely High Capacity Retention. *ACS Energy Lett.* **2017**, *2*, 639–644. https://doi.org/10.1021/acsenergylett.7b00019

(58) Jiang, S.; Sun, H.; Wang, H.; Ladewig, B. P.; Yao, Z. A Comprehensive Review on the Synthesis and Applications of Ion Exchange Membranes. *Chemosphere* **2021**, *282*, 130817. https://doi.org/10.1016/j.chemosphere.2021.130817

(59) Kwabi, D. G.; Ji, Y.; Aziz, M. J. Electrolyte Lifetime in Aqueous Organic Redox Flow Batteries: A Critical Review. *Chem. Rev.* **2020**, *120*, 6467–6489. https://doi.org/10.1021/acs.chemrev.9b00599

(60) Liu, Y.; Goulet, M.-A.; Tong, L.; Liu, Y.; Ji, Y.; Wu, L.; Gordon, R. G.; Aziz, M. J.; Yang, Z.; Xu, T. A Long-Lifetime All-Organic Aqueous Flow Battery Utilizing TMAP-TEMPO Radical. *Chem* **2019**, *5*, 1861–1870. https://doi.org/10.1016/j.chempr.2019.04.021

(61) Ding, J.; Zheng, C.; Wang, L.; Lu, C.; Zhang, B.; Chen, Y.; Li, M.; Zhai, G.; Zhuang, X. Viologen-Inspired Functional Materials: Synthetic Strategies and Applications. *J. Mater. Chem. A* **2019**, *7*, 23337–23360. https://doi.org/10.1039/C9TA01724K

(62) Venturi, M.; Mulazzani, Q. G.; Hoffman, M. Z. Radiolytically-Induced One-Electron Reduction of Methyl Viologen in Aqueous Solution. *Radiation Physics and Chemistry (1977)* **1984**, *23*, 229–236. https://doi.org/10.1016/0146-5724(84)90113-4

(63) Kapoor, M.; Verma, A. Technical Benchmarking and Challenges of Kilowatt Scale Vanadium Redox Flow Battery. *WIREs Energy & Environment* **2022**, *11*. https://doi.org/10.1002/wene.439

(64) Xiang, Z.; Li, W.; Wan, K.; Fu, Z.; Liang, Z. Aggregation of Electrochemically Active Conjugated Organic Molecules and Its Impact on Aqueous Organic Redox Flow Batteries. *Angew Chem Int Ed* **2023**, *62*. https://doi.org/10.1002/anie.202214601

6. Conclusions / Conclusiones

6. Conclusions

This PhD research focuses on three main areas: i) Developing new anolytes for redox flow batteries. ii) Selecting, characterizing, and modifying Ion Exchange Membranes. iii) Testing single-cell redox flow batteries from the developed anolytes.

Conclusions are presented based on these topics, providing valuable insights into each aspect of the study:

6.1. Development of new anolytes:

1) Successfully synthesized 1,1'-1,3-propylene-2,2'-bipyridinium salts with remarkable properties for RFB applications, including high water solubility (up to 2.8 M) and low redox potentials (*ca*. -0.7 V *vs* SHE). Conducted DFT calculations to study the role of structural parameters and substituents, providing insights into electrochemical properties such as redox potential and kinetic constants. Introduced a novel strategy using NBO and ADCH charge analysis to investigate the stability of active materials, leading to the identification of compound **4** as the most stable anolyte candidate for AORFB due to its delocalization and charge distribution.

2) Accomplished an efficient and cost-effective synthesis of a triazine derivative **(SPr)$_3$4TpyTz**, reducing the number of counterion exchanges compared to reported methods. Electrochemical characterization revealed three reversible redox processes at different potentials (-0.47 V, -0.62 V, and -0.82 V *vs* Ag|AgCl (3 M KCl)), indicating its potential as a multiple-electron storage anolyte for RFB. The compound exhibited fast kinetics, high solubility (>0.9 M), and sensitivity to supporting electrolyte concentration.

6.2. Selection, characterization and modification of IEM:

1) Conducted electrochemical characterization of commercially available membranes and separators. Investigated different modification methods, including *in situ* polymerization and Layer-by-Layer techniques, to improve membrane properties by reducing permeability of redox-active materials. Among these, *in situ* polymerization of pyrrole significantly decreased the permeation of RAM without increasing membrane resistance, yielding homogeneous materials. Studied modified versions of selected membranes to understand the effects of modification on transport phenomena.

6.3. Single-cell results:

1) Developed a strong correlation between fundamental theory and main characterization techniques using a well-known system (AQDS as anolyte, $Na_4[Fe(CN)_6]$ as catholyte, Nafion 212® membrane). This initial work provided

insights into the impact of experimental parameters, including pH variation in the electrolyte, O_2 permeation, IEM activation, and capacity-limiting side.

2) Validated the predicting model developed in **Chapter 1** through experimental results, comparing the stability of Compound **2** and **4** in single-cell (0.75%/day *vs* 0.16%/day capacity decay). As anticipated by the model, Compound **4** demonstrated greater stability. Additionally, studied the proton-catalyzed disproportionation of 2,2'-bipyridinium, characterizing side products using NMR, UV-Vis, and CV.

3) Examined the capacity of **$(SPr)_3$4TpyTz** to store multiple electrons. A battery at 100 mM of the triazine anolyte *vs* 100 mM $K_4[Fe(CN)_6]$ showed no capacity decay and achieved an energy efficiency of approximately 75% under suitable conditions. Investigated the role of the supporting electrolyte in the solubility of reduced states of the triazine derivatives. A more concentrated battery (200 mM of **$(SPr)_3$4TpyTz** *vs* 100 mM $K_4[Fe(CN)_6]$) demonstrated a small capacity decay of 0.44%/day and no crossover in 14 days. Furthermore, studied the system using the third and fourth electron, revealing significant capacity decay and an increase in electrolyte pH, suggesting a degradation mechanism through protonation of the reduced triazine.

6. Conclusiones

La investigación de esta tesis doctoral se centra en tres áreas: i) El desarrollo de nuevos anolitos para baterías de flujo redox. ii) La selección, caracterización y modificación de membranas de intercambio iónico. iii) La evaluación en batería de flujo redox, monocelda, de los anolitos desarrollados.

Las conclusiones se presentan en base a los anteriores puntos proporcionando información valiosa sobre cada aspecto del estudio:

6.1. Desarrollo de nuevos anolitos:

1) Se han sintetizado sales de 1,1'-1,3-propilen-2,2'-bipridinio con notables propiedades para su aplicación en baterías de flujo redox, incluyendo alta solubilidad en agua (hasta 2.8 M) y bajos potenciales redox (*ca.* -0.7 V *vs* SHE). Se han realizado estudios DFT con el fin de estudiar el efecto tanto de los parámetros estructurales como de los sustituyentes en las propiedades electroquímicas tales como el potencial redox y las constantes cinéticas. Se ha desarrollado una nueva estrategia utilizando el análisis de los orbitales NBO y las cargas ADCH para investigar la estabilidad de los materiales activos, identificando así el compuesto **4**, como el candidato más estable para uso en baterías de flujo redox acuosas orgánicas debido a la deslocalización y distribución de carga en dicho compuesto.

2) Se ha conseguido desarrollar una síntesis eficiente y económicamente viable de un nuevo derivado de triazina **(SPr)$_3$4TpyTz**, reduciendo el número de intercambio de contraiones comparado con otros métodos reportados. La caracterización electroquímica ha revelado tres procesos redox reversibles a diferentes potenciales (-0.47 V, -0.62 V, and -0.82 V *vs* Ag|AgCl (3 M KCl)), demostrando su viabilidad como anolito para el almacenamiento de múltiples electrones para baterías de flujo redox. El compuesto exhibió rápidas cinéticas, altas solubilidades (>0.9 M) y sensibilidad a la concentración de electrolito soporte.

6.2. Selección, caracterización y modificación de membranas de intercambio iónico:

1) Se ha realizado la caracterización electroquímica de membranas y separadores comercialmente disponibles. Se han investigado diferentes métodos de modificación incluyendo las técnicas de polimerización *in situ* y *Layer-by-Layer* para mejorar las propiedades de las membranas reduciendo su permeabilidad a materiales activos redox. De estos métodos, la polimerización *in situ* de polipirrol consiguió reducir de manera significativa la permeación de materiales redox activos sin aumentar su resistencia, obteniéndose además materiales homogéneos. Las versiones modificadas de las membranas seleccionadas se han estudiado para entender el efecto que la modificación tiene en el fenómeno de transporte.

6.3. Resultados de monocelda:

1) Se ha desarrollado una fuerte correlación entre la teoría fundamental y las principales técnicas de caracterización usando un conocido sistema (AQDS como anolito y $Na_4[Fe(CN)_6]$ como catolito, Nafion 212® como membrana). Este trabajo inicial ha proporcionado conocimiento del impacto de parámetros experimentales incluyendo la variación del pH en el electrolito, la permeación de O_2, la activación de la membrana de intercambio y el lado limitante de la capacidad.

2) Se ha validado el modelo predictivo desarrollado en el **Capítulo 1** mediante resultados experimentales comparando la estabilidad de los compuestos **2** y **4** en monocelda (0.75%/día *vs* 0.16%/día de pérdida de capacidad). Como se anticipó con el modelo, el compuesto **4** ha demostrado mayor estabilidad que el resto de los materiales activos. Adicionalmente, se ha estudiado la desproporción catalizada por protón de los compuestos 2,2'-bipiridinicos, caracterizando los subproductos usando el RMN, UV-Visible y voltametría cíclica.

3) Se ha estudiado la capacidad de **$(SPr)_3$4TpyTz** para almacenar múltiples electrones. Una batería con 100 mM de triazina como anolito *vs* 100 mM de $K_4[Fe(CN)_6]$ no mostro pérdida de capacidad, alcanzando una eficiencia energética en torno al 75% bajo las condiciones de operación. Se ha investigado el rol del electrolito soporte en la solubilidad de las especies reducidas de los derivados de triazina. Una batería más concentrada (200 mM de **$(SPr)_3$4TpyTz** como anolito *vs* 100 mM de $K_4[Fe(CN)_6]$ de catolito) mostro una ligera pérdida de capacidad de 0.44%/día y ningún *crossover* en 14 días. Además, se ha estudiado el sistema utilizando el tercer y cuarto electrón, revelándose una significante pérdida de capacidad y un aumento del pH en el electrolito, lo cual sugiere un mecanismo de degradación a través de la protonación de la triazina reducida.

7. List of abbreviations and acronyms

7. List of acronyms and abbreviations

(SPr_3)4TpyTz	3,3',3''-((1,3,5-triazine-2,4,6-triyl)tris(pyridine-1-ium-4,1-diyl))tris(propane-1-sulfonate)
A	Area
AC	Alternating Current
ACA	Alloxazine Carboxylate
ADCH	Atom Dipole Correction Hirshfeld
AEM	Anion Exchange Membrane
AORFB	Aqueous Organic Redox Flow Batteries
AQDS	Anthraquinone-2,6-disulfonate
$AQDSH_2$	Reduced Anthraquinone-2,6-disulfonate
ARFB	Aqueous Redox Flow Batteries
ASR	Area Specific Resistance
ATP	Adenosine Triphosphate
Bhmbpy	4,4'-(Bis(hydroxymethyl)-2,2'-bipyridine
bpy	2,2'-bipyridine
CD	Capacity Decay
CE	Coulombic Efficiency
CEM	Cation Exchange Membrane
CLS	Capacity Limiting Side
CNT	Carbon Nanotubes
CU	Capacity Utilization
CV	Cyclic Voltammetry
CVD	Chemical Vapor Deposition
D	Diffusion coefficient

7. List of abbreviations and acronyms

DC	Direct Current
Dcbpy	2,2'-bipyridine-4,4'-dicarboxylic acid
DFT	Density Functional Theory
DPV	Differential Pulse Voltammetry
DR	Diffuse reflectance
DSA	Dimensionally Stable Anode
E^o	Standard Redox potential
$E_{1/2}$	Half Wave Potential
EDG	Electron Donating Group
EDTA	Ethylenediaminetetraacetate
EDX	Energy Dispersive X-Ray Analysis
EE	Energy Efficiency
EIS	Electrochemical Impedance Spectroscopy
E_p	Peak potential
$E_{p,a}$	Anodic peak potential
E_{pc}	Cathodic peak potential
ESS	Energy Storage Systems
EWG	Electron Withdrawing Group
FRA	Frequency Response Analyzer
FTIR	Fourier Transform Infrared Spectroscopy
HDPE	High-Density Polyethylene
HF	Hartree Fock
HIGREEW	Affordable High-performance Green REdox floW batteries
HMBC	Heteronucelar Multi Bond Correlation

I	current
IEC	Ion Exchange Capacity
IEM	Ion Exchange Membrane
$\mathbf{i_L}$	Limitting current
j	current density
k^o	Standard rate constant
KS	Kohn-Shan
λ	Marcus Parameter
LbL	Layer-by-Layer
LC	Load Curves
LIB	Lithium-Ion Batteries
LSV	Linear Sweep Voltammetry
MD	Molecular Dynamics
MWCNT	Multi-Walled Carbon Nanotubes
NARFB	Non-Aqueous Redox Flow Batteries
NASA	National Aeronautics and Space Adminstration
NBO	Natural Bond Orbitals
NDI	Naphtalene Diimide
NMR	Nuclear Magnetic Resonance
NOESY	Nuclear Overhauser Effect Spectroscopy
OCV	Open Circuit Voltage
P	Permeability
PANI	Polyaniline
PCET	Proton Coupled Electron Transfer

7. List of abbreviations and acronyms

PE	Polyethylene
PEI	Polyethyleneimide
PFSA	Perfluorosulfonic Acid
PhD	Doctorate of Philosophy
ppm	parts per million
PPy	Polypyrrole
P_s	Permselectivity
PTFE	Polytetrafluoroethylene
PVA	Polyvinyl Alcohol
PVC	Polyvinylchloride
PVDF	Polyvinyldene Fluoride
Q	Capacity
r	Bond distance
R	Resistance
RAM	Redox Active Material
R_{char}	Charge Resistance
RDE	Rotatory Disk Electrode
R_{disch}	Discharge Resistance
RFB	Redox Flow Batteries
R_{ohm}	Ohmnic Resistance
SCF	Self-Consistent Field
SEM	Scanning Electron Microscopy
SIB	Sodium-Ion Batteries
σ	Ionic conductivity

SMD	Solvent Model based on Density
SOC	State of Charge
SR	Swelling Ratio
τ	Transition time
τ_1^o	Dihedral angle
TEMPO	(2,2,6,6-Tetramethylpiperidin-1-yl)oxyl
TEMPOL	(4-hydroxy-2,2,6,6-Tetramethylpiperidin-1-yl)oxyl
θ	Contact angle
TMA	Trimethylammonium
TPT	2,4,6-tri(pyridin-4-yl)-1,3,5-triazine
$\mathbf{U_{cell}}$	Cell potential
UV-Vis	Ultraviolet - Visible Spectroscopy
V	Voltage
VE	Voltage Efficiency
VRFB	All-Vamadium Redox Flow Battery
WU	Water Uptake
Z'	Real part of Impedance
Z''	Imaginary part of Impedance
γ_{LV}	liquid surface energy
γ_{SL}	solid-liquid surface energy
γ_{SV}	Solid surface energy

Annex A: NMR, RDE, solubilities, DFT calculations and cell testing extra information

Annex A: NMR, RDE, solubilities, DFT calculations and cell testing extra information.

^{1}H and ^{13}C NMR spectra of 2,2'-bipyridines 1-8

6,7-dihydrodipyrido[1,2-a:2'1'-c]pyrazine-5,8-diium bromide (**1**)

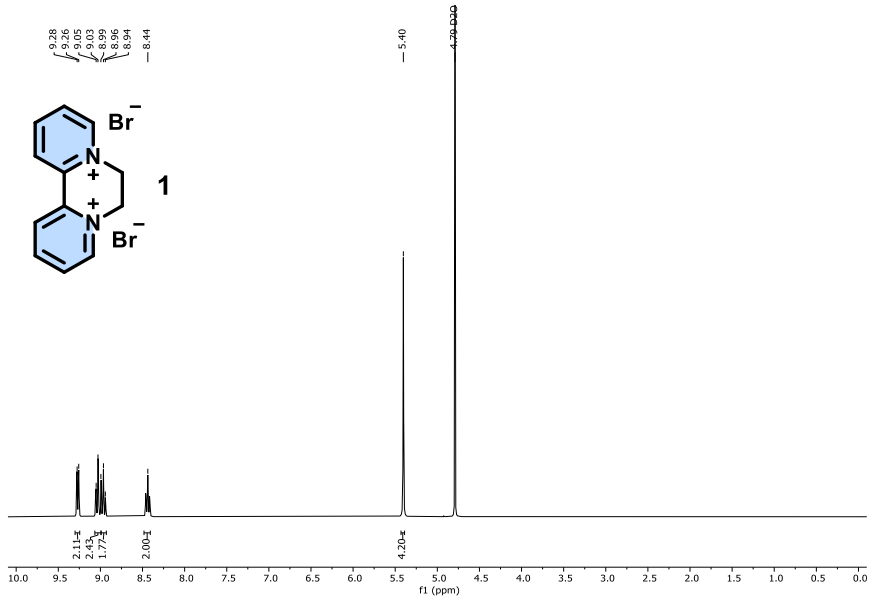

Figure S1: ^{1}H NMR spectrum of **1**.

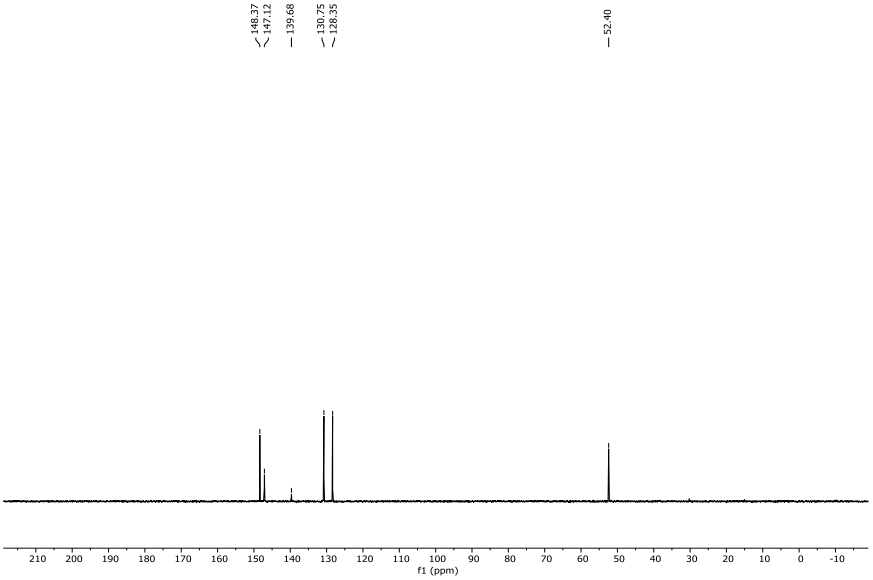

Figure S2: ^{13}C NMR spectrum of **1**.

6,7,8,9-tetrahydrodipyrido[1,2-a:2',1'-c][1,4]diazocine-5,10-diium bromide (**2**)

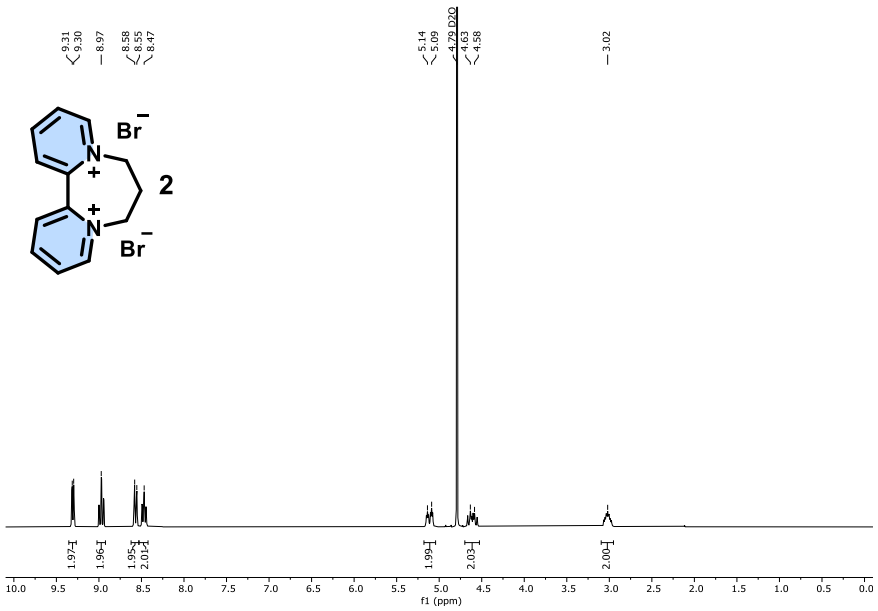

Figure S3: [1]H NMR spectrum of **2**.

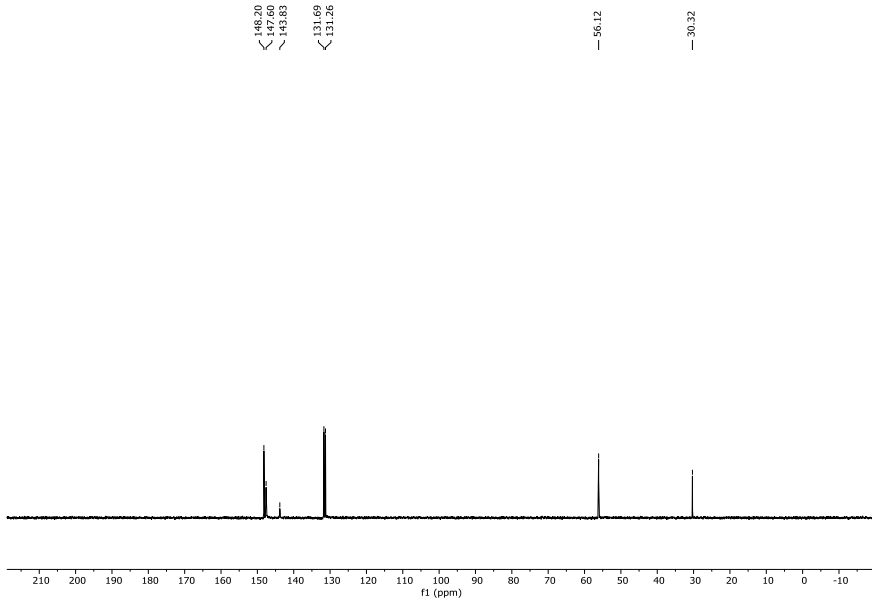

Figure S4: [13]C NMR spectrum of **2**.

6,7,8,9-tetrahydrodipyrido[1,2-a:2',1'-c][1,4]diazocine-5,10-diium bromide (**3**)

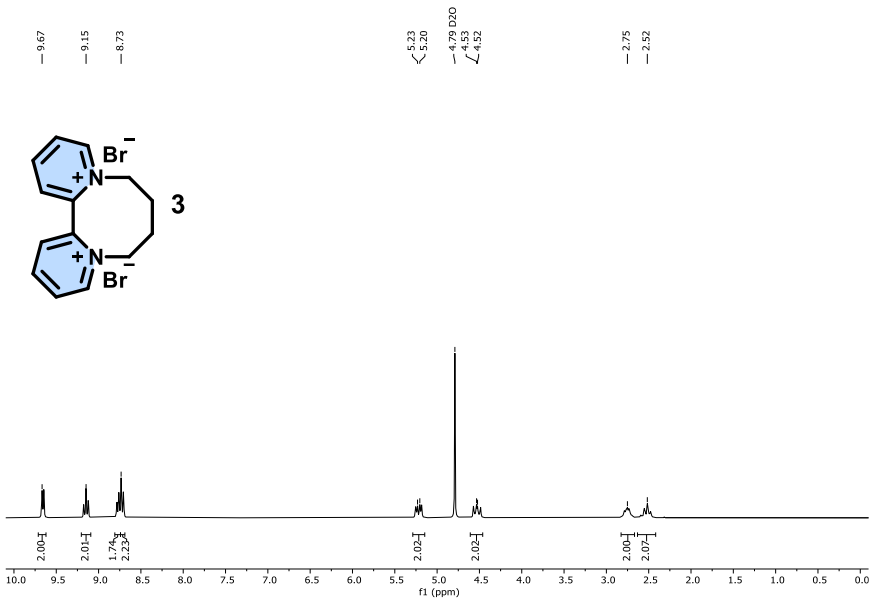

Figure S5: [1]H NMR spectrum of **3**.

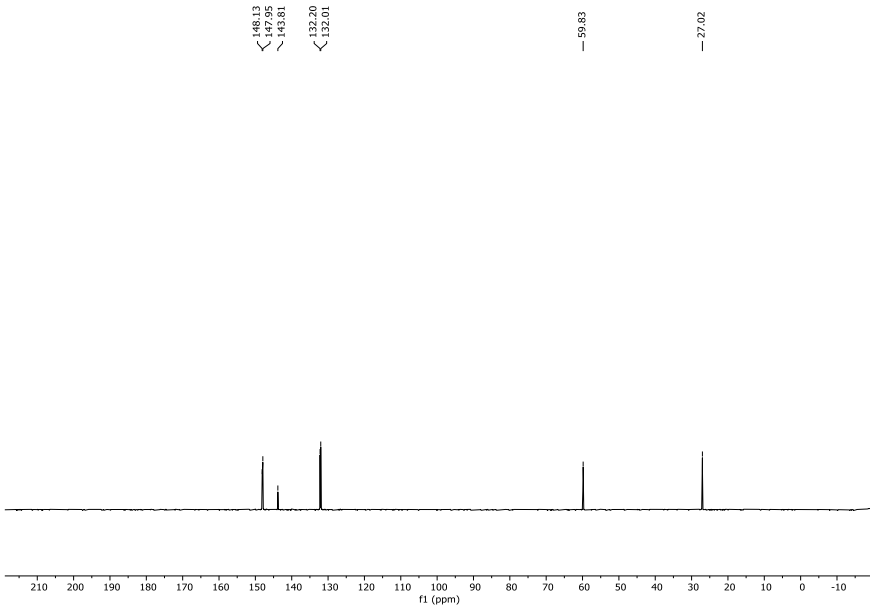

Figure S6: [13]C NMR spectrum of **3**.

3,11-dimethyl-7,8-dihydro-6H-dipyrido[1,2-a:2',1'-c][1,4]diazepine-5,9-diium bromide (**4**)

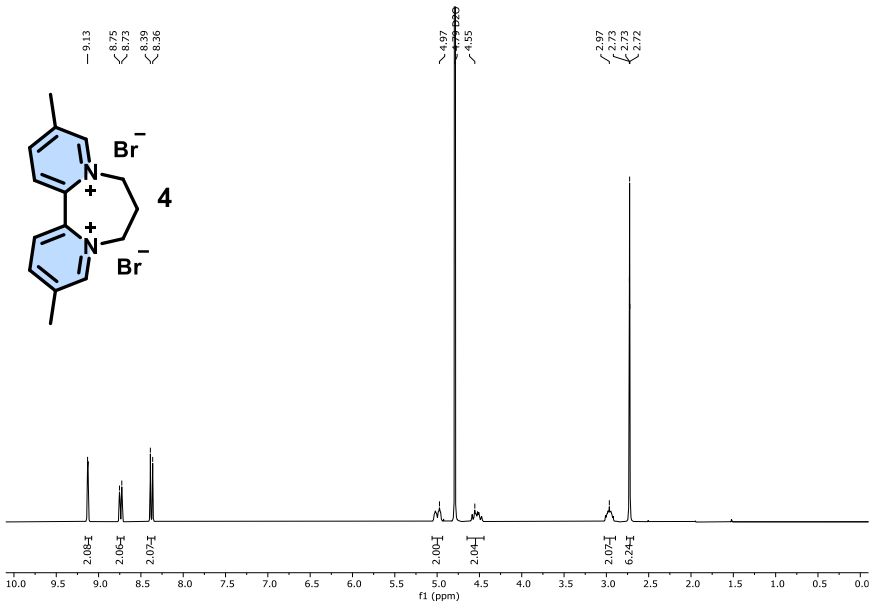

Figure S7: [1]H NMR spectrum of **4**.

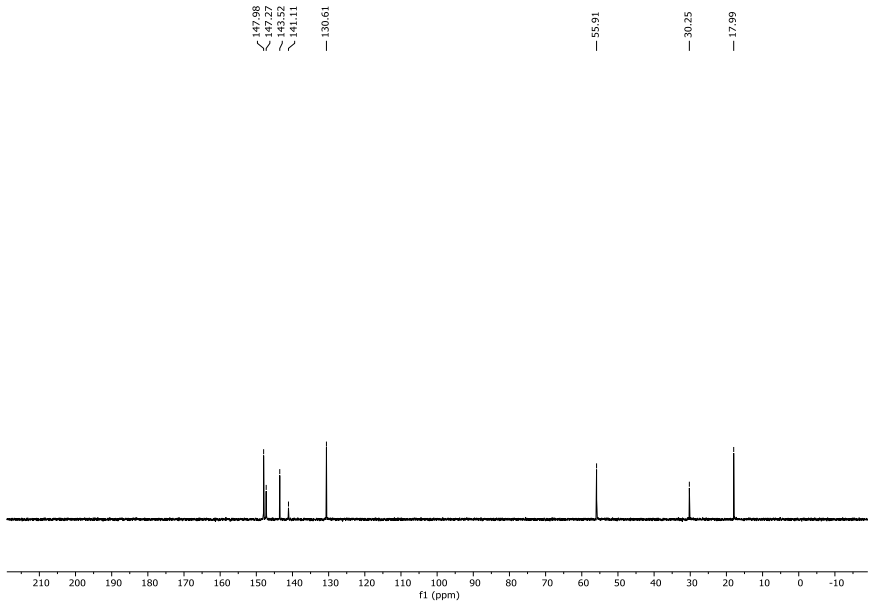

Figure S8: [13]C NMR spectrum of **4**.

2,12-dimethyl-7,8-dihydro-6H-dipyrido[1,2-a:2',1'-c]diazepine-5,9-diium bromide (**5**)

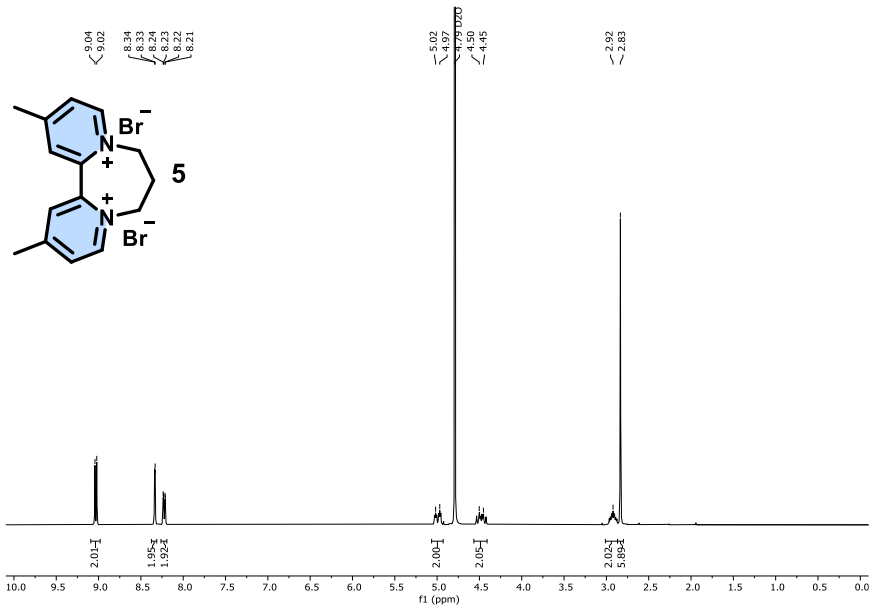

Figure S9: [1]H NMR spectrum of **5**.

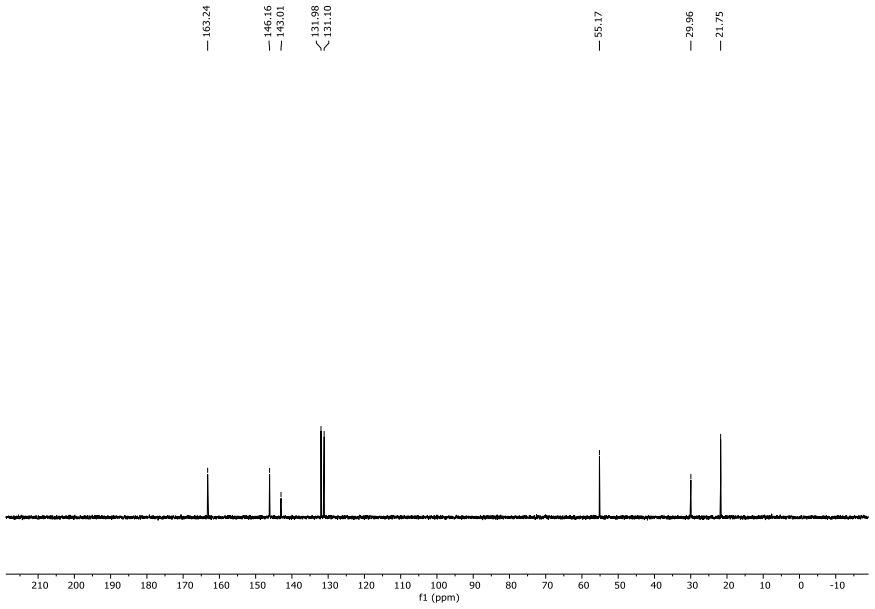

Figure S10: [13]C NMR spectrum of **5**.

2,12-dimethoxy-7,8-dihydro-6H-dipyrido[1,2-a:2',1'-c][1,4]diazepine-5,9-diium bromide (**6**)

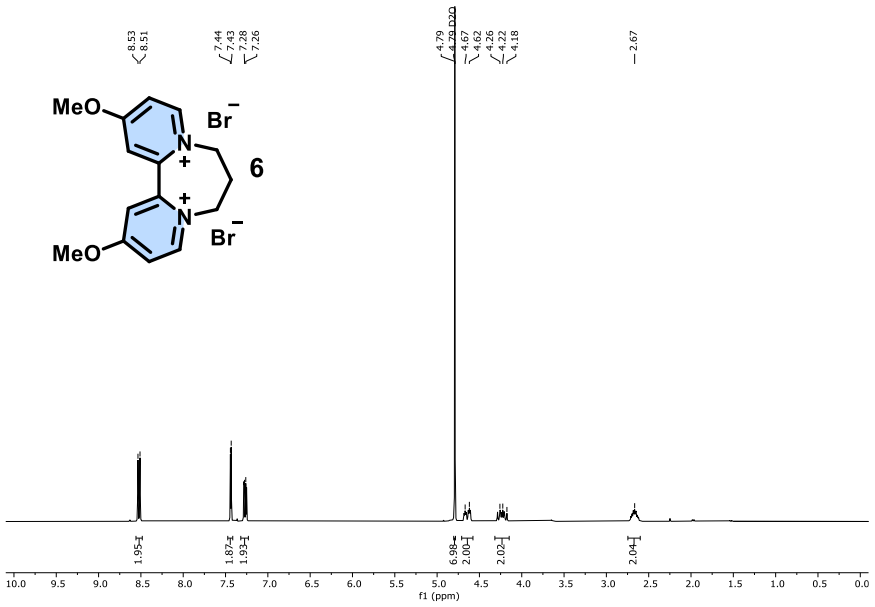

Figure S11: ^{1}H NMR spectrum of **6**.

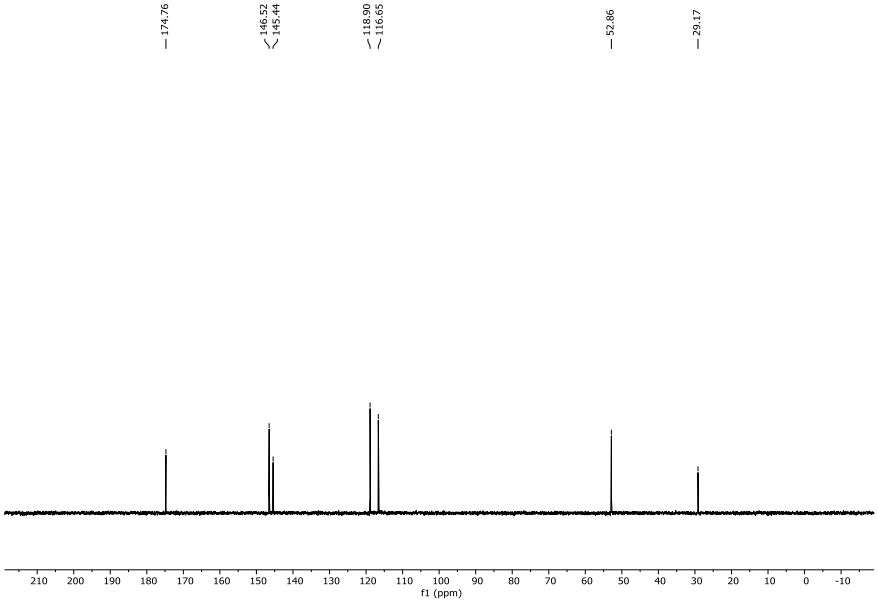

Figure S12: ^{13}C NMR spectrum of **6**.

2,12-dicarboxy-7,8-dihydro-6H-dipyrido[1,2-a:2',1'-c][1,4]diazepine-5,9-diium bromide (**7**)

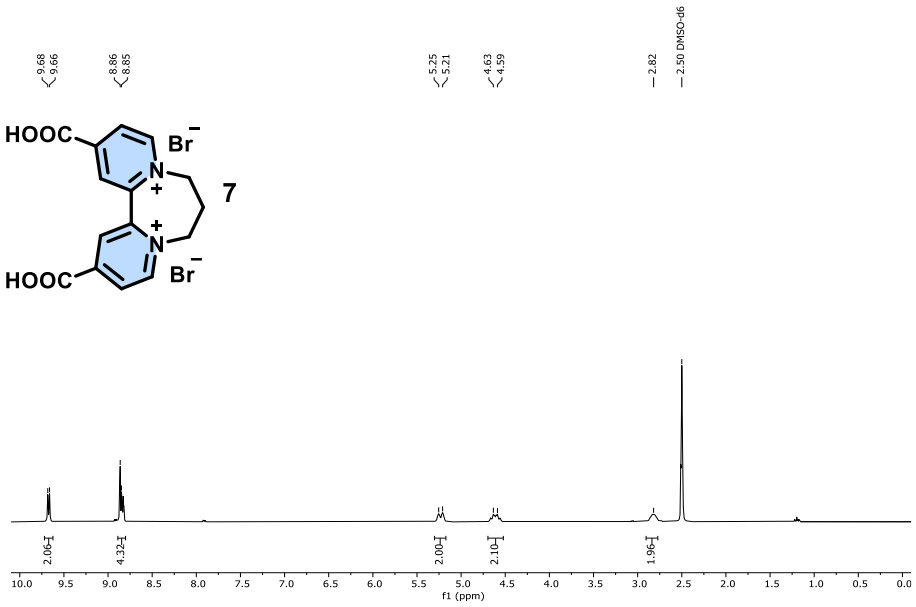

Figure S13: ^{1}H NMR spectrum of **7**.

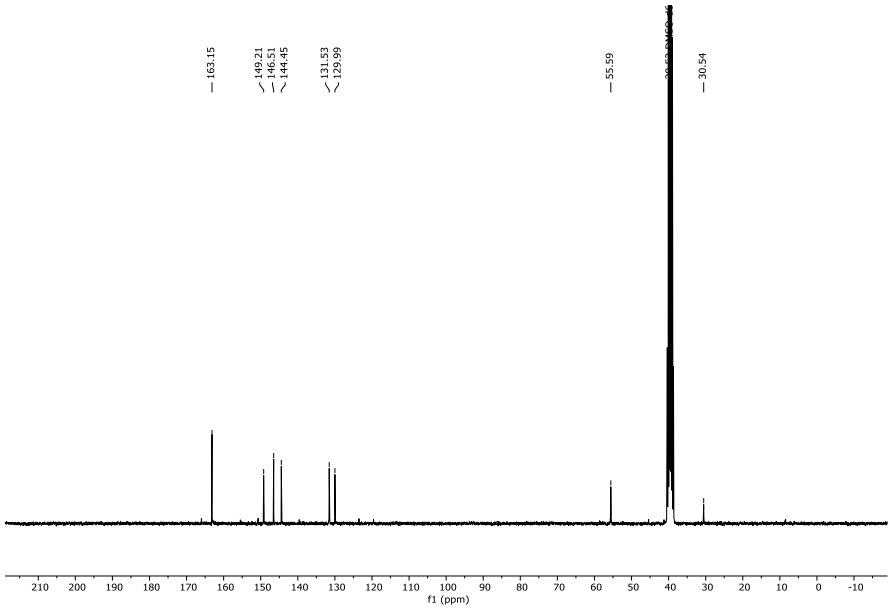

Figure S14: ^{13}C NMR spectrum of **7**.

2,3-dihydro-1H-[1,4]diazepino[1,2-a:4,3-a']diquinoline-4,17-diium bromide (**8**)

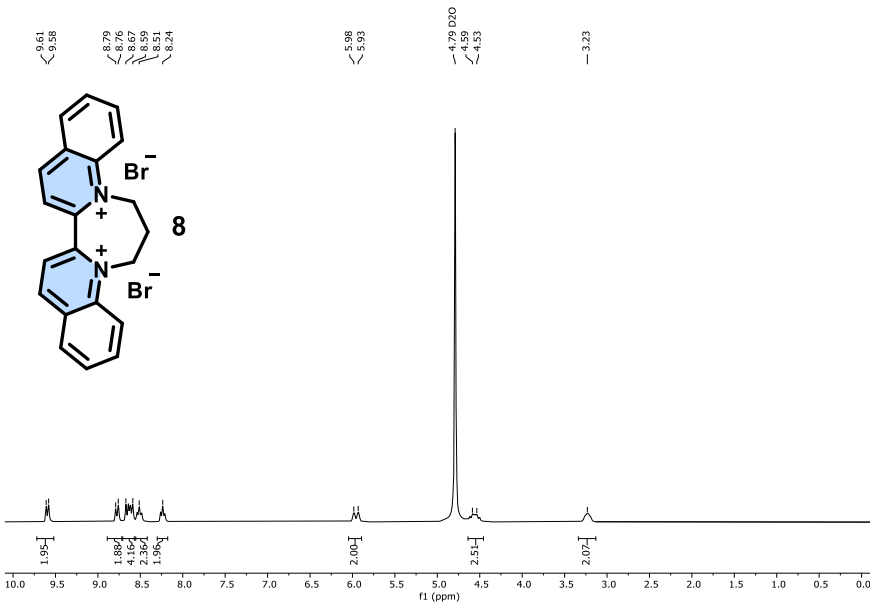

Figure S15: ^{1}H NMR spectrum of **8**.

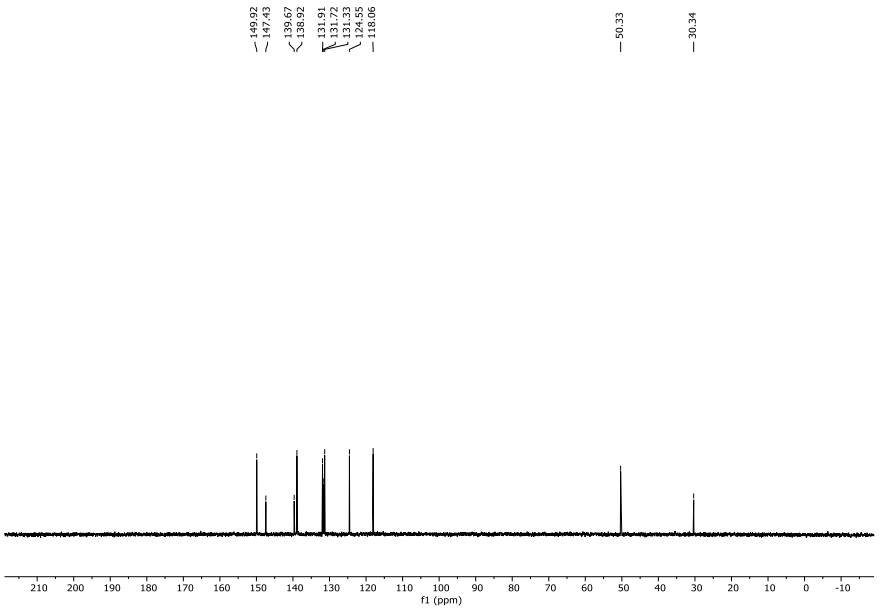

Figure S16: ^{13}C NMR spectrum of **8**.

Rotatory Disk Electrode (RDE) measurements for bipyridines.

Compound **1**

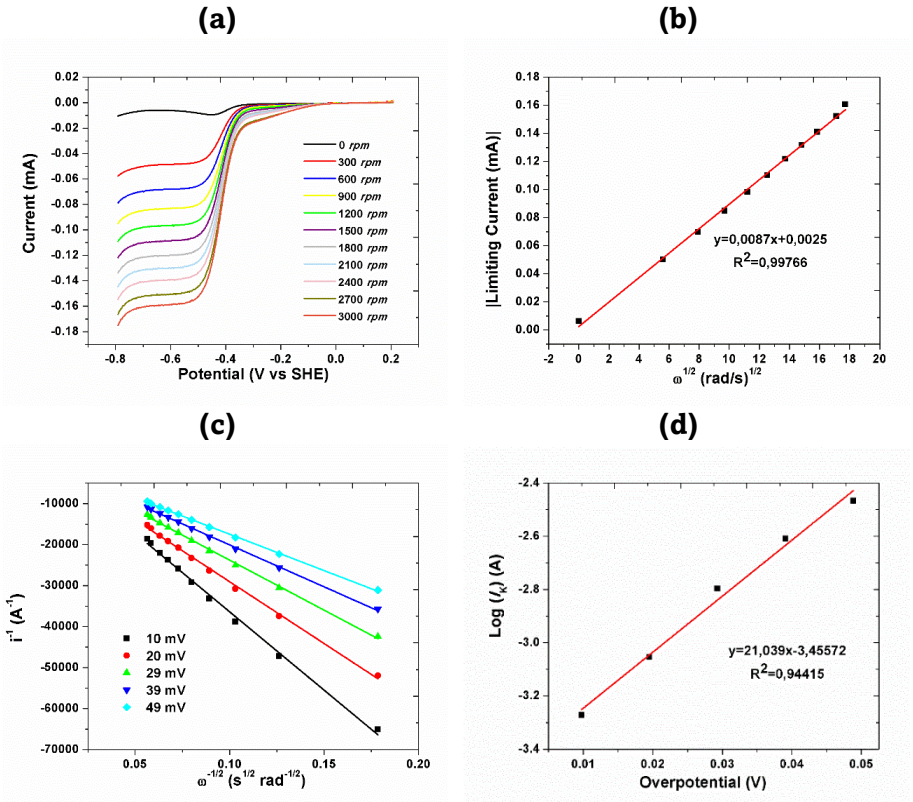

Figure S17: RDE analysis of **1**: (a) Linear Sweet Voltammetry (LSV) scans with rotating working electrode; (b) Levich analysis of the reduction; (c) Kouyecký-Levich plot (d) and Tafel-plot for different overpotentials.

Compound **2**

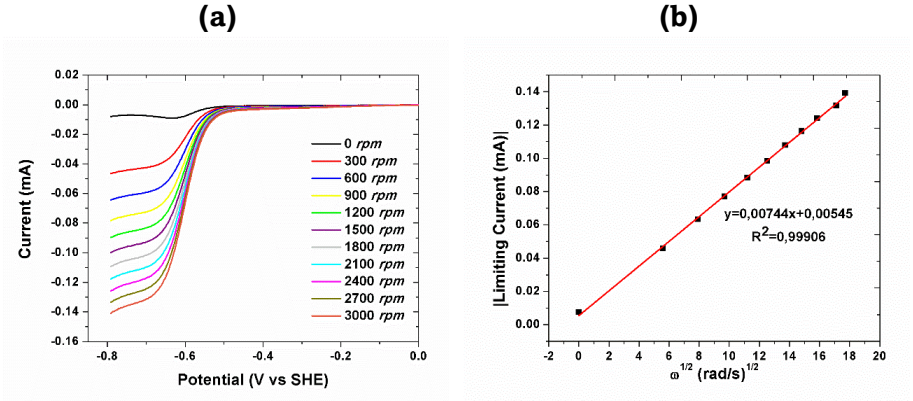

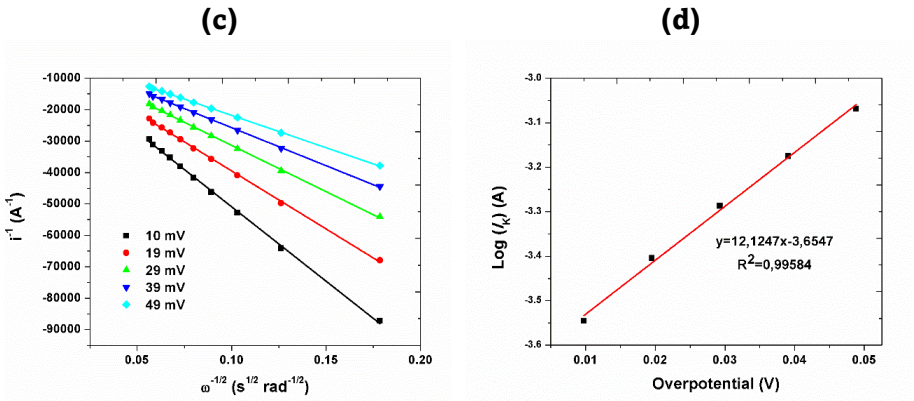

Figure S18: RDE analysis of **2**: (a) LSV scans with rotating working electrode; (b) Levich analysis of the reduction; (c) Kouyecký-Levich plot (d) and Tafel-plot for different overpotentials.

Compound **4**

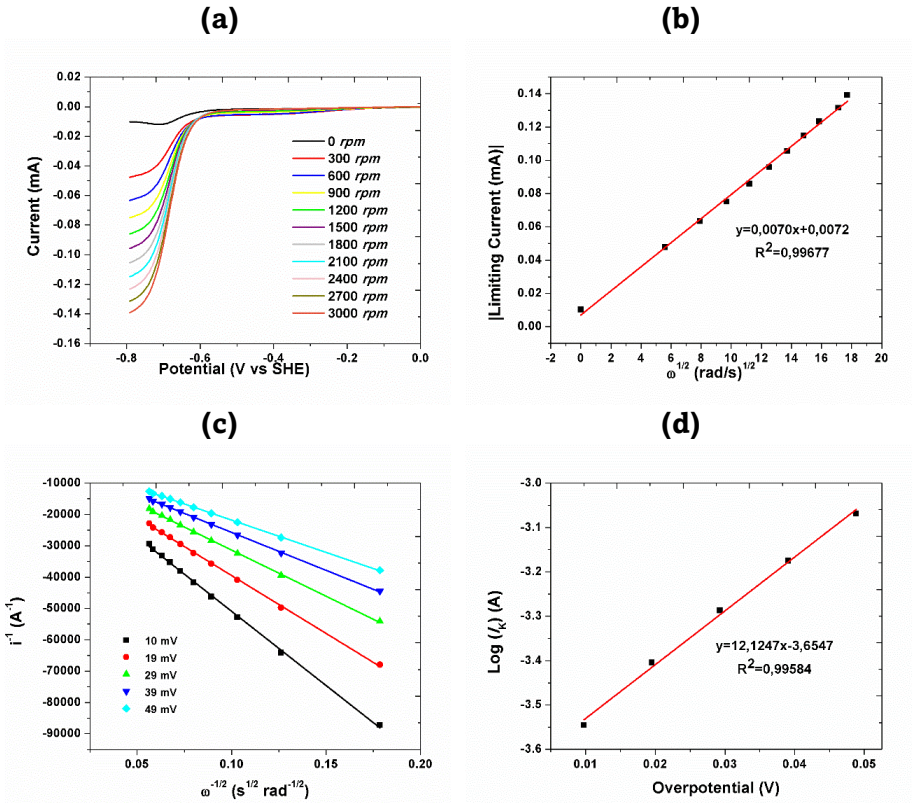

Figure S19: RDE analysis of **4**: (a) LSV scans with rotating working electrode; (b) Levich analysis of the reduction; (c) Kouyecký-Levich plot (d) and Tafel-plot for different overpotentials.

Compound **5**

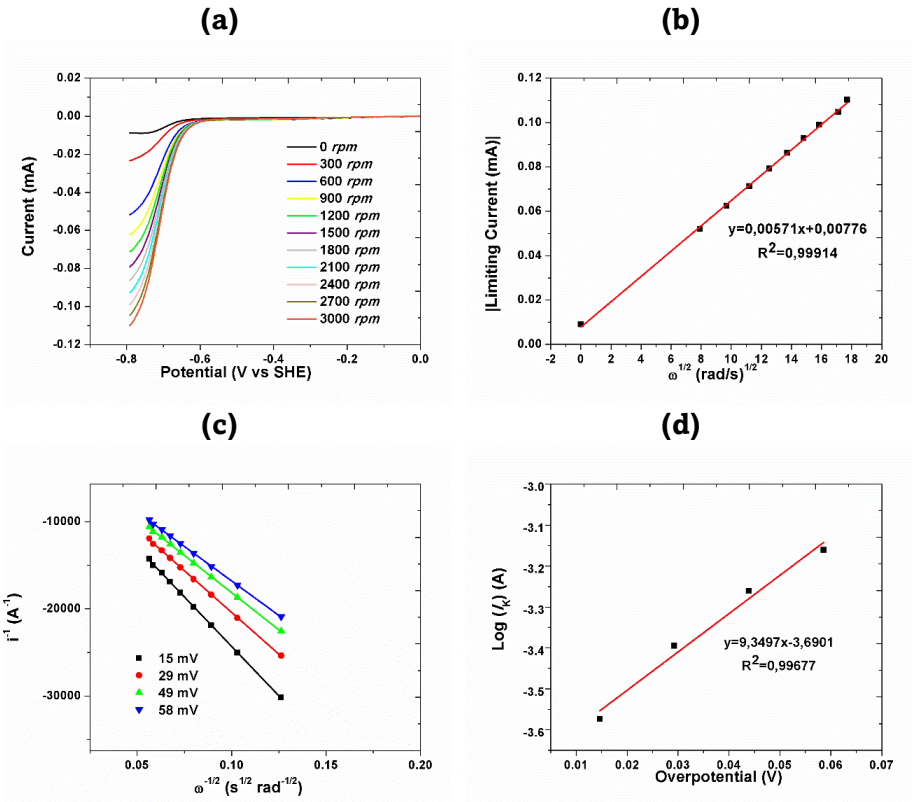

Figure S20: RDE analysis of **5**: (a) LSV scans with rotating working electrode; (b) Levich analysis of the reduction; (c) Kouyecký-Levich plot (d) and Tafel-plot for different overpotentials.

Compound **7**

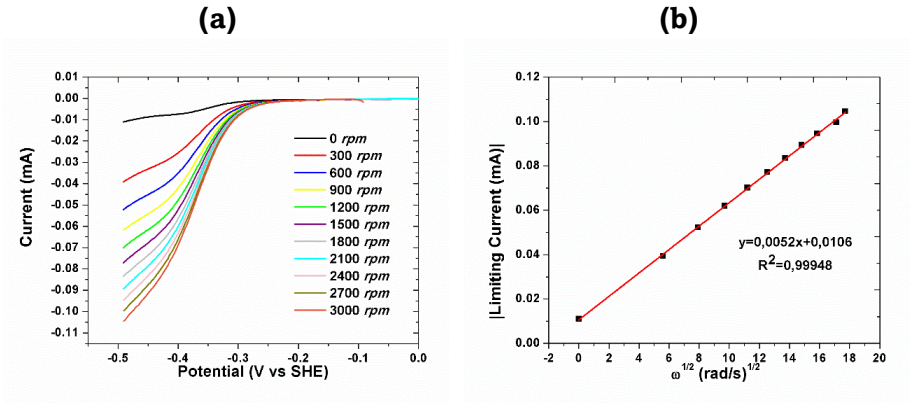

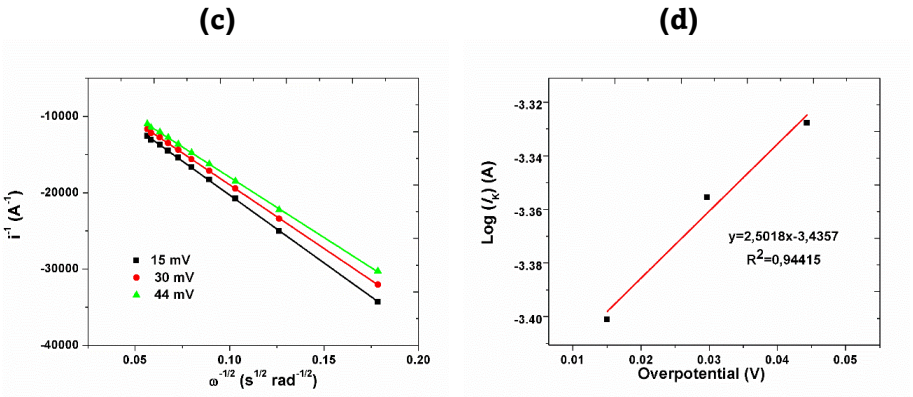

Figure S21: RDE analysis of **7**: (a) LSV scans with rotating working electrode; (b) Levich analysis of the reduction; (c) Kouyecký-Levich plot (d) and Tafel-plot for different overpotentials.

Solubility of bipyridines

Compound **1**

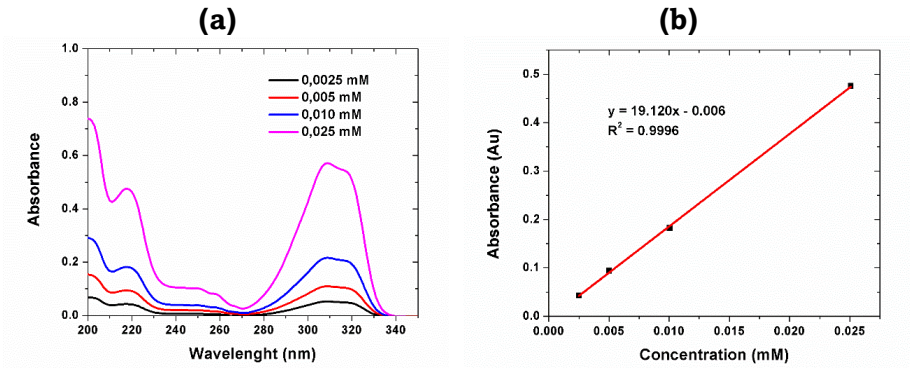

Figure S22: (a) Example of the different UV-Vis spectra of compound **1** at different concentrations and the corresponding calibration curve (b).

Compound **2**

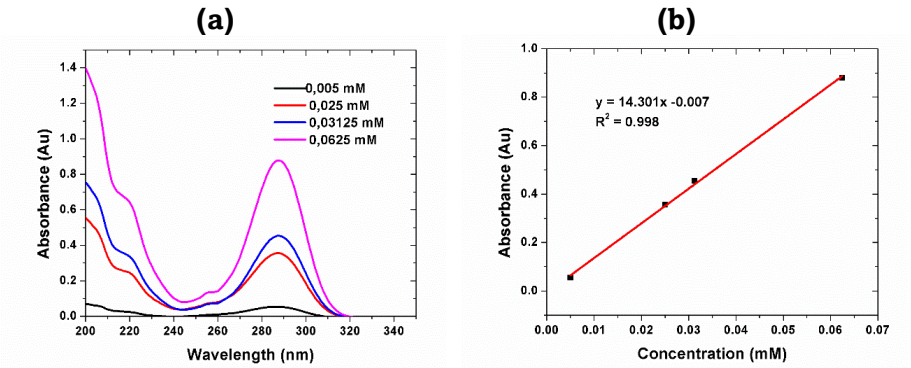

Figure S23: (a) Example of the different UV-Vis spectra of compound **2** at different concentrations and the corresponding calibration curve. (b)

Compound **4**

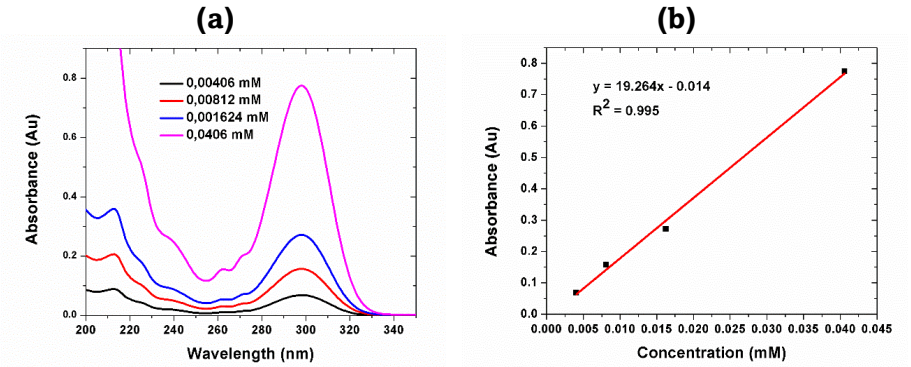

Figure S24: (a) Example of the different UV-Vis spectra of compound **4** at different concentrations and the corresponding calibration curve (b).

Compound **5**

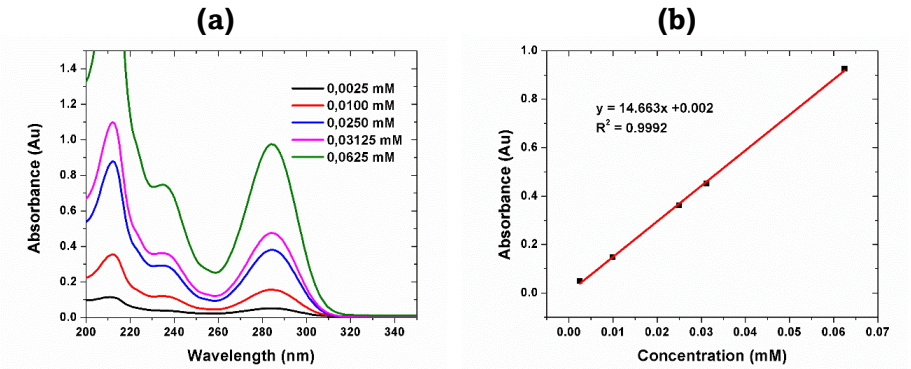

Figure S25: (a) Example of the different UV-Vis spectra of compound **5** at different concentrations and the corresponding calibration curve (b).

DFT Calculation of bipyridines

Geometries using IEF-PCM methodology at B3LYP/6-311++G(d,p) level of theory.

Compound **1**

Oxidized

C	0.214443000	2.741720000	0.804790000
C	-0.018787000	3.503333000	-0.324071000
C	-0.274858000	2.859758000	-1.528676000
C	-0.278804000	1.469476000	-1.578489000
C	-0.018787000	0.736345000	-0.430311000
N	0.207609000	1.396640000	0.740222000
H	-0.479397000	3.430745000	-2.424408000
H	0.406515000	3.173269000	1.775876000
H	-0.009679000	4.580662000	-0.244221000
H	-0.502459000	0.957856000	-2.502285000
C	0.018787000	-0.736345000	-0.430311000
C	0.278804000	-1.469476000	-1.578489000
C	-0.214443000	-2.741720000	0.804790000
C	0.274858000	-2.859758000	-1.528676000
H	0.502459000	-0.957856000	-2.502285000
H	-0.406515000	-3.173269000	1.775876000
H	0.479397000	-3.430745000	-2.424408000
C	0.018787000	-3.503333000	-0.324071000
H	0.009679000	-4.580662000	-0.244221000
N	-0.207609000	-1.396640000	0.740222000
C	-0.465425000	-0.594253000	1.961658000
H	-0.277563000	-1.220291000	2.828897000
H	-1.513141000	-0.289621000	1.955184000
C	0.465425000	0.594253000	1.961658000
H	0.277563000	1.220291000	2.828897000
H	1.513141000	0.289621000	1.955184000

Reduced

C	0.152725000	2.758957000	0.832347000
C	0.081514000	3.527648000	-0.281814000
C	0.116150000	2.868191000	-1.568062000
C	0.119830000	1.513411000	-1.639901000
C	0.081514000	0.684632000	-0.457927000
N	0.221983000	1.390940000	0.778239000
H	0.137366000	3.459313000	-2.475787000
H	0.181094000	3.178282000	1.830440000
H	0.025639000	4.603366000	-0.195649000
H	0.134132000	1.028368000	-2.606454000
C	-0.081514000	-0.684632000	-0.457927000
C	-0.119830000	-1.513411000	-1.639901000
C	-0.152725000	-2.758957000	0.832347000
C	-0.116150000	-2.868191000	-1.568062000
H	-0.134132000	-1.028368000	-2.606454000
H	-0.181094000	-3.178282000	1.830440000
H	-0.137366000	-3.459313000	-2.475787000
C	-0.081514000	-3.527648000	-0.281814000
H	-0.025639000	-4.603366000	-0.195649000
N	-0.221983000	-1.390940000	0.778239000
C	-0.465520000	-0.607250000	1.973357000
H	-0.283875000	-1.228391000	2.850325000
H	-1.505479000	-0.261569000	2.001453000
C	0.465520000	0.607250000	1.973357000
H	0.283875000	1.228391000	2.850325000
H	1.505479000	0.261569000	2.001453000

Compound **2**

Oxidized

C	2.773523000	0.519833000	0.458705000
C	3.500898000	-0.525894000	-0.079831000
C	2.825167000	-1.622200000	-0.597224000
C	1.431704000	-1.641926000	-0.571151000
C	0.740438000	-0.573927000	-0.028369000
N	1.428047000	0.486488000	0.486345000
H	3.368905000	-2.454328000	-1.023946000
H	3.237580000	1.397387000	0.883659000
H	4.579743000	-0.467788000	-0.083658000
H	0.878219000	-2.471983000	-0.986309000
C	-0.740443000	-0.573922000	0.028380000
C	-1.431716000	-1.641920000	0.571161000
C	-2.773523000	0.519840000	-0.458712000
C	-2.825176000	-1.622192000	0.597219000
H	-0.878232000	-2.471978000	0.986321000
H	-3.237570000	1.397400000	-0.883664000
H	-3.368923000	-2.454315000	1.023939000
C	-3.500901000	-0.525884000	0.079817000
H	-4.579747000	-0.467784000	0.083628000
N	-1.428043000	0.486494000	-0.486337000
C	-0.671232000	1.622350000	-1.081341000
H	0.058654000	1.189743000	-1.764288000
H	-1.368962000	2.211656000	-1.668762000
C	0.000011000	2.469265000	-0.000002000
H	-0.729669000	3.112541000	0.494002000
H	0.729701000	3.112526000	-0.494010000
C	0.671242000	1.622350000	1.081345000
H	1.368973000	2.211653000	1.668767000
H	-0.058651000	1.189750000	1.764288000

Reduced

C	2.799896000	0.576018000	0.271400000
C	3.518593000	-0.513561000	-0.124858000
C	2.828139000	-1.716391000	-0.417660000
C	1.457463000	-1.742005000	-0.349390000
C	0.716906000	-0.594340000	0.008485000
N	1.439008000	0.540969000	0.380230000
H	3.373293000	-2.599015000	-0.724910000
H	3.262459000	1.514485000	0.541454000
H	4.594212000	-0.443776000	-0.199136000
H	0.915142000	-2.633155000	-0.632323000
C	-0.716912000	-0.594334000	-0.008450000
C	-1.457481000	-1.741987000	0.349433000
C	-2.799894000	0.576027000	-0.271435000
C	-2.828158000	-1.716370000	0.417670000
H	-0.915168000	-2.633134000	0.632393000
H	-3.262448000	1.514492000	-0.541508000
H	-3.373323000	-2.598985000	0.724927000
C	-3.518603000	-0.513544000	0.124822000
H	-4.594225000	-0.443758000	0.199064000
N	-1.439001000	0.540982000	-0.380215000
C	-0.738495000	1.671034000	-1.016550000
H	-0.042017000	1.244902000	-1.740818000
H	-1.473466000	2.251445000	-1.569242000
C	0.000018000	2.537472000	-0.000012000
H	-0.699310000	3.181045000	0.537996000
H	0.699353000	3.181025000	-0.538033000
C	0.738516000	1.671046000	1.016544000
H	1.473497000	2.251451000	1.569227000
H	0.042033000	1.244932000	1.740816000

Compound **3**

Oxidized

C	2.813150000	0.214089000	0.519706000
C	3.495776000	-0.767204000	-0.171913000
C	2.775437000	-1.768122000	-0.810228000
C	1.384785000	-1.751920000	-0.742412000
C	0.740027000	-0.741335000	-0.050064000
N	1.464843000	0.221659000	0.580431000
H	3.282419000	-2.553114000	-1.355200000
H	3.316966000	1.010304000	1.047627000
H	4.575654000	-0.739219000	-0.194386000
H	0.791117000	-2.510381000	-1.232618000
C	-0.739882000	-0.741449000	0.049398000
C	-1.384197000	-1.752243000	0.741847000
C	-2.813372000	0.213748000	-0.519308000
C	-2.774799000	-1.768675000	0.810318000
H	-0.790159000	-2.510610000	1.231727000
H	-3.317574000	1.009949000	-1.046865000
H	-3.281391000	-2.553761000	1.355530000
C	-3.495554000	-0.767814000	0.172385000
H	-4.575422000	-0.740064000	0.195243000
N	-1.465078000	0.221665000	-0.580516000
C	-0.813651000	1.336474000	-1.336118000
H	0.115287000	0.956556000	-1.756693000
H	-1.480285000	1.560030000	-2.164801000
C	0.812878000	1.336016000	1.336085000
H	1.478832000	1.559246000	2.165380000
H	-0.116353000	0.955920000	1.755839000
C	-0.614246000	2.573761000	-0.456683000
H	-0.534144000	3.428749000	-1.130966000
H	-1.522112000	2.730969000	0.132165000
C	0.614071000	2.573574000	0.456831000
H	1.522111000	2.730452000	-0.131857000
H	0.534163000	3.428312000	1.131401000

Reduced

C	-2.804500000	0.338437000	-0.267608000
C	-3.508041000	-0.725267000	0.212007000
C	-2.810361000	-1.918112000	0.530667000
C	-1.442781000	-1.944242000	0.415576000
C	-0.717401000	-0.812004000	-0.013188000
N	-1.445278000	0.298188000	-0.431271000
H	-3.344108000	-2.785380000	0.895886000
H	-3.281341000	1.259131000	-0.573238000
H	-4.579765000	-0.647051000	0.325848000
H	-0.884879000	-2.817116000	0.725434000
C	0.717406000	-0.812006000	0.013177000
C	1.442793000	-1.944246000	-0.415556000
C	2.804499000	0.338462000	0.267571000
C	2.810375000	-1.918109000	-0.530644000
H	0.884902000	-2.817133000	-0.725397000
H	3.281333000	1.259168000	0.573176000
H	3.344128000	-2.785383000	-0.895838000
C	3.508046000	-0.725251000	-0.212015000
H	4.579769000	-0.647030000	-0.325862000
N	1.445277000	0.298209000	0.431232000
C	0.838008000	1.383794000	1.241826000
H	-0.085916000	1.001832000	1.673360000
H	1.526066000	1.564462000	2.067048000
C	-0.838011000	1.383805000	-1.241823000
H	-1.526067000	1.564493000	-2.067041000
H	0.085918000	1.001865000	-1.673365000
C	0.618093000	2.672936000	0.450632000
H	0.538218000	3.494645000	1.166352000
H	1.515119000	2.868667000	-0.144396000
C	-0.618118000	2.672932000	-0.450593000
H	-1.515148000	2.868627000	0.144438000
H	-0.538262000	3.494656000	-1.166297000

Compound **4**

Oxidized

C	2.773261000	0.577392000	0.473777000
C	3.527382000	-0.463810000	-0.051096000
C	2.830604000	-1.560638000	-0.562062000
C	1.441541000	-1.583931000	-0.546024000
C	0.738947000	-0.514493000	-0.016732000
N	1.426789000	0.543858000	0.493984000
H	3.373882000	-2.397987000	-0.981991000
H	3.227768000	1.460394000	0.898794000
H	0.895634000	-2.419494000	-0.960474000
C	-0.739785000	-0.513035000	0.025450000
C	-1.445095000	-1.580449000	0.555195000
C	-2.771603000	0.578226000	-0.476811000
C	-2.834230000	-1.556993000	0.564425000
H	-0.901266000	-2.415137000	0.974101000
H	-3.223906000	1.460227000	-0.906209000
H	-3.379623000	-2.393264000	0.983765000
C	-3.528445000	-0.461956000	0.046157000
N	-1.425073000	0.544553000	-0.490424000
C	-0.666666000	1.681328000	-1.081171000
H	0.065999000	1.249115000	-1.761468000
H	-1.362183000	2.271115000	-1.670693000
C	0.001809000	2.528735000	0.001302000
H	-0.729299000	3.172078000	0.493311000
H	0.732572000	3.172028000	-0.491280000
C	0.670872000	1.682426000	1.084344000
H	1.367967000	2.272245000	1.672009000
H	-0.061335000	1.252077000	1.766271000
C	-5.026667000	-0.399879000	0.039587000
H	-5.412805000	-0.505608000	1.055801000
H	-5.386865000	0.541096000	-0.374476000

Reduced

C	2.795936000	0.631315000	0.333198000
C	3.542502000	-0.450435000	-0.041081000
C	2.840442000	-1.652357000	-0.343022000
C	1.470261000	-1.682581000	-0.309396000
C	0.716528000	-0.538572000	0.028077000
N	1.429099000	0.593379000	0.413120000
H	3.392793000	-2.536945000	-0.635419000
H	3.245207000	1.575094000	0.609245000
H	0.939902000	-2.577789000	-0.602820000
C	-0.716665000	-0.538283000	-0.026852000
C	-1.470635000	-1.682111000	0.310655000
C	-2.795919000	0.631195000	-0.334575000
C	-2.840833000	-1.652010000	0.343140000
H	-0.940417000	-2.577200000	0.604694000
H	-3.245128000	1.574638000	-0.611881000
H	-3.393295000	-2.536656000	0.635153000
C	-3.542765000	-0.450468000	0.039489000
N	-1.428964000	0.593707000	-0.412515000
C	-0.715652000	1.724146000	-1.032274000
H	-0.002348000	1.299877000	-1.741341000
H	-1.438343000	2.304987000	-1.600653000
C	0.000654000	2.590831000	0.000434000
H	-0.710037000	3.235254000	0.522436000
H	0.712240000	3.234046000	-0.521869000
C	0.716112000	1.723720000	1.033253000
H	1.438769000	2.304019000	1.602244000
H	0.002356000	1.299353000	1.741796000
C	-5.040550000	-0.382496000	0.122356000
H	-5.380346000	-0.576482000	1.144053000
H	-5.413492000	0.596149000	-0.181518000

H	-5.433487000	-1.221018000	-0.555527000
C	5.025591000	-0.400989000	-0.054505000
H	5.405257000	-0.517199000	-1.072121000
H	5.387917000	0.544575000	0.347477000
H	5.436657000	-1.215724000	0.546765000
H	-5.497312000	-1.140039000	-0.520956000
C	5.040297000	-0.382862000	-0.123746000
H	5.381698000	-0.608908000	-1.138108000
H	5.411253000	0.605701000	0.148972000
H	5.497284000	-1.118895000	0.543800000

Compound **5**

Oxidized

C	-2.700489000	0.901374000	-0.771403000
C	-3.477730000	-0.143773000	-0.323311000
C	-2.882014000	-1.259311000	0.272313000
C	-1.486575000	-1.255288000	0.394006000
C	-0.738873000	-0.186652000	-0.060445000
N	-1.357636000	0.876758000	-0.647437000
H	-3.119145000	1.776982000	-1.245118000
H	-0.976057000	-2.084269000	0.863900000
C	0.738868000	-0.186647000	0.060429000
C	1.486581000	-1.255264000	-0.394061000
C	2.700480000	0.901386000	0.771386000
C	2.882017000	-1.259278000	-0.272372000
H	0.976070000	-2.084225000	-0.863995000
H	3.119132000	1.776995000	1.245105000
C	3.477727000	-0.143736000	0.323257000
N	1.357624000	0.876753000	0.647442000
C	0.542159000	2.014256000	1.150358000
H	-0.261742000	1.587242000	1.748553000
H	1.171602000	2.602257000	1.811560000
C	-0.000013000	2.863176000	0.000026000
H	0.782670000	3.506094000	-0.405955000
H	-0.782701000	3.506078000	0.406019000
C	-0.542175000	2.014276000	-1.150325000
H	-1.171615000	2.602287000	-1.811521000
H	0.261732000	1.587277000	-1.748524000
C	-3.705478000	-2.401214000	0.775065000
H	-4.317163000	-2.069501000	1.619275000
H	-4.389293000	-2.747189000	-0.003233000
H	-3.083058000	-3.232803000	1.101133000
C	3.705508000	-2.401213000	-0.775011000
H	4.318741000	-2.069130000	-1.617938000
H	4.387887000	-2.748340000	0.004053000
H	3.083065000	-3.232135000	-1.102727000
H	-4.550386000	-0.082401000	-0.446347000
H	4.550387000	-0.082344000	0.446258000

Reduced

C	2.768018000	0.979817000	0.483406000
C	3.509421000	-0.111972000	0.148707000
C	2.854925000	-1.329645000	-0.200002000
C	1.479603000	-1.330945000	-0.233368000
C	0.713644000	-0.181014000	0.062501000
N	1.403382000	0.956017000	0.484256000
H	3.215459000	1.915956000	0.786167000
H	0.953702000	-2.218609000	-0.557537000
C	-0.713635000	-0.181037000	-0.062796000
C	-1.479511000	-1.331013000	0.233094000
C	-2.768126000	0.979726000	-0.483418000
C	-2.854834000	-1.329787000	0.199928000
H	-0.953524000	-2.218634000	0.557282000
H	-3.215649000	1.915891000	-0.785994000
C	-3.509440000	-0.112127000	-0.148786000
N	-1.403466000	0.956029000	-0.484319000
C	-0.660993000	2.087285000	-1.067575000
H	0.087944000	1.663683000	-1.739212000
H	-1.354757000	2.666571000	-1.672593000
C	-0.000065000	2.954901000	0.000131000
H	-0.737408000	3.598703000	0.484826000
H	0.737324000	3.598726000	-0.484472000
C	0.660811000	2.087113000	1.067707000
H	1.354498000	2.666294000	1.672919000
H	-0.088170000	1.663313000	1.739176000
C	3.661362000	-2.543542000	-0.552836000
H	4.317004000	-2.336313000	-1.404083000
H	4.305215000	-2.831127000	0.283907000
H	3.021763000	-3.389604000	-0.804822000
C	-3.661129000	-2.543718000	0.553088000
H	-4.318406000	-2.335568000	1.402892000
H	-4.303293000	-2.833133000	-0.284368000
H	-3.021393000	-3.388970000	0.807577000
H	4.588572000	-0.042784000	0.162163000
H	-4.588599000	-0.042964000	-0.162053000

Compound **6**

Oxidized

C	-1.493052000	-1.004659000	-0.333688000
C	-0.736255000	0.055868000	0.091109000
C	-2.663947000	1.149635000	0.885209000
C	-3.474449000	0.117465000	0.476462000
C	-2.890486000	-0.996604000	-0.144245000
H	-1.027117000	-1.841750000	-0.832966000
H	-3.063774000	2.025394000	1.375071000
H	-4.536398000	0.195135000	0.649147000
C	0.736256000	0.055870000	-0.091108000
C	1.493054000	-1.004655000	0.333690000
C	2.663946000	1.149639000	-0.885209000
C	2.890489000	-0.996599000	0.144246000
H	1.027121000	-1.841747000	0.832968000
C	3.474450000	0.117471000	-0.476463000
H	3.063771000	2.025399000	-1.375072000
H	4.536398000	0.195142000	-0.649147000
N	1.327207000	1.126910000	-0.708552000
N	-1.327209000	1.126908000	0.708552000
C	-0.489748000	2.262620000	1.172972000
H	-1.087257000	2.850733000	1.863415000
H	0.341269000	1.837632000	1.734706000

Reduced

C	-1.351158000	-0.955620000	-0.185096000
C	-0.717347000	0.280343000	0.098504000
C	-2.913319000	1.161453000	0.496557000
C	-3.532975000	-0.030181000	0.264093000
C	-2.716371000	-1.130761000	-0.105158000
H	-0.757838000	-1.783590000	-0.539653000
H	-3.480251000	2.042682000	0.758643000
H	-4.606422000	-0.089327000	0.343881000
C	0.722496000	0.323247000	0.081779000
C	1.386466000	-0.901703000	0.366701000
C	2.871334000	1.145480000	-0.592343000
C	2.723369000	-1.113552000	0.127696000
H	0.823726000	-1.702632000	0.821182000
C	3.491433000	-0.053654000	-0.425162000
H	3.429098000	2.004426000	-0.937380000
H	4.536647000	-0.144327000	-0.673785000
N	1.553260000	1.388510000	-0.335610000
N	-1.568624000	1.339688000	0.424802000
C	-1.037519000	2.668729000	0.735659000
H	-1.887111000	3.308980000	0.956240000
H	-0.427995000	2.599469000	1.642582000

C	-0.000002000	3.112881000	0.000001000
H	-0.800960000	3.755866000	-0.368993000
H	0.800956000	3.755866000	0.368994000
C	0.489745000	2.262621000	-1.172972000
H	-0.341272000	1.837632000	-1.734705000
H	1.087252000	2.850736000	-1.863414000
O	3.545295000	-2.054748000	0.583822000
O	-3.545293000	-2.054754000	-0.583818000
C	-4.983592000	-2.113072000	-0.439848000
H	-5.448217000	-1.292894000	-0.988032000
H	-5.271995000	-3.065366000	-0.873436000
H	-5.256519000	-2.081306000	0.615432000
C	4.983592000	-2.113079000	0.439842000
H	5.271990000	-3.065369000	0.873440000
H	5.256510000	-2.081330000	-0.615441000
H	5.448229000	-1.292898000	0.988013000

C	-0.226215000	3.216312000	-0.428565000
H	-0.667410000	2.899012000	-1.376345000
H	-0.263304000	4.307382000	-0.405498000
C	1.231824000	2.840996000	-0.328528000
H	1.783778000	3.279948000	-1.158035000
H	1.637551000	3.253864000	0.600669000
O	3.230091000	-2.316134000	0.463312000
O	-3.196002000	-2.346343000	-0.428518000
C	-4.616985000	-2.556382000	-0.422770000
H	-5.109380000	-1.894051000	-1.137838000
H	-4.757439000	-3.591084000	-0.724182000
H	-5.027864000	-2.406039000	0.577647000
C	4.631710000	-2.556409000	0.263548000
H	4.805213000	-3.569556000	0.616796000
H	4.890597000	-2.487490000	-0.795124000
H	5.232778000	-1.855023000	0.846028000

Compound **7**

Oxidized

C	-2.605338000	1.459849000	-1.034424000
C	-3.430799000	0.417018000	-0.659576000
C	-2.887111000	-0.667635000	0.018962000
C	-1.518099000	-0.685234000	0.291411000
C	-0.726093000	0.373925000	-0.115049000
N	-1.285370000	1.427437000	-0.772945000
H	-2.970320000	2.330789000	-1.558172000
H	-1.051319000	-1.510303000	0.811522000
C	0.735910000	0.360878000	0.128260000
C	1.503773000	-0.723755000	-0.252106000
C	2.643300000	1.442876000	0.995163000
C	2.876985000	-0.715594000	-0.002769000
H	1.037507000	-1.557576000	-0.755233000
H	3.027490000	2.320255000	1.493785000
C	3.450048000	0.382969000	0.622945000
N	1.319913000	1.421913000	0.755172000
C	0.472441000	2.573391000	1.175862000
H	-0.377989000	2.156157000	1.713568000
H	1.050667000	3.167160000	1.877023000
C	0.032764000	3.408616000	-0.027163000
H	0.849916000	4.042726000	-0.374296000
H	-0.777222000	4.058746000	0.306848000
C	-0.414915000	2.554698000	-1.213478000
H	-0.978746000	3.142358000	-1.931255000
H	0.430988000	2.110127000	-1.736474000
H	-4.483607000	0.459848000	-0.898748000
H	4.510883000	0.417321000	0.825051000
C	3.764333000	-1.863999000	-0.399113000
O	4.954067000	-1.865886000	-0.205785000
O	3.074076000	-2.849473000	-0.974956000
H	3.678991000	-3.570417000	-1.215170000
C	-3.793808000	-1.819995000	0.377571000
O	-3.621990000	-2.397911000	1.570888000
H	-3.007791000	-1.917606000	2.144636000
O	-4.631353000	-2.209614000	-0.392354000

Reduced

C	-2.704710000	1.548666000	-0.747825000
C	-3.480029000	0.470573000	-0.443285000
C	-2.862348000	-0.718160000	0.027162000
C	-1.487798000	-0.732884000	0.179140000
C	-0.709875000	0.393961000	-0.110936000
N	-1.345550000	1.515836000	-0.622089000
H	-3.117188000	2.474589000	-1.120895000
H	-0.967586000	-1.603312000	0.554097000
C	0.717068000	0.387801000	0.124029000
C	1.486836000	-0.743214000	-0.164784000
C	2.720019000	1.540855000	0.743903000
C	2.862314000	-0.726230000	-0.019764000
H	0.996479000	-1.619650000	-0.561610000
H	3.135813000	2.466766000	1.113221000
C	3.491913000	0.462787000	0.426280000
N	1.359674000	1.506613000	0.635007000
C	0.559085000	2.637374000	1.143672000
H	-0.250197000	2.209902000	1.737636000
H	1.189490000	3.215523000	1.814268000
C	0.011566000	3.503586000	0.011199000
H	0.795413000	4.145821000	-0.394889000
H	-0.770070000	4.146809000	0.419909000
C	-0.538599000	2.644558000	-1.125309000
H	-1.165378000	3.228372000	-1.794350000
H	0.269387000	2.215428000	-1.719933000
H	-4.551758000	0.523979000	-0.560499000
H	4.565901000	0.516725000	0.522382000
C	3.701216000	-1.901655000	-0.350467000
O	4.909571000	-1.918612000	-0.243709000
O	2.983019000	-2.956306000	-0.778957000
H	3.593860000	-3.684312000	-0.972455000
C	-3.731795000	-1.893810000	0.308725000
O	-3.248690000	-2.879561000	1.093102000
H	-2.416985000	-2.639745000	1.522500000
O	-4.845802000	-1.995431000	-0.152966000

Compound **8**

Oxidized

C	2.831083000	-0.260704000	-0.258415000
C	3.498442000	0.856940000	0.334927000
C	2.738066000	1.951025000	0.777850000
C	1.366730000	1.939974000	0.654443000
C	0.740786000	0.841391000	0.067817000
N	1.454912000	-0.206095000	-0.399888000
H	3.237291000	2.798138000	1.231182000
H	0.761839000	2.755948000	1.020889000
C	-0.740389000	0.841627000	-0.064331000
C	-1.365472000	1.940293000	-0.651715000

Reduced

C	2.808562000	-0.283100000	-0.211490000
C	3.528677000	0.882851000	0.165142000
C	2.803874000	2.088257000	0.401515000
C	1.442416000	2.099247000	0.330311000
C	0.719506000	0.933933000	-0.019898000
N	1.428279000	-0.194634000	-0.386962000
H	3.344830000	2.981105000	0.689054000
H	0.889529000	2.986572000	0.601247000
C	-0.719437000	0.934032000	0.021237000
C	-1.442118000	2.099445000	-0.329121000

C	-2.831337000	-0.259735000	0.260394000
C	-2.736499000	1.950820000	-0.778291000
H	-0.759973000	2.756238000	-1.017320000
H	-3.234935000	2.797240000	-1.233743000
C	-3.497545000	0.857041000	-0.335936000
N	-1.455153000	-0.205875000	0.402482000
C	-0.697477000	-1.313891000	1.048279000
H	0.023363000	-0.846674000	1.716877000
H	-1.367756000	-1.890395000	1.671316000
C	-0.001410000	-2.178556000	-0.001693000
H	-0.714517000	-2.820055000	-0.521687000
H	0.710057000	-2.823729000	0.515962000
C	0.696689000	-1.311950000	-1.048689000
H	1.366993000	-1.887441000	-1.672681000
H	-0.023006000	-0.842217000	-1.716759000
C	-3.588114000	-1.374556000	0.674596000
C	-4.954472000	-1.364848000	0.510303000
H	-3.121787000	-2.248113000	1.101040000
C	-4.907860000	0.829223000	-0.479072000
C	-5.624821000	-0.260817000	-0.061347000
H	-5.524860000	-2.229522000	0.825036000
H	-5.396812000	1.684275000	-0.928091000
H	-6.700941000	-0.285472000	-0.172162000
C	3.586627000	-1.376888000	-0.670965000
C	4.953346000	-1.366864000	-0.509883000
H	3.119310000	-2.250902000	-1.095129000
C	4.909136000	0.829668000	0.474258000
C	5.625096000	-0.261156000	0.056905000
H	5.522971000	-2.232403000	-0.823706000
H	5.399243000	1.685769000	0.919978000
H	6.701572000	-0.285108000	0.164222000

C	-2.808680000	-0.282792000	0.212096000
C	-2.803514000	2.088423000	-0.401421000
H	-0.889057000	2.986796000	-0.599617000
H	-3.344264000	2.981235000	-0.689455000
C	-3.528480000	0.883000000	-0.165512000
N	-1.428415000	-0.194563000	0.387879000
C	-0.688598000	-1.297132000	1.033022000
H	0.049844000	-0.834993000	1.688103000
H	-1.369065000	-1.851998000	1.670332000
C	-0.000223000	-2.186378000	0.000205000
H	-0.717603000	-2.829487000	-0.513642000
H	0.717104000	-2.829711000	0.513854000
C	0.688224000	-1.296907000	-1.032335000
H	1.368504000	-1.851591000	-1.670037000
H	-0.050252000	-0.834385000	-1.687162000
C	-3.504223000	-1.488860000	0.403333000
C	-4.880277000	-1.526941000	0.247080000
H	-2.982122000	-2.400576000	0.651842000
C	-4.926897000	0.810479000	-0.313813000
C	-5.600921000	-0.376910000	-0.105144000
H	-5.399597000	-2.465977000	0.393773000
H	-5.462652000	1.708043000	-0.599059000
H	-6.676269000	-0.423896000	-0.221240000
C	3.503828000	-1.489359000	-0.402455000
C	4.880084000	-1.527230000	-0.247766000
H	2.981569000	-2.401032000	-0.650352000
C	4.927273000	0.810508000	0.311780000
C	5.601119000	-0.376906000	0.102797000
H	5.399324000	-2.466290000	-0.394541000
H	5.463323000	1.708275000	0.595828000
H	6.676652000	-0.423657000	0.217286000

Geometries in gas phase at B3LYP/6-311++G(d,p) level of theory.

Compound **1**

Oxidized

C	0.203190000	2.752968000	0.803744000
C	-0.022738000	3.515950000	-0.327467000
C	-0.275142000	2.869643000	-1.533613000
C	-0.278849000	1.475849000	-1.579866000
C	-0.022738000	0.738492000	-0.431443000
N	0.195390000	1.403537000	0.743081000
H	-0.476076000	3.440566000	-2.432358000
H	0.391246000	3.189405000	1.775985000
H	-0.012255000	4.595525000	-0.249889000
H	-0.501469000	0.967680000	-2.507507000
C	0.022738000	-0.738492000	-0.431443000
C	0.278849000	-1.475849000	-1.579866000
C	-0.203190000	-2.752968000	0.803744000
C	0.275142000	-2.869643000	-1.533613000
H	0.501469000	-0.967680000	-2.507507000
H	-0.391246000	-3.189405000	1.775985000
H	0.476076000	-3.440566000	-2.432358000
C	0.022738000	-3.515950000	-0.327467000
H	0.012255000	-4.595525000	-0.249889000
N	-0.195390000	-1.403537000	0.743081000
C	-0.455961000	-0.604447000	1.968642000
H	-0.254140000	-1.228138000	2.837367000
H	-1.510494000	-0.317793000	1.974851000
C	0.455961000	0.604447000	1.968642000
H	0.254140000	1.228138000	2.837367000
H	1.510494000	0.317793000	1.974851000

Reduced

C	0.077761000	2.773099000	0.815094000
C	-0.077761000	3.525953000	-0.309484000
C	-0.193823000	2.864348000	-1.559966000
C	-0.161338000	1.495211000	-1.612506000
C	-0.007851000	0.713222000	-0.440156000
N	0.118892000	1.405515000	0.765137000
H	-0.323737000	3.438316000	-2.468515000
H	0.180919000	3.206317000	1.800971000
H	-0.114008000	4.603467000	-0.232027000
H	-0.285124000	0.994450000	-2.561691000
C	0.007851000	-0.713222000	-0.440156000
C	0.161338000	-1.495211000	-1.612506000
C	-0.077761000	-2.773099000	0.815094000
C	0.193823000	-2.864348000	-1.559966000
H	0.285124000	-0.994450000	-2.561691000
H	-0.180919000	-3.206317000	1.800971000
H	0.323737000	-3.438316000	-2.468515000
C	0.077761000	-3.525953000	-0.309484000
H	0.114008000	-4.603467000	-0.232027000
N	-0.118892000	-1.405515000	0.765137000
C	-0.412169000	-0.638496000	1.980789000
H	-0.163297000	-1.247601000	2.849202000
H	-1.481049000	-0.404328000	2.013472000
C	0.412169000	0.638496000	1.980789000
H	0.163297000	1.247601000	2.849202000
H	1.481049000	0.404328000	2.013472000

Compound **2**

Oxidized

C	-2.790491000	0.513604000	-0.449510000
C	-3.513582000	-0.540600000	0.082709000
C	-2.829214000	-1.636199000	0.595187000
C	-1.432597000	-1.644052000	0.567912000
C	-0.742783000	-0.568969000	0.031693000
N	-1.440794000	0.493269000	-0.475835000
H	-3.368446000	-2.476059000	1.017040000
H	-3.265098000	1.387920000	-0.874810000
H	-4.594882000	-0.492129000	0.084849000
H	-0.877547000	-2.477060000	0.979206000
C	0.742812000	-0.568944000	-0.031665000
C	1.432619000	-1.644029000	-0.567973000
C	2.790541000	0.513650000	0.449508000
C	2.829212000	-1.636192000	-0.595133000
H	0.877553000	-2.476974000	-0.979363000
H	3.265046000	1.388178000	0.874469000
H	3.368498000	-2.475820000	-1.017380000
C	3.513593000	-0.540609000	-0.082569000
H	4.594905000	-0.492327000	-0.084484000
N	1.440793000	0.493304000	0.475762000
C	0.693029000	1.638415000	1.072811000
H	-0.022254000	1.213392000	1.778000000
H	1.399913000	2.233769000	1.646034000
C	-0.000076000	2.483365000	0.000034000
H	0.717000000	3.133386000	-0.506700000
H	-0.717194000	3.133347000	0.506722000
C	-0.693043000	1.638419000	-1.072840000
H	-1.399956000	2.233719000	-1.646082000
H	0.022348000	1.213481000	-1.777967000

Reduced

C	2.805054000	0.573554000	0.274008000
C	3.521927000	-0.515659000	-0.122330000
C	2.830021000	-1.716094000	-0.420837000
C	1.459141000	-1.739619000	-0.355111000
C	0.717344000	-0.593848000	0.006587000
N	1.440800000	0.541895000	0.379522000
H	3.375158000	-2.597949000	-0.730603000
H	3.270427000	1.510664000	0.546703000
H	4.598175000	-0.449195000	-0.194100000
H	0.916730000	-2.628699000	-0.645641000
C	-0.717381000	-0.593846000	-0.006483000
C	-1.459215000	-1.739589000	0.355113000
C	-2.805065000	0.573639000	-0.273995000
C	-2.830094000	-1.716059000	0.420764000
H	-0.916782000	-2.628664000	0.645634000
H	-3.270374000	1.510831000	-0.546575000
H	-3.375314000	-2.597872000	0.730488000
C	-3.521950000	-0.515579000	0.122267000
H	-4.598203000	-0.449136000	0.193981000
N	-1.440785000	0.542003000	-0.379397000
C	-0.740564000	1.670286000	-1.016103000
H	-0.044290000	1.245176000	-1.742239000
H	-1.473946000	2.251378000	-1.572066000
C	0.000143000	2.538794000	-0.000100000
H	-0.696756000	3.186022000	0.538190000
H	0.697265000	3.185626000	-0.538561000
C	0.740590000	1.670342000	1.016150000
H	1.473971000	2.251310000	1.572221000
H	0.044135000	1.245289000	1.742113000

Compound **3**

Oxidized

C	2.829710000	0.201281000	0.515761000
C	3.506682000	-0.787104000	-0.175013000
C	2.776451000	-1.780905000	-0.816791000
C	1.383127000	-1.749141000	-0.748240000
C	0.742282000	-0.734120000	-0.054344000
N	1.478472000	0.225283000	0.576320000
H	3.277384000	-2.571867000	-1.362180000
H	3.344017000	0.991821000	1.045820000
H	4.588793000	-0.772215000	-0.194289000
H	0.787021000	-2.506501000	-1.240687000
C	-0.741922000	-0.734419000	0.053926000
C	-1.382350000	-1.749733000	0.747814000
C	-2.829718000	0.200740000	-0.515260000
C	-2.775649000	-1.781726000	0.816824000
H	-0.785953000	-2.507082000	1.239919000
H	-3.344275000	0.991339000	-1.044999000
H	-3.276297000	-2.572907000	1.362158000
C	-3.506285000	-0.787832000	0.175621000
H	-4.588388000	-0.773067000	0.195436000
N	-1.478522000	0.224854000	-0.576383000
C	-0.839682000	1.353733000	-1.330985000
H	0.083396000	0.979087000	-1.772549000
H	-1.518785000	1.583415000	-2.149830000
C	0.839093000	1.354097000	1.330773000
H	1.518150000	1.584143000	2.149558000
H	-0.083719000	0.978978000	1.772550000
C	-0.624736000	2.585821000	-0.444610000
H	-0.562342000	3.449140000	-1.111399000
H	-1.521988000	2.741794000	0.162366000
C	0.623357000	2.586126000	0.444479000
H	1.520604000	2.742612000	-0.162417000
H	0.560568000	3.449438000	1.111251000

Reduced

C	2.811599000	0.333076000	0.268753000
C	3.511863000	-0.731913000	-0.210193000
C	2.810179000	-1.920546000	-0.534654000
C	1.442331000	-1.941258000	-0.422060000
C	0.717900000	-0.809355000	0.010450000
N	1.449303000	0.300039000	0.428647000
H	3.341941000	-2.788417000	-0.901605000
H	3.292247000	1.251248000	0.577530000
H	4.584612000	-0.659438000	-0.320493000
H	0.882488000	-2.810807000	-0.738829000
C	-0.717906000	-0.809400000	-0.010505000
C	-1.442323000	-1.941368000	0.421737000
C	-2.811618000	0.333199000	-0.268311000
C	-2.810164000	-1.920634000	0.534520000
H	-0.882520000	-2.811061000	0.738197000
H	-3.292270000	1.251469000	-0.576788000
H	-3.341880000	-2.788600000	0.901307000
C	-3.511844000	-0.731874000	0.210518000
H	-4.584566000	-0.659356000	0.321052000
N	-1.449350000	0.300126000	-0.428469000
C	-0.846197000	1.386742000	-1.239644000
H	0.075389000	1.004549000	-1.677728000
H	-1.536759000	1.569604000	-2.063356000
C	0.846079000	1.386780000	1.239592000
H	1.536580000	1.569752000	2.063307000
H	-0.075608000	1.004727000	1.677561000
C	-0.620422000	2.676211000	-0.448385000
H	-0.545095000	3.501831000	-1.160517000
H	-1.514545000	2.873359000	0.151508000
C	0.620554000	2.676177000	0.448080000
H	1.514724000	2.873034000	-0.151842000
H	0.545388000	3.501922000	1.160067000

Annex A: NMR, RDE, solubilities, DFT calculation, and cell testing extra information

Compound **4**

Oxidized

C	2.789168000	0.575834000	0.464739000
C	3.545144000	-0.472858000	-0.050880000
C	2.837035000	-1.568876000	-0.557616000
C	1.445755000	-1.581669000	-0.544342000
C	0.741306000	-0.505886000	-0.023630000
N	1.438313000	0.554024000	0.481030000
H	3.375412000	-2.414560000	-0.970816000
H	3.251514000	1.456743000	0.889989000
H	0.899775000	-2.420276000	-0.956274000
C	-0.741308000	-0.505884000	0.023631000
C	-1.445760000	-1.581667000	0.544345000
C	-2.789169000	0.575839000	-0.464740000
C	-2.837037000	-1.568870000	0.557616000
H	-0.899780000	-2.420272000	0.956279000
H	-3.251509000	1.456753000	-0.889988000
H	-3.375421000	-2.414550000	0.970817000
C	-3.545145000	-0.472849000	0.050876000
N	-1.438310000	0.554024000	-0.481029000
C	-0.690263000	1.699695000	-1.073733000
H	0.028949000	1.275764000	-1.775448000
H	-1.395067000	2.294989000	-1.649347000
C	0.000002000	2.545372000	0.000000000
H	-0.718617000	3.195073000	0.504832000
H	0.718620000	3.195075000	-0.504830000
C	0.690268000	1.699694000	1.073733000
H	1.395072000	2.294990000	1.649346000
H	-0.028945000	1.275766000	1.775449000
C	-5.043039000	-0.420225000	0.048393000
H	-5.429214000	-0.530630000	1.065051000
H	-5.418472000	0.516188000	-0.362900000
H	-5.449389000	-1.243781000	-0.545155000
C	5.043038000	-0.420220000	-0.048396000
H	5.429216000	-0.530556000	-1.065059000
H	5.418459000	0.516171000	0.362959000
H	5.449400000	-1.243806000	0.545104000

Reduced

C	2.802322000	0.629646000	0.332844000
C	3.547924000	-0.452420000	-0.040745000
C	2.841423000	-1.651088000	-0.347686000
C	1.471327000	-1.678343000	-0.316284000
C	0.717047000	-0.535503000	0.024498000
N	1.431974000	0.596561000	0.408982000
H	3.392367000	-2.536045000	-0.641997000
H	3.255208000	1.571547000	0.611605000
H	0.939998000	-2.571113000	-0.616475000
C	-0.717042000	-0.535513000	-0.024539000
C	-1.471312000	-1.678360000	0.316232000
C	-2.802326000	0.629642000	-0.332820000
C	-2.841408000	-1.651104000	0.347666000
H	-0.939980000	-2.571138000	0.616393000
H	-3.255218000	1.571548000	-0.611558000
H	-3.392345000	-2.536070000	0.641963000
C	-3.547917000	-0.452429000	0.040778000
N	-1.431982000	0.596549000	-0.409011000
C	-0.720732000	1.725245000	-1.030438000
H	-0.009004000	1.302170000	-1.742769000
H	-1.443218000	2.306558000	-1.600315000
C	-0.000017000	2.594078000	-0.000015000
H	-0.707657000	3.241050000	0.524547000
H	0.707613000	3.241065000	-0.524570000
C	0.720713000	1.725252000	1.030408000
H	1.443196000	2.306579000	1.600274000
H	0.008994000	1.302173000	1.742746000
C	-5.045813000	-0.391006000	0.119468000
H	-5.389164000	-0.607625000	1.134977000
H	-5.425060000	0.591281000	-0.164280000
H	-5.497568000	-1.134988000	-0.542382000
C	5.045823000	-0.391002000	-0.119366000
H	5.389223000	-0.607693000	-1.134843000
H	5.425054000	0.591307000	0.164326000
H	5.497548000	-1.134936000	0.542558000

Compound **5**

Oxidized

C	2.717059000	0.901497000	0.755918000
C	3.490436000	-0.146700000	0.305053000
C	2.889889000	-1.265008000	-0.287527000
C	1.488057000	-1.248214000	-0.403659000
C	0.741715000	-0.179079000	0.054429000
N	1.370132000	0.886364000	0.637979000
H	3.145285000	1.775257000	1.228751000
H	0.975069000	-2.075092000	-0.877832000
C	-0.741718000	-0.179080000	-0.054429000
C	-1.488059000	-1.248214000	0.403659000
C	-2.717062000	0.901498000	-0.755916000
C	-2.889893000	-1.265007000	0.287528000
H	-0.975071000	-2.075091000	0.877832000
H	-3.145289000	1.775259000	-1.228747000
C	-3.490440000	-0.146700000	-0.305048000
N	-1.370136000	0.886365000	-0.637979000
C	-0.562763000	2.030833000	-1.144707000
H	0.231893000	1.609858000	-1.761756000
H	-1.200048000	2.623913000	-1.796597000
C	-0.000001000	2.878519000	0.000000000
H	-0.772071000	3.528206000	0.418614000
H	0.772070000	3.528205000	-0.418614000
C	0.562760000	2.030832000	1.144707000
H	1.200044000	2.623911000	1.796598000
H	-0.231897000	1.609857000	1.761755000
C	3.697715000	-2.428065000	-0.759475000
H	4.651784000	-2.103484000	-1.177997000
H	3.926080000	-3.079410000	0.093126000

Reduced

C	2.773709000	0.976201000	0.487874000
C	3.512139000	-0.115983000	0.154321000
C	2.857011000	-1.331910000	-0.202363000
C	1.481068000	-1.327854000	-0.239052000
C	0.714301000	-0.179241000	0.059939000
N	1.406044000	0.958429000	0.482009000
H	3.224625000	1.910070000	0.794639000
H	0.954329000	-2.212150000	-0.571758000
C	-0.714301000	-0.179241000	-0.059939000
C	-1.481068000	-1.327854000	0.239052000
C	-2.773709000	0.976201000	-0.487873000
C	-2.857012000	-1.331910000	0.202363000
H	-0.954329000	-2.212150000	0.571757000
H	-3.224625000	1.910070000	-0.794637000
C	-3.512139000	-0.115983000	-0.154320000
N	-1.406044000	0.958429000	-0.482009000
C	-0.664997000	2.088186000	-1.066008000
H	0.082976000	1.666094000	-1.740707000
H	-1.358051000	2.668491000	-1.672427000
C	0.000000000	2.957712000	-0.000001000
H	-0.734241000	3.604784000	0.486538000
H	0.734242000	3.604783000	-0.486540000
C	0.664997000	2.088187000	1.066008000
H	1.358051000	2.668491000	1.672426000
H	-0.082976000	1.666096000	1.740706000
C	3.663598000	-2.543918000	-0.557918000
H	4.322788000	-2.333978000	-1.405677000
H	4.303495000	-2.837048000	0.279840000

H	3.162932000	-3.023371000	-1.499234000
C	-3.697704000	-2.428076000	0.759471000
H	-4.651964000	-2.103561000	1.177601000
H	-3.925662000	-3.079659000	-0.093060000
H	-3.163067000	-3.023133000	1.499537000
H	4.565371000	-0.087497000	0.421521000
H	-4.565374000	-0.087494000	-0.421512000
H	3.028436000	-3.390788000	-0.817565000
C	-3.663598000	-2.543918000	0.557918000
H	-4.322798000	-2.333975000	1.405668000
H	-4.303485000	-2.837054000	-0.279846000
H	-3.028437000	-3.390785000	0.817575000
H	4.591673000	-0.050505000	0.172773000
H	-4.591673000	-0.050504000	-0.172770000

Compound **6**

Oxidized

C	1.492192000	-0.991041000	0.338443000
C	0.739185000	0.072398000	-0.085586000
C	2.682427000	1.155270000	-0.876396000
C	3.487416000	0.118395000	-0.472386000
C	2.897496000	-1.000072000	0.148959000
H	1.028116000	-1.831142000	0.837159000
H	3.089824000	2.029097000	-1.367204000
H	4.551306000	0.185781000	-0.647049000
C	-0.739185000	0.072398000	0.085586000
C	-1.492192000	-0.991041000	-0.338443000
C	-2.682427000	1.155270000	0.876396000
C	-2.897496000	-1.000072000	-0.148959000
H	-1.028116000	-1.831142000	-0.837159000
C	-3.487416000	0.118395000	0.472386000
H	-3.089824000	2.029097000	1.367204000
H	-4.551306000	0.185781000	0.647048000
N	-1.340376000	1.145885000	0.699501000
N	1.340376000	1.145885000	-0.699501000
C	0.511122000	2.287412000	-1.167704000
H	1.116707000	2.880905000	-1.848993000
H	-0.311663000	1.868715000	-1.748557000
C	0.000000000	3.136534000	0.000000000
H	0.790828000	3.786101000	0.382452000
H	-0.790828000	3.786101000	-0.382452000
C	-0.511122000	2.287412000	1.167704000
H	0.311663000	1.868715000	1.748557000
H	-1.116707000	2.880905000	1.848993000
O	-3.529044000	-2.058516000	-0.580542000
O	3.529044000	-2.058516000	0.580542000
C	4.973978000	-2.176697000	0.442662000
H	5.464024000	-1.374852000	0.996166000
H	5.216184000	-3.139624000	0.880649000
H	5.245871000	-2.161644000	-0.613406000
C	-4.973978000	-2.176697000	-0.442662000
H	-5.216184000	-3.139624000	-0.880648000
H	-5.245871000	-2.161643000	0.613406000
H	-5.464025000	-1.374852000	-0.996166000

Reduced

C	-1.344746000	-0.954861000	-0.162786000
C	-0.718430000	0.286003000	0.103878000
C	-2.926182000	1.170410000	0.444315000
C	-3.537322000	-0.025307000	0.223810000
C	-2.712466000	-1.135738000	-0.104764000
H	-0.746183000	-1.789893000	-0.490934000
H	-3.500744000	2.054852000	0.680352000
H	-4.612390000	-0.087556000	0.282646000
C	0.722443000	0.331490000	0.102976000
C	1.387817000	-0.885459000	0.405649000
C	2.859461000	1.130695000	-0.643395000
C	2.718624000	-1.112798000	0.134501000
H	0.836093000	-1.675612000	0.891927000
C	3.472437000	-0.069801000	-0.473765000
H	3.413694000	1.979140000	-1.020637000
H	4.506881000	-0.178817000	-0.759058000
N	1.549789000	1.391575000	-0.346989000
N	-1.577282000	1.353003000	0.393714000
C	-1.055208000	2.678638000	0.725584000
H	-1.911252000	3.320273000	0.921404000
H	-0.477549000	2.607208000	1.654614000
C	-0.199215000	3.242513000	-0.399872000
H	-0.612370000	2.952840000	-1.369570000
H	-0.225011000	4.334040000	-0.352746000
C	1.251337000	2.841108000	-0.263252000
H	1.840080000	3.322052000	-1.043778000
H	1.625615000	3.200981000	0.702704000
O	3.222689000	-2.302100000	0.485558000
O	-3.176211000	-2.352787000	-0.408479000
C	-4.592102000	-2.589373000	-0.415078000
H	-5.088004000	-1.953002000	-1.151899000
H	-4.707791000	-3.632543000	-0.696127000
H	-5.016886000	-2.428091000	0.578490000
C	4.612785000	-2.574927000	0.255898000
H	4.775443000	-3.579887000	0.635810000
H	4.843225000	-2.545596000	-0.811756000
H	5.242380000	-1.868894000	0.802663000

Compound **7**

Oxidized

C	-2.630476000	1.490563000	-0.981970000
C	-3.455039000	0.452375000	-0.595925000
C	-2.908678000	-0.631438000	0.091642000
C	-1.535508000	-0.633300000	0.367714000
C	-0.736194000	0.412901000	-0.064073000
N	-1.300826000	1.462209000	-0.733737000
H	-2.999680000	2.353226000	-1.520575000
H	-1.079069000	-1.458185000	0.900945000
C	0.735980000	0.381064000	0.144050000
C	1.476425000	-0.731424000	-0.219664000
C	2.697256000	1.444942000	0.930611000
C	2.858314000	-0.751071000	-0.002808000
H	0.990476000	-1.576577000	-0.688912000
H	3.115137000	2.327722000	1.396141000
C	3.472075000	0.355750000	0.574909000
N	1.362518000	1.451421000	0.722390000
C	0.553256000	2.635925000	1.132389000

Reduced

C	-2.718078000	1.564835000	-0.702063000
C	-3.489840000	0.483311000	-0.408908000
C	-2.866031000	-0.706196000	0.052992000
C	-1.495053000	-0.721340000	0.202364000
C	-0.708180000	0.409286000	-0.082188000
N	-1.353679000	1.537418000	-0.577676000
H	-3.133394000	2.491888000	-1.071959000
H	-0.984040000	-1.603614000	0.565226000
C	0.718925000	0.395144000	0.127522000
C	1.478846000	-0.751911000	-0.147237000
C	2.757268000	1.537282000	0.685305000
C	2.853534000	-0.747245000	-0.026209000
H	0.980944000	-1.634630000	-0.522290000
H	3.191807000	2.466450000	1.026614000
C	3.508741000	0.444281000	0.379230000
N	1.388950000	1.520080000	0.603306000
C	0.615467000	2.660275000	1.125051000

H	-0.285788000	2.255953000	1.716518000
H	1.164645000	3.241787000	1.797169000
C	0.080641000	3.446853000	-0.077923000
H	0.891285000	4.063429000	-0.473106000
H	-0.698958000	4.129244000	0.268552000
C	-0.430531000	2.570678000	-1.224901000
H	-1.008707000	3.154818000	-1.937063000
H	0.388713000	2.105666000	-1.774915000
H	-4.506805000	0.478894000	-0.852878000
H	4.541797000	0.359649000	0.747695000
C	3.727279000	-1.933137000	-0.379803000
O	4.909881000	-1.923453000	-0.200679000
O	2.996625000	-2.917428000	-0.908045000
H	3.571246000	-3.666618000	-1.143747000
C	-3.771706000	-1.853932000	0.350100000
O	-3.811282000	-2.357362000	1.584010000
H	-3.475308000	-1.759077000	2.265379000
O	-4.325148000	-2.344987000	-0.586269000

H	-0.179728000	2.248107000	1.750014000
H	1.268510000	3.240868000	1.773643000
C	0.034667000	3.524784000	0.005865000
H	0.806263000	4.164808000	-0.428752000
H	-0.728640000	4.178937000	0.434015000
C	-0.555234000	2.658740000	-1.106711000
H	-1.194450000	3.243659000	-1.764907000
H	0.235189000	2.224676000	-1.722782000
H	-4.562113000	0.517988000	-0.538871000
H	4.586870000	0.474322000	0.449606000
C	3.687933000	-1.939472000	-0.346350000
O	4.889334000	-1.942248000	-0.274441000
O	2.943996000	-3.001718000	-0.716230000
H	3.544279000	-3.738740000	-0.909222000
C	-3.742220000	-1.905224000	0.284671000
O	-3.300156000	-2.850681000	1.141872000
H	-2.570816000	-2.535750000	1.688953000
O	-4.782180000	-2.027946000	-0.297288000

Compound **8**

Oxidized

C	2.841466000	-0.267311000	-0.251527000
C	3.511443000	0.861859000	0.329697000
C	2.749123000	1.956563000	0.762697000
C	1.372792000	1.943302000	0.643434000
C	0.741640000	0.843150000	0.066444000
N	1.461157000	-0.211285000	-0.393243000
H	3.247560000	2.810192000	1.207677000
H	0.772155000	2.764370000	1.008887000
C	-0.741686000	0.843151000	-0.066463000
C	-1.372866000	1.943289000	-0.643444000
C	-2.841478000	-0.267353000	0.251503000
C	-2.749196000	1.956515000	-0.762723000
H	-0.772257000	2.764383000	-1.008884000
H	-3.247658000	2.810137000	-1.207693000
C	-3.511483000	0.861788000	-0.329743000
N	-1.461174000	-0.211297000	0.393227000
C	-0.706706000	-1.318723000	1.043224000
H	0.010004000	-0.851985000	1.718518000
H	-1.381154000	-1.895173000	1.664065000
C	0.000005000	-2.186726000	-0.000027000
H	-0.708744000	-2.833645000	-0.522066000
H	0.708748000	-2.833668000	0.521990000
C	0.706742000	-1.318731000	-1.043261000
H	1.381224000	-1.895200000	-1.664052000
H	-0.009944000	-0.852014000	-1.718593000
C	-3.599152000	-1.384298000	0.651823000
C	-4.969149000	-1.367464000	0.495980000
H	-3.138433000	-2.266979000	1.067528000
C	-4.923597000	0.839657000	-0.464120000
C	-5.641477000	-0.253500000	-0.054891000
H	-5.541973000	-2.234004000	0.803362000
H	-5.416711000	1.700753000	-0.898393000
H	-6.719061000	-0.273313000	-0.155930000
C	3.599223000	-1.384284000	-0.651864000
C	4.969227000	-1.367470000	-0.495881000
H	3.138573000	-2.266991000	-1.067612000
C	4.923600000	0.839720000	0.464099000
C	5.641516000	-0.253498000	0.055012000
H	5.542075000	-2.234030000	-0.803168000
H	5.416684000	1.700761000	0.898520000
H	6.719090000	-0.273336000	0.156154000

Reduced

C	2.814133000	-0.285211000	-0.207523000
C	3.533553000	0.883059000	0.163506000
C	2.807286000	2.086682000	0.399774000
C	1.445050000	2.098274000	0.331983000
C	0.719625000	0.934535000	-0.018182000
N	1.430688000	-0.196282000	-0.382231000
H	3.348499000	2.980125000	0.686022000
H	0.892926000	2.984767000	0.608427000
C	-0.719643000	0.934523000	0.018004000
C	-1.445081000	2.098281000	-0.332111000
C	-2.814090000	-0.285200000	0.207353000
C	-2.807321000	2.086725000	-0.399652000
H	-0.892953000	2.984758000	-0.608598000
H	-3.348545000	2.980223000	-0.685695000
C	-3.533584000	0.883087000	-0.163337000
N	-1.430717000	-0.196256000	0.382110000
C	-0.694130000	-1.296439000	1.029721000
H	0.043175000	-0.835570000	1.688219000
H	-1.377767000	-1.851156000	1.665181000
C	-0.000087000	-2.187538000	0.000120000
H	-0.716720000	-2.831818000	-0.514973000
H	0.716429000	-2.831958000	0.515191000
C	0.693884000	-1.296509000	-1.029613000
H	1.377358000	-1.851303000	-1.665135000
H	-0.043458000	-0.835631000	-1.688049000
C	-3.509675000	-1.490141000	0.394643000
C	-4.886447000	-1.525672000	0.243205000
H	-2.989165000	-2.404303000	0.639233000
C	-4.932332000	0.812790000	-0.306777000
C	-5.606534000	-0.373650000	-0.100602000
H	-5.407899000	-2.463697000	0.388353000
H	-5.469544000	1.711325000	-0.586302000
H	-6.682234000	-0.418783000	-0.211383000
C	3.509895000	-1.490223000	-0.394761000
C	4.886673000	-1.525669000	-0.243207000
H	2.989417000	-2.404345000	-0.639495000
C	4.932311000	0.812840000	0.306888000
C	5.606620000	-0.373540000	0.100598000
H	5.408246000	-2.463662000	-0.388118000
H	5.469501000	1.711429000	0.586240000
H	6.682309000	-0.418655000	0.211562000

Cell testing of bipyridines

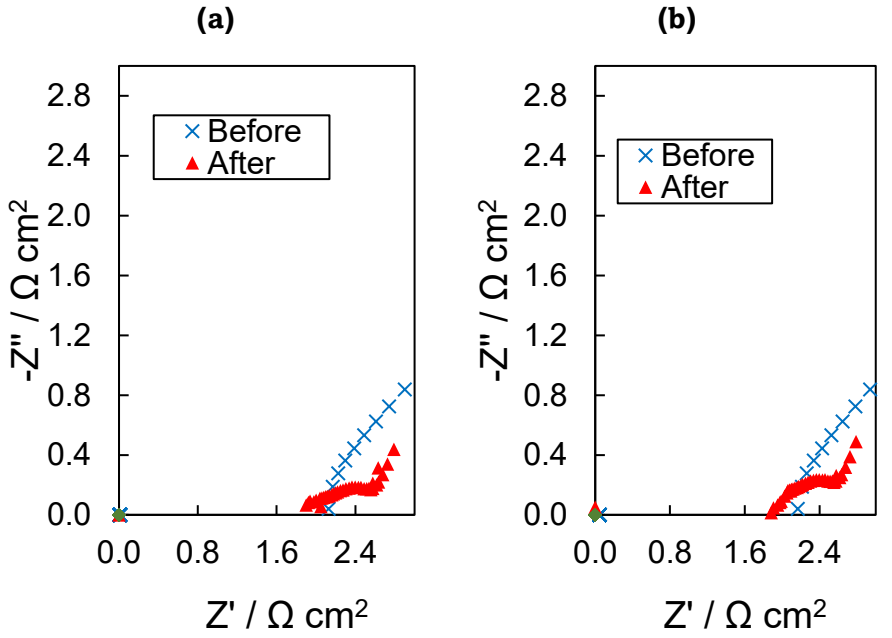

Figure S26: Electrochemical impedance spectroscopy before and after cycling (a) Compound **2** *vs* TEMPOL, (b) Compound **4** *vs* TEMPOL.

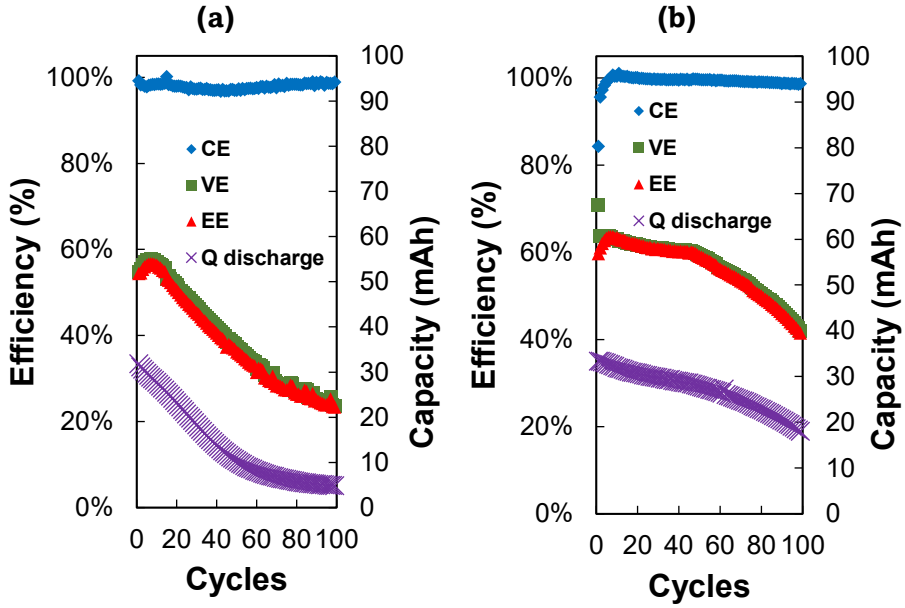

Figure S27: Long term cycling profile of capacity, coulombic, voltage and energy efficiencies *vs* cycle number of the battery at 100 mA/cm^2. (a) Compound **2** *vs* TEMPOL, (b) Compound **4** *vs* TEMPOL.

Degradation of bipyridinium electrolytes

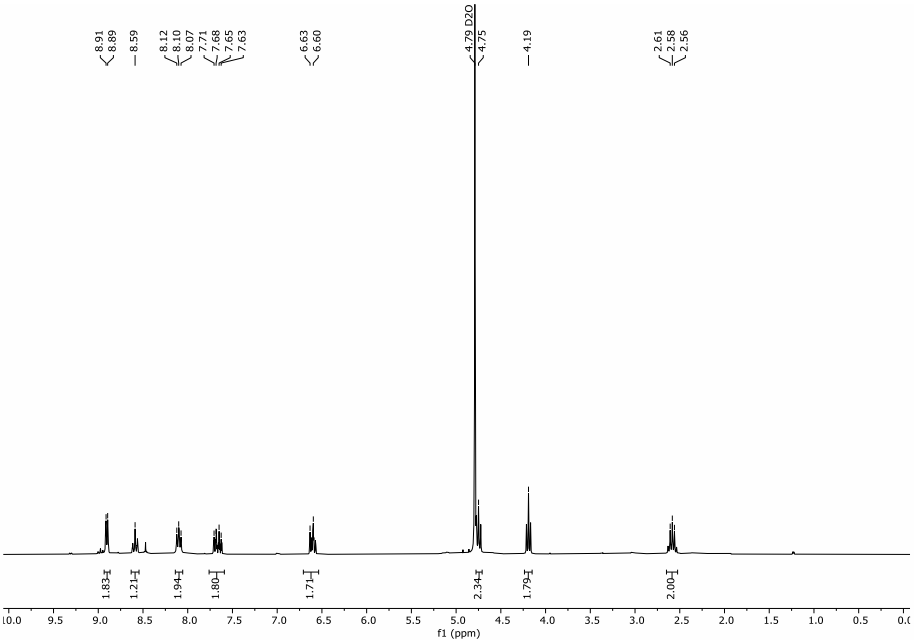

Figure S28: [1]H NMR spectrum of compound **2b**.

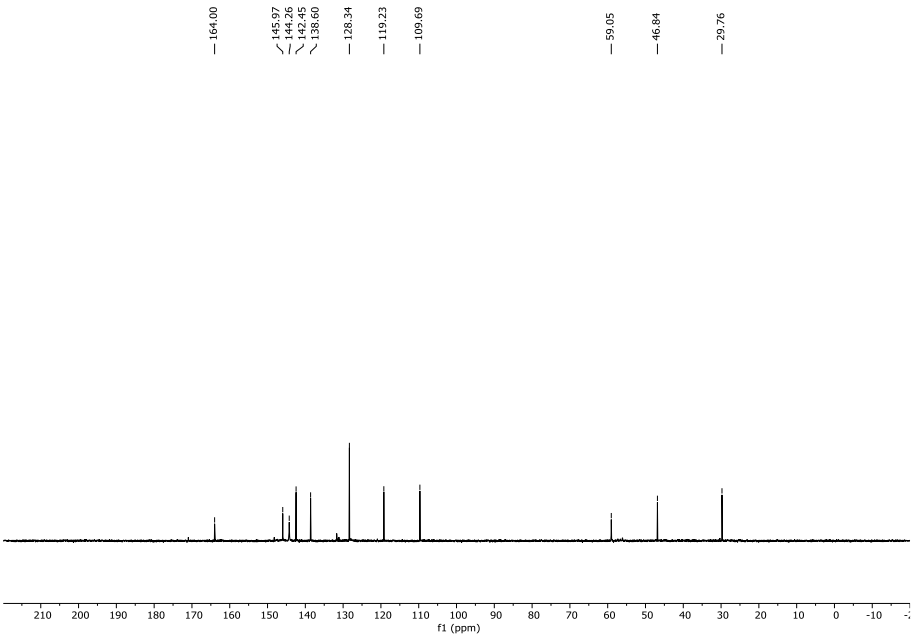

Figure S29: [13]C NMR spectrum of compound **2b**.

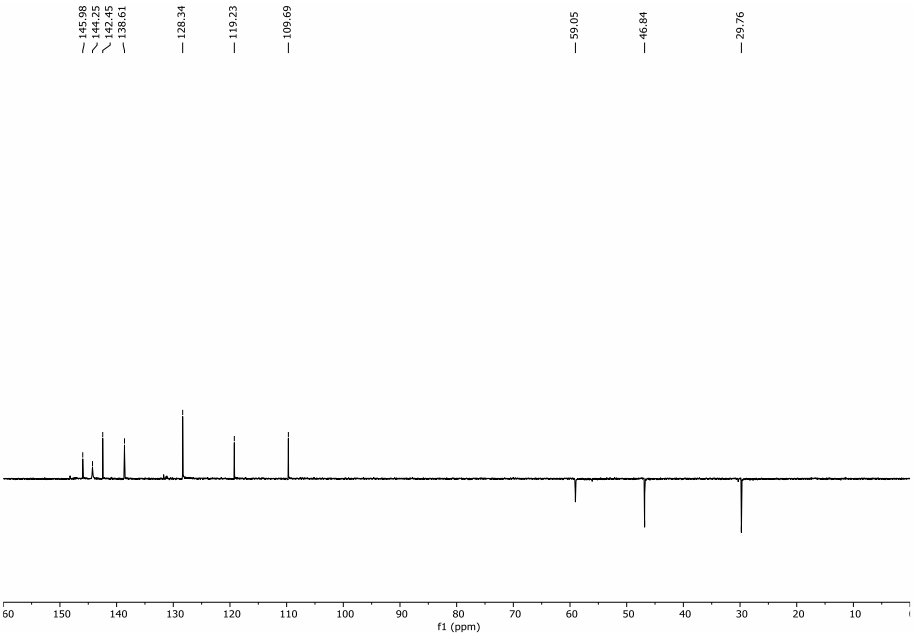

Figure S30: ^{13}C DEPT 135 spectrum of compound **2b**.

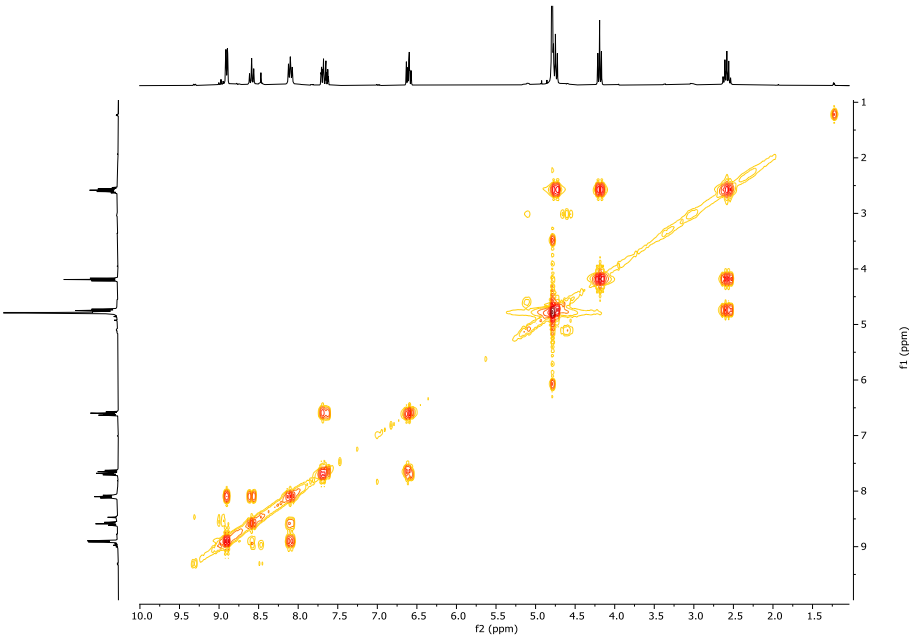

Figure S31: Bidimensional ^{1}H-^{1}H COSY spectrum of compound **2b**.

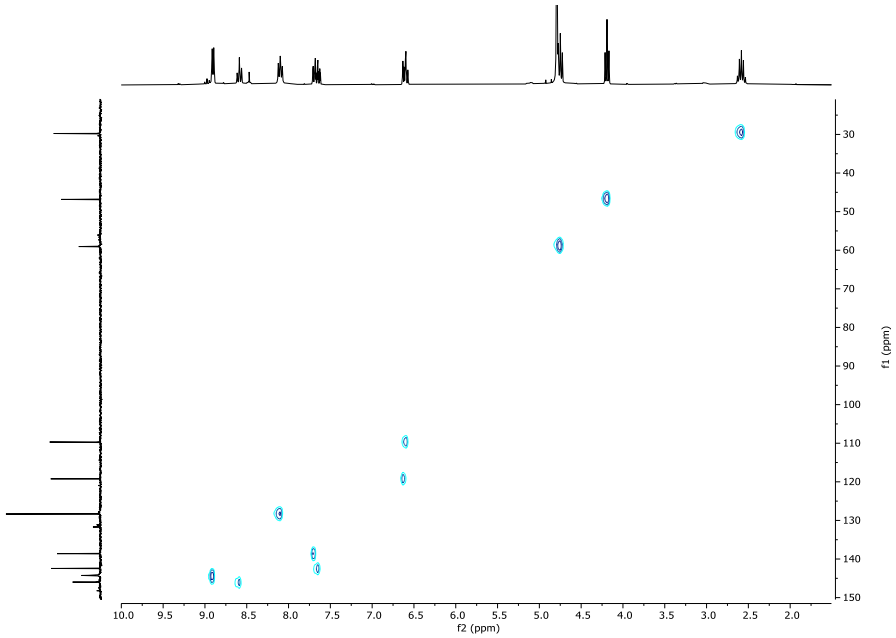

Figure S32: Bidimensional ^{1}H-^{13}C HSQC spectrum of compound **2b**.

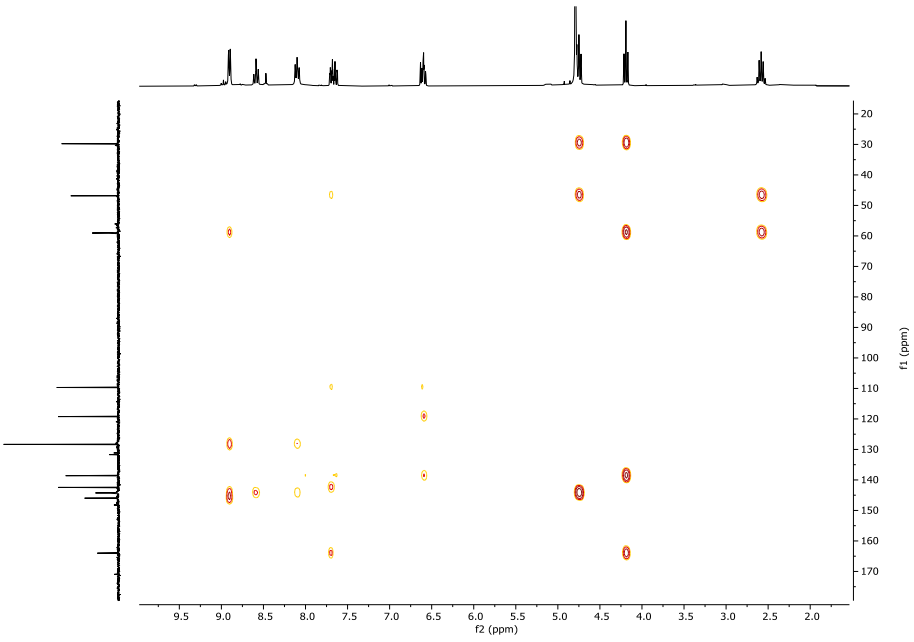

Figure S33: Bidimensional ^{1}H-^{13}C HMBC spectrum of compound **2b**.

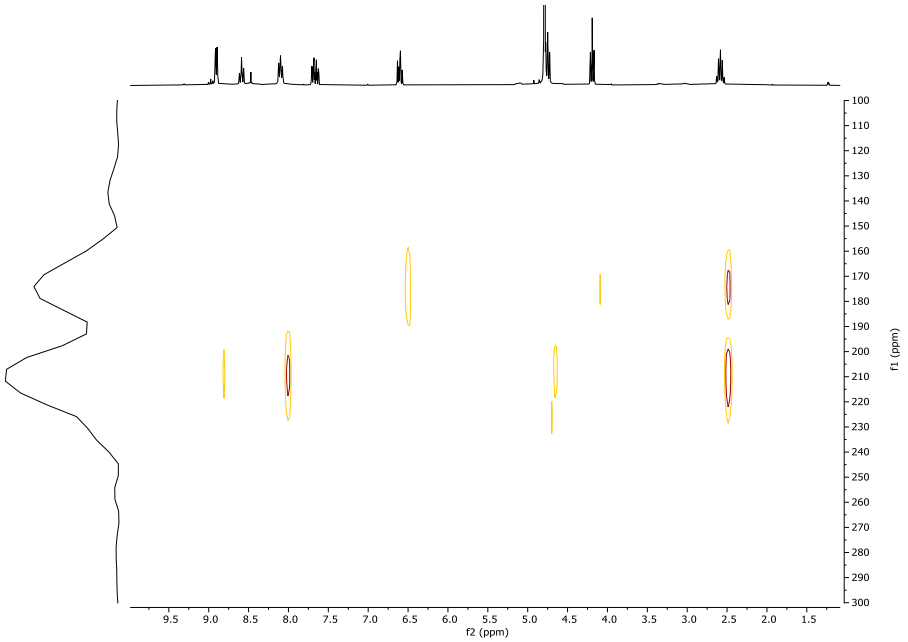

Figure S34: Bidimensional ^{1}H-^{15}N HMBC spectrum of compound **2b**.

*6,7,8,13a-tetrahydrodipyrido[1,2-a':2',1'-c] diazepin-5-ium bromide (**2b**).* The title product was obtained after 1 electron charging process of compound **2** and subsequent isolation. ^{1}H NMR (300 MHz, D_2O) δ 8.93 – 8.88 (m, 2H, $C^{9}H$,$C^{5}H$), 8.59 (tt, *J* = 7.9, 1.4 Hz, 1H, $C^{11}H$), 8.14 – 8.05 (m, 2H, $C^{12}H$, $C^{10}H$), 7.72 – 7.59 (m, 2H, $C^{2}H$,$C^{3}H$ or $C^{4}H$), 6.67 – 6.60 (m, 1H, $C^{1}H$), 6.62 – 6.54 (m, 1H, $C^{2}H$,$C^{3}H$ or $C^{4}H$), 4.78 – 4.71 (m, 2H, $C^{8}H$), 4.19 (t, *J* = 6.9 Hz, 2H, $C^{6}H$), 2.58 (p, *J* = 7.1 Hz, 2H, $C^{7}H$). ^{13}C NMR (75 MHz, D_2O) δ 164.00 (C^{13}), 145.97 (C^{11}), 144.26 (x 2C, C^{9}, C^{5}), 142.45 (C^{2} ,C^{3} or C^{4}), 138.60 (C^{2} ,C^{3} or C^{4}), 128.34 (x 2C, C^{12}, C^{10}), 119.23 (C^{2} ,C^{3} or C^{4}), 109.69 (C^{1}), 59.05 (C^{8}), 46.84 (C^{6}), 29.76 (C^{7}). ^{15}N NMR (50 MHz, D_2O) δ 210.2 (N+), 174.9 (N).

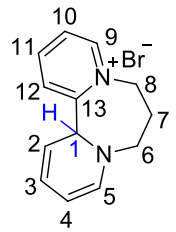

2b

Electrochemical characterization of $Na_4[Fe(CN)_6]$ and AQDS systems

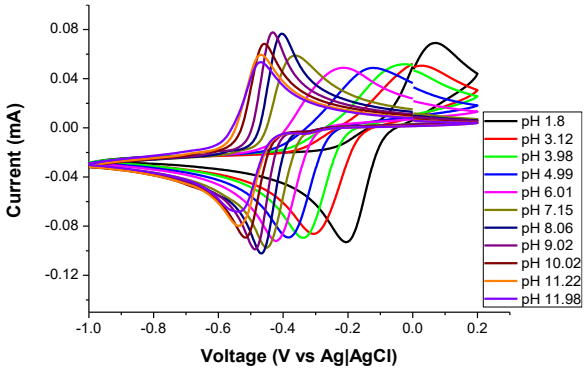

Figure S35: CV of 10 mM AQDS solution measured on glassy carbon working electrode (WE) at different pH values.

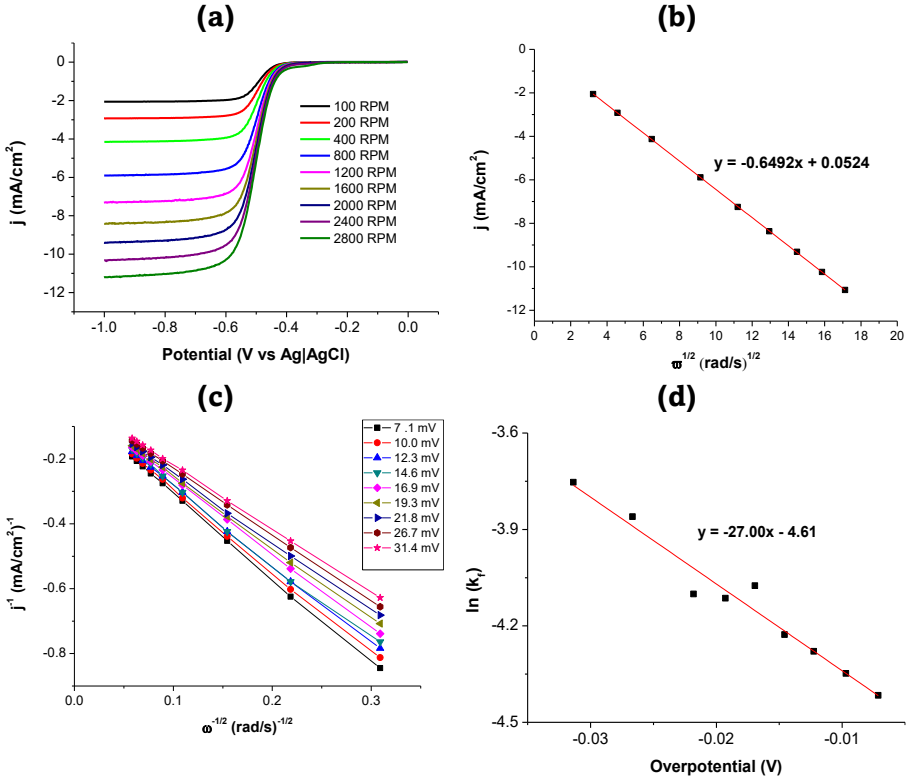

Figure S36: RDE analysis of **AQDS** electrolyte on glassy carbon working electrode: (a) LSV scans with rotating disc working electrode; (b) Levich analysis of the reduction limiting currents; (c) Koutecký-Levich plot (d) and Tafel-plot for different overpotentials.

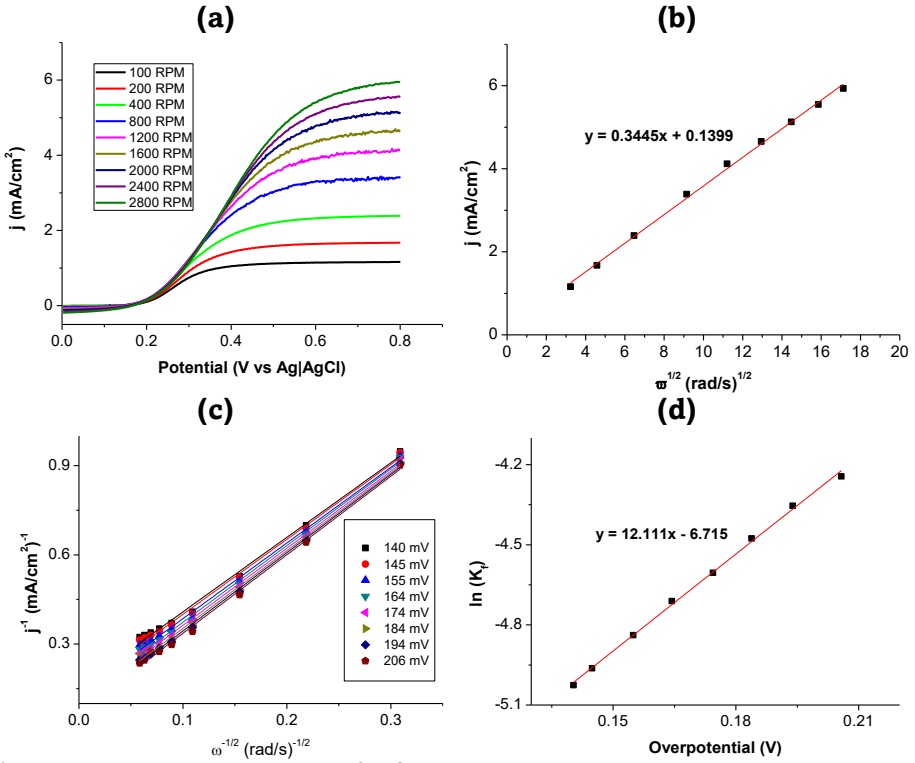

Figure S37: RDE analysis of **$Na_4[Fe(CN)_6]$** electrolyte on glassy carbon working electrode: (a) LSV scans with rotating disc working electrode; (b) Levich analysis of the oxidation limiting currents; (c) Koutecký-Levich plot (d) and Tafel-plot for different overpotentials.

Solubility of $Na_4[Fe(CN)_6]$ and AQDS systems

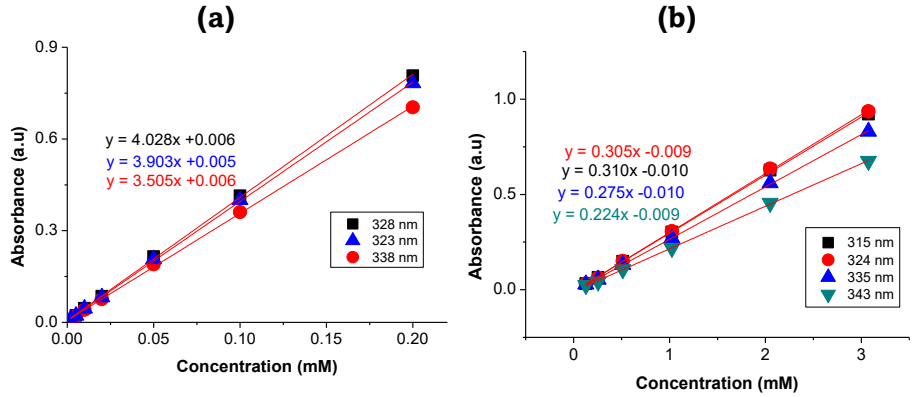

Figure S38: UV-Vis calibration curves at different wavelengths for the (a) AQDS and (b) $Na_4[Fe(CN)_6]$ respectively.

Single-cell details of $Na_4[Fe(CN)_6]$ and AQDS systems

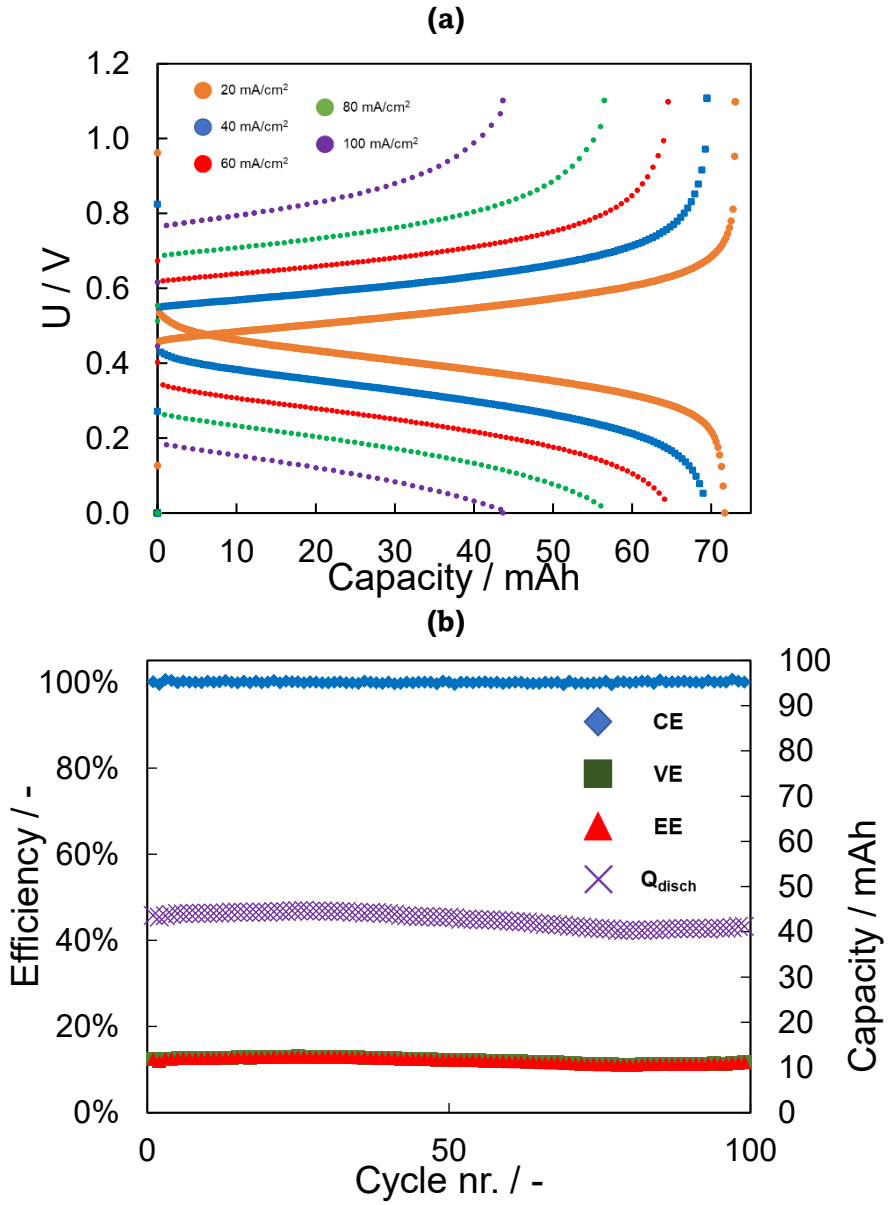

Figure S39: (a) E_{cell} *vs* Capacity plot at different current densities (20, 40, 60, 80 and 100 mA/cm^2) for the battery using 0.08 M AQDS in 1 M **acetate buffer 1 M (pH 4.5)** *vs* 0.2 M $Na_4[Fe(CN)_6]$ in **acetate buffer 1 M (pH 4.5)** as electrolytes and N212® activated membrane inside homemade glovebox. (b) Coulombic, Voltage, Energy Efficiencies and $Q_{discahrge}$ for the battery cycle 100 cycles at 100 mA/cm^2 using 0.08 M AQDS in acetate buffer 1 M (pH 4.5) *vs* 0.2 M $Na_4[Fe(CN)_6]$ in **acetate buffer 1 M (pH 4.5)** as electrolytes and N212® activated membrane inside homemade glovebox.

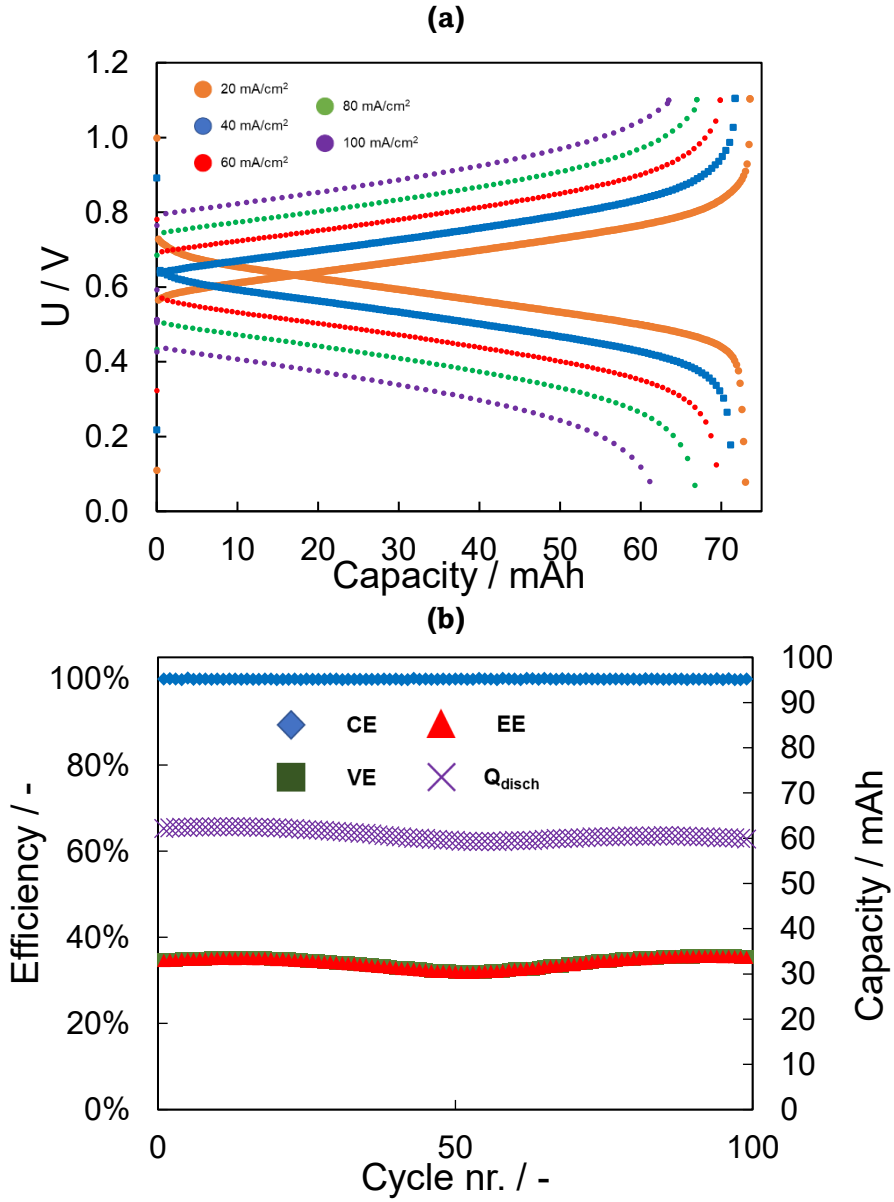

Figure S40: (a) E_{cell} *vs* Capacity plot at different current densities (20, 40, 60, 80 and 100 mA/cm^2) for the battery using 0.08 M AQDS in 1 M **phosphate buffer 1 M (pH 7.5)** *vs* 0.2 M $Na_4[Fe(CN)_6]$ in **phosphate buffer 1 M (pH 7.5)** as electrolytes and N212® activated membrane inside homemade glovebox. (b) Coulombic, Voltage, Energy Efficiencies and $Q_{discahrge}$ for the battery cycle 100 cycles at 100 mA/cm^2 using 0.08 M AQDS in **phosphate buffer 1 M (pH 7.5)** *vs* 0.2 M $Na_4[Fe(CN)_6]$ in **phosphate buffer 1 M (pH 7.5)** as electrolytes and N212® activated membrane inside homemade glovebox.

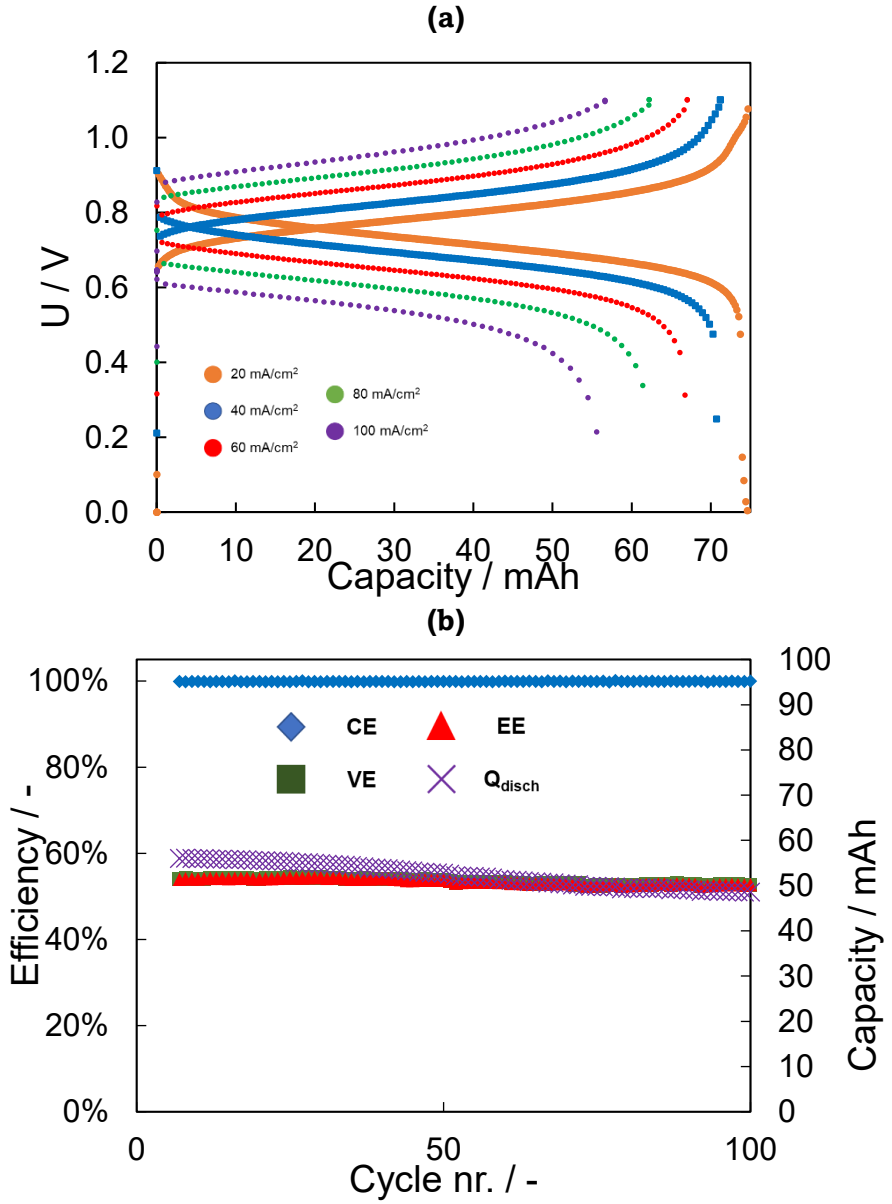

Figure S41: (a) E_{cell} *vs* Capacity plot at different current densities (20, 40, 60, 80 and 100 mA/cm^2) for the battery using 0.08 M AQDS in 1 M **carbonate buffer 1 M (pH 10.5)** *vs* 0.2 M $Na_4[Fe(CN)_6]$ in **carbonate buffer 1 M (pH 10.5)** as electrolytes and N212® activated membrane inside homemade glovebox. (b) Coulombic, Voltage, Energy Efficiencies and $Q_{discahrge}$ for the battery cycle 100 cycles at 100 mA/cm^2 using 0.08 M AQDS in **carbonate buffer 1 M (pH 10.5)** *vs* 0.2 M $Na_4[Fe(CN)_6]$ in **carbonate buffer 1 M (pH 10.5)** as electrolytes and N212® activated membrane inside homemade glovebox.

Table S1: Coulombic, voltage, energy efficiencies and capacity decay at different current densities for the battery at different pH.

pH	*I* (mA/cm^2)	CE (%)	VE (%)	EE (%)	CU (%)	Capacity decay (mAh/cycle)	Capacity decay (%$Q_{theo.}$/cycle)
pH 4	20	96.8	70.0	67.8	89.4	-0.962	-1.12
	40	99.8	47.1	47.0	81.2	-0.06	-0.07
	60	100	32.1	32.1	75.2	0.036	0.04
	80	100	21.2	21.2	65.6	0.022	0.03
	100 (100c)	100	12.2	12.2	53.3	-0.049	-0.06
pH 7	20	99.4	81.8	81.3	87.3	-0.192	-0.22
	40	99.8	66.3	66.2	83.7	-0.045	-0.05
	60	100	54.1	54.1	81.2	0.01	0.01
	80	100	44.0	44.0	77.9	0.045	0.05
	100 (100c)	100	34.1	34.1	74.5	-0.028	-0.03
pH 10	20	98.9	88.0	87.0	89.5	0.142	0.17
	40	99.7	79.0	78.7	83.5	-0.153	-0.18
	60	99.8	69.9	69.8	78.5	-0.157	-0.18
	80	99.9	61.4	61.4	72.5	-0.071	-0.08
	100 (100c)	99.9	53.4	53.4	66.7	-0.092	-0.11

Table S2: Coulombic, voltage, energy efficiencies and capacity decay at different current densities for the battery exposed to different concentrations of O_2.

O_2	*I* (mA/cm^2)	CE (%)	VE (%)	EE (%)	CU (%)	Capacity decay (mAh/cycle)	Capacity decay (%$Q_{theo.}$/cycle)
Exposed to atmospheric O_2 concetrations	20	79.3	84.0	66.6	41.1	-4.01	-6.00
	40	90.2	65.8	59.3	10.5	-0.51	-0.76
	60	92.0	48.3	44.4	4.5	-0.234	-0.35
	80	62.3	1.14	0.77	2.3	-1.3	1.87
	100 (100c)	---	---	---	---	---	---
Home-made glovebox	20	97.8	90.0	88.1	59.1	-0.81	-1.2
	40	99.7	83.1	82.8	53.1	-0.17	-0.26
	60	99.7	75.2	75.0	50.4	-0.13	-0.29
	80	99.7	67.6	67.5	48.1	-0.12	-0.18
	100 (100c)	99.8	60.3	60.1	44.9	-0.09	-0.14
Commercial glovebox	20	99.5	69.5	69,1	93.2	-0.°	-0.44
	40	99.0	82.8	82.0	85.7	-0.392	-0.58
	60	99.3	76.7	76.1	80.2	-0.29	-0.43
	80	99.5	69.5	69.1	74.2	-0.071	-0.08
	100 (100c)	99.6	63.1	63.9	67.4	-0.062	-0.09

Table S3: Coulombic, voltage, energy efficiencies and capacity decay at different current densities for the battery using the activated or non-activated membrane.

Membrane	*I* (mA/cm^2)	CE (%)	VE (%)	EE (%)	CU (%)	Capacity decay (mAh/cycle)	Capacity decay (%$Q_{theo.}$/cycle)
Activated	20	97.8	90.0	88.1	59.1	-0.81	-1.2
	40	99.7	83.1	82.8	53.1	-0.17	-0.26
	60	99.7	75.2	75.0	50.4	-0.13	-0.29
	80	99.7	67.6	67.5	48.1	-0.12	-0.18
	100 (100c)	99.8	60.3	60.1	44.9	-0.09	-0.14
NON-activated	20	97.8	89.0	87.0	48.4	-1.09	-1.63
	40	99.8	79.0	78.9	40.6	-0.1	-0.15
	60	99.9	69.6	69.5	38.6	-0.05	-0.07
	80	99.8	61.3	61.2	36.4	-0.05	-0.07
	100 (100c)	99.8	52.9	52.8	32.7	-0.05	-0.07

Table S4: Coulombic, voltage, energy efficiencies and capacity decay at different current densities for the battery being the catholyte and the anolyte the capacity limiting side.

CLS	*I* (mA/cm^2)	CE (%)	VE (%)	EE (%)	CU (%)	Capacity decay (mAh/cycle)	Capacity decay (%$Q_{theo.}$/cycle)
Anolyte	20	97.8	90.0	88.1	59.1	-0.81	-1.2
	40	99.7	83.1	82.8	53.1	-0.17	-0.26
	60	99.7	75.2	75.0	50.4	-0.13	-0.29
	80	99.7	67.6	67.5	48.1	-0.12	-0.18
	100 (100c)	99.8	60.3	60.1	44.9	-0.09	-0.14
Catholyte	20	98.0	91.5	89.7	89.0	0.283	0.33
	40	99.0	85.1	84.3	83.4	-0.21	-0.24
	60	99.3	78.9	78.4	78.7	-0.28	-0.32
	80	99.6	72.7	72.4	73.3	-0.164	-0.19
	100 (100c)	99.7	66.6	66.4	67.5	-0.151	-0.18

^{1}H and ^{13}C NMR spectra of (SPr)$_3$4TpyTz

2,4,6-tris-(4-pyridyl)-1,3,5-triazine (**TPT**)

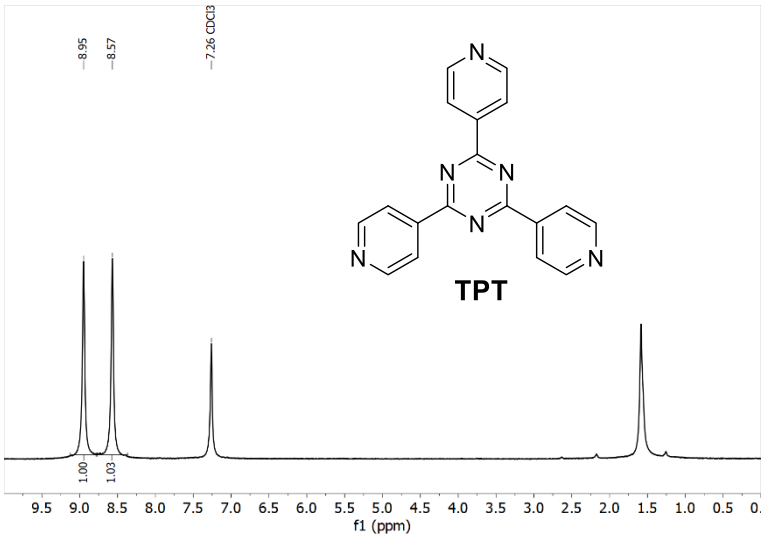

Figure S42: ^{1}H NMR spectrum of **TPT**.

3,3',3''-((1,3,5-triazine-2,4,6-triyl)tris(pyridine-1-ium-4,1-diyl))tris(propane-1-sulfonate) **(SPr)$_3$4TpyTz**

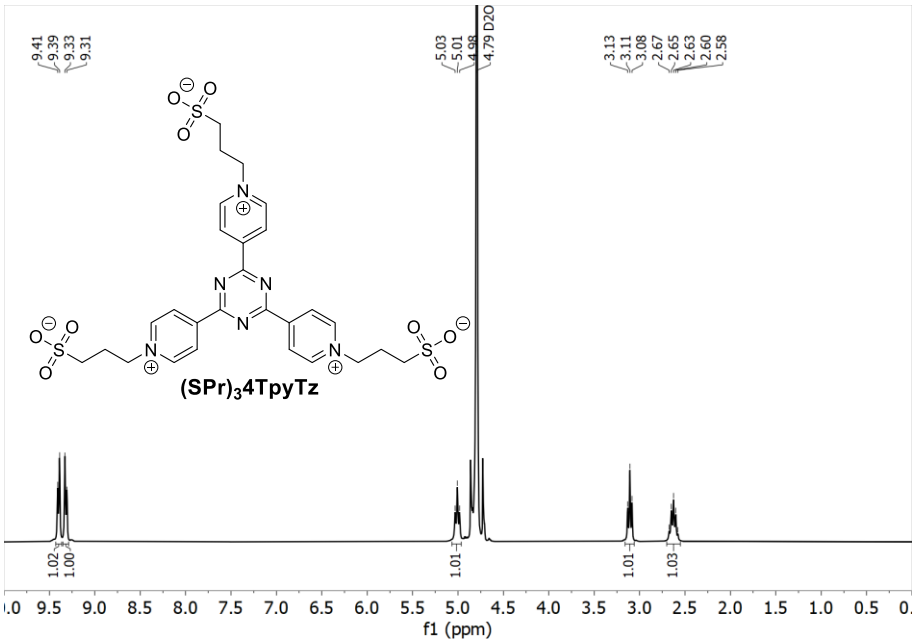

Figure S43: ^{1}H NMR in D_2O of compound **(SPr)$_3$4TpyTz.**

Electrochemical characterization of $(SPr)_3$4TpyTz

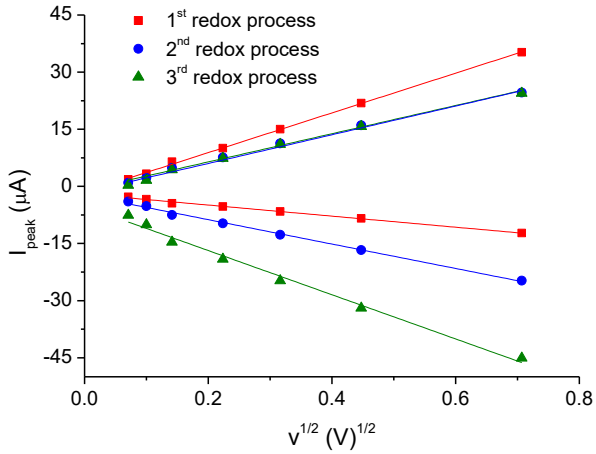

Figure S44: Peak current (anodic and cathodic) *vs* square root of the scan rate for the first (red) second (blue) and third (green) redox processes of 1 mM **$(SPr)_3$4TpyTz** in 1 M KCl.

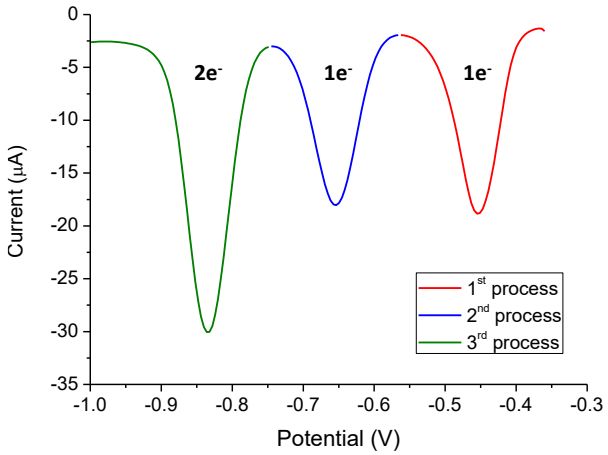

Figure S45: Differential Pulse Voltammetry of 1 mM **$(SPr)_3$4TpyTz** in 1 M KCl.

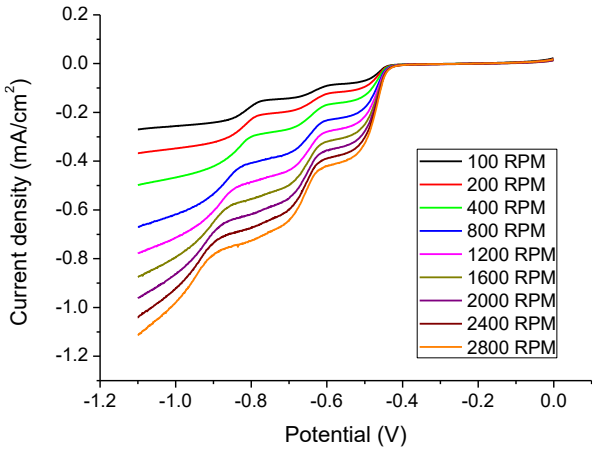

Figure S46: Rotating Disk Electrode study of the reduction of 1 mM of **(SPr)$_3$4TpyTz** in 1 M KCl on a GC electrode at rotation rates from 100 to 2800 rpm.

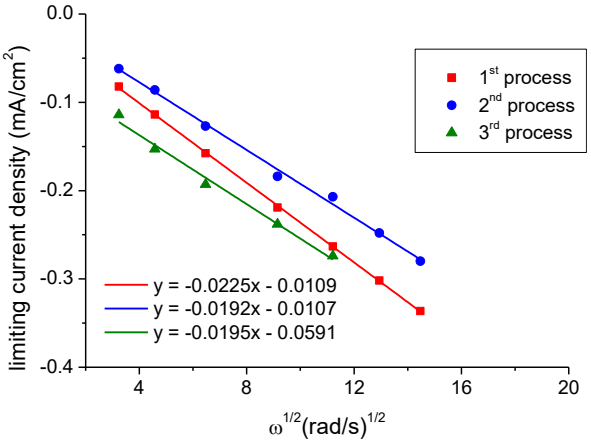

Figure S47: Levich plot for the first (red), second (blue), and third (green) redox processes (limiting current *vs* square root of rotation rate in rad/s) of 1 mM of **(SPr)$_3$4TpyTz** in 1 M KCl. Note that all the slopes are almost equal but the fact that the third process involves 2 electrons make the diffusion coefficient lower.

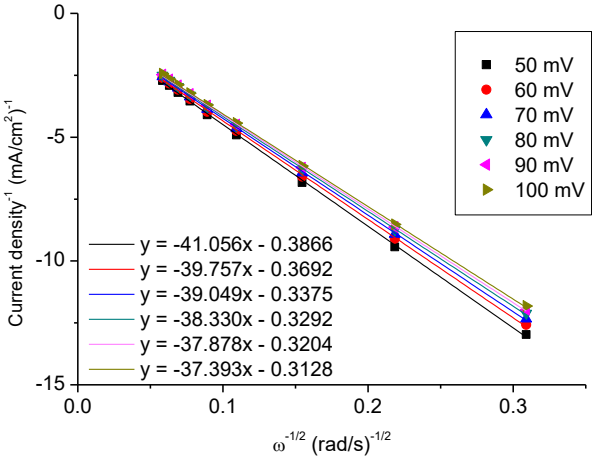

Figure S48: Koutecky-Levich plot at different overpotentials for the first reduction process of 1 mM of **(SPr)$_3$4TpyTz** in 1 M KCl.

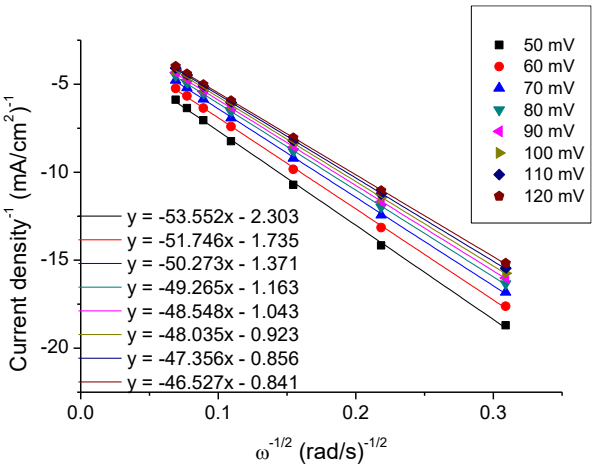

Figure S49: Koutecky-Levich plot at different overpotentials for the second reduction process of 1 mM of **(SPr)$_3$4TpyTz** in 1 M KCl.

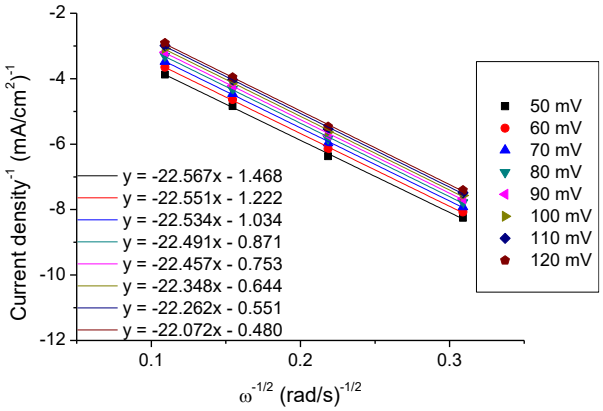

Figure S50: Koutecky-Levich plot at different overpotentials for the third reduction process of 1 mM of **(SPr)$_3$4TpyTz** in 1 M KCl. The third process present contribution of the other two processes moving away from the Koutecky-Levich approach.

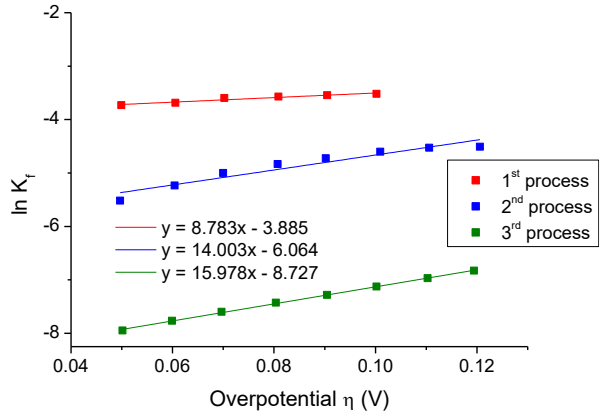

Figure S51: Tafel plot, the logarithm of kinetically limited current *vs* overpotential for the first (red) second (blue) and third (green) redox processes of 1 mM of **(SPr)$_3$4TpyTz** in 1 M KCl.

Solubility of $(SPr)_3$4TpyTz

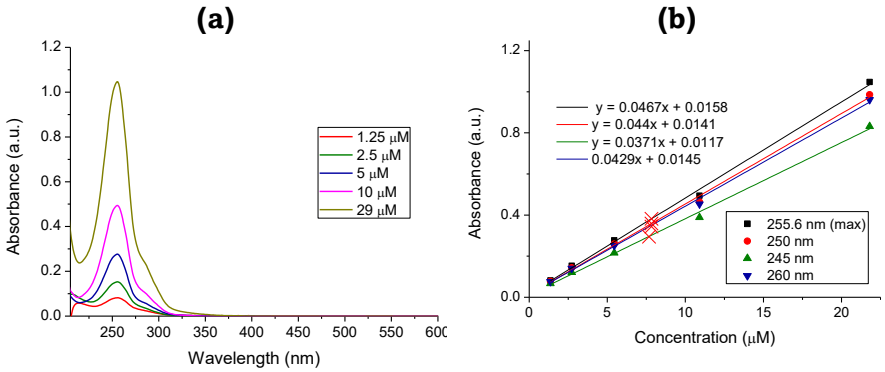

Figure S52: (a) UV-Vis spectra at different concentrations of compound **$(SPr)_3$4TpyTz** in 1 M KCl (b) Calibration curves at different wavelengths and saturated solution (red crosses).

DFT Calculation $(SPr)_3$4TpyTz

Optimized geometries of compound **$(SPr)_3$4TpyTz**

$(SPr)_3$4TpyTz

Oxidized				Reduced			
6	1.288148000	-0.223624000	-1.057641000	6	1.044190000	0.781271000	-1.374753000
6	-0.450522000	1.205076000	-1.061185000	6	-1.192470000	0.530528000	-1.367395000
6	-0.818679000	-1.014898000	-1.043739000	6	0.146036000	-1.306974000	-1.396272000
6	-0.972714000	2.594199000	-1.055451000	6	-2.554086000	1.126529000	-1.360936000
6	-2.345765000	2.831935000	-1.025335000	6	-3.686749000	0.313667000	-1.366220000
6	-0.100737000	3.676862000	-1.073004000	6	-2.726046000	2.509681000	-1.353906000
6	-2.801624000	4.128099000	-1.008932000	6	-4.934365000	0.888582000	-1.368319000
1	-3.056284000	2.017325000	-1.013745000	1	-3.595049000	-0.763241000	-1.371047000
6	-0.609525000	4.957791000	-1.052034000	6	-3.996947000	3.035316000	-1.356120000
1	0.970418000	3.533162000	-1.096827000	1	-1.873951000	3.174339000	-1.348905000
1	-3.854474000	4.377500000	-0.983811000	1	-5.848267000	0.309476000	-1.371964000
1	0.012001000	5.844519000	-1.038586000	1	-4.192397000	4.099735000	-1.350789000
6	2.751456000	-0.469265000	-1.056264000	6	2.238119000	1.666554000	-1.372027000
6	3.648331000	0.597626000	-1.059622000	6	2.093541000	3.051714000	-1.320453000
6	3.247292000	-1.767909000	-1.047185000	6	3.524808000	1.131571000	-1.423999000
6	4.997937000	0.337781000	-1.054677000	6	3.212243000	3.851200000	-1.323800000
1	3.303235000	1.621915000	-1.067942000	1	1.113640000	3.505343000	-1.278972000
6	4.609869000	-1.973963000	-1.039291000	6	4.609964000	1.974276000	-1.426392000
1	2.583403000	-2.621062000	-1.043938000	1	3.678879000	0.062569000	-1.464648000
1	5.744155000	1.121768000	-1.059563000	1	3.162378000	4.931440000	-1.283053000
1	5.063324000	-2.956972000	-1.008804000	1	5.631214000	1.618623000	-1.465590000
6	-1.759873000	-2.161747000	-1.025350000	6	0.301618000	-2.716648000	-1.411801000
6	-3.132586000	-1.950965000	-1.087775000	6	-0.819229000	-3.594864000	-1.416962000
6	-1.279198000	-3.466991000	-0.937825000	6	1.585300000	-3.332958000	-1.421590000
6	-3.986863000	-3.032279000	-1.060188000	6	-0.642239000	-4.941772000	-1.432900000
1	-3.544192000	-0.953549000	-1.153030000	1	-1.824503000	-3.197422000	-1.408578000
6	-2.173130000	-4.510219000	-0.917185000	6	1.702359000	-4.686814000	-1.437360000
1	-0.219375000	-3.673541000	-0.887368000	1	2.481488000	-2.728457000	-1.416593000
1	-5.065638000	-2.939458000	-1.083009000	1	-1.469731000	-5.639811000	-1.434303000
1	-1.863875000	-5.544752000	-0.850668000	1	2.660708000	-5.190145000	-1.441131000
7	-1.334829000	0.211279000	-1.054377000	7	-1.113285000	-0.779162000	-1.385581000
7	0.483925000	-1.283407000	-1.043838000	7	1.257703000	-0.513588000	-1.393972000
7	0.869731000	1.038952000	-1.065706000	7	-0.156254000	1.387603000	-1.358381000

7	-3.499282000	-4.282781000	-0.983666000	7	0.604440000	-5.498664000	-1.458725000
7	5.455983000	-0.929453000	-1.048754000	7	4.442645000	3.310263000	-1.384621000
7	-1.937917000	5.161905000	-1.026912000	7	-5.073868000	2.228453000	-1.371699000
6	-4.422148000	-5.442636000	-0.896403000	6	0.760005000	-6.952557000	-1.354419000
1	-5.351255000	-5.145260000	-1.377723000	1	-0.077198000	-7.414252000	-1.880964000
1	-3.967062000	-6.234633000	-1.488346000	1	1.678572000	-7.226696000	-1.876021000
6	-4.636781000	-5.895083000	0.557285000	6	0.803380000	-7.403340000	0.098924000
1	-3.912839000	-5.398505000	1.207354000	1	-0.110846000	-7.082147000	0.606002000
1	-4.424229000	-6.964180000	0.617824000	1	1.648627000	-6.925224000	0.602210000
6	-6.038945000	-5.688139000	1.115742000	6	0.936297000	-8.913627000	0.190558000
1	-6.792407000	-6.216280000	0.526642000	1	0.084472000	-9.416823000	-0.273851000
1	-6.078937000	-6.070863000	2.137410000	1	1.847931000	-9.265013000	-0.299324000
6	-2.478962000	6.541035000	-0.939713000	6	-6.428897000	2.818024000	-1.306510000
1	-3.367560000	6.557124000	-1.567975000	1	-7.099402000	2.141938000	-1.836751000
1	-1.734868000	7.201623000	-1.379263000	1	-6.395850000	3.765881000	-1.843445000
6	-2.816349000	6.926365000	0.510099000	6	-6.861525000	3.010865000	0.138241000
1	-3.852113000	7.269824000	0.542160000	1	-6.840922000	2.048881000	0.657593000
1	-2.764718000	6.040787000	1.147597000	1	-6.160723000	3.681433000	0.643166000
6	-1.962778000	8.033779000	1.114367000	6	-8.263206000	3.594035000	0.189242000
1	-2.307992000	8.243299000	2.128732000	1	-8.988751000	2.925703000	-0.280826000
1	-2.031778000	8.957928000	0.535833000	1	-8.311557000	4.561151000	-0.317186000
6	6.922586000	-1.154170000	-0.988915000	6	5.629806000	4.189287000	-1.315124000
1	7.111844000	-2.135426000	-1.419066000	1	6.417487000	3.714629000	-1.900225000
1	7.368896000	-0.403892000	-1.638901000	1	5.362431000	5.131727000	-1.792839000
6	7.464181000	-1.033409000	0.445188000	6	6.056579000	4.396537000	0.129386000
1	8.296955000	-0.327455000	0.436522000	1	5.234786000	4.847568000	0.692208000
1	6.698409000	-0.600204000	1.092743000	1	6.284792000	3.428714000	0.584253000
6	7.983576000	-2.322087000	1.070574000	6	7.279615000	5.295352000	0.190910000
1	8.363135000	-2.107653000	2.071450000	1	7.070089000	6.283375000	-0.226249000
1	8.798508000	-2.755289000	0.485843000	1	8.119134000	4.863029000	-0.359045000
16	6.764464000	-3.622564000	1.276477000	16	7.849238000	5.555927000	1.869002000
16	-0.213432000	7.659521000	1.256602000	16	-8.829048000	3.866009000	1.866729000
16	-6.578367000	-3.979347000	1.212245000	16	1.010980000	-9.492542000	1.883462000
8	0.333671000	8.681601000	2.182069000	8	-10.203438000	4.412858000	1.728131000
8	0.352383000	7.777027000	-0.119649000	8	-7.876374000	4.835681000	2.469695000
8	5.546443000	-2.967300000	1.823236000	8	6.717348000	6.191924000	2.593874000
8	7.379935000	-4.596952000	2.210367000	8	9.032093000	6.446649000	1.743907000
8	-6.917658000	-3.563968000	-0.180828000	8	-0.250070000	-9.040087000	2.529175000
8	-5.429885000	-3.213020000	1.765101000	8	2.220537000	-8.864760000	2.479609000
8	-7.765482000	-3.989549000	2.102339000	8	1.113607000	-10.972489000	1.789057000
8	-0.123473000	6.272675000	1.786345000	8	-8.796370000	2.537048000	2.532083000
8	6.535595000	-4.202266000	-0.079880000	8	8.189605000	4.208978000	2.399546000

Cell testing of $(SPr)_3$4TpyTz

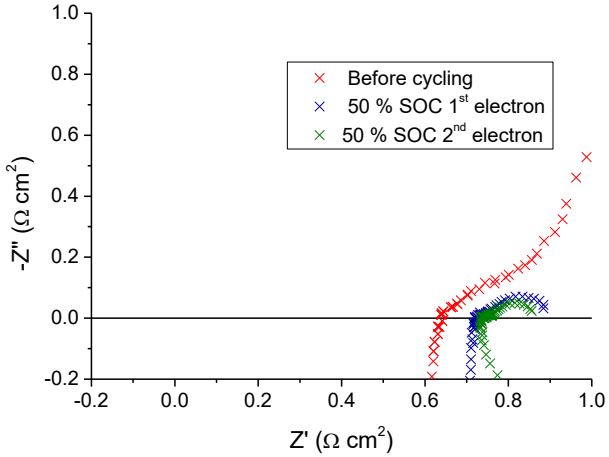

Figure S53: Electrochemical impedance spectroscopy for the battery 100 mM **$(SPr)_3$4TpyTz** in 3 M KCl *vs* 100 mM $K_4[Fe(CN)_6]$ in 1 M of KCl before cycling (red crosses) 50% SOC for the first process (blue crosses) and 50% SOC for the second process (green crosses).

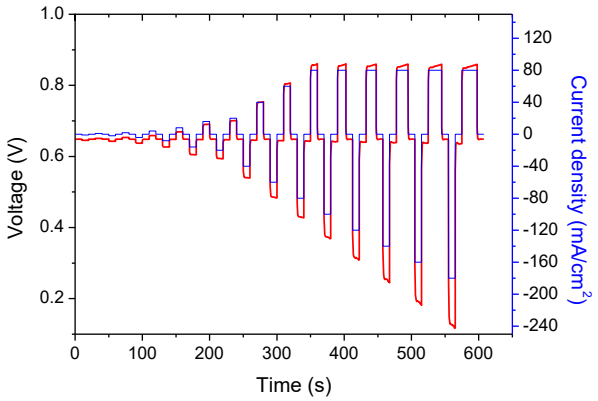

Figure S54: Current and voltage profile at consecutive charging, OCV and discharging at different currents for polarization curve of the first electron of the battery 100 mM **$(SPr)_3$4TpyTz** in 3 M KCl *vs* 100 mM $K_4[Fe(CN)_6]$ in 1 M of KCl.

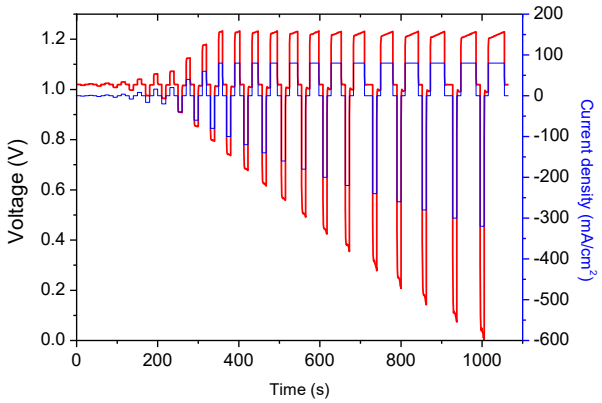

Figure S55: Current and voltage profile at consecutive charging, OCV and discharging at different currents for polarization curve of the second electron of the battery 100 mM **(SPr)$_3$4TpyTz** in 3 M KCl *vs* 100 mM $K_4[Fe(CN)_6]$ in 1 M of KCl.

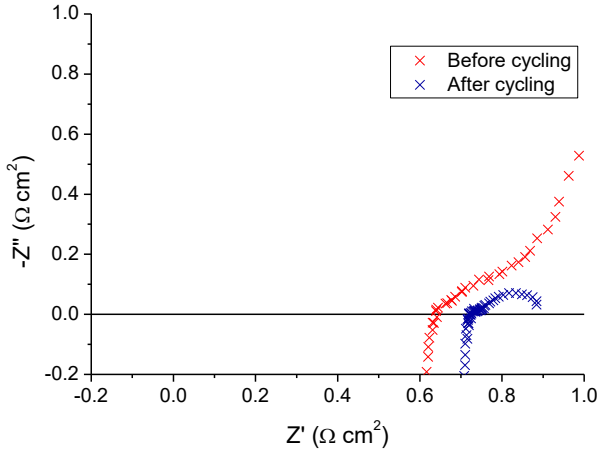

Figure S56: Electrochemical impedance spectroscopy for the battery 200 mM **(SPr)$_3$4TpyTz** in 3 M KCl *vs* 300 mM $K_4[Fe(CN)_6]$ in 1 M of KCl before and after 14 days of cycling the battery.

Annex B: Perspectives of RFB by Juan Asenjo Pascual

Annex B: Perspectives of RFB

Vanadium *vs* Organic Redox Flow Batteries:

Vanadium Redox Flow Batteries (VRFB) have reached the market based on the scalability, high storage capacity, long life, recyclability of the electrolytes, and high efficiency of the batteries. These excellent characteristics have been reached after more than 20 years of research on all the separate components.[1] Nowadays, Aqueous Organic RFB (AORFB) attract the interest of our community because of their promise as alternatives to VRFB, such as availability or high tunability of their electronic properties.[2]

The current potential showed by VRFB is 1.26 V under strong acidic conditions, while promising candidates for AORFB systems already display potentials in the 0.8-1.2 V range.[3,4,5,6] In principle, the high tunability of organic molecules make it possible to design a large number of candidates which could fill the potential window, although some studies show that molecules that present high values of potential tend to decompose faster.[7] From my point of view, the stability of the molecule is a key parameter, and maybe it is better to sacrifice some potential in order to operate with a more stable candidate. Regarding energy density, the solubility of these compounds could be optimized to reach values higher than 4 M, although electrolytes with high concentration of redox active materials might show high viscosities which could translate into pumping energy losses.[8] Consequently, the typical capacity of promising organic redox active materials is around 40Ah/L, or even higher. Matching the potential and the capacity of the organic molecules, AORFB could reach energy densities around 32-48Wh/L, which are slightly higher than the energy density displayed by VRFB.

It is true that all these values are reported in the literature from an academic point of view, and a lot of work must be done to implement these organic redox active materials in the battery market. From my experience, organic electrolytes are a very promising candidates, but we must understand the differences between lab-scale prototypes and industrial scale. Hence, my recommendation is to use VRFB as starting point, while developing smaller AORFB stacks until same performance can be achieved.

Future in RFB

From my point of view, Vanadium RFB are well placed in the market and replacing them will be quite difficult in the short term, and there are many providers and customers that do not exist for AORFB at this moment. Over the next years, I will research and develop aqueous systems to be implemented in large scale in the future.

AORFB must be taken into account because of their advantages compared with Vanadium Redox Flow Batteries: neutral pH of the electrolytes, do not need to be used in combination with Nafion membranes, potentially cheaper redox active materials, environmentally sustainable, lower CAPEX and OPEX… I think that the

next battery will be a AORFB using symmetric cell design (in order to avoid the crossover of redox active materials, it is one of the major problems of organic molecules). There are reported organic molecules that show really low-capacity decay, display multielectron redox processes, and more importantly, are cost-effective.

References:

(1) Lourenssen, K.; Williams, J.; Ahmadpour, F.; Clemmer, R.; Tasnim, S. Vanadium Redox Flow Batteries: A Comprehensive Review. *Journal of Energy Storage* **2019**, *25*, 100844. https://doi.org/10.1016/j.est.2019.100844

(2) Singh, V.; Kim, S.; Kang, J.; Byon, H. R. Aqueous Organic Redox Flow Batteries. *Nano Res.* **2019**, *12*, 1988–2001. https://doi.org/10.1007/s12274-019-2355-2

(3) Luo, J.; Hu, B.; Debruler, C.; Bi, Y.; Zhao, Y.; Yuan, B.; Hu, M.; Wu, W.; Liu, T. L. Unprecedented Capacity and Stability of Ammonium Ferrocyanide Catholyte in PH Neutral Aqueous Redox Flow Batteries. *Joule* **2019**, *3*, 149–163. https://doi.org/10.1016/j.joule.2018.10.010

(4) DeBruler, C.; Hu, B.; Moss, J.; Liu, X.; Luo, J.; Sun, Y.; Liu, T. L. Designer Two-Electron Storage Viologen Anolyte Materials for Neutral Aqueous Organic Redox Flow Batteries. *Chem* **2017**, *3*, 961–978. https://doi.org/10.1016/j.chempr.2017.11.001

(5) Lv, X.-L.; Sullivan, P.; Fu, H.-C.; Hu, X.; Liu, H.; Jin, S.; Li, W.; Feng, D. Dextrosil-Viologen: A Robust and Sustainable Anolyte for Aqueous Organic Redox Flow Batteries. *ACS Energy Lett.* **2022**, *7*, 2428–2434. https://doi.org/10.1021/acsenergylett.2c01198

(6) Liu, Y.; Goulet, M.-A.; Tong, L.; Liu, Y.; Ji, Y.; Wu, L.; Gordon, R. G.; Aziz, M. J.; Yang, Z.; Xu, T. A Long-Lifetime All-Organic Aqueous Flow Battery Utilizing TMAP-TEMPO Radical. *Chem* **2019**, *5*, 1861–1870. https://doi.org/10.1016/j.chempr.2019.04.021

(7) Kwabi, D. G.; Ji, Y.; Aziz, M. J. Electrolyte Lifetime in Aqueous Organic Redox Flow Batteries: A Critical Review. *Chem. Rev.* **2020**, *120*, 6467–6489. https://doi.org/10.1021/acs.chemrev.9b00599

(8) Fan, H.; Wu, W.; Ravivarma, M.; Li, H.; Hu, B.; Lei, J.; Feng, Y.; Sun, X.; Song, J.; Liu, T. L. Mitigating Ring-Opening to Develop Stable TEMPO Catholytes for PH-Neutral All-Organic Redox Flow Batteries. *Adv Funct Materials* **2022**, *32*, 2203032. https://doi.org/10.1002/adfm.202203032

Annex C: Publications and conferences

The work presented in this doctoral thesis has given rise to the following publications in peer-reviewed international scientific journals:

Annex C: Publications and Conferences

Publications

1. **Juan Asenjo-Pascual**, Ivan Salmeron-Sanchez, Juan Ramón Avilés-Moreno, Pablo Mauleón, Petr Mazur, Pilar Ocón. Understanding Aqueous Organic Redox Flow Batteries: A Guided Experimental Tour from Components Characterization to Final Assembly. *Batteries* **2022**, *8*, 193. https://doi.org/10.3390/batteries8100193 (Impact Factor, IF=5.1).

2. **Juan Asenjo-Pascual**, Ivan Salmeron-Sanchez, Pablo Mauleon, Maddalen Agirre, Ana Catarina-Lopes, Oihane Zugazua, Eduardo, Sánchez-Díez, Juan Ramón Aviles-Moreno, Pilar Ocón. DFT Calculation, a Practical Tool to Predict the Electrochemical Behaviour of Organic Electrolytes in Aqueous Redox Flow Batteries. *J. Power Sources* **2023**, *564,* 232817. https://doi.org/10.1016/j.jpowsour.2023.232817 (Impact Factor, IF=9.794).

3. **Juan Asenjo-Pascual**, Cedrik Wiberg, Mahsa Shahsavan, Ivan Salmeron-Sanchez, Pablo Mauleon, Juan Ramon Avilés-Moreno, Pilar Ocón, Pekka Peljo. Sulfonate-Based Triazine Multiple-Electron Anolyte for Aqueous Organic Flow Batteries. *ACS Appl. Mater. Interfaces* **2023** (Accepted) https://doi.org/10.1021/acsami.3c05850. (Impact Factor, IF=10.383).

4. Ivan Salmeron-Sanchez, **Juan Asenjo-Pascual**, Juan Ramon Aviles-Moreno, Juan Carlos Pérez-Flores, Pablo Mauleon, Pilar Ocón. Chemical Physics Insight of PPy-baed Modified Ion Exchange Membranes: A Fundamental Approach. *J. Membr. Sci.* **2022**, *643*, 120020. https://doi.org/10.1016/j.memsci.2021.120020 (Impact Factor, IF=10.53).

5. Ivan Salmeron-Sanchez, **Juan Asenjo-Pascual**, Juan Ramon Aviles-Moreno, Pilar Ocón. Microstructural Description of Ion Exchange Membranes: The Effect of PPy-based Modifications. *J. Membr. Sci.* **2022**, *659*, 120771. https://doi.org/10.1016/j.memsci.2022.120771 (Impact Factor, IF=10.53).

6. Advances in Energy Research / *Chapter title: On latest advances in promising anion exchange membranes for electrochemical energy systems*. Ivan Salmeron-Sanchez, **Juan Asenjo-Pascual**, Juan Ramón Avilés-Moreno and Pilar Ocón. Accepted December **2022**. *NOVA publishers*.

7. Current Trends and Future Developments on (Bio-) Membranes: Recent achievements for ion-exchange membranes / *Chapter title: 2. Organic ion exchange membranes*. Ivan Salmeron-Sanchez, **Juan Asenjo-Pascual**, Juan Ramón Avilés-Moreno and Pilar Ocón. Accepted July **2022**. *Elsevier*.

Other publications (out of the thesis period)

1. Andrea Guerrero-Corella, **Juan Asenjo-Pascual**, Tushar Janardan Pawar, Sergio Díaz-Tendero, Ana Martín-Somer, Clarisa Villegas Gómez, José L. Belmonte-Vázquez, Diana E. Ramirez-Ornelas, Eduardo Peña-Cabrera, Alberto Fraile, Daviz Cruz Cruz, Jose Alemán. BODIPY as Electron Withdrawing Group for the Activation of Double Bonds in Asymmetric Cycloaddition Reactions. *Chem. Sci.* **2019**, *10*, 4346. https://doi.org/10.1039/C9SC00959K (Impact Factor, IF=5.938).

2. Tomas Rigotti,* **Juan Asenjo-Pascual**,* (coauthors) Ana Martín-Somer, Paula Milán Rois, Marco Cordani, Sergio Díaz-Tendero, Álvaro Somoza, Alberto Fraile, Jose Alemán. Boron Dipyrromethene (BODIPY) as Electron-Withdrawing Group in Asymmetric Copper-Catalyzed [3+2] Cycloadditions for the Synthesis of Pyrrolidine-Based Biological Sensors. Adv. Synth. Catal. **2020**, *362,* 1345. https://doi.org/10.1002/adsc.201901465 (Impact Factor, IF=9.974).

3. Claudio D. Navo, Nuria Mazo, Paula Oroz, Marta I. Gutiérrez-Jiménez, Javier Marín, **Juan Asenjo-Pascual**, Alberto Avenoza, Jesús H. Busto, Franciso Corzana, María M. Zurbano, Gonzalo Jiménez-Osés, Jesús M. Peregrina. Synthesis of Nβ-Substitued α,β-Diamino Acids via Stereoselective *N*-Michael Additions to a Chiral Bicyclic Dehydroalanine. *J. Org. Chem.* **2020**, *85*, 3134. https://doi.org/10.1021/acs.joc.9b03020 (Impact Factor, IF=4.354).

Conferences and Workshops

1. "V Workshop de la Red E3TECH / I Workshop Iberoamericano a Distancia 'Aplicaciones Medioambientales y Energéticas de la Tecnología Electroquímica' (V E3TECH) (online) POSTER CONTRIBUTTION: Estudio de Interacciones Electrolito/Membrana Mediante Cálculos DFT para Aplicaciones en Baterías de Flujo **Juan Asenjo-Pascual**, Iván Salmeron Sanchez, Eduardo Sánchez Díez, Pablo Mauleon, Juan Ramón Aviles Moreno, Pilar Ocón. ASSISTANCE to the I Jornadas E3TECH 'La tecnología electroquímica al servicio de la Sociedad: aplicaciones en medio ambiente y energía'." October 2020.

2. REDOXFLOW2020 organized by Group De Recherche RedoxFlow Nancy (France)" (online) ORAL CONTRIBUTTION: Synthesis, Characterization and DFT Calculation of New Bipyridine-type Electrolytes for Aqueous Redox Flow Batteries **Juan Asenjo-Pascual**, Iván Salmeron Sanchez, Eduardo Sánchez Díez, Pablo Mauleon, Juan Ramón Aviles Moreno, Pilar Ocón. November 2020.

3. NEXT GENERATION – Flow Battery Conference and Networking Event organized by Fraunhofer ICT (Germany) (online) ORAL CONTRIBUTTION: DFT Calculation, a Practical Tool for Predicting the Electrochemical Behaviour of Organic Electrolytes. **Juan Asenjo-Pascual**, Iván Salmeron Sanchez, Eduardo Sánchez Díez, Pablo Mauleon, Juan Ramón Aviles Moreno, Pilar Ocón. ASSISTANCE to the FLORES Networking Workshop. July 2021.

4. Prague Flow Battery Seminar 2021 organized by Laboratory of Energy Storage of University of Chemistry and Technology Prague (Czech Republic) (online) ORAL CONTRIBUTTION: Organic Redox Active Materials; on the Importance of Using DFT Calculation for the Design of New Electrolytes. **Juan Asenjo-Pascual**, Iván Salmeron Sanchez, Eduardo Sánchez Díez, Pablo Mauleon, Juan Ramón Aviles Moreno, Pilar Ocón. October 2021.

5. Nordic Flow Battery Network: Autumn School. Turku (Finland) ORAL CONTRIBUTTION: Organic Redox Active Materials; on the Importance of Using DFT Calculation for the Design and Understand New Electrolytes. **Juan Asenjo-Pascual**, Iván Salmeron Sanchez, Eduardo Sánchez Díez, Pablo Mauleon, Juan Ramón Aviles Moreno, Pilar Ocón. November 2021.

6. I HIGREEW Wokshop "The crucial role of energy transition: Redox Flow Batteries and their Future in Energy Storage. CONTRIBUTTION: Membrane Development for RFBs. Iván Salmeron Sanchez, **Juan Asenjo-Pascual**, Eduardo Sánchez Díez, Pablo Mauleon, Juan Ramón Aviles Moreno, Pilar Ocón. March 2022.

7. Nordic Flow Battery Network: Autumn School. Turku (Finland) ORAL CONTRIBUTTION: Organic Redox Active Materials; on the Importance of Using DFT Calculation for the Design and Understand New Electrolytes. **Juan Asenjo-Pascual**, Iván Salmeron Sanchez, Eduardo Sánchez Díez, Pablo Mauleon, Juan Ramón Aviles Moreno, Pilar Ocón. November 2021.

8. BALIHT Workshop I. Novel technologies and components for organic redox flow batteries. Online. April 2023. Attender.

9. HIGREEW Final Workshop. Vitoria Gasteiz (Spain). May 2023. Attender.

10. International Flow Battery Forum 2023. Prague (Czech Republic) Attender. June 2023.

International Secondment

Research stay in the group of Research in Battery Materials and Technologies of Turku University (Finland) under the supervision of Prof. Pekka Peljo (July to November 2022).

The purpose of the stay was the development, characterization, and evaluation of new triazine based anolytes for Aqueous Redox Flow Batteries systems. Besides, basic theoretical and experimental concepts about solid boosters and their applicability in Aqueous Flow Batteries. This stay gave rise to the scientific contribution number **3** entitled: Sulfonate-Based Triazine Multiple-Electron Anolyte for Aqueous Organic Flow Batteries and the work is summarized in **chapter 1** and **3**.